

© 2017

Max Loeb Balter

ALL RIGHTS RESERVED

ROBOTIC DEVICES FOR AUTOMATED
VENIPUNCTURE AND
DIAGNOSTIC BLOOD ANALYSIS

BY MAX LOEB BALTER

A dissertation submitted to the
Graduate School—New Brunswick
Rutgers, The State University of New Jersey
and

The Graduate School of Biomedical Sciences

In partial fulfillment of the requirements

For the degree of

Doctor of Philosophy

Graduate Program in Biomedical Engineering

Written under the direction of

Dr. Martin L. Yarmush

And approved by

New Brunswick, New Jersey

May, 2017

ABSTRACT OF THE DISSERTATION

Robotic Devices for Automated Venipuncture and Diagnostic Blood Analysis

by Max Loeb Balter

Dissertation Director: Dr. Martin L. Yarmush

Diagnostic blood testing is the most ubiquitous clinical procedure in the world, and influences 80% of medical decisions made in hospital, ambulatory, and primary care settings. However, manual blood draw success rates depend heavily on clinician skill and patient physiology, and results are generated almost exclusively in centralized labs from large-volume samples using labor-intensive analytical techniques. This dissertation describes the development of a medical device that enables complete end-to-end blood testing by performing blood draws and providing diagnostic results in fully automated fashion. The device couples an image-guided venipuncture robot, to address the challenges of routine venous access, with a centrifuge-based blood analyzer to obtain quantitative measurements of hematology within minutes of the sample collection. The system uses 3D near-infrared and ultrasound imaging to guide the robotic needle insertion, a sample handling module to deliver the sample to the processing unit, and an analyzer capable of performing multi-analyte detection. In a series of engineering tests, phantom studies, and motion tracking experiments, the venipuncture robot demonstrated sub-millimeter accuracy, real-time needle servoing in response to moving targets, and improved cannulation success rates compared to manual techniques. Multi-analyte detection was then demonstrated on the blood analyzer through white blood cell counting using a bulk-cell analysis approach, and an absorption-based hemoglobin assay. Once translated, this technology has the potential to impact a number of clinical environments, including laboratory testing facilities, pediatric hospitals, oncology care centers, and emergency settings. The underlying technological advancements cover a spectrum of research disciplines, including hematology and diagnostic medicine, optics and microfluidics, as well as robotics and medical device development.

ACKNOWLEDGEMENTS

First and foremost I would like to thank Dr. Alvin Chen who was an incredible mentor, research partner, and friend throughout this journey. Words cannot express my gratitude for your tutelage and guidance over the years. Working side-by-side with you was an absolute pleasure and I will be forever grateful for this experience.

I would like to thank my advisors, Dr. Martin Yarmush and Dr. Tim Maguire, for their support and encouragement throughout this endeavor. Dr. Yarmush always believed in me, and gave me the opportunity and independence to flourish in his lab. I am grateful for all the scientific insights and life lessons you have taught me that will be remembered well beyond graduate school. I would like to thank Dr. Tim Maguire, who was the most passionate advisor one could have. It was a privilege working with you on all sorts of exciting projects and being exposed to the business side of technology development. I would also like to thank my committee members, Dr. Mark Pierce and Dr. Kevin Nikitzuk, for providing me with invaluable feedback.

I would like to acknowledge all the brilliant people in the Yarmush group for making the lab a stimulating and fun place to work. Special thanks to Dr. Mehdi Ghodbane who served as a great role model who I continue to look up to today. Much thanks to my friends I met at Rutgers, specifically, Dr. Jack Zheng, Dr. Jean Lo, Alex Fromholtz, and Alex Gorshkov. You guys are some of the friendliest, most down-to-earth people I know. I would also like to express my gratitude to all the undergraduates who contributed to the project. It was a pleasure teaching and learning from so many students. Special thanks to Brian Bixon, Amara Colinco, Siva Yedithi, and Nick Demaio.

Finally, large sections of this dissertation are composed of articles already published or in review for publication (¹⁻¹⁰). To my dear reader, please refer to these articles for a more succinct discussion of this work.

DEDICATION

I would like to dedicate this thesis to my family. You have always encouraged me to pursue my passions no matter how weird or nerdy they may be. Mom, ever since you bought me my first Lego set, I fell in love with engineering and never looked back. You have always been my number one supporter and I am forever grateful for the opportunities you have provided me. Dad, we have shared so many incredible memories over the years and I appreciate all that you have done for me. Emily and Sam, you were awesome siblings—enough said. And Jackie, your compassion, care, and patience over the past few years has been amazing.

TABLE OF CONTENTS

Abstract	ii
Acknowledgements	iii
Dedication	iv
List of Tables	xiii
List of Figures	xiv
1. Introduction	1
1.1. Diagnostic Blood Testing	1
1.2. Venipuncture	2
1.3. Imaging Assist Devices	4
1.3.1. US Imaging Technology	4
1.3.2. VIS Light Imaging Technology	7
1.3.3. NIR Light Imaging Technology	8
1.3.4. Bimodal Imaging Technology	9
1.3.5. Summary of Imaging Technologies	10
1.4. Medical Robotics	10
1.4.1. Needle Insertion Robots	11
1.4.2. Venipuncture Robots	12
1.5. Lab Testing	17
1.5.1. Point-of-Care Testing	18
1.5.1.1. Finger-prick vs. Venipuncture	19
1.5.1.2. Limited Assay Menu	19
1.5.1.3. Central Lab Testing	20
1.5.2. Centrifugal Microfluidics	21
1.5.3. Complete Blood Counting	21
1.5.4. Previous Work on Leukocyte Counting	22

1.5.5.	End-to-end Lab Automation	24
1.6.	Summary and Scope of Thesis	25
1.6.1.	Device Overview	25
1.6.2.	Novel Contributions	27
2.	Development of Robotic Venipuncture Devices	29
2.1.	First-generation Device	29
2.2.	Second-generation Device	29
2.2.1.	Venipuncture work-flow	31
2.2.2.	System Architecture	32
2.2.2.1.	Hardware	33
2.2.2.1.1.	Optical and US Image Acquisition	33
2.2.2.1.2.	7-DOF Robot	34
2.2.2.1.3.	Central Processor	34
2.2.2.2.	Software	35
2.2.2.2.1.	Automated Stereo Camera Calibration	35
2.2.2.2.2.	Automated Ultrasound Calibration	36
2.2.2.2.3.	Vein Segmentation and Image Guidance	37
2.2.3.	Needle Manipulator	38
2.2.3.1.	Serial Arm Design	38
2.2.3.2.	Kinematics	42
2.2.3.3.	Motor Torque and Power Calculations	45
2.2.3.4.	Motor Selection	46
2.2.3.5.	Motor Control System	48
2.2.3.6.	Open Loop Transfer Functions	50
2.2.4.	Automated Needle Handling	53
2.2.4.1.	Needle Grip-and-Release Mechanism	54
2.2.4.2.	Needle Re-loader Mechanism	55
2.2.4.3.	Needle Uncapping System	56

2.2.5.	Experimental Testing	57
2.2.5.1.	Control Loop Simulations	57
2.2.5.2.	Serial Arm Tracking Experiments	59
2.2.5.3.	Needle Positioning Testing	61
2.2.5.4.	Phantom Cannulation Testing	65
2.3.	Third-generation Device	67
2.3.1.	System Design Overview	69
2.3.1.1.	Host Processor	69
2.3.1.2.	Base Positioning System	70
2.3.1.3.	Compact Manipulator Unit	71
2.3.1.3.1.	NIR Imaging	73
2.3.1.3.2.	US Imaging	74
2.3.1.3.3.	Force Sensing	74
2.3.1.4.	Robot Kinematics	75
2.3.1.5.	Vision, Ultrasound, and Force-based Motion Control	76
2.3.1.6.	Human Factors Components	78
2.3.1.6.1.	Arm rest	78
2.3.1.6.2.	Automated Consumables Handling	79
2.3.2.	Experimental Testing	81
2.3.2.1.	Kinematic Workspace Simulations	81
2.3.2.2.	Free-space Positioning	82
2.3.2.3.	Stereo Vision Guidance	85
2.3.2.4.	Ultrasound Guidance	88
2.3.2.5.	Force Sensing	90
2.3.2.6.	Force Guidance	92
2.3.2.7.	Phantom Cannulation Testing	93
2.3.2.8.	Modeling Needle Tissue Interaction	96
2.3.2.8.1.	Computational Models	96
2.3.2.8.2.	Experimental Evaluation	98

2.3.3.	Summary and Outline of Future Work	102
2.4.	Ultrasound Computer Vision Algorithms	105
2.4.1.	Needle Localization & Tracking	107
2.4.1.1.	Needle Detection & Tracking Methods	107
2.4.1.1.1.	Corner Detector & Kalman Filter	108
2.4.1.1.2.	Gabor Filter & Hough Transform	110
2.4.1.2.	Experimental Results	112
2.5.	Summary and Discussion	115
2.5.1.	Merits and Pitfalls of Automated Venipuncture	116
3.	Development of Blood Diagnostic Devices	117
3.1.	Sample Handling Module	119
3.1.1.	First-generation Design	119
3.1.2.	Second-generation Design and Prototype	120
3.1.2.1.	Blood Collection Carousel	120
3.1.2.2.	Syringe Pump	122
3.1.3.	Third-generation Design and Prototype	124
3.1.3.1.	Integrated Blood Collection Carousel	125
3.1.3.2.	Peristaltic Fluid Delivery	125
3.1.3.3.	System Evaluation	126
3.1.3.3.1.	Experimental Protocol	126
3.1.3.3.2.	Results	127
3.1.4.	Fourth-generation Design and Prototype	127
3.1.4.1.	Design Improvements	130
3.1.4.2.	Sample Dispenser Unit	131
3.2.	Static WBC Counting Device	133
3.2.1.	First-generation Microscope Design	133
3.2.2.	Sample Labeling & Detection Chip Design	136
3.2.3.	WBC Segmentation & Subtype Classification	137

3.2.3.1.	Background	138
3.2.3.2.	Algorithm Development	139
3.2.3.3.	Classification of WBC Subtypes	141
3.2.4.	Experimental Testing	143
3.2.4.1.	Lab Microscope	143
3.2.4.2.	Custom-built Microscope	144
3.2.5.	Limitations with Static Cell Counting	147
3.3.	Optical Absorption Device	148
3.3.1.	Absorption Methodology	149
3.3.2.	Absorption Testing Instrument	150
3.3.2.1.	Detection Chips	151
3.3.2.2.	Experimental Methods	152
3.3.3.	Experimental Testing	153
3.3.4.	Summary and Future Work	157
3.4.	Centrifuge Blood Analyzer	159
3.4.1.	First-generation Analyzer	159
3.4.1.1.	Chip Design and Fabrication	161
3.4.1.2.	Experimental Methods & Results	162
3.4.1.3.	Limitations	163
3.4.2.	Second-generation Analyzer	164
3.4.2.1.	Centrifuge	164
3.4.2.2.	Microfluidic Chip	165
3.4.2.3.	Optical Detection System	165
3.4.2.4.	Blood Analysis of Simulated White Cell Count	166
3.4.2.4.1.	Experimental Protocol	166
3.4.2.4.2.	Results	167
3.4.2.5.	Limitations	168
3.4.3.	Third-generation Analyzer	168
3.4.3.1.	Experimental Materials & Methods	170

3.4.3.1.1.	Leukocyte Staining Methodology	170
3.4.3.1.2.	Second-gen Fluorescent Microscope	171
3.4.3.1.3.	Glass Capillary Tube Testing	173
3.4.3.1.3.1.	Image Acquisition and Processing	173
3.4.3.1.4.	Acrylic Chip Testing	176
3.4.3.1.4.1.	Image Acquisition and Processing	178
3.4.3.2.	Experimental Results	178
3.4.3.2.1.	Glass Capillary Tube Testing	178
3.4.3.2.2.	Acrylic Chip Testing	183
3.4.3.3.	Discussion	184
3.4.4.	Detection of Cells, Proteins, and Chemistries On-chip	186
3.4.4.1.	Chip Design	191
3.4.4.2.	Capillary Burst Valves	193
3.4.4.2.1.	Numerical Burst Frequency Calculations	194
3.4.4.2.2.	Experimental Testing	195
3.4.4.2.2.1.	Test Platform	195
3.4.4.2.2.2.	Numerical and Experimental Results	197
3.4.4.3.	Plasma Extraction via On-chip Pumping	198
3.4.4.3.1.	Chip Design	200
3.4.4.3.2.	Chip Fabrication	202
3.4.4.3.3.	Experimental Testing	204
3.5.	Summary and Discussion	206
4.	Conclusion	208
4.1.	Summary	208
4.2.	Future Directions	210
4.2.1.	Venipuncture Robot	210
4.2.1.1.	Human Factors Engineering	210
4.2.1.2.	Maintenance Considerations	211

4.2.1.3.	Cost Considerations	212
4.2.1.4.	Device Miniaturization	212
4.2.1.5.	Embedded System Design	213
4.2.2.	Medical Robotics	214
4.2.3.	Diagnostic Blood Testing	215
4.2.3.1.	POC Technology	216
4.2.3.2.	Common Versus Esoteric Testing	217
4.2.4.	Robots of the Future	218
Appendix A.	Venipuncture Robot	219
A.1.	Derivation of Kinematic Equations—Gen-2 4-DOF Manipulator	219
A.2.	Gen-2 Manipulator Motor Torque and Power Calculations	221
Appendix B.	Blood Diagnostic Devices	226
B.1.	Centrifuge Blood Analyzer	226
B.1.1.	Image Processing for Quantifying Buffy Coat Areas	226
B.1.1.1.	Image Acquisition and Image Loading	226
B.1.1.2.	Grayscale Conversion	227
B.1.1.3.	Merging Green and Red Channel Images	227
B.1.1.4.	Image Processing and Quantification of Buffy Coat	227
B.1.1.4.1.	Green Channel Images	227
B.1.1.4.2.	Red Channel Images	228
B.1.2.	Printed Circuit Board Design Details	229
Appendix C.	Device Troubleshooting	233
C.1.	Design and Prototyping	233
C.2.	Motor and Sensor Integration	234
C.3.	Motor Control	235
Appendix D.	Equipment User Manuals	237
D.1.	Stratasys Mojo 3D-Printer	237

D.2. Epilog Zing 24, 60 W Laser Cutter	243
D.3. Stika Vinyl Cutter	253
References	279

LIST OF TABLES

1.1. Venipuncture robot design requirements	15
2.1. DH-parameters of the second-gen device	43
2.2. Motor torque and power requirements for the serial arm	46
2.3. Summary of selected motors for the serial arm	48
2.4. Motor constants used for the open loop transfer function modeling.	52
2.5. Needle tip positioning results	63
2.6. Kinematic joint space of the third-gen device	76
2.7. DH-parameters of the third-gen device	76
2.8. Needle tip positioning errors in the third-gen device	85
2.9. US vessel tracking results	90
2.10. Mechanical properties used for vein rolling simulations	99
2.11. US needle tracking results	114
3.1. Experimental design for Vacutainer collection time	127
3.2. Physical properties of WBCs	134
3.3. Color-coded leukocyte counting approach	171
3.4. Porcine blood sample control levels	173
3.5. Estimated monocytes from pixel clustering	181
3.6. Centrifuge spin profile for plasma extraction	204
B.1. Electronic circuit board components	231

LIST OF FIGURES

1.1. Centralized lab testing	2
1.2. Costs associated with difficult venous access	4
1.3. US-guided venipuncture	5
1.4. Venipuncture assisted with the Sonic Window device	6
1.5. Veinlite VIS light imaging device	7
1.6. Accuvein AV400 NIR light imaging device	8
1.7. Summary of imaging assist technologies	10
1.8. Bloodbot robotic venipuncture device	13
1.9. Semi-automated venipuncture device	13
1.10. Phlebot robotic venipuncture device	14
1.11. Veebot automated venipuncture robot	15
1.12. Design of the first-gen venipuncture robot	16
1.13. Example POC blood analyzers	18
1.14. Blood test ordering patterns in the ED	20
1.15. HemoCue WBC Diff POC blood analyzer	23
1.16. The QBC Star POC blood analyzer	23
1.17. Automated blood testing and analysis device	25
1.18. Fully integrated device concept design	26
1.19. Fully integrated device prototype	27
2.1. Design of the second-gen venipuncture robot	30
2.2. System architecture of the second-gen device	32
2.3. Stereo camera calibration	35
2.4. Ultrasound image calibration	37
2.5. Overview of image processing routine in the second-gen device	38
2.6. Serial manipulator design of the second-gen device	40
2.7. Operating workspace of the second-gen device	44

2.8. Motor control scheme of the second-gen device	50
2.9. Serial arm DC-brushed motor model	51
2.10. Needle gripping and release mechanisms	55
2.11. Needle re-loader of the second-gen device	56
2.12. SimuLink block diagram for motor control	57
2.13. Serial arm tracking study – qualitative results	60
2.14. Serial arm tracking study – quantitative results	61
2.15. Experimental setup of needle positioning testing	62
2.16. Needle tip positioning errors maps	64
2.17. Phantom cannulation testing	66
2.18. Design of the third-gen venipuncture robot	68
2.19. System architecture of the third-gen venipuncture robot	70
2.20. Needle manipulator of the third-gen venipuncture robot	72
2.21. Catheter insertion mechanism	73
2.22. Motion control scheme in the third-gen device	77
2.23. Arm rest concept design and prototype	79
2.24. Automated needle handling and consumables	80
2.25. Kinematics of the third-gen device	82
2.26. Dexterous workspace of the third-gen device	83
2.27. Needle tip positioning studies with the third-gen device	84
2.28. Stereo vision tracking experimental setup	86
2.29. Stereo vision tracking results	87
2.30. US-guided vessel tracking experimental setup	88
2.31. US-guided vessel tracking results	89
2.32. Force sensing concept mechanism	91
2.33. Force sensing testing apparatus	92
2.34. Preliminary force sensing results	92
2.35. Bimodal force sensing	93
2.36. Force guided needle insertion	94

2.37. Phantom cannulation testing with the third-gen device	95
2.38. Beam bending model for rolling veins	97
2.39. Simulated and experimental vessel deformation studies	100
2.40. Robotic needle guidance in response to vessel motion	101
2.41. Robotic needle guidance in response to vessel motion	106
2.42. Needle tracking experimental set-up	108
2.43. Needle tracking via corner detector and kalman filtering	111
2.44. Needle tracking via Gabor filtering and the Hough Transform	113
3.1. Design of the blood draw and analysis device	118
3.2. Blood collection carousel initial prototype	121
3.3. Miniaturized blood collection carousel	122
3.4. Syringe pump initial design and prototype	123
3.5. Miniaturized syringe pump prototype	123
3.6. Sample handling module process flow, steps 1–3	124
3.7. Sample handling module process flow steps 4–6	125
3.8. Collection carousel & peristaltic pump testing	128
3.9. Tube switching pump design	129
3.10. Redesign of tube switching pump	131
3.11. Sample dispenser design	132
3.12. Dispenser pump prototype	133
3.13. Design of the first-gen microscope	134
3.14. Prototype of the first-gen microscope	135
3.15. First-gen microfluidic chip design	137
3.16. Single WBC segmentation scheme	140
3.17. Microscope image acquisition	141
3.18. WBC subtype classification	142
3.19. WBC morphological feature extraction	142
3.20. WBC segmentation in 40x microscopy images	143
3.21. WBC segmentation in 10x microscopy images	144

3.22. 5.5x WBC images from custom-built microscope	145
3.23. 22.2x WBC images from custom-built microscope	146
3.24. Design and prototype of the photometry module	149
3.25. Absorption coefficients for Hgb and water	150
3.26. HemoCue Hgb absorption chip	151
3.27. Custom acrylic chip for absorption studies	152
3.28. Hgb absorption results: HemoCue chip + bright LED	153
3.29. Hgb absorption results: HemoCue chip + standard LED	154
3.30. Hgb absorption results: custom chip + bright LED	155
3.31. Hgb absorption results: custom chip + standard LED	156
3.32. Hgb absorption: comparison of standard and bright LED	157
3.33. Glu absorption results: HemoCue chip + standard LED	158
3.34. First-gen centrifuge analyzer	160
3.35. Components of the first-gen centrifuge analyzer	160
3.36. Early chip designs for the centrifugal analyzer	161
3.37. Experimental testing of the first-gen centrifuge analyzer	162
3.38. Absolute WBC standard curve from first-gen analyzer	163
3.39. Simulated WBC count on the centrifuge analyzer	167
3.40. Differential leukocyte counting via bulk-cell analysis	169
3.41. Second-gen fluorescent microscope	172
3.42. Expanded buffy coat in capillary tubes	174
3.43. Buffy coat image acquisition and processing in capillary tubes	175
3.44. Acrylic chip leukocyte testing	177
3.45. Variability in capillary tube buffy coat measurements	179
3.46. WBC standard curves: length of buffy coat in capillary tubes	180
3.47. WBC standard curves: area of buffy coat in capillary tubes	181
3.48. 3-part WBC counting via pixel clustering	182
3.49. WBC standard curves: area of buffy coat in acrylic chips	183
3.50. Centrifuge-based blood analyzer design concept	187

3.51. Centrifuge blood analyzer design with electronics	188
3.52. Centrifuge blood analyzer prototype	189
3.53. Centrifuge analyzer electrical adapter design	190
3.54. Fabricated electrical adapter circuit board	190
3.55. Blood analyzer prototype with tube switching pump	191
3.56. Blood analyzer CD-like disc concept	192
3.57. Centrifuge test platform	195
3.58. Capillary burst valve visualization	197
3.59. Capillary burst valve results	199
3.60. Centrifugal capillary-based pumping	200
3.61. Centrifugo-pneumatic pumping	201
3.62. Centrifugo-pneumatic pumping chip designs	202
3.63. Centrifugo-pneumatic pumping chip design exploded view	203
3.64. Five-layer chip fabrication and assembly	203
3.65. Centrifugo-pneumatic pump testing	205
4.1. Semi-automated venipuncture device design	213

Chapter 1

Introduction

1.1 Diagnostic Blood Testing

Diagnostic blood testing is the most common medical routine performed in the world, and in many ways, forms the cornerstone of modern medicine¹¹. Specifically, in the U.S., blood tests are performed 2 billion times each year and influence 80% of medical decisions made in hospital, ambulatory, and primary care settings^{12,13}. However, blood draw success rates depend heavily on clinician skill and patient physiology, and diagnostic results are generated almost exclusively in centralized labs from large-volume blood samples using labor-intensive analytical techniques¹⁴.

As seen in Fig. 1.1, samples are traditionally drawn manually by venipuncture, analyzed in a centralized lab, and then results are returned to the medical staff to guide the intervention. This approach requires the transport of samples to a testing facility, as well as highly trained personnel to run the analyses on large, bench-top instruments, resulting in long turnaround times, on the order of hours to days. Unexpected delays and errors can also arise due to difficulties in performing the venipuncture and from inefficiencies during the transport and subsequent analysis of the blood sample. Such delays have been shown to reduce specimen quality and increase turnaround times, potentially leading to erroneous test results, misguided treatment plans, and lengthened hospital stays^{15–20}. Delays are particularly common in difficult patients, such as children, elderly, chronically-ill and obese populations, where small and fragile vessels or high levels of body fat may reduce the visibility of veins or make them more difficult to accurately puncture^{21–23}.

The accuracy and turnaround time of blood testing is especially important in time critical settings such as the emergency department (ED). Of the 350 million tests performed in U.S. EDs each year, 25% are given urgent priority, indicating a turnaround time of 30–60 min, and 15% are given emergent priority, indicating a turnaround time of 15–30 min^{13,24}. In these situations, failing to recognize the onset of critical conditions may have harmful

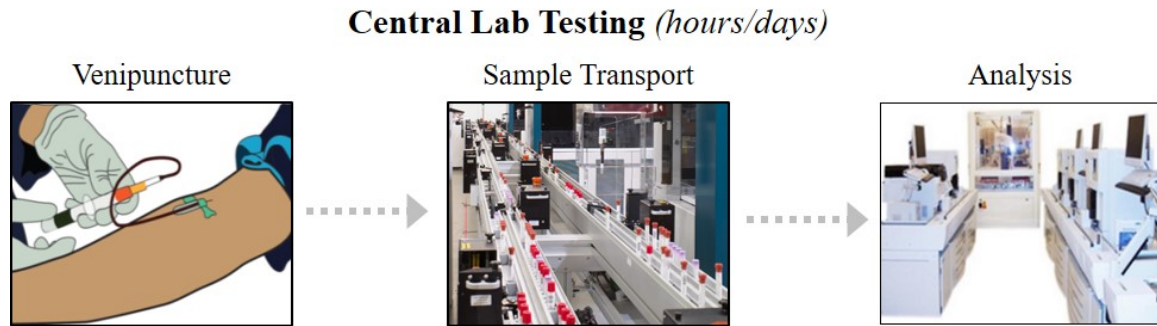


Figure 1.1: The standard approach for blood testing includes three major steps: (1) performing the venipuncture, (2) transporting samples to a centralized lab, and (3) running the analysis. Finally, results are then returned to the medical staff to guide the intervention. Delays and errors can occur along each step in the process.

consequences^{25,26}. **Hence, there is a need for a device that can rapidly withdraw blood and run diagnostic analyses in a single automated step, particularly in emergency care settings.**

The following sections in Chapter 1 will first discuss the challenges associated with venipuncture and subsequently diagnostic blood testing. A summary concludes the chapter, which highlights the key components of the automated blood testing and analysis device, and outlines the scope of this dissertation.

1.2 Venipuncture

Venipuncture—the process of introducing a needle into a suitable vessel—is the first step in diagnostic blood testing and for delivering fluids to the venous bloodstream. The procedure is traditionally guided by visual inspection and palpation of the peripheral forearm veins. Once a suitable vein is located, a needle is then inserted into the center of the vessel. Oftentimes however, it is difficult to estimate the depth of the vein or steer the needle if the vein moves or rolls. In these situations, it is easy for the needle tip to slip and miss the vessel or pierce through the back of the vein wall. Poorly introduced needles may then result in complications such as increased pain, internal bleeding, or extravasation^{27–29}. Moreover, manual needle insertion requires complex visuomotor coordination in real-time, and the success rate is highly dependent on clinician skill and experience.

The challenges of venipuncture are exacerbated in obese and dark-skinned patients where

locating a vein can be difficult, as well as in pediatric and geriatric populations where the veins are often small and weak. In these cases, success rates are highly dependent on patient physiology. For these difficult case, failure rates can be as high as 70%³⁰, whereas for the general U.S. population, failure rates are reported to be around 33%^{29,31}. For the case of delivering vital fluids to the peripheral circulation, repeated failure to start an intravenous (IV) line may necessitate alternative pathways such as central venous catheters or peripherally inserted central catheters^{32,33} that incur a much greater safety risk to the patient and practitioner, as well as added time and cost to the procedure^{21,33–35}. These alternative pathways have also been shown to increase the chance of tissue damage and blood-borne disease transmission, such as Hepatitis B (HBV), Hepatitis C (HCV), and Human Immunodeficiency virus (HIV).

An estimated 100K blood-borne infections are reported to occur annually due to accidental needle stick injuries among healthcare workers,³⁴ with the majority being HBV transmission (76K). The resulting cost of a needle stick injury includes post-exposure care, treatment of the illness, lost work time, psychological stress, as well as time and money to investigate the source of the accident. As a result, **venipuncture is the number one cause of patient and clinician injury in the U.S.**, where up to 1 and 2 million injuries are reported each year for practitioners, and patients respectively^{21,34–37}.

Consequently, due to the ubiquity of venipuncture, the high failure rate, and the high incidence of injury, difficult venous access (DVA) is estimated to cost the U.S. healthcare system \$4.7B annually^{27,38}. Fig. 1.2 shows the escalating costs associated with DVA in a standard venipuncture ward in the U.S.

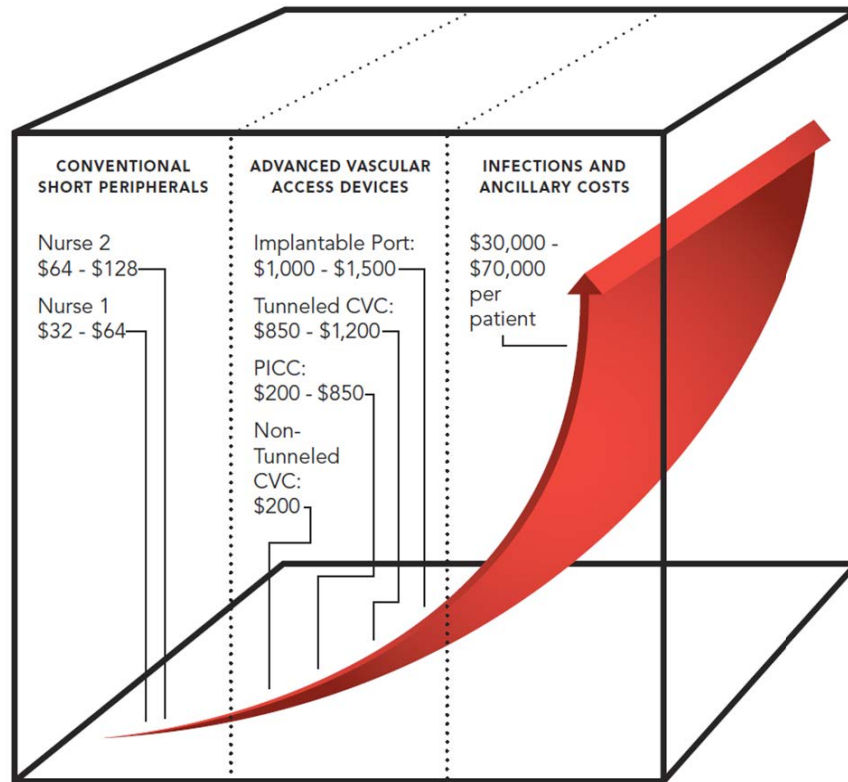


Figure 1.2: Escalating costs associated with difficult venous access. Costs stem from disposables, time, alternative pathways, and complications. *CVC* = Central Venous Catheter; *PICC* = Peripherally Inserted Central Catheter. Image obtained from Christie Medical Holdings, Inc.³⁹

1.3 Imaging Assist Devices

To address the challenges of venipuncture, various imaging technologies have been developed to aid clinicians in finding veins that utilize ultrasound (US)^{40,41}, visible (VIS) light^{42,43}, or near-infrared (NIR) light⁴⁴⁻⁵².

1.3.1 US Imaging Technology

Medical US systems have become widely adopted in recent years due to the increasing computing power of electronics, as well as the flexibility of these systems to operate in multiple clinical environments⁵³. Recently several US devices have been commercialized as plug-and-play portable systems for personal laptops and tablets that can display high resolution images of internal organs⁵⁴⁻⁵⁶. Acoustic waves can penetrate readily into human

tissue, allowing both superficial and deep tissue structures to be visualized by controlling the transducer frequency⁵⁷. However, US-guided venipuncture is a non-intuitive process that requires significant clinician skill and experience to steer the needle into the target vein. In many cases, a second operator is needed—one clinician to orient the probe on the patient, and the other to insert the needle (as seen in Fig. 1.3). This disrupts and prolongs the venipuncture protocol, and also involves learning new visuomotor skills since the US screen is placed away from the patient and practitioner, making it difficult to simultaneously watch the image and cannulate the vein. Furthermore, it is often difficult to observe the needle in the US image due to erratic back-scatter from the metallic material. Image artifacts and speckle can also reduce the signal quality, especially in high Body Mass Index (BMI) populations, where the acoustic signal can be heavily attenuated due to dense adipose in the hypodermis⁵⁸.



Figure 1.3: Two clinicians performing US-guided venipuncture. One clinician is tasked with orienting the probe on the patient, while the other inserts the needle. Image obtained from Constantino et al⁵⁹.

Recent attempts to move the US image closer to the patient, have resulted in a device called the Sonic Flashlight which displays the image directly on the patient's skin⁶⁰. A flat-panel display coupled with a half-silvered mirror is mounted directly to the transducer

to superimpose an image of the underlying vasculature. This allows the clinician to focus directly on the patient during cannulation, as opposed to looking away at an external monitor. However, the resulting image overlaid on the patient is small, because the underlying tissue structures need to be displayed in real anatomical scale for proper image registration. Lacking magnification, the clinician may be unable to visualize small veins, and unable to discern vessels from other surrounding tissue.

A similar hand-held device, the Sonic Window (BK Ultrasound, Analogic, Inc.), uses C-mode US imaging to display a longitudinal view of the vessel on the user interface directly above the site⁵⁶. In this fashion, the image displays the vessel in real anatomical scale to assist with performing the needle insertion. An interesting feature of the device is real-time tracking, in which the depth of the US scan is automatically adjusted to center the vessel in the image for enhanced visibility. So far, the device has only been used to puncture large vessels, on the order of 5 mm in diameter or greater, for example, in dialysis procedures. It may be challenging to image vessels <3 mm in diameter, due to the small display screen and lack of magnification capabilities.



Figure 1.4: US-guided venipuncture with the Sonic Window device⁶¹.

Several other products exist that help clinicians perform US-guided vessel punctures. One example is the Pinpoint disposable (Bard Medical, C. R. Bard, Inc.) that offers a sterile cap and needle guide that attaches to standard US transducers to assist with the

needle insertion. A common source of error in US-guided interventions is losing the needle in the image due to an off-plane insertion. With the use of a needle guide, the device ensures that the needle is maintained within the US image plane throughout the procedure. However, transducers have unique geometries and trying to adapt devices to conform to these unique designs is challenging and may be impractical.

Another auxiliary product to facilitate percutaneous needle insertions is the eZGuide guidance technology (ezono AG). This device uses electromagnetic needle tracking technology to enable visualization of the needle in any plane. Nonetheless, the clinicians is still tasked with inserting the needle free-hand, and the system requires the use of needles that are made of materials that can be magnetized. Both of these limitations will likely prevent the device from being used for venipuncture procedures.

1.3.2 VIS Light Imaging Technology

The second category of assist devices takes advantage of visible light (400–700 nm wavelength) to image veins. Two such devices that have reached market penetration include the Venoscope Vein Finder⁴³ (Venoscope, LLC) and the Veinlite LEDX⁴² (TransLite, LLC). Fig. 1.5 shows an image of the Veinlite device.



Figure 1.5: Venipuncture assisted with the Veinlite VIS light imaging device⁶².

Due to the limited penetration depth of VIS light through human skin tissue (i.e., <3 mm), these systems have been predominately used to assist with performing neonatal

and infant venipunctures. In these cases, the device makes contact with the skin, transilluminating vessels from underneath the forearm or hand. Similar to US imaging technology, the need to make contact with the arm of the patient complicates the procedure, and requires the use of a sterile barrier. Moreover, other disadvantages of transillumination techniques include the risk of burns (due to the device making contact with the skin) and the need to reduce ambient lighting to improve visibility⁶³. Alternative uses for VIS light devices include sclerotherapy for spider and varicose vein treatment, where the limited penetration depth is not a factor in these superficial vein therapies.

1.3.3 NIR Light Imaging Technology

The final category consists of NIR imaging devices, two of which have achieved prominent market entry: the VeinViewer^{39,48} (Christie Medical Holdings, Inc.) and the AV400 System⁶⁴ (AccuVein, Inc.). These devices image veins under NIR light and project a picture of the underlying vasculature onto the skin to guide the venipuncture, as seen in Fig. 1.6. Early evidence demonstrated that these systems can improve visualization of peripheral veins, particularly in difficult patients^{44,52,65,66}. **However recent clinical evaluation studies have shown no improvement in first-stick success with NIR imaging devices compared to manual cannulation**^{67–73}. In fact, numerous surveys have indicated that clinicians find NIR imaging devices difficult to operate, and offer little to no help in performing the venipuncture⁶⁸.



Figure 1.6: Venipuncture assisted with the AV400 NIR light imaging device⁷⁴.

The main drawbacks of NIR devices include the following. First, they only provide 2D vessel images and no depth information. This means the clinician has to estimate the depth of the vessel during the puncture—a challenging task for occluded veins. Second, NIR devices lack the resolution needed to detect subtle vessel motion, and oftentimes, overestimate the true width of veins by re-projecting an enhanced view of the vasculature onto the arm of the patient. Third, they still rely on the clinician to manually insert the cannula and detect when the venipuncture has occurred by observing a sudden *pop* or pressure difference. Observing this *pop* can be a difficult task for inexperienced clinicians, and is considered more of an art form learned through extensive clinical practice.

Many times, clinicians will solely use a NIR device to locate a suitable vein, and then mark the site with a pen. The practitioner will then remove the device and perform the venipuncture blind, because the NIR image provides no information on how deep to insert the cannula. Additionally, because NIR devices project a visible image of the vasculature on the peripheral forearm, clinicians can have difficulty observing flashback in the cannula—a key indicator of a successful venipuncture.

1.3.4 Bimodal Imaging Technology

Efforts to combine optical and acoustic imaging has spurred the development of needle tracking devices such as the Clear Guide ONE (Clear Guide Medical) which uses stereo and US imaging to guide the cannula via trajectory predictions^{75,76}. Specifically, the Clear Guide ONE overlays the needle and end point target on an external US monitor to provide real-time data on the location and depth of the needle, and thus simplifies the insertion process for the clinician. However, this device relies on the clinician to select the injection site, only detects the needle in the image, and was specifically designed for biopsies, sclerotherapy, and ablation procedures—all of which require needle lengths >6 cm for deep tissue insertions.

1.3.5 Summary of Imaging Technologies

Overall, research findings have been mixed regarding the efficacy of imaging devices, with several studies observing **no significant differences in first-stick success rates, number of attempts, or procedure times in comparison to standard venipuncture**^{67,68}. An overview of imaging assist technology is outlined in Fig. 1.7.





	Manual Phlebotomy	SonoSite	VeinViewer [®] ES	Veinlite [®]
				
User Needs				
Mode of operation	VIS light & palpation	Ultrasound	NIR light	Trans-illumination (VIS light)
Completion time	22.9 min	16.1 min	13.5 min	11.75 min
First-stick accuracy	50-80%	74%	65%	60%
Portable	✓	-	✓	✓
Automated intervention	-	-	-	-
Practitioner safety	-	-	-	-

Figure 1.7: Summary of imaging assist technologies.

The absence of clinical improvement may suggest that difficult insertion of the cannula, instead of the initial localization of the vein, is the primary cause of failure during venous cannulation. During manual needle insertion, there is a risk of piercing through the back of the vein wall, which could result in internal bleeding, hematoma formation, nerve injury, or other more serious injuries. As an alternative approach, robotic technology can be leveraged to assist clinicians in performing the venipuncture. A detailed discussion of medical robots, particularly needle insertion robots, is presented in the following sections.

1.4 Medical Robotics

Medical robots have played a key role over the past decade in assisting health care practitioners to perform a wide range of clinical interventions⁷⁷⁻⁹⁴. These robots are primarily

used to manipulate medical instruments within the operating workspace of the procedure.

Thus far, the most well-known and successful surgical robot is the da Vinci Surgical System^{95,96} (Intuitive Surgical Inc., Sunnyvale). The device operates under open-loop control in a master-slave configuration, where the surgeon performs the procedure on the master console, while the robot slave translates these directions into robotic movements. Advantages of using robotics in this manner include: (1) increased dexterity; (2) increased accuracy and precision; (3) reduced trauma to the patient and therefore reduced recovery time; and (4) leveling of the playing field—allowing less experienced surgeons to perform more complex procedures. There are, however, several disadvantages associated with medical robotics, including: (1) increased initial fixed costs for the equipment; (2) high learning curve to become familiar with the controls; and (3) lack of haptics or force feedback during the procedure. So far, surgical robotic systems have been targeted for minimally invasive procedures, yet future research has focused on making these systems even less invasive through the use of single-port laparoscopy^{97–101}. As an example, this includes adapting the device to perform natural orifice transluminal endoscopic surgery—surgical procedures performed through natural openings in the body (e.g., the mouth, nose, or anus)^{102–104}. Surgical robots have also been developed for prostatectomy^{83,105–107}, orthopedic surgery^{82,108,109}, neurosurgery^{110–113}, and brachytherapy^{114,115,115–118}, and animal research^{119,120}. Several review papers provide in-depth discussions of the history, current trends, and future outlook of medical robots (^{77,78,80,121–126}).

1.4.1 Needle Insertion Robots

In many cases, the robot’s performance depends heavily on its ability to obtain accurate information about the spatial positioning of the tools and the target. This positioning information may then be used as feedback in the robot’s motion control scheme. One clinical application in which positioning feedback is especially important is percutaneous needle insertion. Manually introducing a needle blind through soft tissue can be challenging when solely relying on anatomical landmarks or haptic cues. Success rates often depend on the experience of the practitioner and the physiology of the patient, and poorly introduced needles can result in damage to the surrounding tissue that may lead to a wide range of

complications³⁴. To augment the needle insertion process, various imaging modalities may be utilized before the procedure to plan the path of the needle, or during the procedure to servo the needle in real-time. To date, the majority of research in needle insertion robotics has focused on complex surgical procedures.

For example, Podder et al. demonstrated the use of US-based robotic needle servoing for autonomous prostate seed placement in brachytherapy. Kobayashi et al. described a 3-DOF needle insertion surgical robot, combining force sensing and US imaging for central venous catheterization^{127,128}. Furthermore, Tanaka et al. combined vision-based position and force information in a bilateral control system to achieve haptic feedback in an endoscopic surgical robot¹²⁹. In addition, numerous research groups have also studied needle–tissue interactions during percutaneous surgical interventions, developing theoretical models, and confirming results experimentally with robotic systems^{130–134}.

1.4.2 Venipuncture Robots

Outside the operating room, the most commonly performed percutaneous needle insertion procedure is venipuncture. As stated earlier, over 2.7 million venipunctures are carried out each day in the U.S., for the purpose of collecting blood samples or delivering vital fluids to the peripheral circulation^{28,29}. Several research groups have investigated the use of robotics to assist with the venipuncture procedure.

Okuno et al. was the first to demonstrate the potential of automated blood sampling by measuring the force required for the venipuncture¹³⁶. Conducting studies on rabbit ear veins, they confirmed successful vessel puncture by observing the peak in the force profile. Despite being the first researchers to report the concept of automated venipuncture, their experimental device consisted solely of a 1-DOF linear stage on which a force sensor was attached. Zivanovic et al. presented a slightly more advanced device—aptly referred to as Bloodbot (Fig. 1.8)—that utilized force and position profiles while pressing a probe against the skin to determine the location of vessels^{135,137}. However, the force/position profiles only provided information on the stiffness of the underlying tissue; thus, making it difficult to differentiate between various tissue types (e.g., vessels versus muscle). Moreover, in the current design, the device relied on a 1-DOF robotic mechanism, and the palpation probe

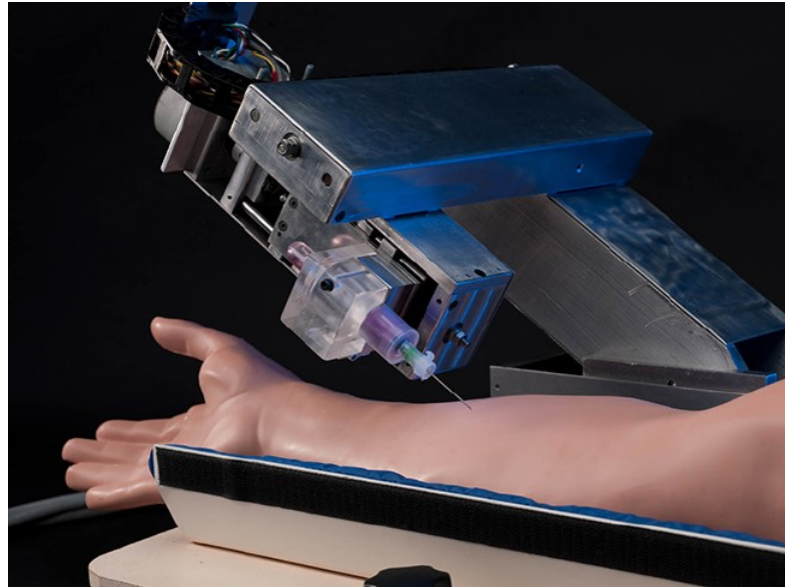


Figure 1.8: Prototype of the Bloodbot robotic venipuncture device¹³⁵.

had to be manually replaced with a needle to perform the venipuncture.

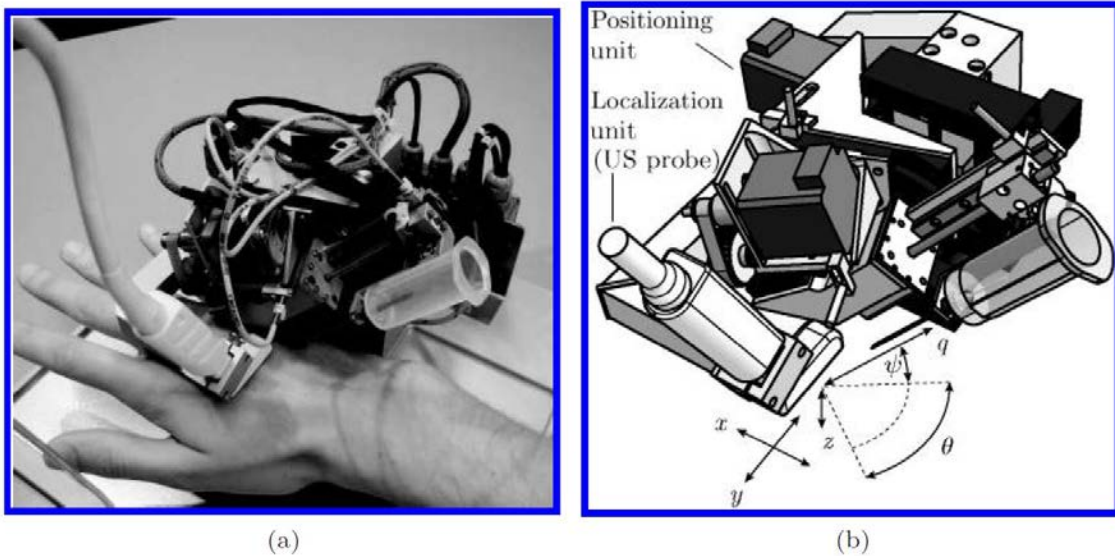


Figure 1.9: (a) Prototype and (b) design of a semi-automated venipuncture device. The robot features an US probe, servoed in two linear degrees-of-motion, to localize veins, and a needle manipulator with four degrees-of-motion to perform the insertion. Image obtained from DeBoer et al¹³⁸.

De Boer et al. developed a 6-DOF semi-automated device in which the clinician had to manually position the system over the target location and then the device used US imaging and force sensing to guide the needle insertion¹³⁸. Conducting experiments on

tissue phantoms, the authors characterized the effects of varying insertion speed. Comparing high (19 mm/s) versus slow insertion velocities (2 mm/s), slower speeds resulted in less tissue deformation, though this could result in an unpleasant burning sensation for the patient. Brewer et al. reported a vein-finding robot using NIR optical detection in¹³⁹, and a robotic device for IV catheterization in¹⁴⁰. These prototypes were complex, bulky, and attempted to automate all aspects of the procedure (i.e., from swabbing the patient's arm with alcohol to performing the catheter insertion).

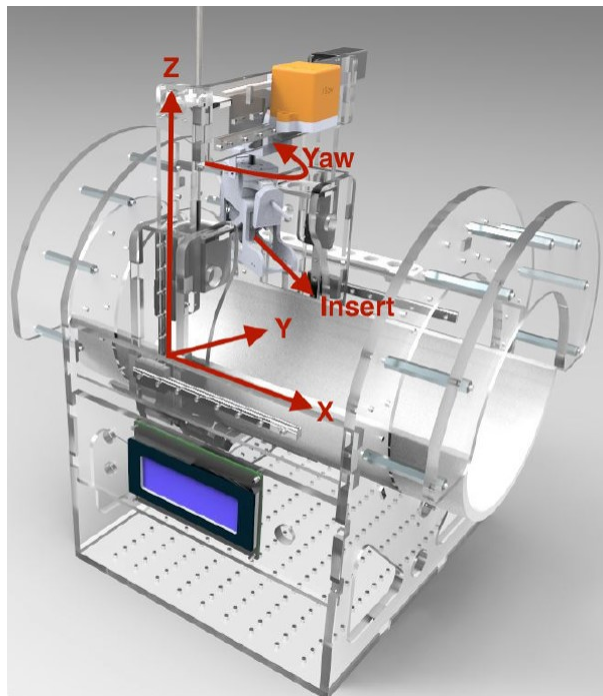


Figure 1.10: Design of the Phlebot robotic venipuncture device. Image obtained from Carvalho et al¹⁴¹.

Finally, Carvalho et al. presented a compact, portable device, named Phlebot (Fig. 1.10), that relied on NIR monocular imaging and force feedback to localize and puncture vessels¹⁴¹. The mechanical system consisted of 4-DOF (3-DOF gantry and 1-DOF for the needle insertion). Results demonstrated proof-of-concept of identifying candidate venipuncture sites on 9 human forearms, though vessels were modeled as straight lines in the images, which is not always the case in human subjects. Furthermore, phantom cannulations evaluated their puncture detection system, monitoring axial forces at the needle tip as well as position, velocity, and motor current.



Figure 1.11: (a) The Veebot automated venipuncture robot, with the end-effector containing the imaging and needle insertion unit mounted on an industrial-sized robotic arm. (b) The Veebot performing a venipuncture on a human subject¹⁴².

Currently, there are two devices designed to perform automated, image-guided venipuncture. The first—VeeBot (Fig. 1.11)—utilizes an industrial-sized, commercial robotic arm with the imaging (mono-camera plus US) and needle insertion systems mounted to the end-effector. The device first uses 2D NIR imaging and laser range-finding for depth perception, and then servos a Doppler US scanner over the target to confirm blood flow before finally performing the venipuncture. Reports have indicated that the device can locate a suitable vein about 83% of the time¹⁴². However, this data excludes success rates for the actual robotic needle insertion, and has not been published in a peer-reviewed journal. Moreover, the size, weight, and cost of the robotic arm may inhibit clinical usability of the system. Not to mention the robot appears extremely intimidating from a psychological standpoint.

The other system designed for automated venipuncture, developed by our group, is the

Table 1.1: Summary of design requirements and engineering constraints.

Design Criteria	Engineering Constraint
Accuracy	Cannulate \varnothing 2.0–3.5 mm veins
Imaging depth	Image veins up to 10 mm deep
Real-time tracking	Segment and track veins at >15 Hz loop rate
Size & weight	Portable (<30x30x30 cm) & lightweight (<10 kg)
Time of procedure	Perform the venipuncture in <5 min

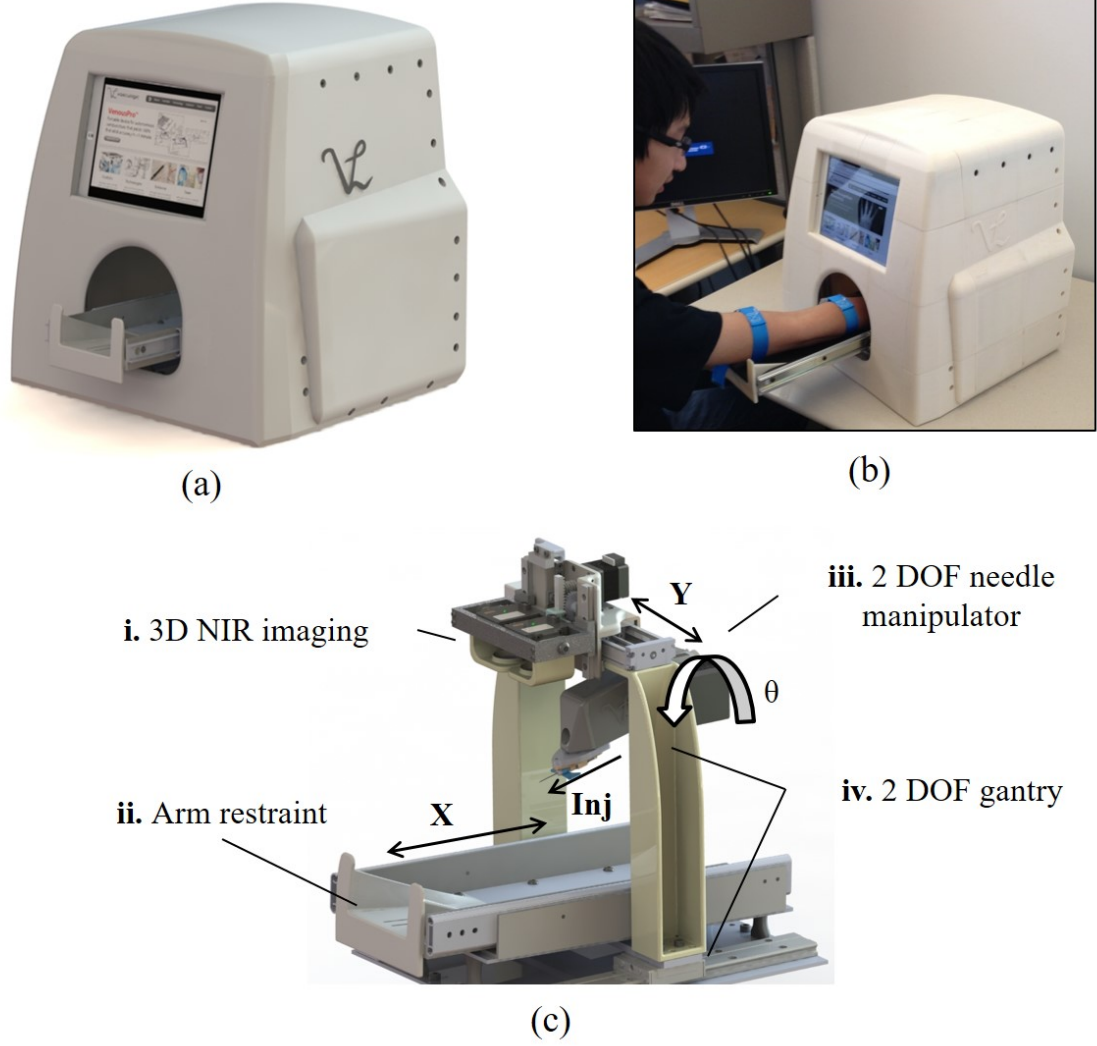


Figure 1.12: (a) The design and (b) prototype of the first-gen venipuncture robot¹⁴³. (c) The robotic system, illustrating the i. NIR imaging setup, ii. arm restraint, iii. 2-DOF needle manipulator (θ and Inj), and iv. 2-DOF gantry (x and y).

VenousPro device. High-level design requirements indicated that the device must: (1) significantly increase first-stick accuracy in difficult patients compared to existing methods; (2) reduce the procedure time of diagnostic and therapeutic interventions requiring venipuncture, especially in time-critical settings; and (3) substantially decrease the injury risks and workloads placed on the hospital staff. Additional considerations such as device cost, size, and ease-of-use were also critical design requirements as summarized in Tab. 1.1.

A first generation (first-gen) prototype was introduced in Chen et al.¹⁴³, which utilized

3D NIR imaging to guide a 4-DOF robot (Fig. 1.12). The system was shown to significantly increase vein visualization compared to a clinician, and to cannulate a phlebotomy training arm with 100% accuracy. Nevertheless, while the first-gen device was successful in demonstrating proof-of-concept, several limitations were observed.

First, the device lacked three critical degrees-of-motion needed to adapt the cannulation procedure to human physiological variability. Namely, the ability to: (1) align the needle along the longitudinal axis of any chosen vein; (2) gradually adjust the angle of the needle during the insertion process; and (3) adjust the vertical height of the needle manipulator. The second limitation of the device was that it did not incorporate closed-loop needle steering to account for subtle arm and tissue motion. Third, the device required manual camera-to-robot calibration prior to the procedure. Fourth, the device relied on manual handling of the needle by the practitioner, and thus could not address the risks associated with accidental needle stick injuries. Finally, the imaging capability of the device was found to be reduced in pediatric and high-BMI patients due to the limited resolution of optical techniques alone.

To address the shortcomings of the initial prototype, the first part of my thesis (Chapter 2) focused on developing a second generation (second-gen) and third generation (third-gen) device—designing, fabricating, and programming key subsystems of both prototypes.

1.5 Lab Testing

Performing the venipuncture is just the first step in diagnostic blood testing. After obtaining the sample, it is then transported and analyzed in a centralized lab before the results are finally sent back to the medical staff to guide the intervention. This is a time consuming and segmented process that requires specialized facilities, expensive equipment, and a large labor force. Not only do unexpected delays arise due to difficulties in performing the venipuncture^{21–23}, but they also occur as a result of inefficiencies during the transport and analysis of the sample¹⁵. Such delays have been shown to reduce specimen quality and increase turnaround times, potentially leading to erroneous test results, misguided treatment regimes, and lengthened hospital stays^{15–17,144,145}.

1.5.1 Point-of-Care Testing

Point-of-care (POC) testing has shown the potential to reduce turnaround times and expedite the clinical decision making process^{146–151}. One of the potential benefits of POC testing is that traditional laboratory venipuncture can be replaced by a fingerstick capillary draw, which requires much less skill to perform and which removes a significantly smaller volume of blood. Commercially available devices have been developed for many assays. For example, handheld analyzers such as the iSTAT device^{147,152} use disposable microfluidics-based cartridges to assess basic chemistry, blood gases, and protein markers, primarily using capillary blood from the finger. Automated cell counters such as the Chempaq XBC¹⁵³ and HemoCue WBC¹⁵⁴ have also been introduced to perform cell counts from capillary blood. Yet despite the commercialization of a wide range of analyzers, these devices are used for less than 10% of all blood tests¹³. The main limitations with bedside analyzers include the reliance on capillary blood from finger-pricks, narrow assay panels, expensive consumables, and low-throughput compared to centralized lab testing.






	Cell Counting	Blood Chemistry	Protein Markers	Hematology	Viral / Bacteria
Device	HemoCue WBC 	Abaxis Piccolo 	i-STAT 	HemoCue Hb301 	Daktari CD4 
Chip Material	Polystyrene microcuvette	Injection molded plastic	Plastic cartridge with silicon microchip	Polystyrene microcuvette	Plastic cartridge
Reagent Storage	On cartridge	Dry reagents on disk	On cartridge	On cartridge	No reagents
Sample Treatment	- Hemolyze RBCs - Stain WBCs	Stain biomarkers	Sample labeling	Convert Hgb to methemoglobin	None
Fluid Actuation	Capillary	Centrifugal and capillary	Pneumatic and capillary	Capillary	Pneumatic
Signal Detection	Imaging system to enumerate WBCs	Absorbance	Electrochemical	Absorbance	Electrochemical

Figure 1.13: Examples of POC blood analyzers used in the clinic.

1.5.1.1 Finger-prick vs. Venipuncture

Blood from a finger is not the same as blood from a vein^{155,156,156–164}. Small molecules, like glucose (Glu), can easily move through capillary networks in the body, which is why finger-prick samples can be used to test its concentration. However, large, medically important molecules like cells, proteins, and lipids are not always found in uniform concentrations throughout the capillary network. Testing for these analytes from a finger-prick sample could result in inaccurate results, potentially leading to a misguided treatment plan. Furthermore, the composition of blood from a finger-prick can vary from the same person (e.g., drop-to-drop variability and different concentrations in different fingers¹⁶⁵). This problem does not happen in blood drawn from a vein. Also, miniscule finger-prick samples ($<50\ \mu\text{l}$) contain both blood and tissue fluid, which introduces noise into the analyzer, making it more difficult to extract meaningful data from the analysis and perform a wide range of tests on a single sample. Consequently, there have been many concerns about the accuracy of finger-prick draws in comparison to venipuncture, with numerous studies indicating a lack of agreement between test results^{155,157,158,166–168}.

Moreover, many people consider finger-prick capillary draws to be more painful, in comparison to venous collection¹⁶⁹. This is largely due to the presence of sensitive nerves in the finger-tips, while smaller, less traumatic needles are being developed for near painless venipuncture.

1.5.1.2 Limited Assay Menu

Bedside analyzers are also capable of only performing a narrow set of tests (Fig. 1.13). However, multi-assay panels are frequently requested in the ED, for example, to assess cardiac status¹⁷⁰, kidney function¹⁷¹, septic shock¹⁷², anemia¹⁷³, acute myocardial infarction¹⁷⁴, as well as blood gas and chemistry levels¹⁷⁵. For example, a study of the testing patterns in the ED at Massachusetts General Hospital (MGH) in the U.S. showed that diagnostic tests are not ordered individually, but nearly always in combination with other panels (Fig. 1.14)^{176,177}. For example, patients that showed symptoms for chest pain, seizure, or abdominal pain had blood tests for cell counts, chemistries, and proteins (Fig. 1.14). In order

to perform these tests would require multiple blood samples and analyzers. This lack of integration with different assays is a major drawback for current systems. While the quality of POC testing has made significant advances in the past decade, partial assay menus and platform fragmentation have relegated most devices to only the most specialized environments¹². To overcome this, the convergence of a wide range of assays into a single platform is critical.

	CBC	Blood Chemistry	Immunoassay
Abdominal Pain	✓	✓	
Chest Pain	✓	✓	✓
Pregnant	✓	✓	✓
Mental Illness	✓	✓	✓
Respiratory Pain	✓	✓	
Weak or Dizzy	✓	✓	
Fever or Infection	✓	✓	

	CBC	BMP	Hepatic	Amy/Lip	Tox
Cardiac	100%	93%	62%	37%	20%
Tox	100%	95%	81%	40%	
Amy/Lip	100%	94%	100%		
Hepatic	96%	96%			
BMP	97%				
CBC					

Figure 1.14: Studies of an ED POC testing program at MGH demonstrating the importance of test availability in a critical care setting. (a) Testing for top 7 complaints. (b) Test panel co-ordering for a subset of the most common tests/panels ordered in the ED. Tables adapted from Lee-Lewandrowski et al.¹⁷⁶ and Johnson et al¹⁷⁷.

1.5.1.3 Central Lab Testing

Finally, while POC testing holds great promise for improving the availability of common diagnostic tests, the traditional lab will still play a critical role in performing more complex assays; when such assays are needed, as is often the case, a venipuncture draw will still be required in combination with the POC testing^{156,178–180}. For these reasons, a complete POC testing solution should not only perform a broad range of assays, but should also be capable of improving the clinical work-flow when either venous or capillary draws are required. As such, **there is an unmet need for technologies that can combine the breadth and accuracy of traditional testing with the speed and convenience of POC devices.**

For the second part of this dissertation (Chapter 3), a series of POC testing devices were developed using optical detection and centrifugal microfluidics for multi-analyte analysis.

1.5.2 Centrifugal Microfluidics

Over the last decade, centrifugal microfluidics has emerged as a niche platform, providing key features that make it ideally suited for integrating a range of blood tests on one self-contained chip. Here, all steps from sample preparation to analysis can be automated by controlling the speed of the centrifuge motor: reagent storage and release¹⁸¹, sedimentation and plasma extraction^{182,183}, liquid transport and pumping^{184,185}, metering and valving^{186,187}, mixing and washing¹⁸⁸, and analyte detection¹⁸⁹. Also, centrifugal microfluidics obviates the need for external pumps or robotic pipettors to manipulate samples and reagents—resulting in a compact device that can be used in decentralized settings. More details on centrifugal microfluidics can be found in numerous review papers^{190–193}.

The majority of research in centrifugal microfluidics has focused on the detection of chemistries^{194,195}, proteins^{196,197}, nucleic acids^{198,199}, and rare cells^{200,201}, with several analyzers entering the market. For example, the Piccolo Xpress device (Abaxis, Inc.) automates the detection of chemistries on-disc²⁰², and the LabGEO IB10 (Samsung) performs automated immunoassays with multiplexing capabilities²⁰³. However, the enumeration of common cells on-disc remains a challenge¹⁹³.

1.5.3 Complete Blood Counting

In 2005, the Center for Disease Control reported that 160 million complete blood counts (CBC) were performed in ambulatory and emergency settings, making the CBC the most ordered blood test in the U.S.¹³. The reason why the CBC is so ubiquitous is because it provides an indicator of patient health by analyzing the types and numbers of cells in blood²⁰⁴. The main components of a CBC include red blood cell (RBC), white blood cell (WBC), and platelet (PLT) counts. Additional blood parameters, including hemoglobin (Hgb) concentration, hematocrit (Hct), mean cell volume (MCV), and WBC differential counts, also help in the diagnosis of a variety of diseases²⁰⁵.

Blood is a complex fluid composed of three main cell types: RBCs, WBCs, and PLTs, suspended in plasma that contains various proteins (e.g., fibrinogen, albumin, globulins and other clotting factors). Plasma constitutes about 55% of the blood volume, whereas RBCs

make up about 45% of the volume, and the WBCs plus PLTs comprise <1%. Blood cells can be further segregated according to the level of activation, maturity, or abnormality. Specifically, RBCs are grouped into three main subtypes: reticulated red cells (reticulocytes), nucleated red blood cells, and mature RBCs. Conversely, WBCs are classified as lymphocytes (20–45%), monocytes (3–11%), neutrophils (40–75%), basophils (0–1%), or eosinophils (0–7%), in which the latter three are referred to as granulocytes. These subtypes can be classified based on morphological features such as size, geometry, and granularity. In whole blood, RBCs outnumber WBCs by approximately 1000:1²⁰⁵. However, the diagnostic value of WBC counts in particular, cannot be overstated as they can provide clinicians with key information regarding patient health, especially when diagnosing the common flu (high lymphocyte count) or bacterial infection (high granulocyte count).

1.5.4 Previous Work on Leukocyte Counting

Several groups have described centrifugal microfluidic systems for leukocyte isolation and detection. Shiono et al. presented a device for continuous WBC separation by density gradient centrifugation²⁰⁶. Here, a series of Percoll dilutions with varying densities were continuously introduced to the spinning disc to fractionate the buffy coat into three sub-types (i.e., lymphocytes (lym), monocytes (mon), and granulocytes (gran)). Despite promising separation efficiency and reproducibility, the system was reported to take up to two hours to process blood samples, and detection was performed off-disc. Schaff et al. provided proof-of-concept for differential leukocyte counting via centrifugal microfluidics using two cell lines with different densities (K562 and Jurkat cells)²⁰⁷. However, no cell quantification data was presented to evaluate the accuracy and repeatability of this method. More recently, Kinahan et al. demonstrated the use of pneumatic siphon valving and density-gradient medium to extract leukocytes from whole blood²⁰⁸. Nevertheless, the device only exhibited a leukocyte extraction efficiency of 34% compared to hospital laboratory data. Furthermore, detection was performed off-chip and no differential data was reported.

Apart from disc-based devices, there are several commercial point-of-care analyzers that perform leukocyte counting, such as the HemoCue WBC (Danaher, Inc.) and QBC Star Analyzer (Drucker Diagnostics). The HemoCue device uses a static cell counting approach



Figure 1.15: The HemoCue WBC Diff blood analyzer, which claims to perform a 5-part WBC differential via static cell counting²⁰⁹.

based on imaging and enumerating leukocytes stained with methylene blue²¹⁰. Recently, HemoCue has extended this approach to extract a 5-part differential via image processing techniques (Fig. 1.15)²⁰⁹. However, this device is still awaiting FDA approval, and the accuracy of this method remains unclear.



Figure 1.16: The QBC Star blood analyzer. (a) Prototype of the device with a built-in centrifuge to separate blood into its biological constituents, and (b) the corresponding glass capillary tube disposable, which houses the blood sample²¹¹.

Conversely, the QBC Star Analyzer (Fig. 1.16) uses a bulk-cell analysis approach in glass capillary tubes, where the thickness of the buffy layers is correlated with a 2-part

leukocyte differential^{211,212}. The system is also capable of performing other components of the complete blood count, including Hgb, Hct, and PLT measurements. Nevertheless, the device is rather bulky (i.e., 41 x 41 x 41 cm; 8.6 kg²¹¹), a number of manual steps are still required to process the sample, and the reliability of the detection system is unclear under varying conditions (e.g., different tube orientations).

To address these limitations, the second part of this dissertation has mainly focused on the detection of WBCs on the centrifugal microfluidics platform. This work serves as a foundation for developing more complex assays in the future, such as protein, chemistry, and rare cell detection. In this fashion, the device can perform multi-analyte analysis and provide information on patient health at the POC.

1.5.5 End-to-end Lab Automation

The quest to achieve an end-to-end solution in blood testing has driven the rapid adoption of automation solutions across many diagnostic facilities²¹³⁻²¹⁵. Lab automation systems have been developed to improve efficiency and reduce human error within centralized facilities^{216,217}. Such systems include automated tube handling devices (e.g., AutoMate 2500 from Beckman Coulter), robotic pipetting instruments (e.g., Precision XS from BioTek), and automated hematology analyzers (e.g., XP-300 from Sysmex).

Additionally, total lab automation systems exist that combine tube handling, sample preparation, and analysis units to fully automate diagnostic testing (e.g., XN-9000 from Sysmex). These fully integrated robotic systems are driven by assembly-line automation software and computer management systems. However, these systems are large, expensive, and decoupled from the blood sampling process, thus limiting their applicability in POC settings.

With the advent of miniaturized robotic and microfluidic systems, the technology is in place to combine the breadth and accuracy of traditional laboratory testing with the speed and convenience of POC testing. Such a technology would represent a significant leap forward in realizing the ultimate goal of an automated, end-to-end solution for diagnostic blood testing.

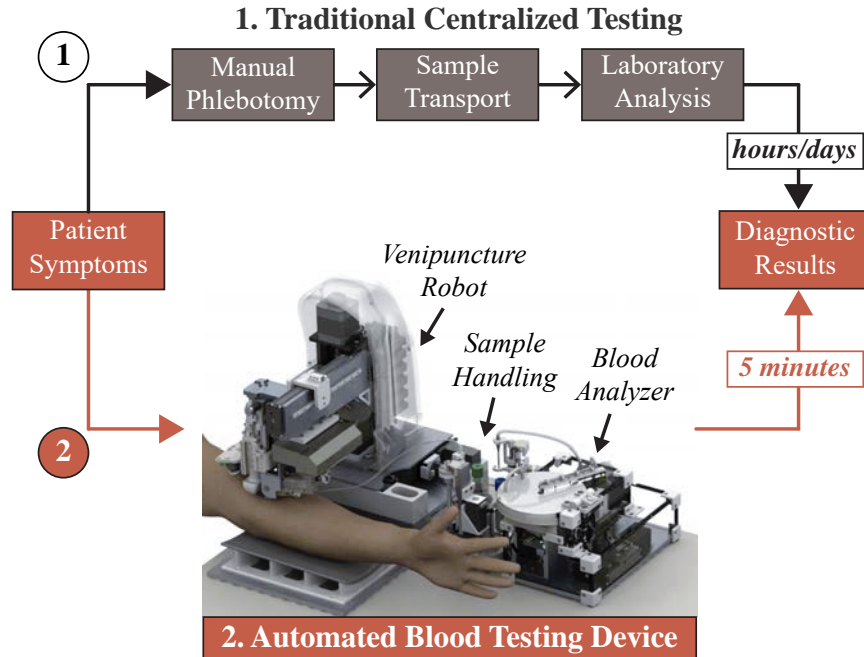


Figure 1.17: Automated blood testing device that collects and analyzes the sample at the POC. The technology is designed to replace the standard manual phlebotomy and central lab testing process (1-top). Instead, the device automatically draws blood and provides quantitative measurements of hematology (2-bottom). The system combines a robotic venipuncture device, sample handling module, and blood analyzer unit.

1.6 Summary and Scope of Thesis

Despite recent progress in robotics, automation, and *in vitro* diagnostics, clinical adoption of these technologies has remained limited, and no end-to-end solution for complete POC testing exists today. To address this, my dissertation has focused on developing a platform device that enables end-to-end testing by performing blood draws and providing diagnostic results in a fully automated fashion (Fig. 1.17). By significantly reducing turnaround times, the device also has the capacity to expedite hospital work-flow, allowing practitioners to devote more time to treating patients. As a result of the improved work-flow, costs due to delays and complications may potentially be reduced.

1.6.1 Device Overview

The system couples an image-guided venipuncture robot, to address the challenges of routine venous access with a centrifugal microfluidic platform that performs the diagnostic analysis.

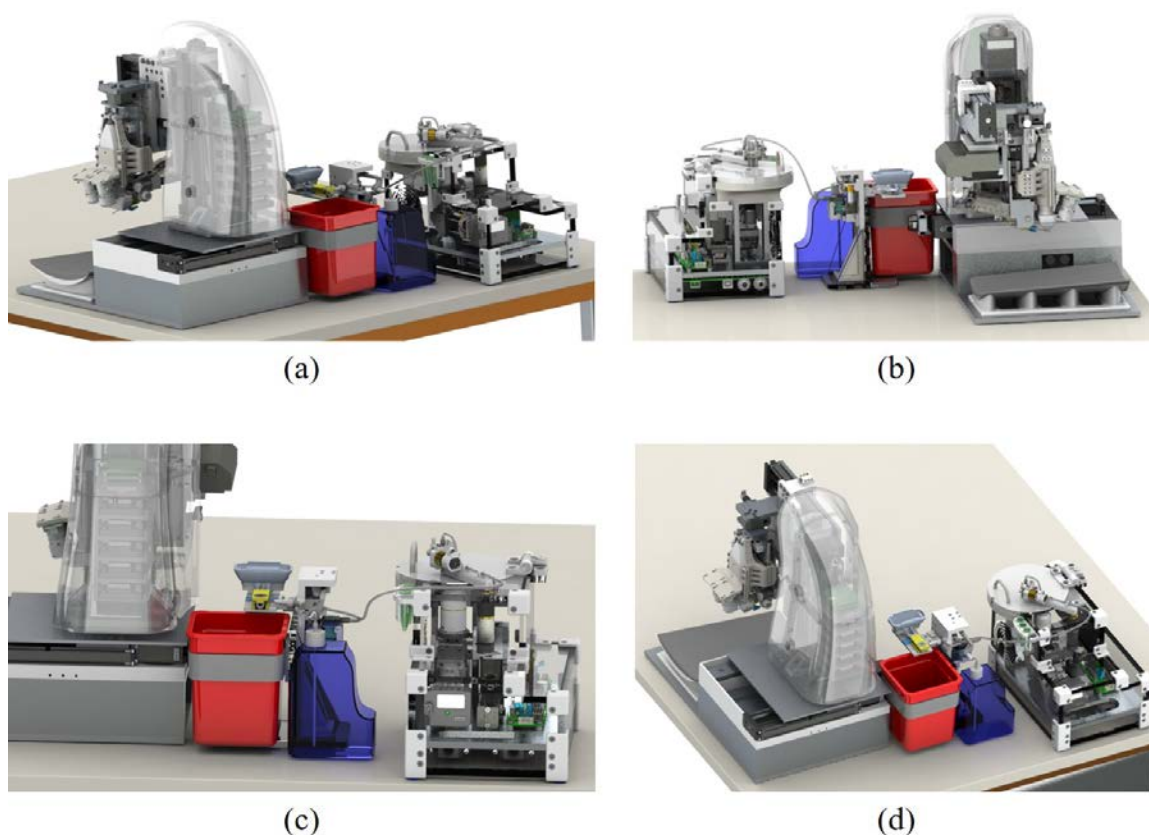


Figure 1.18: Design concept of the automated blood testing and analysis device.

The device is segmented into three distinct subsystems—a robotic venipuncture device, automated sample handling module, and centrifuge-based blood analyzer unit, which form the core elements of my thesis. Figure 1.18 and 1.19 show the design and prototype of the full system respectively.

The venipuncture device uses a combination of 3D NIR and Doppler US imaging to localize blood vessels under the skin, and a robotic manipulator that orients and inserts the needle into the indicated vessel based on real-time image analysis and force feedback^{1–3}. The blood sample is then extracted and transferred to the analysis unit, which provides blood measurements on sample volumes of $\sim 200\ \mu\text{l}$ in approximately 5 minutes using centrifugal microfluidics and optical detection. Currently, the device is capable of performing key components of the CBC: a 3-part WBC differential and Hgb measurement, with the capacity to expand to other protein and chemistry assays in the future using this centrifuge platform. The reason for choosing to pursue these assays in the diagnostic unit was to address the

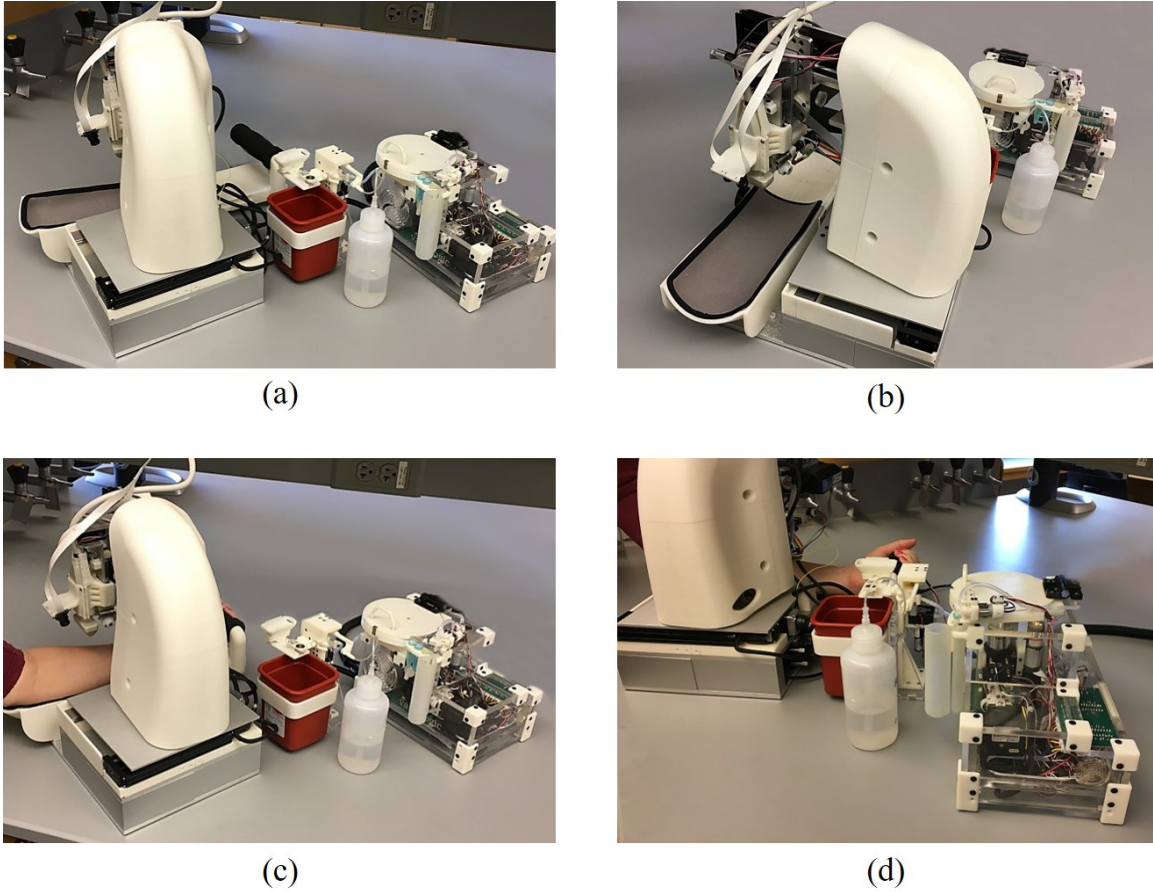


Figure 1.19: Implementation of the automated blood testing and analysis device.

two most commonly requested blood tests—WBC counts and Hgb measurement²¹⁸.

1.6.2 Novel Contributions

Being that this project was a close collaboration between two students, there will be some overlap between the presented work in this dissertation and in the dissertation of Dr. Alvin Chen. Nonetheless, the complexity of this project warranted a team of researchers working together to develop this device. Whereas Dr. Chen’s work focused predominantly on the image processing and software components of the venipuncture robot, my contributions were focused on the design and implementation of prototypes, motion control software development, and integrating the robot with a diagnostic module. Specifically, the work presented in this dissertation covers the development of:

1. Two novel venipuncture robots that address key limitations with the first-gen device.

This work is presented in Chapter 2, and has resulted in three journal publications^{1,3,8}, two conference proceedings^{2,10}, plus three publications in preparation^{6,219,220}.

2. A sample handling module that rapidly transfers the drawn blood sample to the diagnostic unit via a two-stage pumping mechanism. This work is presented in the first part of Chapter 3.
3. A POC diagnostic blood analyzer that utilizes centrifugal microfluidics and optical detection that is capable of measuring cells, proteins, and chemistries. The presented data highlights results on a 3-part WBC assay, plus Hgb and Glu measurements. This work is presented in the second part of Chapter 3 and has resulted in one journal publication⁵, one conference proceeding⁴, plus one publications in preparation⁷.

Chapter 2

Development of Robotic Venipuncture Devices

This Chapter is segmented into three main sections: (1) robotic development and testing of the second-gen prototype (Section 2.2), (2) robotic development and testing of the third-gen prototype (Section 2.3), and (3) implementation and evaluation of needle localization algorithms in US images (Section 2.4).

2.1 First-generation Device

While the first-gen venipuncture device was successful in demonstrating proof-of-concept, a major redesign of the robot was needed for the system to be usable in the clinic. The robot—measuring 46x46x46 cm—comprised a 2-DOF gantry system and a 2-DOF needle manipulator, where all motions were actuated by stepper motors (Zaber Technologies Inc). With 4-DOF in total, the device could introduce the cannula into the vein at a specified angle based on NIR feedback¹⁴³.

However, two critical degrees-of-motion were lacking: the ability to align the needle longitudinally with the vein, and the ability to adjust the vertical height of the needle. Moreover, the device solely relied on NIR imaging to localize blood vessels and guide the robot. In many cases, NIR imaging lacks the resolution needed to image small veins, and has a limited penetration depth of around 3 mm through skin tissue. Thus, it was challenging for the first-gen device to operate on pediatric patients, whose veins can be as small as 1–2 mm in diameter, and obese patients, whose vessels reside >3 mm underneath dense layers of adipose tissue.

2.2 Second-generation Device

The second-gen device (as seen in Fig. 2.1) was developed to address the aforementioned limitations with the previous system and incorporate other features, such as automated

needle handling¹. This device incorporated 7-DOF, including the original 4-DOF of the first-gen device and three added DOF that dramatically extended the kinematics and operating workspace for the needle insertion task. The major mechanical enhancement of the second-gen device was the implementation of a miniaturized 4-DOF serial manipulator arm that steers the needle under closed-loop kinematic and image-guided controls. Additionally, US imaging was incorporated into the new device to improve vein visualization in patient demographics that challenged the original system.

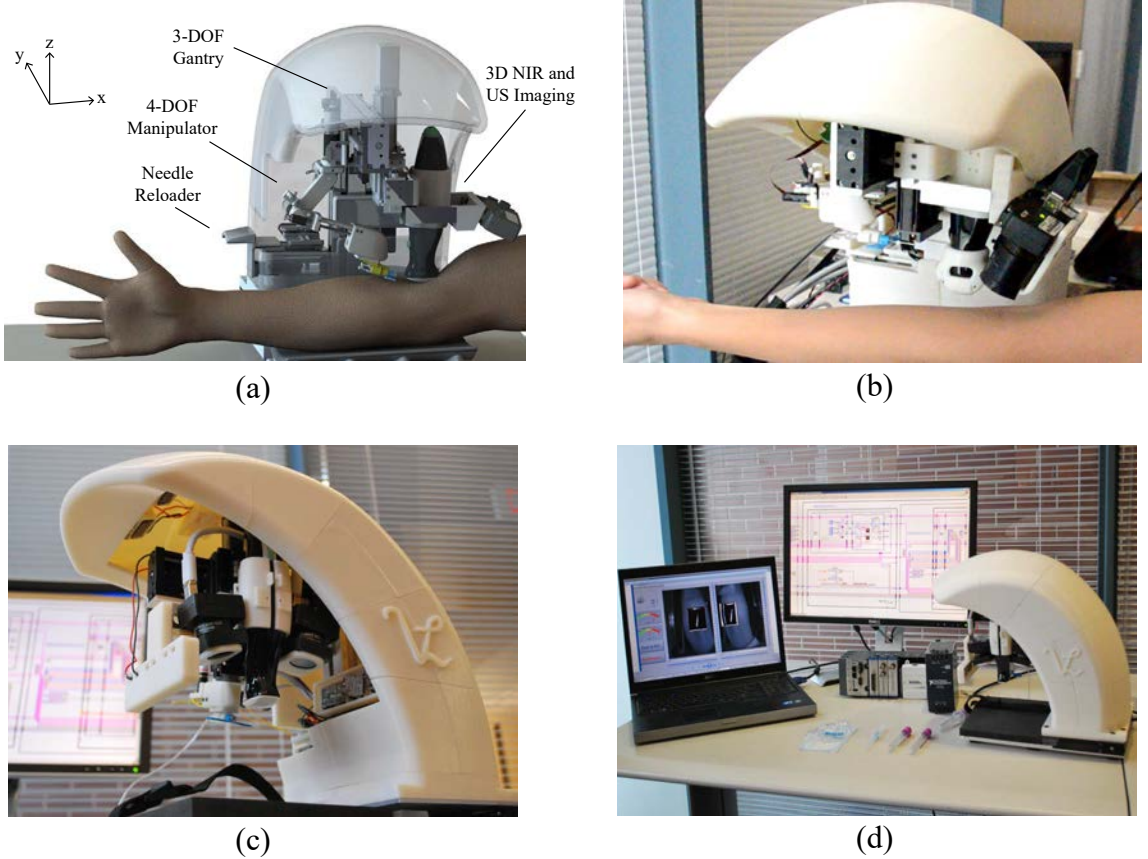


Figure 2.1: (a) Design and (b–d) prototype of the second-gen venipuncture robot. Figure reproduced with permission from IEEE¹ (year of original publication: 2015).

Figure 2.1a illustrates a rendered CAD model of the system, which combines NIR and

¹Much of the work presented in this section first appeared in: The system design and evaluation of a 7-DOF image guided venipuncture robot. *IEEE Transactions on Robotics* 2015; 31(4):1044–1053¹. All excerpts represent the original work of Max Balter, whose specific contributions as first author included: designing and conducting the experiments; generating the presented data and corresponding figures; writing, editing, and revising the original text; and addressing reviewers' comments as corresponding author of the original manuscript submission.

US imaging, a 3-DOF gantry system, and a 4-DOF manipulator. The rest of the images in Fig. 2.1 show the physical device, which is significantly smaller than the first-gen device (30 x 25 x 25 cm, 3.5 kg vs. 46 x 46 x 46 cm, 10 kg). The open half-shell design allows the device to be easily integrated into the existing phlebotomy work flow.

2.2.1 Venipuncture work-flow

This process starts with the clinician first swabbing the injection site with alcohol, either in the antecubital fossa (for blood draws) or anterior forearm (for IV therapy). The clinician then loads the cannula into the back of the device with the cap still in place. The robot grabs the needle using an electromagnet (EM) embedded in the end-effector, and as the manipulator translates in the y -direction, the cap is removed.

Once the needle is loaded, the patient places their arm in the device, which incorporates an arm rest that lightly restrains the arm via an adjustable handle bar to reduce large movements. The NIR imaging system and image analysis software, which then scans the arm and segments the veins, is described in detail in Chen et al.¹⁴³. Briefly, the device uses 940 nm NIR light to improve the contrast of subcutaneous peripheral veins, and extracts the 3D spatial coordinates of the segmented veins from images acquired by a pair of calibrated stereo cameras. Suitable veins, selected based on continuity, length, and vessel diameter¹⁴³, are displayed on the device’s graphical user interface (GUI), from which the clinician selects the final cannulation site. Then the US probe lowers down on the patient’s arm to provide a magnified longitudinal image of the chosen vein, and confirms venous blood flow. Finally, the robot aligns the cannula along the longitudinal axis of the vein and inserts the needle at 30°, as commonly observed in the clinic. The manipulator then gradually lowers the insertion angle to 15° upon contact with the skin surface, until the tip reaches the center of the vein.

Once securely positioned in the vessel, the cannula disengages from the robot, and by virtue of the open shell design, the clinician can access the patient’s arm to finish the procedure. In the case of a blood draw, this includes interchanging blood vials, removing and disposing of the needle, and placing a bandage over the injection site.

The GUI allows the clinician to oversee the full robotic venipuncture, and intervene if

necessary. In addition, the GUI directs the clinician through the protocol steps by prompting checks and reminders to ensure that both the patient and practitioner remain safe throughout the phlebotomy. The total procedure time using the robot is estimated to be <5 min for all patients, where the system executes the steps from imaging the veins to cannulating the vessel in <2 min¹⁴³. Compared to manual phlebotomy, where the time-to-completion can range from 7 min in normal adult patients, to >30 min in difficult populations²¹, the robot has the potential to perform the cannulation in significantly less time.

2.2.2 System Architecture

The key elements in the system architecture are categorized into the imaging component, main computer, image processing unit, and robotic assembly (Fig. 2.2), each with their respective safety mechanisms. For example, a watchdog protocol was implemented to monitor the activity of the processing unit, controls, and electronics. In addition, all actuators have non-backdrivable gearheads that lock in position when torque is removed to ensure no free motion at the robot joints. Lastly, there is a push-button brake that shuts down the electrical hardware to lock the joints, located by the GUI.

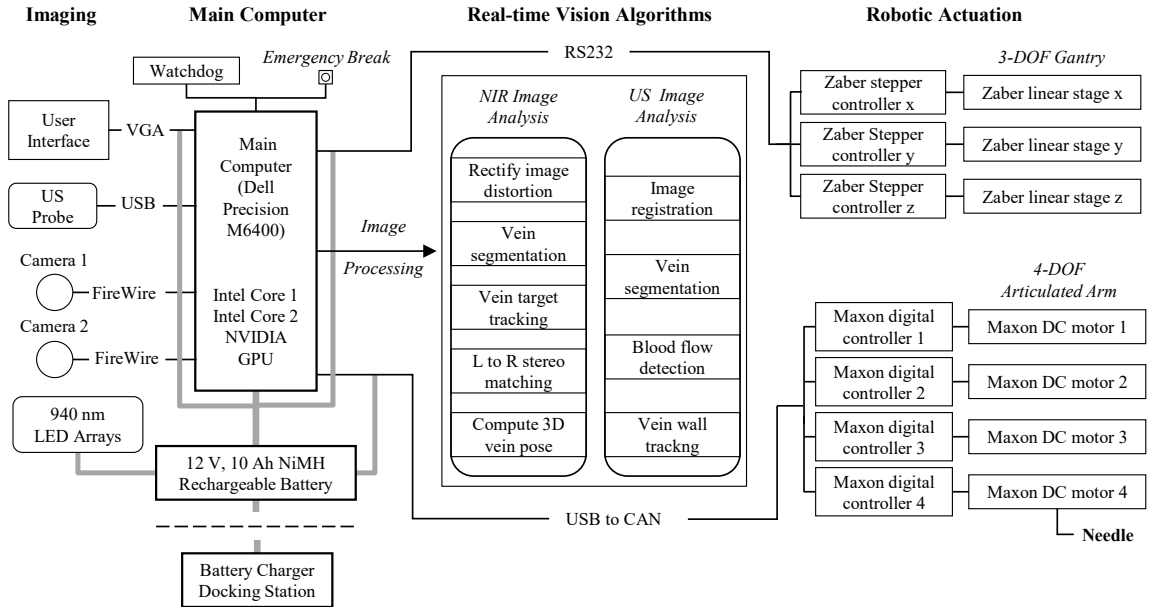


Figure 2.2: Hardware and software system architecture design, depicting the process flow from image acquisition, signal processing, and robotic controls. Figure reproduced with permission from IEEE¹ (year of original publication: 2015).

2.2.2.1 Hardware

The device is fabricated out of 6061 machined aluminum, rapid prototyped ABS thermo-plastic, precision ball bearing linear sliders, as well as off-the-shelf electronic components including actuators, motor drivers, LEDs, and the US probe.

2.2.2.1.1 Optical and US Image Acquisition

The device exploits the unique properties of the NIR spectrum (700–1000 nm) to image the subcutaneous veins. Namely, NIR light exhibits decreased scatter and reflection on the skin tissue surface compared to VIS light, and deoxyhemoglobin (DHb) in veins shows increased absorption in the NIR range²²¹. This results in a 3–4 mm penetration depth that highlights the contrast of superficial veins. However, in obese and pediatric populations whose veins often lay underneath a dense layer of adipose tissue, NIR light is unable to image the vessels. Thus, we implemented US imaging to increase the penetration depth to 4 cm, ensuring that the device can be used across all demographics.

The imaging sub-assembly consisted of two CMOS cameras (Firefly MV, FMVU-03MTM-CS, Point Grey Research Inc.) with extended sensitivity in the NIR spectrum, as well as a 12 MHz brightness mode (B-mode) portable US transducer (Near Field Vascular, 99-5934, Interson Inc.). The cameras provide a coarse 3D map of the venous structure, and once a suitable injection site is selected, the US probe drops down to provide a high magnification longitudinal view of the chosen vein. Wide-angle (100°) lenses were fitted to each camera to enable a sufficient field-of-view (FOV) to image peripheral forearm veins (wrist to 4 cm proximal to the elbow). The cameras and US probe were securely mounted to the 3-DOF gantry system via machined aluminum brackets. NIR images were captured at 30 Hz each and transmitted to the GPU for processing. The US probe operated at 20 frames/s, enabling the 256 acoustic scan lines to be processed in real-time. The resolution of the NIR image was 1 mm in x and y , and 2 mm in z , whereas the resolution in the US image was 0.015 mm in x and z .

2.2.2.1.2 7-DOF Robot

The robotic system was comprised of a 3-DOF Cartesian gantry (x , y , z as depicted in Fig. 2.1) and a 4-DOF serial needle manipulator arm. Precision lead-screw linear stages were used for the Cartesian positioning system (LSM series, Zaber Technologies Inc), whereas DC brushed motors, with gear heads and magnetic-based incremental encoders (A-max 16, Maxon Motors) were used for the 4-DOF serial arm. Translation in x and y positions the US probe and needle manipulator above the injection site, and z translation allows the US probe to lower onto the patient's arm. The linear stages were driven by NEMA 08, 2-phase stepper motors (Zaber Technologies Inc) with a resolution of $0.1905\ \mu\text{m}$, peak thrust of 25 N, max speed of 5.8 cm/s, and minimal backlash ($<13\ \mu\text{m}$)—satisfying the power and precision requirements needed for each axis. The steppers operated under open-loop control using dedicated motor drivers for each stage with $1/64$ step resolution.

The serial arm provided longitudinal alignment along the vein, positioned the needle at a 30° insertion angle, and performed the injection using a linear spindle drive (RE 8, Maxon Motors). Motor torque and power calculations governed the selection of low-backlash ($<0.3^\circ$) gearhead motors for joints 1–3 (Fig. 2.6), and a linear spindle drive for the injection system. The joint motors can supply up to 30 N-cm of torque, with a closed-loop positioning resolution of 0.002° , by means of the attached 512 cpt quadrature encoders. Conversely, the spindle drive outputs a max force of 8 N which has been shown to be sufficient to pierce human skin tissue and the vein wall¹³⁸. An EM (EM050, APW Company) with a 9 N holding force was embedded in the distal end of the end-effector to serve as the needle attach and release mechanism.

2.2.2.1.3 Central Processor

A compact PC (Dell Precision M6400) in conjunction with a graphics card (NVIDIA Quadro FX 3700M) was utilized for all experiments conducted in this study. The graphics processor handled the majority of the image processing pipeline as outlined in Fig. 2.2, whereas the CPU handled the robotic kinematic controls and GUI display.

2.2.2.2 Software

Calibration of the NIR and US imaging systems, as well as the vision algorithms used to guide the robot, are summarized below. All vision and motion control software was written in LabVIEW (National Instruments, Inc.) and C++.

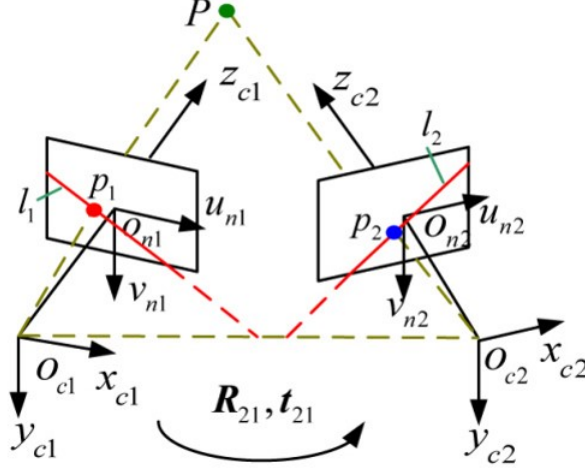


Figure 2.3: Intrinsic and extrinsic camera parameters of the stereo setup. Image adapted from Bouguet et al²²².

2.2.2.2.1 Automated Stereo Camera Calibration

Camera calibration software was adapted from the Caltech Toolbox²²² and re-written in LabVIEW. A planar grid with circular control points was machined to the base of the system. During the calibration, the grid is imaged by the stereo camera pair at different viewing heights to form a non-planar, cubic calibration rig. The cameras were positioned vertically by the z -axis of the 3-DOF gantry system. The intrinsic and extrinsic parameters of the stereo setup—as outlined in Fig. 2.3—are then extracted using the method of Heikila et al.²²³, allowing the camera coordinates to be registered to the robot frame. Specifically, Eq. 2.1 is used to transform the image frame to the camera frame:

$$\begin{aligned} (x_{u,v})_1 &\xrightarrow{P_1} (X_C)_1 \\ (x_{u,v})_2 &\xrightarrow{P_2} (X_C)_2 \end{aligned} \quad (2.1)$$

where the general intrinsic matrix, P , is specified in Eq. 2.2:

$$P = \begin{bmatrix} -fk_u & 0 & u_0 & 0 \\ 0 & -fk_v & v_0 & 0 \\ 0 & 0 & 1 & 0 \end{bmatrix} \quad (2.2)$$

where f is the camera focal length, k_u and k_v are the pixel width and height respectively, u_0 is the x -coordinate at optical center, and v_0 is the y -coordinate at the optical center. Equation 2.3 can then be used to transform the camera frames to the robot frame:

$$\begin{aligned} (X_C)_1 &\xleftrightarrow{R_{21}, t_{21}} (X_C)_2 \\ (X_C)_{1,2} &\xrightarrow{R_r, t_r} (X_R) \end{aligned} \quad (2.3)$$

where R_{21} and t_{21} are the rotation matrix and translation vector respectively, for correlating the camera frames, whereas, R_r and t_r are the rotation matrix and translation vector for correlating the camera frame to the robot frame. Taken together, the 3x3 rotation matrix coupled with the 3x1 translation vector is called the homogeneous transformation matrix.

With this setup, the resulting re-projection error was approximately ± 0.1 mm, which translated to an (x, y, z) image reconstruction error of approximately 1 mm, given the image resolution of the cameras.

2.2.2.2.2 Automated Ultrasound Calibration

In order to register the US system to the robot frame, the curvilinear coordinate system of the US transducer must be converted to the rectangular coordinate system of the image displayed on-screen. In this scan conversion process, the raw B-mode scan lines extracted from the curved US transducer are spatially interpolated based on the known geometry of the transducer, sampling frequency, and line density²²⁴. Small spatial errors in the scan conversion are then minimized using an N-shaped fiducial-based calibration method²²⁵, which allows the pixel coordinates of the US image to be mapped back to the robot coordinates. Figure 2.4, displays the US image during the calibration, with labeled fiducial coordinates.

Specifically, pixel coordinates are mapped to the US frame using Eq. 2.4:

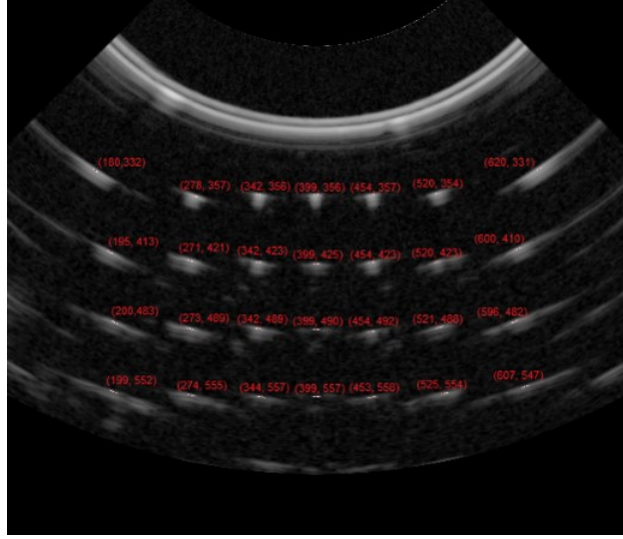


Figure 2.4: Ultrasound image during calibration of intrinsic parameters.

$$(x_{u,w}) \xrightarrow{r,\theta} (X_{US}) \quad (2.4)$$

where r and θ are polar coordinate units. Then the US frame is correlated to the robot frame using Eq. 2.5:

$$(X_{US}) \xrightarrow{R_r, t_r} (X_R) \quad (2.5)$$

where R_r and t_r are the rotation matrix and translation vector respectively, for correlating the US frame to the robot frame.

2.2.2.2.3 Vein Segmentation and Image Guidance

Image analysis algorithms for the NIR and US systems were executed in parallel on a GPU to increase the cycle rate (Fig. 2.2, center). Fig. 2.5 outlines the main image analysis steps, as detailed in¹⁴³. Briefly, veins are first extracted from the NIR images by analyzing their 2nd-order geometry²²⁶. Suitable veins, determined based on their diameter, length, continuity, and contrast, are displayed on the GUI for selection by the practitioner via clinical judgment. During the needle insertion, the selected vein is segmented in real-time

from the longitudinal US image using the region growing algorithm in Adams et al²²⁷. The center of the segmented vein is then calculated continuously at high resolution (0.015 mm), allowing the exact depth of the cannulation target to be known throughout the insertion. The US image can also be used to detect blood flow and visualize the needle.

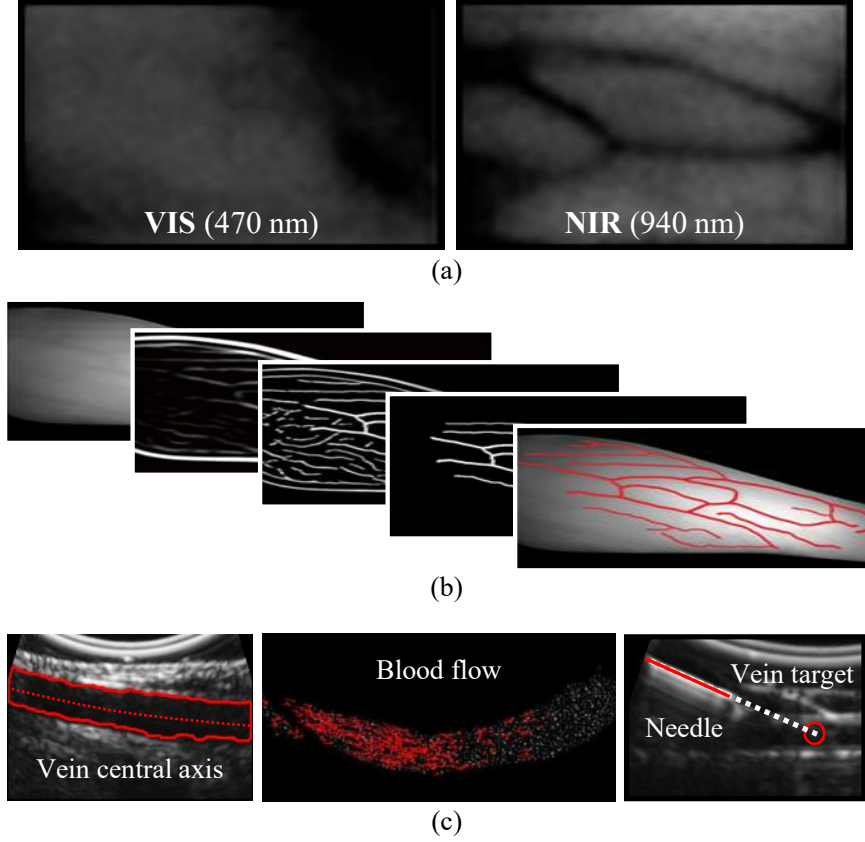


Figure 2.5: Overview of the software scheme. (a) VIS versus NIR light, demonstrating increased vein contrast under NIR light. (b) NIR image processing steps from raw image (left) to segmented veins (right). (c) From left to right: US longitudinal segmentation, blood flow detection, and needle visualization. Figure reproduced with permission from IEEE¹ (year of original publication: 2015).

2.2.3 Needle Manipulator

2.2.3.1 Serial Arm Design

The needle manipulator on the first-gen device consisted of a 2-DOF mechanism to: (1) set the insertion angle, and (2) cannulate the selected vein under NIR guidance. All actuators were stepper-based and operated under open loop commands, hence the motors could not

provide real-time feedback control to locate the needle tip via forward kinematics. Furthermore, with only one revolute degree-of-motion, the manipulator had a highly limited workspace, and was unable to align the needle with the orientation of the vein. To address these problems, the needle manipulator was redesigned in the second-gen device based on the following engineering constraints.

1. The manipulator should have the accuracy to cannulate veins as small as $\varnothing 2$ mm (seen in pediatric populations).
2. The needle insertion force should be >5 N (shown to be sufficient to pierce human skin tissue¹³⁸).
3. The robotic arm should be compact (<30 cm³) and lightweight (<0.4 kg).
4. The manipulator should have an operating workspace >175 cm³ (sufficient for the needle insertion task¹⁴³).
5. The end-effector should have a safety quick release mechanism to disengage the cannula from the robot.

Several designs were considered, including parallel, serial, and decoupled systems. Although parallel robots offer high accuracy, stiffness, and low inertia, oftentimes the workspace of a parallel manipulator is smaller than the robot itself. The needle manipulator on our device needs to be compact, yet have a large enough workspace to align and reach all possible vein injection sites on the forearm (i.e., workspace >175 cm³). Decoupled systems often involve complex mechanisms, and are constrained to disjointed motions. To achieve a big enough workspace with a decoupled manipulator, the system would be large and bulky.

Conversely, a serial arm can provide a large enough workspace using simple, compact mechanisms, while also allowing for smooth, human-like joint trajectories. For these reasons a serial manipulator arm was selected to servo the needle. Fig. 2.6 illustrates the robotic arm concept and corresponding kinematic link chains. Having any more than 4-DOF may introduce redundancies in the needle pose; hence we chose to move forward with a 2 link, 4-DOF manipulator design, as depicted in Fig. 2.6. A compact serial arm design also allows

the device to keep the needle hidden from the patient at all times prior to the venipuncture. When folded in its home position, the manipulator has a volume of 2 x 2 x 6 cm, yet once fully extended, the needle can reach points as far as 16 cm from the robot arm origin.

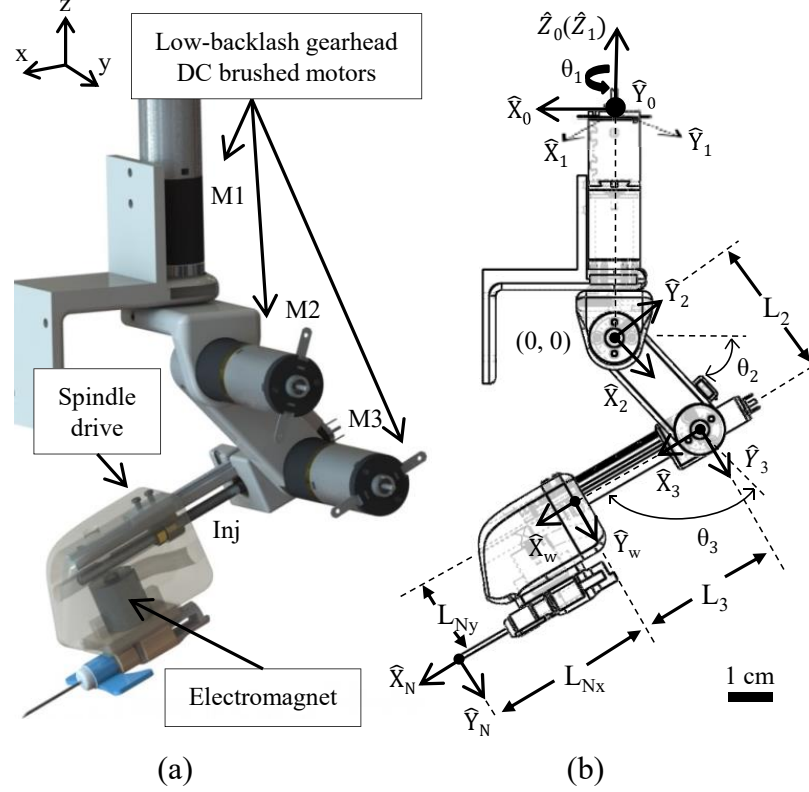


Figure 2.6: (a) Design and (b) kinematic joint frames of the 4-DOF serial arm. Coordinate axis in (a) corresponds to the notation of the 3-DOF gantry. Figure reproduced with permission from IEEE¹ (year of original publication: 2015).

After selecting the 4-DOF serial arm concept, the next step was to formulate actuation and mechanism designs to induce motion in the links. A number of serial-based medical robots incorporate cable-pulley systems^{77,101,116,228–230} to allow the motors to be placed a far distance away from the actuated joints. The most well-known medical robot that uses this design is the da Vinci surgical system (Intuitive Surgical Inc.)⁹⁶. Cable-pulley based systems have several advantages over other gearing mechanisms; namely they are backlash-free. In addition, because cables and pulleys can be extended over far distances, the motors can be placed off the arm toward the base of the robot, decreasing the size and simplifying sterilization protocols for the end-effector.

The da Vinci system uses their cable-pulley based manipulator arms as disposable items

that are replaced around every ten surgical procedures⁹⁶. After use, the tension in the cables diminishes, which can potentially result in slip at the cable-pulley interface; thus posing safety issues. This is a major disadvantage in cable-pulley systems. To avoid slip, one can either perform maintenance on the system to ensure the tension is appropriate, or replace the manipulator that uses the cables and pulleys after extensive use. Maintaining tension in the cables is a tedious and laborious process, while replacing the entire cable-pulley mechanism can be extremely costly. For venipuncture, with over 1B procedures performed annually, tightening the pulleys or replacing the needle manipulator after use would be highly impractical. In addition, belts and cables are compliant. By compromising stiffness, it can be difficult to achieve high precision, which is a critical design requirement in our venipuncture device. For these reasons, we chose not to pursue a cable-pulley system for the serial arm.

Several other drive trains for rotational link motion were then considered, such as timing belts/pulleys, harmonic drives, bevel gears, spur gears, and worm gears. However, most of these were not appropriate for our application. Specifically, although timing belts/pulleys and harmonic drives are backlash-free, the gears are bulky, and thus did not meet our size requirements. In addition, both belts and the compliant spines on harmonic drives are flexible components, which can potentially decrease accuracy and precision in the system. Bevel and spur gears are also large, can be complicated to implement, and can introduce excessive backlash in the system if not properly set. Worm gears are self-locking, but are difficult to reliably set for low backlash. Furthermore, they operate based on sliding friction, which causes wear in the gears, is energy inefficient, and requires lubrication over the life cycle of the mechanism¹²⁵.

Ultimately, a direct drive actuation scheme was selected in the revolute links to keep the joints compact and stiff. Low-backlash ($<0.3^\circ$) precision gear heads (GS16VZ, Maxon Precision Motors, Inc.) were integrated into the motors, and the output of the gear axles were directly attached to each rotational link in the manipulator chain. Direct drive actuation minimizes backlash as well as Coulomb friction in the links, and is also simple to implement. Constant force springs were also incorporated into each link to eliminate the subtle backlash present in the gearheads, and to provide an additional safety feature in case

of a power or controller malfunction.

For the linear injection system, a spindle drive was used to provide smooth linear motion, while minimizing backlash (1.8°). The spindle ball-screw mechanism is also the most common transmission method for precise linear motion¹²⁵. Since our system must have the precision to cannulate veins as small as $\varnothing 1$ mm, the spindle drive—which has a reported 0.112 mm positioning accuracy²³¹—satisfies this criteria. Figure 2.6 illustrates the design concept and functional prototype of the compact, lightweight, 4-DOF serial arm that provides increased range of motion to improve cannulation accuracy. All custom designed linkage parts were rapid prototyped with a desktop 3D printer (Mojo, Stratasys Ltd.) using ABS plastic.

2.2.3.2 Kinematics

Robot kinematics is the study of rigid link body motion, disregarding the forces that induce it. The kinematics of a manipulator arm include the geometrical and time-based properties of the motion, where the robot links are modeled as rigid bodies and each joint is assumed to have purely rotational (i.e., revolute) or translational (i.e., prismatic) movement. To deal with the complex geometry of the manipulator, it is necessary to assign coordinate frames to each robot joint, and frames that describe the relationship between the overall robotic system (i.e., base, wrist, and tool frame).

As the robot arm articulates, the locations of the link frames change; thus it is critical to define the kinematic equations that correlate the link frames, in order to determine the needle tip position and pose at all times. Forward kinematics is used to extract the needle tip position from the joint parameters, whereas inverse kinematics is used to calculate the joint angles required to position the needle tip at the desired location. The kinematic equations for the manipulator arm were derived using a standard Denavit-Hartenberg (DH) convention^{232,233}. Here, the 3D position of the target vein is inputted into the inverse kinematic equations, which then outputs the required joint parameters to position the needle tip at the desired point. In short, i = joint number; a_i = distance from \hat{Z}_i to \hat{Z}_{i+1} measured along \hat{X}_i ; α_i = angle from \hat{Z}_i to \hat{Z}_{i+1} measured about \hat{X}_i ; d_i = distance from \hat{X}_{i-1} to \hat{X}_i measured along \hat{Z}_i ; θ = angle from \hat{X}_{i-1} to \hat{X}_i measured along \hat{Z}_i ; W = wrist

frame on the end-effector; L_2 = length of link 2; L_3 = length of link 3. Fig. 2.6b shows the assignment of link frames, and Table 2.1 contains the DH parameters used to solve the kinematic equations.

Table 2.1: DH parameters of the 4-DOF serial arm kinematic chain. Table reproduced with permission from IEEE¹ (year of original publication: 2015).

i	α_{i-1}	a_{i-1}	d_i	θ_i
1	0	0	0	θ_1
2	90°	0	0	θ_2
3	0	0	L_2	θ_3
W	0	0	L_3	0

The parameters specified in the DH table link the manipulator origin frame to the wrist frame at the distal end of the end-effector as governed by Eq. 2.6. The needle tip position is then computed using a wrist-to-tool transform.

$${}^0_W T = {}^0_1 T(\theta_1) * {}^1_2 T(\theta_2) * {}^2_3 T(\theta_3) * {}^3_W T(L_3) \quad (2.6)$$

Using Eq. 2.6, the operating workspace was computed to be 310 cm^3 for the needle manipulator, and is displayed in Fig. 2.7. The length of links 2 and 3 were optimized by running kinematic simulations so that the volume of reachable workspace was sufficient for the needle insertion task (i.e., 175 cm^3 as governed by a clinical survey¹⁴³).

The LabVIEW graphical programming environment (National Instruments, Inc.) was extensively used for the kinematic programming. Specifically, LabVIEW has a built-in *Robotics Toolbox* that includes functions to solve both forward and inverse kinematic equations when given the DH parameters. A detailed derivation of the kinematic equations for the manipulator arm, including the transformation matrices is provided in Appendix A.1. Having a robust and efficient method of calculating the joint angles from the end effector position in Cartesian coordinates is crucial to the functioning of the manipulator arm. The robotic system needs the ability to input the 3D injection point (x, y, z) selected by the imaging controls, and output the corresponding manipulator joint angles $(\theta_1, \theta_2, \theta_3)$. This way, the robot arm can accurately and precisely position and insert the needle into the

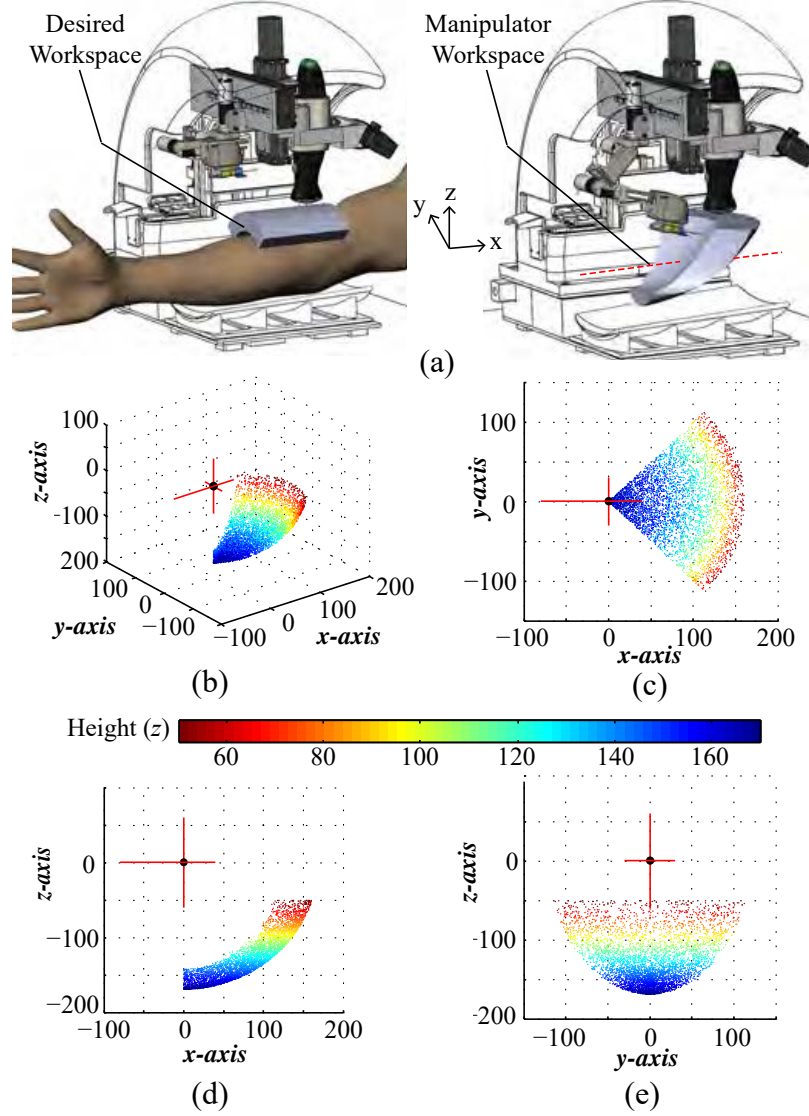


Figure 2.7: (a) Desired (left) and dexterous (right) workspace of the manipulator highlighted in gray in the CAD model. Dotted red line in the manipulator workspace image indicates that the workspace can be translated ± 50 mm along x to adjust to the patient's arm size. (b–e) Manipulator operating workspace from the serial arm origin with practical limits set on the M1 joint rotation ($\pm 45^\circ$) and z height ($z < -20$ mm). Units are in mm. Figure reproduced with permission from IEEE¹ (year of original publication: 2015).

desired target vein. In addition, as a result of the real-time architecture of the kinematic algorithms (< 30 ms loop rate), the manipulator can dynamically reposition the needle to account for vein or tissue motion.

2.2.3.3 Motor Torque and Power Calculations

Using SolidWorks CAD software to obtain mass and inertial properties of the ABS parts, the required torques necessary to actuate each link were calculated. These power and torque values led to the selection of four motors, labeled in Fig. 2.6. Starting with motor 3 that rotates the base joint connecting the bottom and top arms, the required torque was calculated from Eq. 2.7.

$$T = F * d \quad (2.7)$$

Here, the force due to the weight of the links includes the mass of the bottom link, plus the linear injection assembly. In total, the force is 0.33 N. Assuming the center of mass along the bottom arm is 7.88 cm from the point of rotation (to account for the linear injection assembly at the distal end) and that motor 3 experiences max torque when the bottom arm is parallel with the floor, the max required torque is 2.58 N-cm. Motor 3 must also satisfy the required mechanical power output from Eq. 2.8.

$$P_{out} = T_{out} * \omega_{out} \quad (2.8)$$

Assuming a max rotational speed of 10 rpm, this led to a power output of 27 mW. To satisfy these criteria, motor 3 was selected with $P > 27$ mW and $T > 2.58$ N-cm. However, 2.58 N-cm is the max required torque, so this motor does not have to continuously supply 2.58 N-cm, but rather just has to be able to handle intermittent high torque situations.

A similar approach was taken to calculate the required torque and power output for motor 2 which rotates the top arm (including motor 3 and the linear injection assembly). The required max torque and power output for motor 2 were calculated as 5.62 N-cm and 58.9 mW respectively. More detailed engineering calculations are included in Appendix A.2 for reference.

Moving to motor 1, which swivels the robot arm from the top, we made the assumption that it is rotating a cylindrical flywheel with a variable radius depending on how far both

links are stretched out. The required torque was calculated from Eq. 2.9:

$$T = \frac{J}{9.55 * 10^4} * \frac{N}{t} \quad (2.9)$$

where J is the moment of inertia [kg-cm²], N is the rotational speed [rpm], and t is the time to accelerate to that rotational speed [sec]. Additionally, the moment of inertia was calculated using Eq. 2.10:

$$J = \frac{1}{8} * WD + WS^2 \quad (2.10)$$

where W is the mass of the rotating object [kg], D is the cylinder diameter [cm], and S is the turning radius [cm]. The resulting max moment of inertia, torque, and power output were calculated to be 9.06 kg-cm², 0.095 N-cm, and 0.99 mW respectively.

Lastly, for the needle injection motor on the bottom link, the required torque and power were calculated based on an axial injection force of 5 N, which has been shown to be the max required force to pierce human skin tissue and cannulate the underlying vein^{138,230,234}. The resulting max torque and power output were calculated as 3 N-cm and 0.35 W respectively. Table 2.2 summarizes the motor requirements for each joint in the needle manipulator.

Table 2.2: Motor torque and power requirements for each joint in the manipulator.

Motor	Torque (N-cm)	Power (mW)
1	0.095	0.993
2	5.62	58.9
3	2.58	27.0
Inj	2.50	26.2

2.2.3.4 Motor Selection

Electrical actuators were then sourced based on the motor torque and power calculations. Various motor classes were considered including stepper, DC brushless, and DC brushed motors. The first subset—stepper motors—allow for precise position control in the form of angular steps. Here, a full motor rotation is divided into equal steps and the rotor's

pose can be set to move and hold at one of these angles using an open-loop controller (i.e., no feedback is required if the motor properly satisfies the system's torque requirements). However, to achieve this holding torque, the stator and surrounding EMs are often large and heavy to accommodate the high continuous holding current. Running high current through the motor windings also tends to heat up the motor, posing a safety concern for medical robots. Since the serial arm motors are mounted directly to the links themselves, the large weight and excessive heating in stepper motors make them impractical for our application.

Similar to stepper motors, DC brushless motors consist of permanent magnets that rotate around a fixed armature, while a controller switches the electrical phase to the windings resulting in rotation at the motor shaft. Although, DC brushless motors have no issues supplying current to the rotating armature, the electronic controls that continuously switch the phase to the windings tend to be highly complex and expensive.

Conversely, DC brushed motors operate based on a commutator reversing the current direction through the motor coil via contact brushes. Here, the brushes make contact with the commutator as the motor shaft rotates. Upon excessive use, sometimes the brushes can wear down and must be replaced. Having to replace brushes is rare and is usually only the case if motors are run continuously at high speeds for extended periods of time (i.e., months to years). In our case, the motors in the needle manipulator will be operating intermittently at low speeds (<10 rpm). DC brushed motors are also much simpler to control than DC brushless motors, because there is no need to switch the current to the motor windings via the electronic controller. By simply adjusting the input voltage and current, the speed and torque can be controlled in DC brushed motors. Because of the ease of control and low duty-cycle for the actuators in the robotic arm, DC brushed motors were selected.

The needle manipulator is an ultra-precise positioning system; hence, it was crucial to select DC brushed motors that have self-contained sensors attached to the rotating axles. These sensors provide feedback to the host processor—relaying the needle tip position in real-time. We selected motor assemblies with low backlash ($<0.3^\circ$) gearheads and incremental quadrature encoders for the rotational joints (Maxon Precision Motors, Inc.). The low backlash, high gear ratio drivetrains ensure adequate stiffness in the joints, and prevent back-drivability. A miniature spindle drive linear actuator was selected for the injection

system at the distal end of the robotic arm. The actuator has a stroke length of 5.5 cm and a linear speed of 2.5 cm/s to ensure quick cannula insertion. Table 2.3 lists the key mechanical and electrical parameters for each motor assembly, including the specific parts for each component.

Table 2.3: Summary of the selected motor parameters, with Maxon Motor part numbers listed in parentheses.

	Motor (Stall Torque [N-cm]; No Load Speed [rpm])	Gearhead (Gear Ratio)	Encoder (Counts [cpt])
M1	47.8; 11500 (PN: 110075)	84:1 (PN: 416391)	512 (PN: 201937)
M2	47.8; 11500 (PN: 110075)	108:1 (PN: 327788)	512 (PN: 201940)
M3	47.8; 11500 (PN: 110075)	108:1 (PN: 327788)	512 (PN: 201940)
Inj	9.25; 15600 (PN: 347727)	4:1 (PN: 427967)	100 (PN: 334910)

2.2.3.5 Motor Control System

As depicted in Fig. 2.8, the motor control scheme is as follows. First, the 3D coordinates of the selected target vein center are outputted from the US vein segmentation algorithm and inputted into the inverse kinematic equations. Here, the joint parameters needed to position the needle at the desired location prior to the cannulation are calculated. The manipulator has the ability to dynamically steer the needle in real-time by tracking the injection site and vein walls in the US image to account for patient arm movement, vein/tissue deformation, and vein rolling. Specifically, a trajectory planner is used that calculates the needle path, interpolating from the start and end points at a 20 Hz cycle rate using an exponential decay function. This allows us to continuously feedback the updated desired injection site extracted from the US image. In this fashion, the US serves as image feedback to guide the needle manipulator in a closed form control loop.

During the cannulation, the insertion angle is gradually decreased from 30° to 15° following contact with the skin surface. Here, the cannula is steered into the vein until the needle tip reaches the center. By tracking the target vessel in real-time throughout the insertion,

the device is able to compensate for rolling veins, tissue motion, and the viscoelastic nature of human tissue.

To send signals from the host processor to the actuators, two modes of motor control were investigated: analog and digital. The first consisted of sending analog voltage signals from a data acquisition board (USB-6009, National Instruments, Inc.) to two motor controllers (Sabertooth 2x5, Dimension Engineering, LLC) where 0 V corresponded to full forward; 5 V, full backward; and 2.5 V, the zero point. The encoder signals from the motors were read from a secondary microcontroller (Mega 2560, Arduino) using interrupt pins at a baud rate of 115200 to ensure no pulses were missed. Since all motors are moving at relatively low speeds (<10 rpm), the Arduino board was more than capable of counting the encoder signals. The Sabertooth motor drivers operate based on speed control, meaning when the speed is 0, the torque on the rotor is also 0. This turned out to be problematic, because the torque is dependent on the motor speed. Hence, it is impossible to directly adjust the torque values in the motors using this control method.

Alternatively, digital control techniques, such as pulse-width modulation (PWM), take advantage of the on/off nature of digital systems to control the motor power supply. This is accomplished by switching the power on and off at high frequencies (>10 kHz). The main advantage of PWM control is that the power loss is close to 0 in the device. When the switch is on, there is almost no voltage drop across the switch, and when the switch is off, there is almost no current flow²³⁵. The second motor control technique consisted of four independent digital position controllers (EPOS2 24/2, Maxon Precision Motors, Inc.) for each joint.

The digital motor drivers operate based on a controller area network (CAN) protocol to communicate with the host processor and send 32-bit PWM signals (100 kHz switching frequency) to the motors. These controllers provide position, velocity, and current control, taking advantage of an acceleration and velocity feed forward control scheme (Fig. 2.8). The sampling rate of the PI current, PI speed, and PID positioning compensator are 10, 1, and 1 kHz respectively, and the counter samples the encoder pulses at 5 MHz. These cycle rates are more than sufficient to dynamically adjust the needle position based on image feedback from the US image. By virtue of the built-in current control loop, these

drivers are able to supply a holding torque to stabilize the joints once they reach the desired angles. The Maxon built-in PID tuner and LabVIEW library were used to implement these controllers into the device architecture.

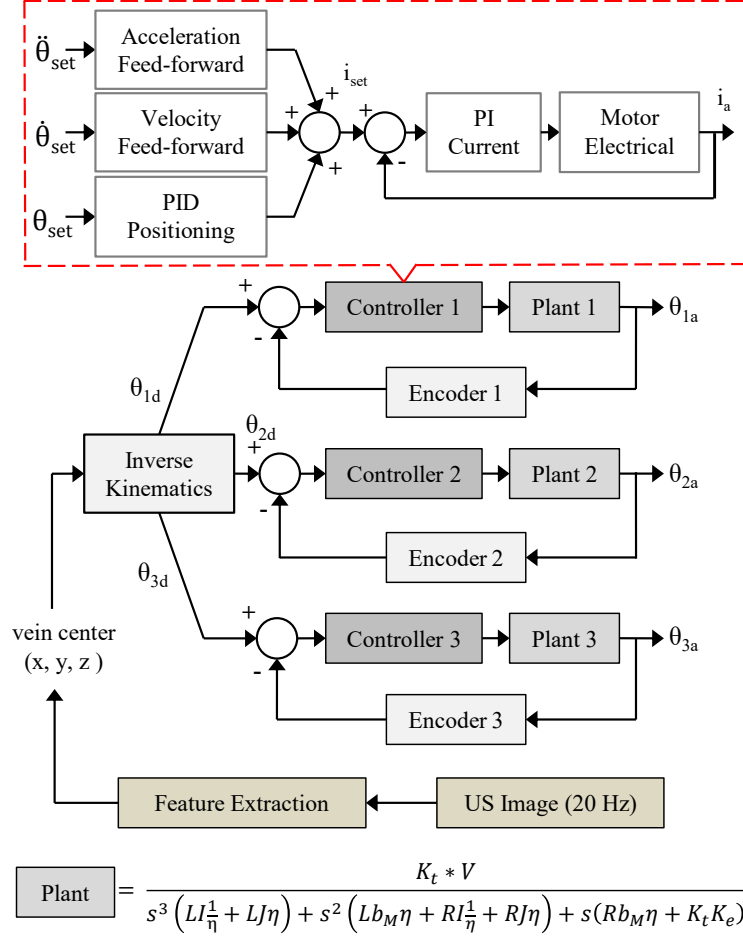


Figure 2.8: Motor position feedback control scheme for the 4-DOF serial arm. The 3D target injection site is updated from the US image at 20 Hz. Plants 1–3 have different rotational inertia ($I_1 = 9057$, $I_2 = 2000$, $I_3 = 700$ g-cm²). Figure reproduced with permission from IEEE¹ (year of original publication: 2015).

2.2.3.6 Open Loop Transfer Functions

Open loop transfer functions were derived for the DC brushed motors based on the schematics in Fig. 2.9 to run control and response simulations. Using a mesh current analysis for the electrical circuit in Fig 2.9a, Eq. 2.11 was derived. Derivations were based on the conventions discussed in Craig et al.²³³.

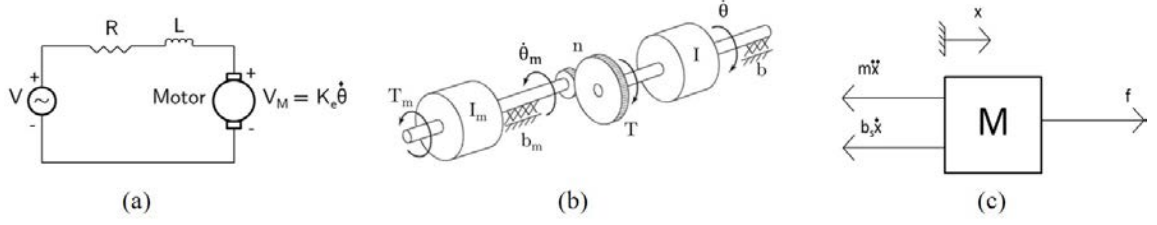


Figure 2.9: (a) Electrical and (b) mechanical schematic of a geared DC brushed motor. (c) Mechanical model of the injection system, where block M represents the mass the motor must move. R = resistance; L = inductance; V = applied voltage; K_e = EMF constant; $\dot{\theta}$ = angular velocity; $\ddot{\theta}$ = angular acceleration; b = damping coefficient; I = moment of inertia; T = torque; n = gear ratio; f = force; and b_s = damping constant.

$$Ri + L \frac{di}{dt} = V - K_e \dot{\theta} \quad (2.11)$$

Eq. 2.12 was then derived using Newton's second law for the system in Fig. 2.9b.

$$\left(\frac{1}{\eta} + \eta J \right) \ddot{\theta} + \left(\frac{1}{\eta} b + \eta b_m \right) \dot{\theta} = T_M = K_t i \quad (2.12)$$

Taking the Laplace transform of Eq. 2.12 and rearranging terms led to Eq. 2.13.

$$\theta(s)s \left(\frac{1}{\eta} Is + \eta Js + \frac{1}{\eta} b + \eta b_m \right) = K_t I(s) \quad (2.13)$$

Taking the Laplace transform of Eq. 2.11 and rearranging terms led to Eq. 2.14.

$$I(s) = \frac{V - K_e \theta(s)s}{Ls + R} \quad (2.14)$$

Substituting Eq. 2.14 into Eq. 2.13 yielded:

$$\theta(s)s \left(\frac{1}{\eta} Is + \eta Js + \frac{1}{\eta} b + \eta b_m \right) = K_t \left(\frac{V - K_e \theta(s)s}{Ls + R} \right) \quad (2.15)$$

Rearranging terms in Eq. 2.15 to obtain the appropriate transfer function with the output

(motor shaft position) over the input (voltage):

$$\frac{K_t}{s \left(\frac{1}{\eta} I s + \eta J s + \frac{1}{\eta} b + \eta b_m \right) (L s + R) + K_t K_e s} = \frac{\theta(s)}{V} = \frac{Output}{Input} \quad (2.16)$$

Grouping like terms, the final transfer function for motors 1, 2, and 3 was:

$$\frac{\theta(s)}{V} = \frac{K_t}{s^3 \left(L I \frac{1}{\eta} + L J \eta \right) + s^2 \left(L b \frac{1}{\eta} + L b_m \eta + R I \frac{1}{\eta} + R J \eta \right) + s \left(\frac{1}{\eta} R b + R b_m \eta + K_t K_e \right)} \quad (2.17)$$

The motor constants in the transfer function were provided with the actuators, and are listed in Tab. 2.4. This transfer function was used to model motors 1, 2, and 3. The only parameters that differed were the inertia terms, which were obtained from the CAD model. The open loop plant model for the linear injection motor is similar to Eq. 2.17, but contains an extra term to account for the linear movement of the injection system. The mass of the linear injection piece was modeled according to Fig. 2.9c. Equations 2.18, 2.19, and 2.20 were derived based on this mechanical system.

Table 2.4: Motor constants used for the open loop transfer function modeling.

Parameter	Motor			
	1	2	3	Inj
Rotor inertia (J [g-cm ²])	0.849	0.849	0.849	0.0355
Rotor viscous damping (b_m [mN-s-m])	3.64E-3	3.64E-3	3.64E-3	5.49E-4
Torque constant (K_t [mN-m/A])	9.17	9.17	9.17	7.11
Back-EMF constant (K_e [mV/rad/s])	9.18	9.18	9.18	7.13
Motor resistance (R [Ω])	23.0	23.0	23.0	92.2
Motor inductance (L [mH])	0.83	0.83	0.83	0.606
Load viscous damping (b [N-s/m])	0	0	0	3.0E-3
Load inertia (I [g-cm ²])	9057	2000	700	1860
Gear ratio (η)	84:1	108:1	108:1	4:1
Damping on linear sliders (b_s [N-s/m])	N/A	N/A	N/A	1.0

$$f = m\ddot{x} + b_s\dot{x} \quad (2.18)$$

$$T_L = rf \quad (2.19)$$

$$x = r\theta \quad (2.20)$$

Combining Eq. 2.18, 2.19, and 2.20, the load torque on the injection motor was:

$$T_L = mr^2\ddot{\theta} + b_sr^2\dot{\theta} \quad (2.21)$$

This load torque was then inserted into the mechanical DC motor model in Eq. 2.22.

$$\eta(b_m\dot{\theta} + J\ddot{\theta}) + T_L = T_M = K_t i \quad (2.22)$$

Taking the Laplace transform of Eq. 2.22, combining it with Eq. 2.14, and performing the same steps used to obtain the transfer function for the previous motors, the plant model for the linear injection motor becomes:

$$\frac{\theta(s)}{V} = \frac{K_t}{s^3(\eta JL + mr^2L) + s^2\left(\eta b_mL + \frac{1}{\eta}JR + mr^2R + b_sr^2L\right) + s(b_sr^2R + K_tK_e + \eta b_mR)} \quad (2.23)$$

2.2.4 Automated Needle Handling

An automated needle handling system was implemented to limit practitioner contact with exposed sharps, reduce the risk of accidental needle sticks, and improve safety throughout the procedure. The goal was to develop a system that automates the needle loading, uncapping, and release process. In return, this would also improve the ease-of-use of the device and enable shorter procedure times. The automated needle handling system was designed, iteratively prototyped, and tested. Specifically, the design was split into three modular

components representing the key steps in the needle handling protocol for the device: (1) needle loading, (2) needle uncapping, and (3) needle attach and release from the robotic end-effector. Each subsystem was designed to be compatible with the pre-existing robotics implemented in the device, including the 3-DOF gantry and 4-DOF articulated serial arm.

2.2.4.1 Needle Grip-and-Release Mechanism

Two preliminary concept designs were considered for automated needle gripping and release (Fig. 2.10). The first design consisted of an EM embedded in the end-effector of the manipulator arm and a disposable plastic clip containing a steel washer for attachment to the needle. When the EM is turned on, the end-effector securely grabs the needle with a 2 N holding force, and the device proceeds with the phlebotomy. At the end of the procedure, the manipulator can dispose the needle in a sharps container by turning off the EM, thereby releasing the cannula. The second concept idea utilized a miniature DC motor and spur gear drive train to open and close a two prong gripper at the distal end of the end-effector. In this design, no needle clip was required; however, there was added complexity from incorporating the actuator.

Both designs were rapid prototyped via 3D-printing. From qualitative observations, several flaws were noticed in the two prong gripper idea while testing the mechanism. Specifically, the large amount of backlash present in the spur gear drive train limited the repeatability in the system. Although the prongs could successfully grab the needle at first, after successive trials, the motor required a different position command to lock the needle, due to the backlash. This fluctuating position command to grab and release the needle would be difficult to predict and program into the device.

Additionally, due to the complex geometry of Butterfly needles (e.g., from Becton Dickinson), the prongs had difficulty picking up the needle in the proper orientation every time. If the manipulator grabs the needle in the wrong position, this causes errors in the kinematics, and can potentially lead to a missed stick. Conversely, the EM-based design was simple to implement and control. Fig. 2.10a shows the rapid prototyped needle clip that latches onto the barrel of the cannula, as well as the steel washer in the center of the clip. Here, the needle easily clips into the plastic holder ensuring the cannula is positioned in the

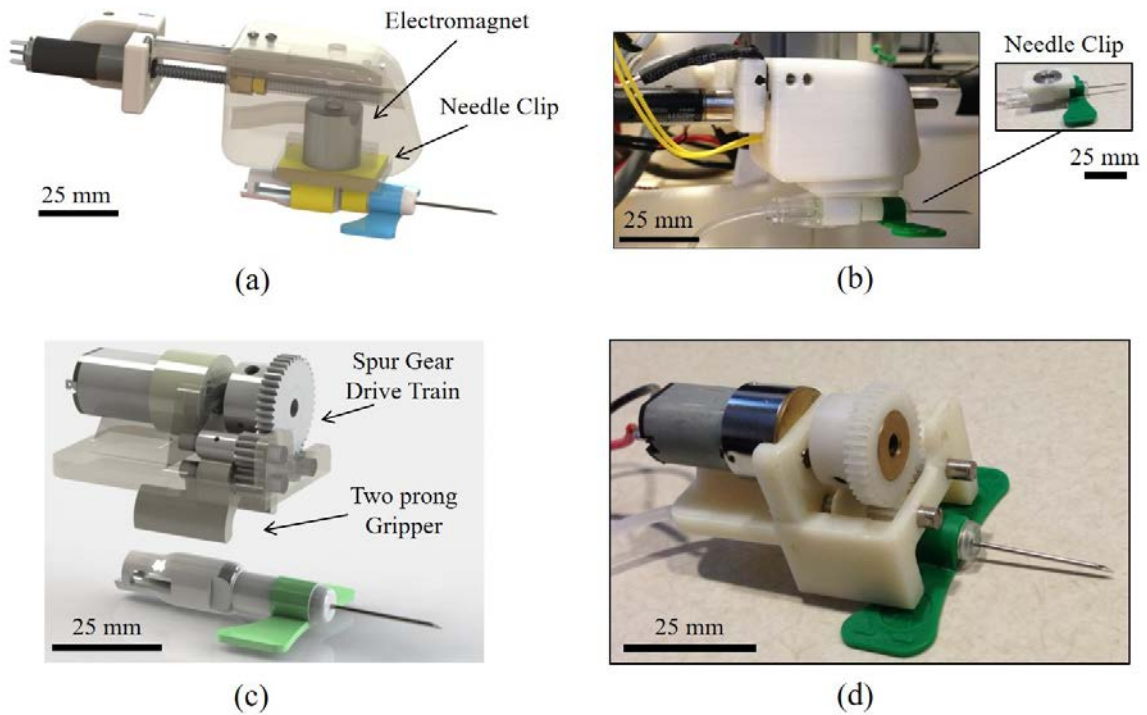


Figure 2.10: Needle gripping and release mechanisms. (a) EM-based needle attachment design and (b) prototyped end-effector. Inset shows the needle clip wrapped around the cannula. (c) Actuated two prong gripper design model and (d) prototype.

proper orientation for the manipulator to grab it. We decided to move forward with more rigorous testing using the EM-based prototype based on these observations.

2.2.4.2 Needle Re-loader Mechanism

The re-loader mechanism consisted of a mount for the needle, linear ball bearing sliders, and a spring-based push-to-open grab latch. As illustrated in Fig. 2.11, the protocol for using this system is as follows. First, the clinician loads the needle, with the attached clip containing the EM, onto the designated slot on the re-loader with the cap still in place (Fig. 2.11a). The clinician then pushes the latch closed, aligning the cannula in the proper position and orientation for the robotic arm (Fig. 2.11b). When the manipulator is ready to grab the needle, the robot gantry unit translates horizontally in the y -direction, engages the EM in the end-effector, and latches onto the needle via the strike plate (i.e., steel washer) embedded in the needle clip. After the venipuncture, the robot disengages the needle by deactivating the EM, placing the exposed cannula in a sharps container. Once the clinician

completes the procedure (e.g., interchanging blood vials in the case of a blood draw), the needle cap is manually disposed, and a new Butterfly needle can be loaded.

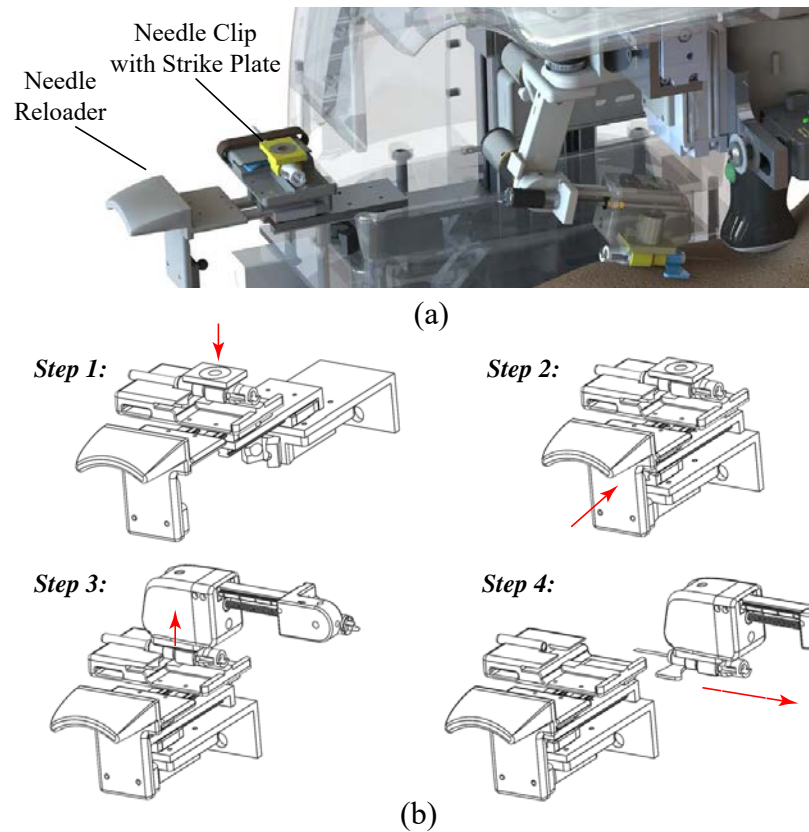


Figure 2.11: (a) CAD rendering of the needle re-loader system, and (b) step-by-step protocol: 1. The clinician manually loads the needle into the tray; 2. the clinician closes the tray; 3. the manipulator grabs the needle via an electromagnetic mechanism; and 4. the manipulator translates to remove the cap and proceeds with the venipuncture. Figure reproduced with permission from IEEE¹ (year of original publication: 2015).

2.2.4.3 Needle Uncapping System

Two approaches to uncap the needle while in the re-loader tray were investigated. The first consisted of a Velcro strap connected to the re-loader tray that wrapped around the needle cap. After placing the cannula in the indicated slot, the clinician would then strap the Velcro around the cap, serving as a mechanism to hold the cap in place while the robotic end-effector grabs the needle. The main limitation with this method was that it required the clinician to manually strap the Velcro around the needle cap with the proper amount of tension. If the strap was too loose, then the cap would not be removed, and if the strap was

too tight, then the cannula may bend. The second concept involved designing a notch in the re-loader tray for the needle cap to reside. An adhesive rubber was placed on the walls of the notch to grip the cap once the end-effector latched onto the needle. From qualitative observations, the second design was more effective at consistently removing the needle cap. Hence, we selected this method to undergo rigorous testing with the full needle handling system described below.

2.2.5 Experimental Testing

2.2.5.1 Control Loop Simulations

Using the open-loop plant equations for each motor, simulations were conducted using MATLAB (The MathWorks, Inc.) to validate each model. In an open loop control system there is no feedback; hence, in these simulations, providing a step voltage input resulted in continuous position movement at constant velocity. Here, we tested for the response time of each plant model (i.e., time to reach constant velocity) and correlated these velocities with the indicated values from the motor spec sheets.

After validating the open loop models, the next step was to close the loop and create a negative feedback positioning system. The robot manipulator was assumed to be linear, because of the small size and large gear ratios in the motors. This assumption permitted the use of a linear control method in the feedback loop. We utilized SimuLink to create block diagrams for each actuator in the manipulator arm and ran simulations with a proportional, integral, and derivative (PID) compensator (Fig. 2.12).

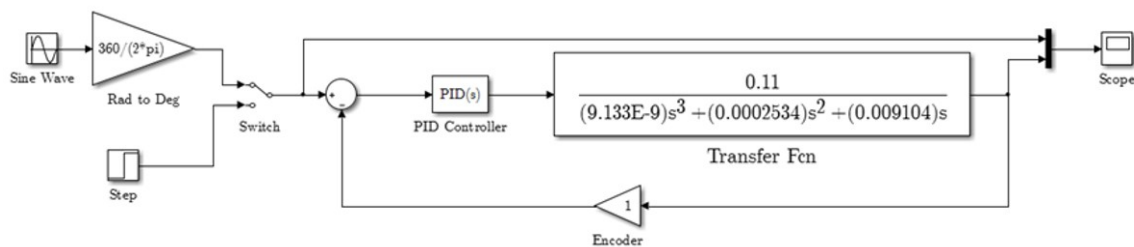


Figure 2.12: Example of a SimuLink block diagram used to run closed loop positioning simulations and design suitable PID controllers for each motor in the 4-DOF serial arm.

The purpose of a PID controller is to decrease the error between the desired and actual signal as quickly as possible without introducing noise and ancillary oscillations into the system. Each term has its own function: the proportional constant works to decrease rise time, the integral term acts to eliminate steady state error, and the derivative constant reduces system overshoot. The design requirements for the control system included: (1) overshoot $<5\%$, (2) rise time <0.2 s, (3) settling time <0.4 s, and (4) no steady state error. Considering these criteria and using SimuLink's built-in PID Tuner, optimal P (K_p), I (K_i), and D (K_d) gains were obtained for each plant model in the manipulator arm based on a unit step response. The output PID parameters also included a noise filter on the derivative term as shown in Eq. 2.24, to eliminate unwanted oscillations in the case of a disturbance to the system.

$$U(S) = G_{pid}(s)E(s) = \left(K_p + \frac{K_i}{s} + \frac{K_d s}{\tau_f s} + 1 \right) E(s) \quad (2.24)$$

Using these PID gains, frequency tracking simulations were then performed using a sine wave input to evaluate the controller response to a smooth signal. The sine wave amplitude for all rotational plants was maintained at 10° , while the amplitude for the injection system was maintained at 5 mm. In addition, the frequency was varied from 180 deg/s to 22.5 deg/s to simulate the absolute max and min speed ranges the manipulator will encounter during use.

The results of the simulations are presented in Fig. 2.14, illustrating that all systems are stable and controllable. In a highly geared joint ($n \gg 1$) the inertia of the motor axle can be a significant portion of the combined effective inertia. This allowed us to make the assumption that the effective inertia is constant, even though the inertia of each joint actually varies with configuration and load. In highly geared manipulators, the variations represent a smaller percentage than they would in a direct drive manipulator²³⁶. To ensure that the motion of the robot link is never under-damped, the value of the inertia load was selected to be the max value that it encounters (I_{max}). This resulted in a system that was critically damped or over-damped in all situations.

2.2.5.2 Serial Arm Tracking Experiments

When designing a servo-based system, it is critical to understand how to send signals to the plant (i.e., the motor in our case) and how to read the feedback from the sensor. For the venipuncture robot, this all must occur in real-time. The controller sending signals to the motor must be fast enough to make subtle position adjustments based on the feedback from the sensor. Likewise, the sensor must be sampled at a high enough frequency to determine the correct motor position at all times.

To develop a closed loop positioning system with the prototyped manipulator, two control schemes were investigated, as previously introduced. The first utilized a data acquisition board (USB-6009, National Instruments, Inc.), two motor drivers (Sabertooth 2x5, Dimension Engineering, LLC), and a secondary microcontroller (Mega 2560, Arduino). Analog voltage signals at 14-Bit resolution were sent from the data acquisition board to the motor drivers to amplify the current which was then sent to the motors. The Arduino board sampled the incremental encoders at 10 kHz using 115200 baud on the interrupt pins.

The tuned PID gains obtained from the MATLAB simulations were inputted into the control loop to finalize the serial arm feedback positioning system. However, there were several limitations with this method that became apparent during testing. Namely, the Dimension Engineering motor drivers only operate based on speed/voltage control, not torque/current control. Hence, these drivers are not capable of providing a holding torque once a specified angle is reached on the motor. Instead, once the desired position is attained, the voltage (and thus the power) supplied to the motors drops to 0, which could cause the motor to lose its position if an excessive amount of torque is applied at the end-effector. Also, this technique required three microcontroller boards and extensive wiring, which complicated the system and increased the overall form factor of the device.

The second control scheme utilized the Maxon digital position controllers, sending PWM signals to the motors. With a built-in current control loop, these drivers were able to supply a holding torque once the motors reached the desired angles, enabling the joints to lock their positions. The digital position controllers also included built-in PID tuners and an extensive LabVIEW control library.

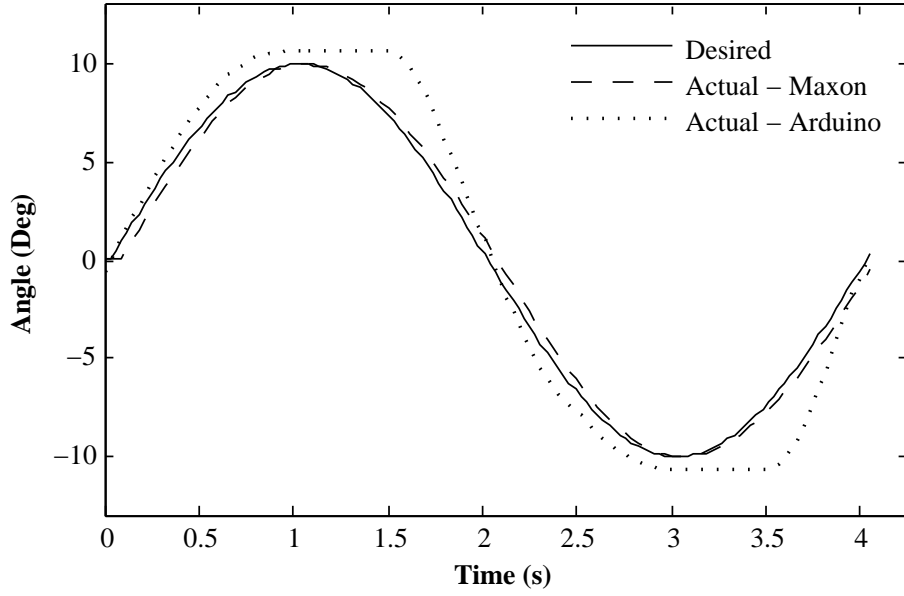


Figure 2.13: Qualitative sine wave frequency test results for joint 2 (amplitude = 10° , and frequency = 90 deg/s), comparing the desired vs actual signal from the Maxon controller and NI/Arduino controller. Figure reproduced with permission from IEEE¹ (year of original publication: 2015).

To evaluate the control schemes in the robot arm, frequency tracking experiments were performed for each joint independently using sine wave inputs. Sine wave frequencies were varied from $45\text{--}180 \text{ deg/s}$ to simulate the absolute min and max speed ranges the manipulator would encounter during a venipuncture procedure. The wave amplitude was maintained at 10° for each revolute joint and 5 mm for the injection system. Both the tested frequencies and amplitudes were the same as those used for the simulations. As an example, qualitative tracking results for joint 2 are shown in Fig. 2.13. Figure 2.14 displays the results from these experiments, showing RMS errors at the needle tip. Frequency testing indicated that each joint was controllable and highly repeatable (mean standard deviation across all tests was 0.005 mm).

The results (Fig. 2.14) indicated that the digital Maxon controllers outperformed the NI/Arduino control scheme for each joint across all tested frequencies. Using a two-sample t-test computation, the Maxon control technique was significantly better ($p < 0.001$) than the NI/Arduino method. Another observation, was the extremely low standard deviation in both control schemes. This implied that each plant was controllable, reliable, and

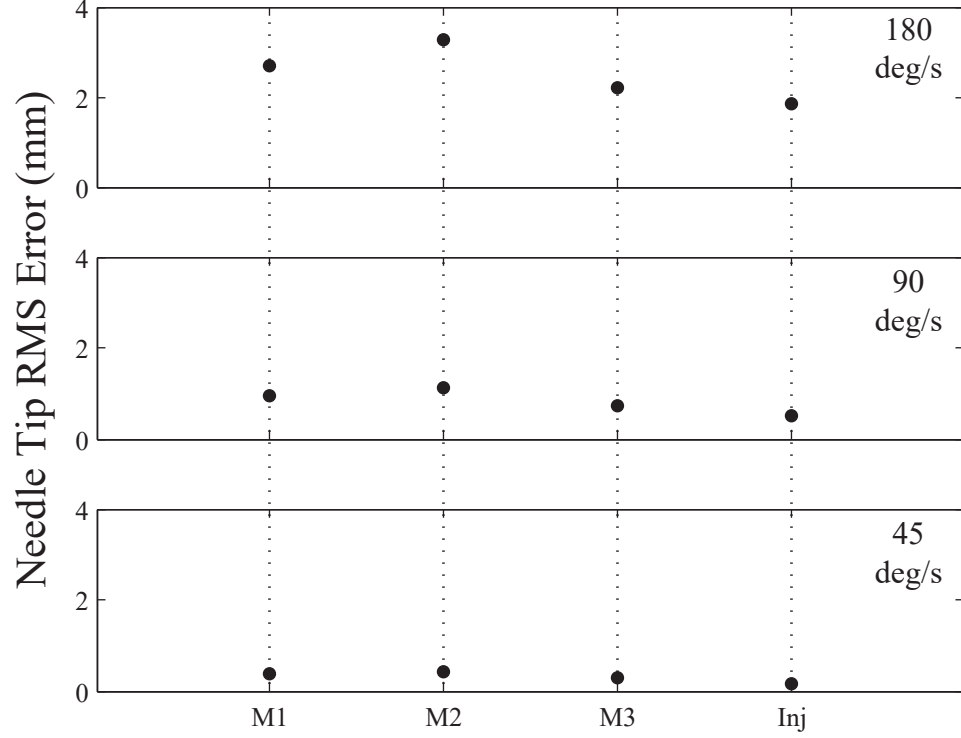


Figure 2.14: Average RMS error ($n=3$) for each joint in the needle manipulator at high (180 deg/s), mid (90 deg/s), and low (45 deg/s) frequency levels. M1 = motor 1; M2 = motor 2; M3 = motor 3; Inj = injection actuator. Figure reproduced with permission from IEEE¹ (year of original publication: 2015).

repeatable—all critical points when designing a precise positioning system that must have the ability to cannulate veins as small as 1 mm in diameter.

2.2.5.3 Needle Positioning Testing

To test the positioning accuracy, precision, and operating workspace of the needle manipulator, we conducted studies in which we positioned the needle tip on the center of $\varnothing 4$ mm circles on a calibration grid. The circles were oriented on a flat plane in a 7x7 grid separated by 7 mm center-to-center. The grid structure was rigidly mounted to the base of the robot (Fig. 2.15a); hence we could relate the coordinates of the circles with the robot coordinate frame by extracting the dimensions from the CAD model.

In all experiments, the robot arm was initially set on the gantry, so the needle was in-plane with the middle circles along the y -axis. For each trial, the experimental protocol included extracting the center of the circle (x, y, z) via the robot frame, then using this

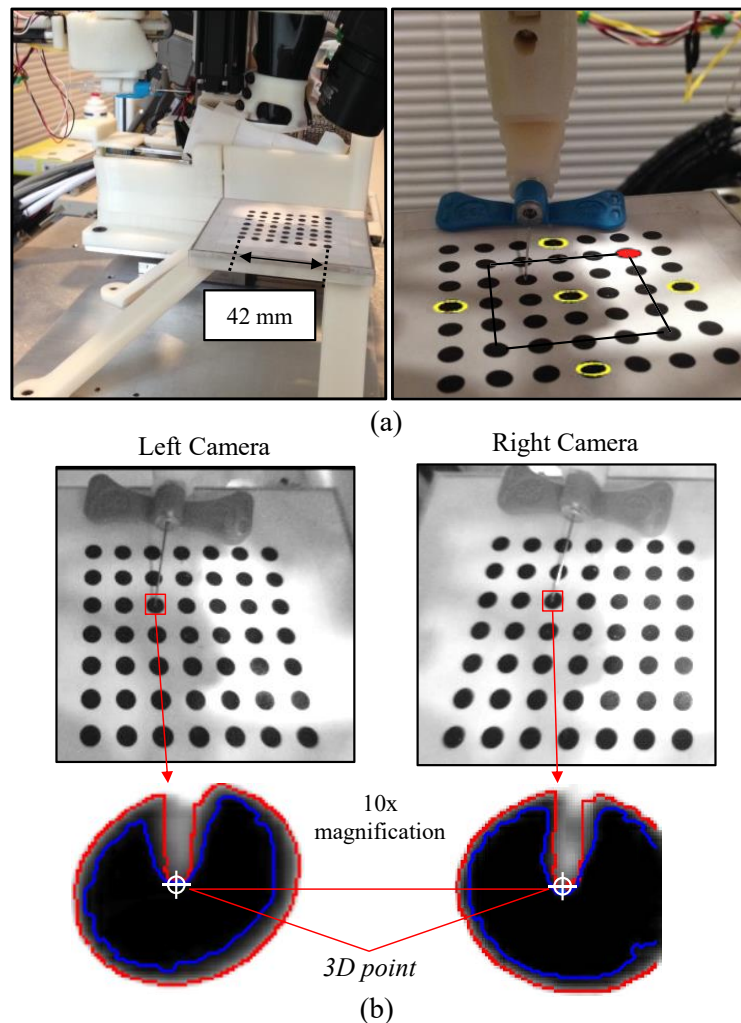


Figure 2.15: (a) Experimental setup of the needle positioning testing (left) and an image of the robot calibration grid (right). Yellow circles denote those used for repeatability testing; inner 5x5 grid outlined in black, indicates circles used for positioning studies; and red circle indicates plot origins in Fig. 2.16. (b) Stereo NIR images with the needle tip outlined in red, and 10x magnified images illustrating the region grow (blue) and edge detection (red) algorithms to segment the needle tip. Final needle tip selection was performed manually to ensure minimal errors. The 10x images have a pixel resolution of 0.1 mm. Figure reproduced with permission from IEEE¹ (year of original publication: 2015).

coordinate as the input into the inverse kinematic controls of the manipulator to set the required joint parameters to position the needle tip on the center of the circle. Finally, the desired circle center location extracted from the CAD model was compared to the actual needle tip position using the fixed cameras on the robot. Needle tip segmentation was achieved using a region grow formula with a Canny edge detector. To ensure minimal errors, the needle tip was manually selected in the post-processed images. Fig. 2.15b shows

stereo NIR images of the needle tip positioned at the center of a test circle on the calibration grid, as well as the resulting needle tip segmentation from the region grow algorithm and edge detector.

To first test the repeatability of the needle manipulator, we ran 50 trials on the five yellow outlined circles labeled in Fig. 2.15a, and compared the actual versus desired needle tip position. The average 3D positioning error (mean \pm standard deviation) was 0.81 ± 0.02 , 0.79 ± 0.01 , 0.94 ± 0.02 , 0.66 ± 0.02 , and 0.52 ± 0.02 mm for the front, middle, back, left, and right circles respectively. These circles were chosen to test the repeatability of the manipulator across the workspace area. Though the positioning errors were greater than expected, the low standard deviation values indicated that the serial arm was extremely repeatable.

Table 2.5: Mean (n=25) needle tip positioning errors; dx , dy , and dz refer to the needle tip error in the x , y , and z dimensions respectively. All units are in mm. Table reproduced with permission from IEEE¹ (year of original publication: 2015).

	Before Compensation				After Compensation			
Platform Height	dx	dy	dz	3D	dx	dy	dz	3D
66	0.33	2.80	0.71	2.95	0.078	0.06	0.17	0.21
70	0.28	1.75	0.49	1.87	0.099	0.16	0.09	0.24
74	0.36	1.12	0.61	1.40	0.084	0.09	0.12	0.20
78 (ref)	0.72	0.11	0.58	0.94	0.085	0.09	0.08	0.16
82	0.35	0.95	0.55	1.23	0.090	0.11	0.12	0.21
86	0.28	1.97	0.70	2.17	0.093	0.14	0.12	0.23
90	0.33	2.01	0.64	2.19	0.145	0.10	0.11	0.22
Avg	0.38	1.53	0.61	1.82	0.096	0.11	0.11	0.20

To further test the free-space positioning accuracy, the calibration grid was removed, and the needle tip was then placed at the coordinate of every circle within the inner 5x5 grid, as indicated by the black square outlined in Fig. 2.15a. During the experiment, the height of the grid was varied over seven heights at vertical increments of 4 mm. In this way, the accuracy of the robot was evaluated over 175 evenly spaced positions within a 28 x 28 x 24 mm work volume. By determining the exact offset of the manipulator at each grid point,

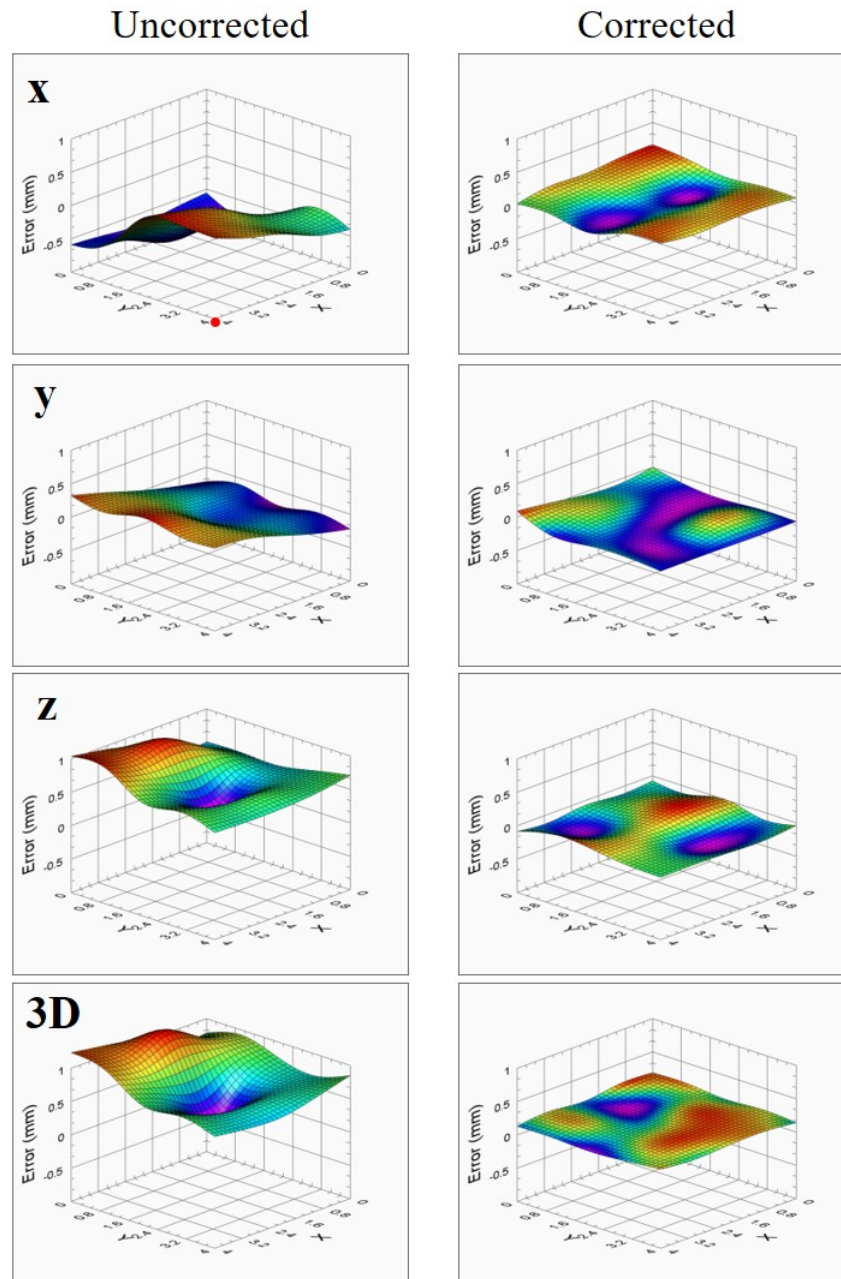


Figure 2.16: Needle tip positioning error maps in the uncorrected (left) and corrected (right) states for x , y , z , and 3D at a 78 mm platform height. Bi-cubic interpolation was used to estimate errors between dots in the calibration grid. Significantly greater accuracy was observed after error compensation in x , y , z , and 3D ($p < 0.001$, two-sample t-test). Red circle in top left plot indicates the origin corresponding to the red circle in Fig. 2.15. Figure reproduced with permission from IEEE¹ (year of original publication: 2015).

and then interpolating (bi-cubic method) at every position in between, dense x , y , and z error correction maps were created at different heights. Fig. 2.16 displays the qualitative

error maps at a z height of 78 mm, and Table 2.5 presents the quantitative results across the seven heights.

Because of the high repeatability in the serial arm, we were able to input these error maps into our motor control algorithms to compensate for the subtle positioning inaccuracies. As shown in Fig. 2.16 and Table 2.5, the robot demonstrated significantly reduced error after repeating the workspace accuracy experiments following error correction (3D: 0.201 mm) compared to before (3D: 1.824 mm). Overall, the results indicate that the manipulator was able to position the needle at a desired location both with high accuracy (mean positioning error: 0.21 mm) and precision (standard deviation: 0.02 mm) over the 3D workspace of a typical venipuncture procedure.

The positioning errors observed in the manipulator may have stemmed from several sources. Namely, the needle tip extraction method used to determine the actual needle tip location had an accuracy of 0.1 mm due to the resolution in the NIR images (1 mm in x and y , 2 mm in z). In the future, we will design a clip with one calibration circle that can attach to the end effector via the EM. This will allow us to match the desired versus actual circle center location, and thus improve the robot calibration process, because segmenting a circle is much easier than segmenting the needle tip. Additionally, errors may have stemmed from subtle inaccuracies in the fabrication and machining of robotic components.

2.2.5.4 Phantom Cannulation Testing

Finally, the image guided needle positioning accuracy of the venipuncture robot was evaluated on a skin-mimicking phantom model embedded with surrogate veins. The phantom, which measured 80 x 50 x 10 mm, was fabricated out of gelatin (12 g/100 ml) to provide an elastic, skin-like matrix. The surrogate veins consisted of silicone tubing (Silastic silicone elastomer tubing, Dow-Corning) of two diameters (3.2 and 1.8 mm). The elastic modulus of the tubing (9.5 kPa) closely matched that of typical adult peripheral veins (7-10 kPa). Blood-mimicking fluid (black India ink, diluted to 0.45 ml/100 ml to match the absorption coefficient of hemoglobin at 940 nm) was introduced into each vein prior to the experiment.

Fig. 2.17a illustrates the experimental setup, with the phantom model contained in a 3D-printed enclosure in which all veins lay 2 mm beneath the surface of the gelatin matrix.

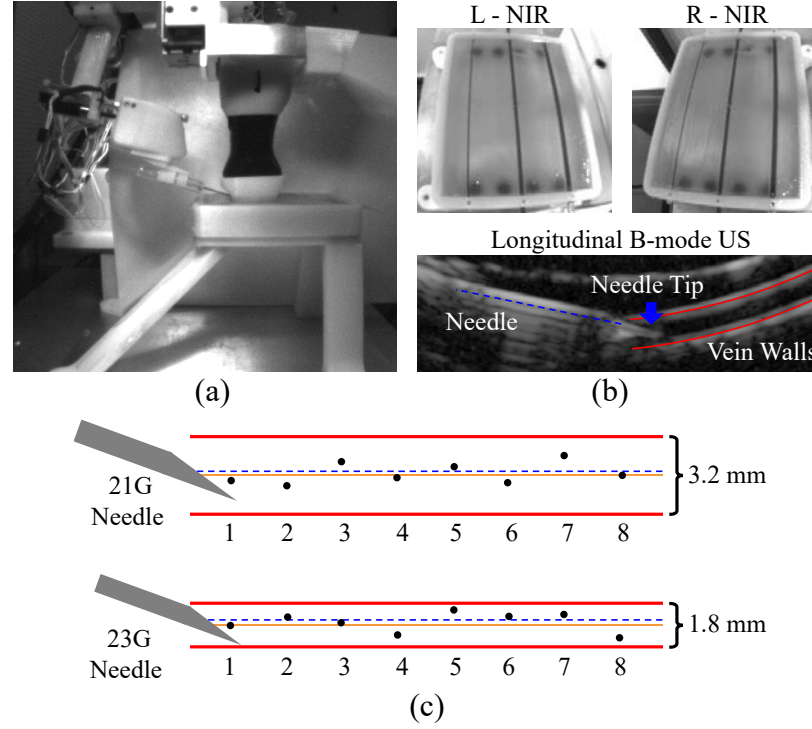


Figure 2.17: (a) Experimental setup for phantom cannulation testing. (b) Left and right NIR images of an *in vitro* tissue phantom (top), and longitudinal US image during a needle insertion on the $\varnothing 1.8$ mm vein (bottom). (c) Results from the cannulation study—orange solid line refers to the desired vein center and black dots indicate the actual location of the needle (center of the cannula opening) for each trial. The dashed blue line indicates the average position of the needle within the vein over the 8 trials. Figure reproduced with permission from IEEE¹ (year of original publication: 2015).

In total, 16 phantom vein cannulation trials were performed—eight for each vein diameter. The study evaluated the complete device work-flow, including the coarse-fine stereo NIR and longitudinal US imaging approach (Fig. 2.17b) as well as the 3-DOF gantry and 4-DOF manipulator controls. Briefly, the device imaged and segmented the phantom veins using 3D NIR imaging, and tracked the center of the selected vein using the US system. The robot then inserted the cannula bevel-up at 15° under US image guidance until the needle tip reached the center of the vein. Between each trial, the needle was retracted, the robot was homed, and then the cannulation was repeated after shifting the cannulation site 10 mm along the length of the vein. After the study, the recorded US images were manually segmented and analyzed. The center of the vein was determined as the equidistant point between the upper and lower vessel walls (Fig. 2.17b, lower). The final needle insertion position was determined as the center of the cannula opening at the bevel tip.

Cannulation results are presented in Fig. 2.17c. The RMS errors were 0.3 ± 0.2 mm and 0.4 ± 0.2 mm for the $\varnothing 3.2$ mm and $\varnothing 1.8$ mm veins respectively. In all 16 trials, the robot was able to successfully cannulate the vein target on the first insertion attempt. In each of the 8 trials on the 3.2 mm vein, the final needle tip position was closer to the vein center than to either vein wall, while this was true in 6 of the 8 trials on the $\varnothing 1.8$ mm vein.

2.3 Third-generation Device

The previous device contained 7-DOF—a 3-DOF Cartesian gantry positioned the imaging components, and a 4-DOF serial arm guided the needle into the vein². Despite promising results discussed in Section 2.2.5, several limitations in the robotic design were observed. First, the previous systems lacked the ability to align both the needle insertion and imaging subsystems with the vessel since the imaging components were positioned by a gantry system. Thus, while the device could be tested on phantom models with parallel, unidirectional vessels, human cannulations would have been difficult due to the wide range of vessel orientations in people. Second, the previous devices lacked a radial degree of rotation allowing the robot to reach lateral vessels on the sides of the forearm. As a result of the missing degrees-of-motion, the previous prototypes were unable to fully utilize the combined NIR and US image information to adjust the position and orientation of the needle in 3D space. This kinematic control is critical in allowing the system to adapt to gross arm motions and subtle vessel movements during the insertion.

In this section of the thesis, the development of the third-gen automated venipuncture device is described, which provides significant advancements over previous prototypes that are critical for eventual clinical translation. The device (as seen in Fig. 2.18) combines 3D NIR and US imaging, computer vision and image analysis software, and a 9-DOF needle manipulator within a portable shell. The device operates by mapping the 3D position of

²Much of the work presented in this section first appeared in: Adaptive kinematic control of a robotic venipuncture device based on stereo vision, ultrasound, and force guidance. IEEE Transactions on Industrial Electronics. Special Section on: Motion Control for Novel Emerging Robotic Devices and Systems 2016 (in press)³. All excerpts represent the original work of Max Balter, whose specific contributions as co-first author included: designing and setting up the experiments; analyzing the presented data and generating corresponding figures; writing, editing, and revising the original text; and addressing reviewers' comments as corresponding author of the original manuscript submission.

a selected vessel and introducing the needle into the center of the vein based on real-time image and force guidance.

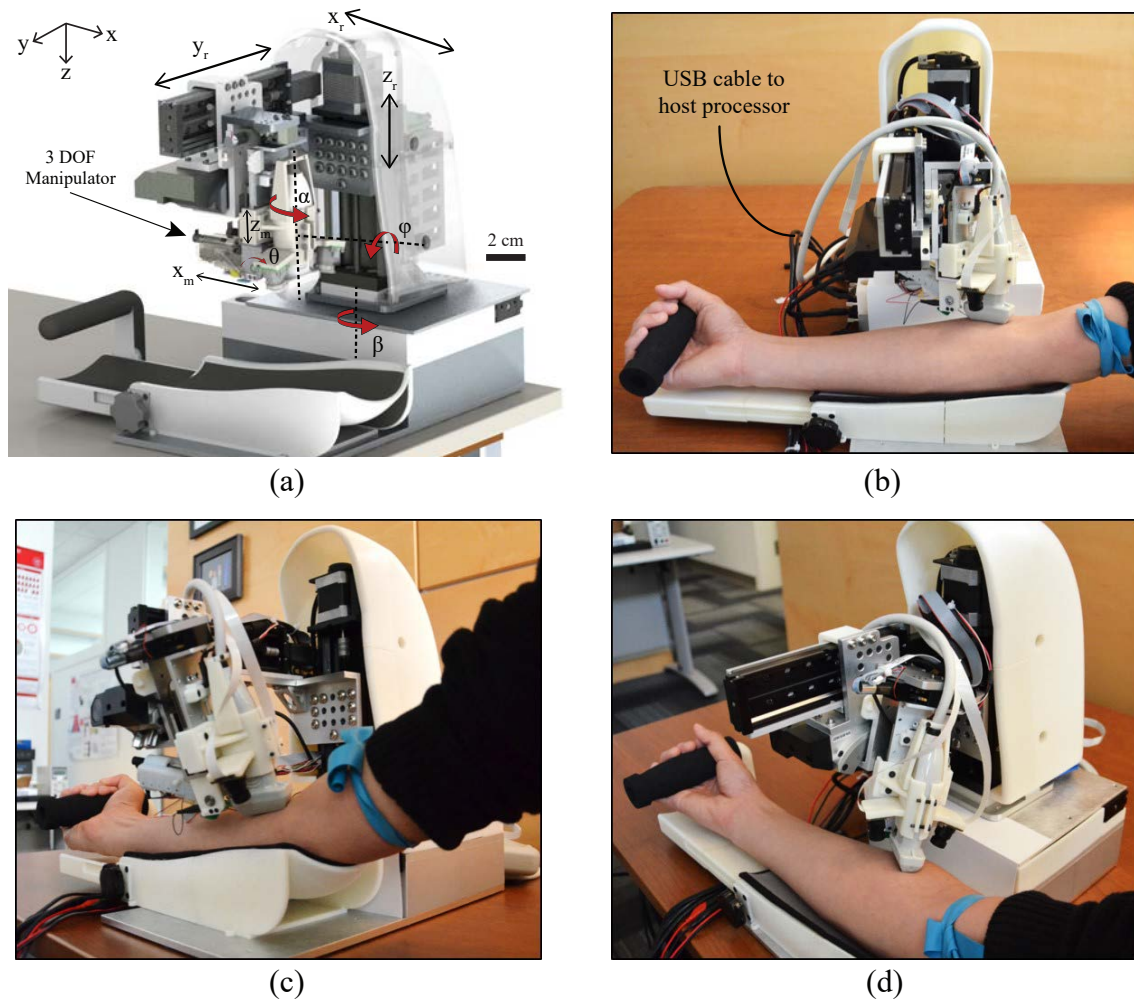


Figure 2.18: (a) Conceptual design (CAD render) of the robotic system, and (b–d) implementation of the device. Longitudinal orientation of the US transducer shown here as an alternative to the transverse orientation in (a). Figure reproduced with permission from IEEE³ (year of original publication: 2017).

The advancements introduced in this device include the following. First, the mechanical configuration of the third-gen system is completely redesigned to incorporate the added DOF without compromising portability. Second, the NIR, US, and needle insertion subsystems are integrated into a compact end-effector that allows each subsystem to remain aligned regardless of the end-effector orientation. Third, a force sensor is coupled to the needle insertion mechanism as an added method of feedback during the venipuncture. Fourth,

a new kinematic model is introduced to reflect the eye-in-hand configuration of the camera system, and separate motion control schemes are implemented that utilize the stereo vision, US, and force measurements to adjust the needle orientation in real-time. Finally, experimental results are provided that measure the positioning accuracy and speed of the robot under each mode of guidance.

2.3.1 System Design Overview

The protocol to perform a venipuncture using the device begins with disinfecting the forearm and applying a tourniquet. The device then scans the patient's forearm, using the NIR system to create a 3D map of the vessels and estimate their depth below the skin. Once a cannulation site is selected by the clinician via the GUI, the US probe is positioned over the site to provide a magnified cross-sectional view of the vessel and confirm blood flow. The coordinates of the cannulation site are directed to the robot, which then orients and inserts the needle. The device is comprised of three subsystems: the host processor, base positioning system, and manipulator unit (which contains the imaging and needle insertion components) as described below. Figure 2.19 outlines the new system architecture for the third-gen device.

2.3.1.1 Host Processor

The device runs off a laptop computer (i7-4710HQ 2.5 GHz CPU) serving as the host processor, communicating with the actuators and sensors via a USB bus. The image processing steps are accelerated on an embedded GPU (Nvidia Quadro K2200M), whereas all other tasks (e.g., path planning, motor control, and GUI functions) are executed on the CPU. With this architecture, the computer can perform the imaging and robotics computations at real-time frame rates using 800 MB and 500 MB of CPU and GPU memory respectively. 100 MB/s of data is communicated between the laptop and the robot via a single USB3 cable. Inside the robot, a receiver hub splits the input into 4 independent outputs that connect to the cameras, US system, base positioning system, and manipulator unit.

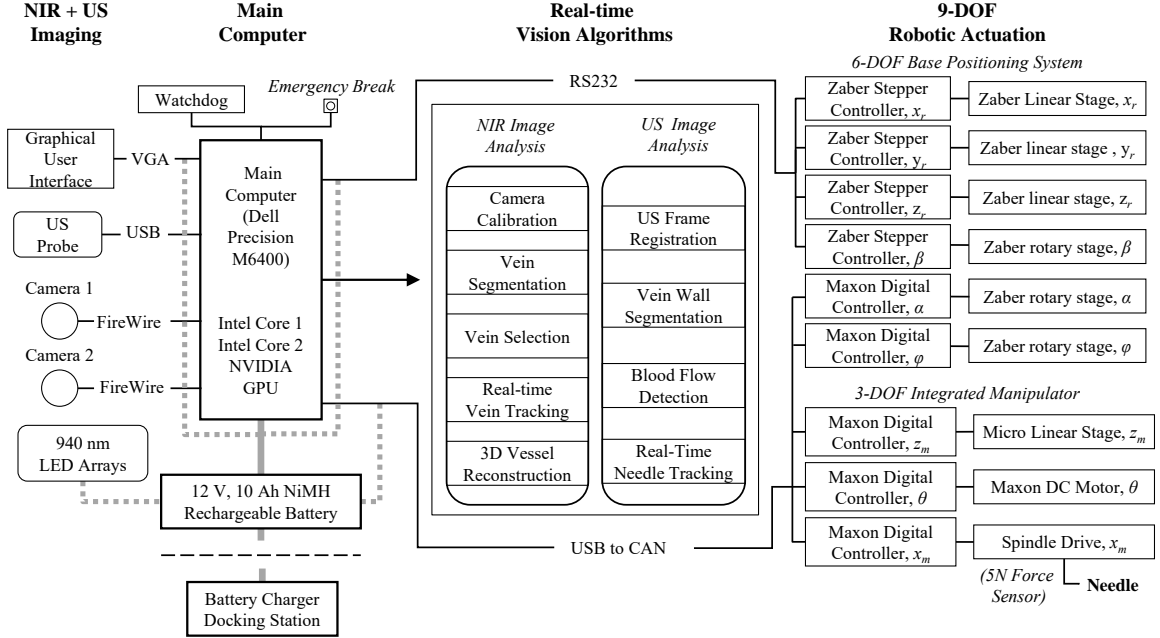


Figure 2.19: Hardware and software architecture of the third-gen device. Main hardware subsystems are the CPU and GPU, camera and US controllers, positioning controllers for the 9-DOF robot, power management system, and display. Main software subsystems include the GUI (run asynchronously on the CPU), real-time vision algorithms (deployed to the GPU), robotics processing (deployed to the CPU or the individual controllers), and the safety monitoring systems (run on the CPU).

2.3.1.2 Base Positioning System

The base positioning system serves to orient the imaging and needle insertion end-effector unit over the target vessel. As illustrated in Fig. 2.18, the gantry includes 6-DOF—three prismatic joints and three revolute joints. The prismatic joints form a Cartesian positioner (x_r , y_r , and z_r), whereas revolute joints α and ϕ allow the robot to align with the vein. β allows the entire robot to rotate before and after the procedure, but is not part of the kinematic geometry during the needle insertion. The α rotation is actuated by a miniature rotary stage (3M-R, National Aperture, Inc.) positioned directly above the US probe, while the ϕ rotation is controlled by a goniometer cradle (BGS50, Newport, Inc.). The use of a goniometer allows the axis of rotation to be offset from the stage and aligned with the axis of the forearm. This design is key to providing circumferential motion around the forearm to reach vessels at either side, without increasing the size of the device.

2.3.1.3 Compact Manipulator Unit

In previous designs, the base rotational joint of the serial arm manipulator (Fig. 2.20a), was positioned a large distance from the needle tip. Though extending the operating workspace of the manipulator, the articulated arm compromised joint stability, as minute rotational errors at the joints could lead to large positioning errors at the needle tip. While our previous studies showed that these errors could be minimized after calibrating the robot¹, relying on calibration before each use may be impractical. Furthermore, because the manipulator was not kinematically coupled with the imaging system, lateral rotations by the manipulator to align with the vessel would bring the needle out of the US image plane during the cannulation.

The design changes for the manipulator in the third-gen device were as follows. First, the new kinematic geometry allowed the insertion angle (θ in Fig. 2.20b) to be controlled independently of the other degrees of motion. This was made possible by a linear stage that adjusts the height of the needle (z_m) without affecting the height of the US probe. Combined with a servo that sets the insertion angle and a spindle drive that translates the needle (x_m), the manipulator could target vessels at depths ranging from 1–10 mm below the skin surface, at insertion angles of 0–30°. Second, the distance between the needle tip and the needle’s center of rotation (curved red arrow in Fig. 2.20a) was minimized to increase joint stability and reduce errors. Lastly, the lateral rotation (θ_1 in the previous manipulator as shown in Fig. 2.20a) was incorporated into the base positioning system (α in Fig. 2.18a), allowing the US probe and needle to rotate together and thereby remain in alignment at all times.

The needle manipulator can also be interchanged with a mechanism that is capable of inserting a peripheral catheter for intravenous fluid delivery (Fig. 2.21). Here, the procedural protocol is more advanced. As outlined in Fig. 2.21, the steps include: inserting the catheter; retracting the needle, while at the same time, stabilizing the catheter sleeve in the vessel; and connecting a fluid line to the catheter hub. The linear insertion is actuated by the same spindle drive implemented in the needle manipulator, whereas the position of the catheter sleeve relative to the needle is controlled by an EM embedded in the drive unit

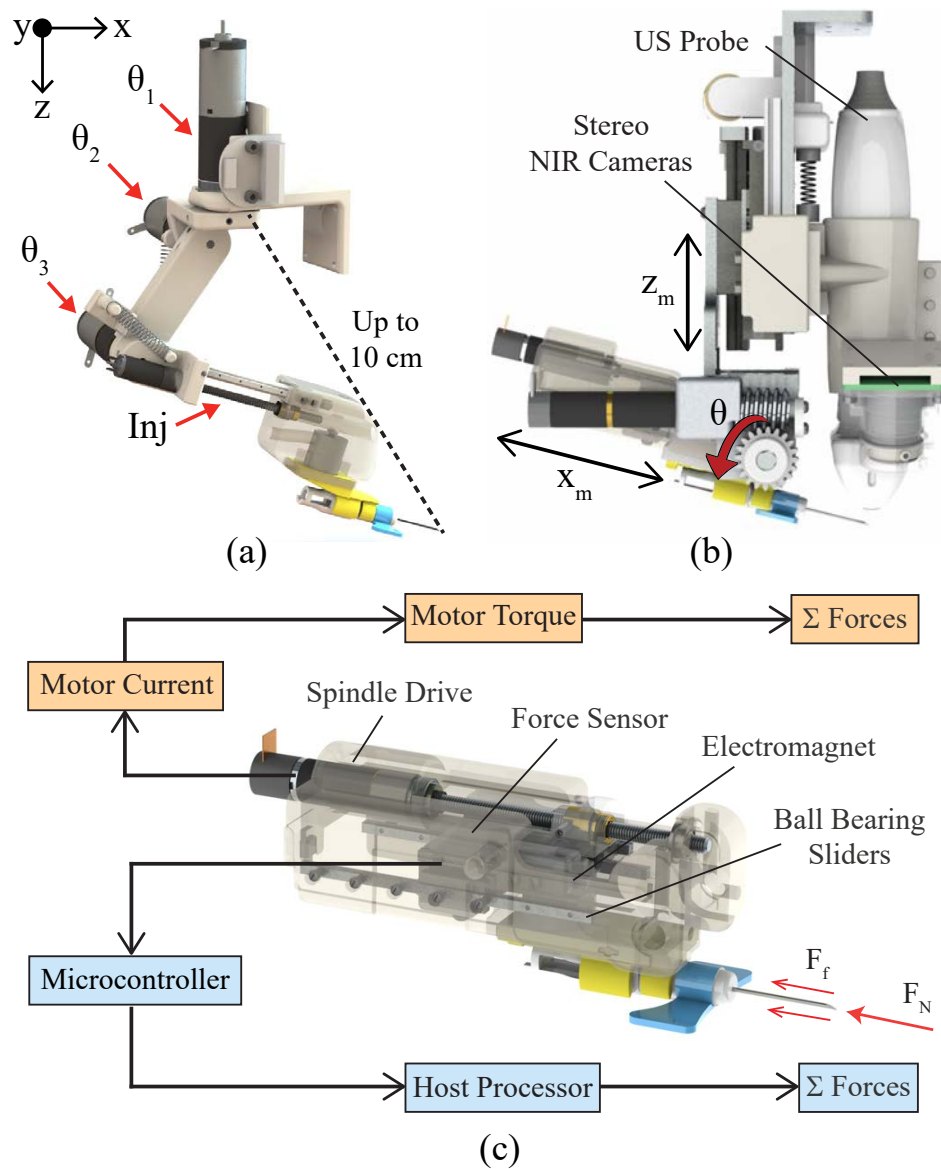


Figure 2.20: Needle manipulator unit. (a) 4-DOF serial arm implemented in previous designs, shown decoupled from the imaging system. Distance between the base joint and needle tip (dotted line) reached up to 10 cm at full extension, compromising joint stability. (b) The new compact manipulator coupling the redesigned needle insertion mechanism with the NIR-US imaging unit. (c) Bimodal force sensing implemented in the insertion system using a 5 N load cell (light blue), and computing force from the motor current (orange). Figure reproduced with permission from IEEE³ (year of original publication: 2017).

and a steel washer in the catheter clip.

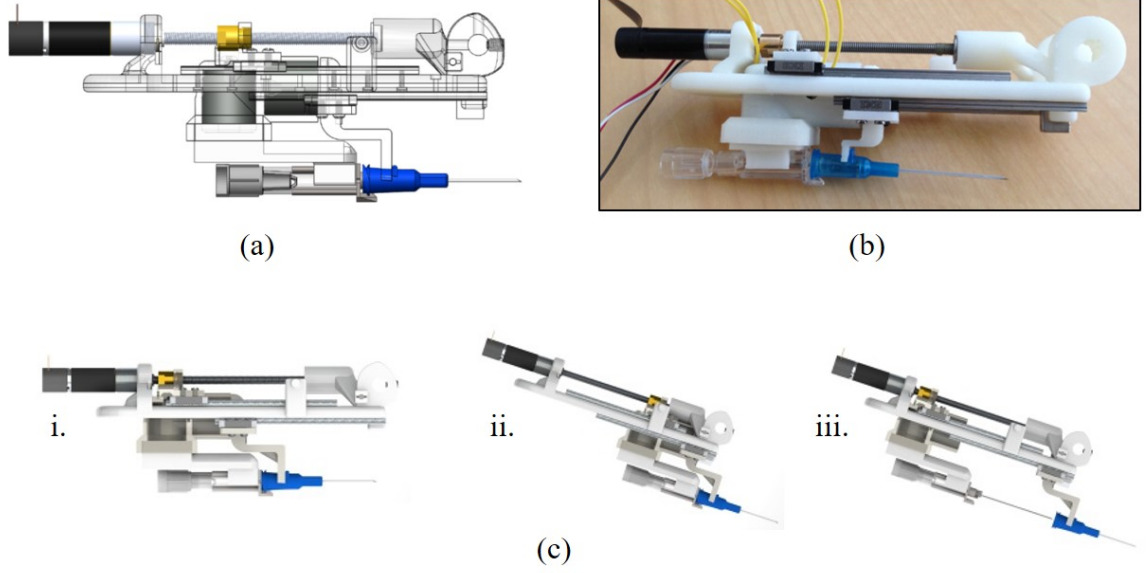


Figure 2.21: (a) Design and (b) prototype of the catheter insertion mechanism. (c) Steps in the process include: i. catheter in the home position, ii. catheter inserted, and iii. needle retracted, while the catheter sleeve remains in the vein.

2.3.1.3.1 NIR Imaging

Two arrays of 940 nm light-emitting diodes provide NIR illumination, which allows blood vessels up to 4 mm in depth to be visualized by the cameras due to the reduced scatter of light in the NIR range. A detailed description of the NIR imaging system and computer vision software is provided in¹⁴³. Briefly, stereo cameras mounted in an eye-in-hand configuration on the manipulator, are used to provide a 3D map of the vasculature. Blood vessels are then segmented, and cannulation sites are ranked based on vessel geometry. Once the clinician selects the cannulation target via the GUI, the 3D coordinates of the vessel are directed to the robot. During the cannulation, the vessel target and surrounding feature points are tracked from frame-to-frame in real-time. The feature points are selected via the SIFT algorithm²³⁷, and only features appearing along epipolar lines in both cameras are used for tracking. The tracking approach is based on sparse optical flow²³⁸.

To further reduce the size of the manipulator in the third-gen device, miniaturized ($\varnothing 0.9$ cm) NIR-sensitive cameras (VRmMS-12, VRmagic AG) were used. The data update rate is 40 fps for image capture, 20 fps for image processing, and 10 fps for stereo correspondence. The stereo imaging system was calibrated using a fixed planar grid with circular points²²³.

Rather than needing a separate motorized stage to adjust the grid height, the cameras were moved vertically via the existing z_r stage, allowing the intrinsic and extrinsic camera parameters to be computed within the robot workspace.

2.3.1.3.2 US Imaging

The US imaging system (SmartUS, 18 MHz transducer, Telemed UAB) provides a magnified view of the vessel and also has Doppler capabilities for blood flow detection. The US imaging is further used to visualize the needle during the insertion. The initial coordinate of the needle tip in the US image is localized based on the robot kinematics, whereas the vessel center is localized initially by manual user selection. After the initial frame, both the needle tip and vessel center are tracked in subsequent frames using optical flow. The maximum B-mode image acquisition rate is 60 fps, while the image processing rate is 20 fps.

The transducer has also been reoriented on the device to provide transverse, cross-sectional imaging. In the previous device, the image plane of the US probe was oriented longitudinally (i.e., in the x -direction in Fig. 2.20). However, vessels tend to roll in the axial y -direction during the needle insertion. In these cases, the vessel would roll out of the US image plane, making it impossible for the robot to track. In contrast, the transverse orientation of the US probe allows the target vessel to be tracked over a larger cross-section.

2.3.1.3.3 Force Sensing

In addition to visualizing the needle in the US image, we also implemented a force sensor in the manipulator to detect when the needle punctures the skin and vessel wall. Axial forces along the needle vary throughout the insertion due to the natural inhomogeneity of human skin tissue²³⁹. The sensor measures these forces, relaying information to the robotics to help compute the position of the needle tip. Especially in cases where the US image is noisy, the transducer may be unable to receive the acoustic signals from the needle. Instead, by observing the peaks in the force profile during the cannulation, we can determine the following puncture events: (1) *tissue deformation*, which begins when the needle contacts the tissue and continues until the insertion force reaches a local maximum; (2) *puncture*, which occurs when a crack propagates through the tissue following the force peak; and (3)

removal of the needle from the tissue.

The force-sensitive insertion mechanism consists of a linear stage actuated by a lead screw spindle drive (RE 8, Maxon Precision Motors, Inc.) and supported by ball bearing sliders. As the spindle translates to advance the cannula, normal and friction forces acting on the needle cause it to push against a force sensor (FSG-5N, Honeywell Inc.) embedded in the manipulator. This generates an analog signal which is then digitized by a 12-bit A/D converter. The computer simultaneously monitors the forces applied against the sensor and the electrical current running through the windings of the DC-brushed spindle drive to determine puncture events.

2.3.1.4 Robot Kinematics

Kinematic equations were derived using a series of matrix transforms, linking the Cartesian (x_r , y_r , and z_r) and rotational joints (α and ϕ) of the gantry with the manipulator joint frames (z_m , θ , and x_m). Equation 2.25 outlines the overall transformation matrix used to correlate the needle tip frame with the robot origin frame. In this case, N equal 9—the number of DOF in the robot. Table 2.6 outlines the kinematic joint space of the robotic system and Tab. 2.7 lists the DH-parameters. For the base positioning system, the parameters specified in the DH table link the origin frame at the base of the system to the wrist, which is coupled to the US transducer. Meanwhile, the DH parameters for the needle manipulator link the manipulator origin frame, with a constant offset from the US transducer frame, to the distal end of the end-effector. The needle tip position is calculated using a wrist-to-tool transform. As mentioned earlier, the β revolute joint is independent of the needle insertion kinematics—it functions to rotate the device away from the patient, providing space for the clinician to disinfect the forearm and apply a tourniquet before the procedure and clean the device afterward.

$${}^0_N T = {}^0_1 T * {}^1_2 T * {}^2_3 T * {}^{N-1}_N T \quad (2.25)$$

Table 2.6: Kinematic joint space of the robotic system. Joints 1–6 comprise the gantry; 7–9 the manipulator. Table reproduced with permission from IEEE³ (year of original publication: 2017).

Joint	Motion	Travel Range
1 – β	Base rotation	0–90°
2 – x_r	Scan along arm length	0–100 mm
3 – y_r	Scan across arm width	0–100 mm
4 – z_r	Adjust manipulator height	0–100 mm
5 – ϕ	Roll rotation (about x)	-30–30°
6 – α	Yaw rotation (about z)	-45–45°
7 – z_m	Adjust needle height	0–25 mm
8 – θ	Adjust insertion angle	0–30°
9 – x_m	Needle insertion length	0–35 mm

Table 2.7: DH parameters of the 9-DOF robotic system. Joints: 1–7 for the base; joints: 8–11 for the manipulator. Table reproduced with permission from IEEE² (year of original publication: 2015).

i	Type	α_{i-1}	a_{i-1}	d_i	θ_i
1	Revolute, β	0	0	0	0
2	Prismatic, z_r	90°	0	0	0
3	Prismatic, x_r	90°	0	0	0
4	Prismatic, y_r	90°	0	0	0
5	Revolute, ϕ	-90°	0	0	0
6	Revolute, α	-90°	0	40 mm	0
7	US probe offset, p	0	0	95 mm	0
8	Prismatic, z_m	90°	0	0	0
9	Revolute, θ	90°	0	0	0
10	Prismatic, x_m	0	0	25 mm	0
11	Needle, n	0	0	-56 mm	0

2.3.1.5 Vision, Ultrasound, and Force-based Motion Control

The motion control scheme of the robot (Fig. 2.22) consists of three phases—NIR stereo vision-based servoing, US-based servoing, and finally the needle insertion using force guidance. The first phase involves extracting the 3D position of the insertion site from the stereo images, and directing this coordinate to the robot. This positions the end-effector unit over

that location, aligning the needle with the vessel orientation. Desired joint angles are derived from the kinematics of the eye-in-hand camera configuration, and low-level position commands are sent to the motor drivers.

The Cartesian gantry utilizes bipolar stepper motors and controllers capable of high-resolution micro-stepping ($0.19 \mu\text{m}$) and high repeatability ($<4 \mu\text{m}$). Attached encoders provide the position and velocity about each joint. Conversely, the rotary stages in the gantry contain DC-brushed motors, actuated via positioning controllers (EPOS EPOS 24/2, 390438, Maxon Precision Motors, Inc.). In the second phase, the 5-DOF on the base positioning system are further utilized to make fine position adjustments once the US probe is lowered, to enhance visualization of the vessel.

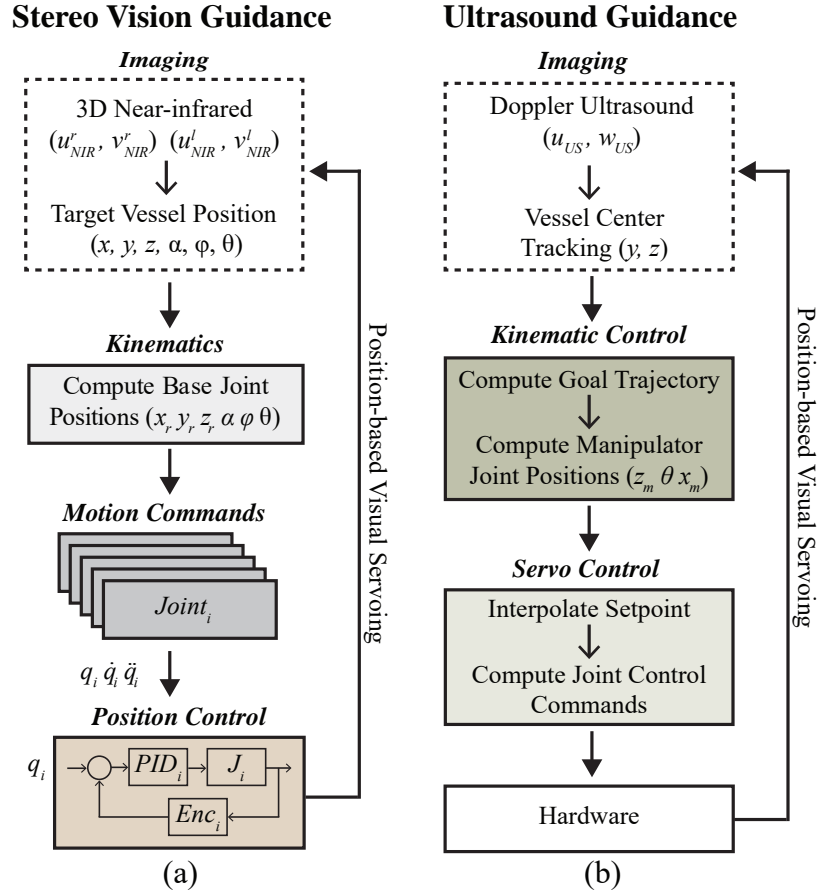


Figure 2.22: Motion control scheme in which position data is extracted from the image sensors and used to guide robotic motions. (a) Stereo vision-based, and (b) US-based visual servoing. During the venipuncture, the force sensor helps compute the needle tip location, serving as the third method of feedback. Figure reproduced with permission from IEEE³ (year of original publication: 2017).

Once each actuator reaches the set point wherein the US probe is oriented and centered over the target vessel, the robot then finely positions the needle via the the 3-DOF on the manipulator. At this point, the US probe is lowered over the forearm to display a clear image of the vessel. The needle orientation is then adjusted in real-time based on inputs from the US image and force sensor to position the needle tip in the center of the vein. Extrapolating the vein center coordinates from the US image, and tracking the needle tip during the insertion, the desired needle tip position is modified to accommodate subtle tissue motion during the procedure. Finally, in the third phase, force and current signals measured during the needle insertion are registered with the US image data to confirm the puncture of the target vessel.

Position-based visual servoing was implemented, as opposed to an image-based approach for several reasons. Namely, the needle is not in the FOV of the cameras, thus there is no way to use an image-based servoing scheme for vision-guided tasks. For US-guided tasks, where the needle is in the FOV during the venipuncture, image-based servoing has several drawbacks^{240,241}. First, task singularities can arise in the interaction matrix potentially resulting in unstable behavior. Second, occlusion of the needle may occur in the US image due to the inherently noisy acoustic signals. During the venipuncture, the needle may appear as a discontinuous line segment, resulting in feature extraction errors and posing challenges in designing a suitable controller.

2.3.1.6 Human Factors Components

Designs and prototypes for four hardware components that directly interface with the patient and practitioner—namely, the arm rest, consumables, and automated needle handling system—were also incorporated into the third-gen device.

2.3.1.6.1 Arm rest

The arm rest served to minimize motions at the wrist and elbow without the need for an explicit strap. The arm rest (as seen in Fig. 2.23) has an adjustable handle for the patient to grab onto that exposes at least the top half of the forearm to the device. This allows the device to scan, search, and select the optimal cannulation sites. Additionally, the US

probe further reduces arm motions by applying a slight pressure against the median cubital area of the forearm. This serves to stabilize the vessel distal from the cannulation site. A tourniquet can also be integrated to improve ease-of-use.

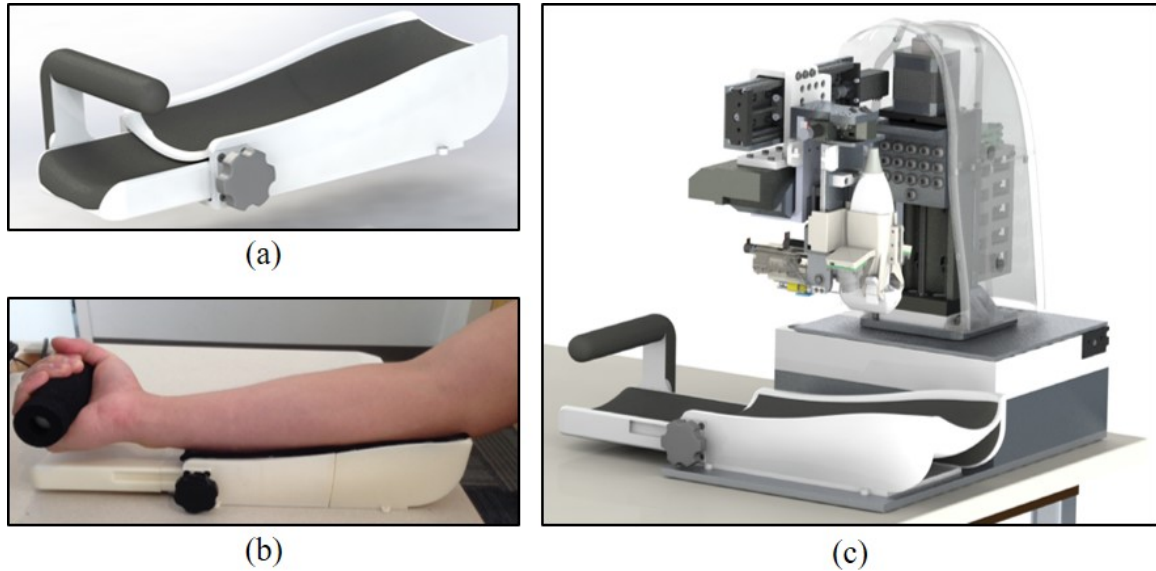


Figure 2.23: Arm rest concept design and prototype. (a) CAD rendering and (b) rapid prototyped model of the arm rest. (c) Venipuncture device illustrating the location of the arm rest on the system.

Several methods to sterilize the arm rest were considered. In the first, the arm rest is disinfected by the clinician with an antibacterial wipe after each use of the device. In the second, the arm rest is covered by a disposable cover that is replaced manually after each use. The third approach also incorporates a disposable cover, but the cover is dispensed as part of the system (e.g., via an integrated roller dispenser). If the arm rest comes in contact with blood, a more stringent sterilization technique such as heat, gas, or radiation, would be needed to treat the component.

2.3.1.6.2 Automated Consumables Handling

In the second-gen device, we introduced robotic functionality allowing the device to fully automate the loading and uncapping of the needle before the blood draw and disposal of the needle afterward. The system was implemented to completely remove practitioner contact with exposed sharps. To allow the system to adapt to a wide range of needles, a universal

clip was further designed (Fig. 2.24a, left) that serves as a low-cost consumable item to be used with the device. A second consumable item (Fig. 2.24a, top right) comprises a clip containing sterile, solid 0.5% agarose gel that serves as the acoustic transmission material for the US probe. The advantage of the clip design is eliminating the need to apply a liquid gel onto the arm of the patient—normally a messy and time-consuming process.

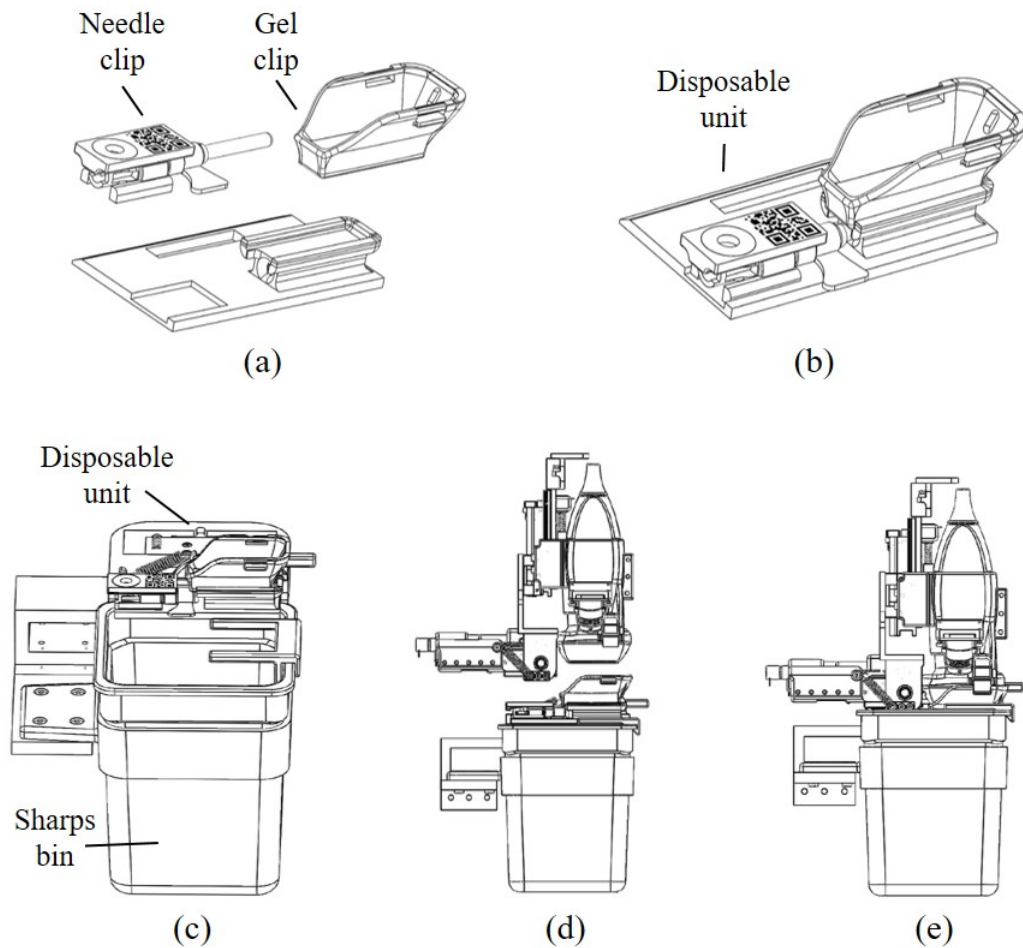


Figure 2.24: Automated needle handling and consumables system. (a) The re-loader unit depicting how the needle and gel clip attach to the tray, and (b) the pre-packaged form of the disposable. (c) The re-loader system showing the disposable unit integrated with a sharps bin, which is mounted to the back of the device. (d) Schematic of how the manipulator can be positioned above the re-loader, and (e) how it can grab the needle and US gel.

To allow the device to operate with minimal human intervention, the needle handling system was expanded to simultaneously load the needle and US gel clip in a single, automated step. Both consumable items would be packaged together in a sterile unit (Fig.

2.24b). The clinician would only have to place the package in an indicated holder behind the device and peel off the plastic cover. The base positioning system would rotate—via the β axis of motion—the needle manipulator directly over the pre-packaged consumable unit (Fig. 2.24d). In one actuated motion, the needle manipulator would then engage the needle via the EM attachment mechanism while securing the US gel clip via a press-fit mechanism (Fig. 2.24e). After the procedure, the needle, needle clip, and US gel clip would all be disposed into a sharps container within the venipuncture device. Like the arm rest, the consumables have the potential of coming into contact with the patient and therefore need to be manufactured and packaged in a sterile environment.

2.3.2 Experimental Testing

2.3.2.1 Kinematic Workspace Simulations

Forward and inverse kinematics experiments were conducted to evaluate the workspace of the system. To ensure that the device was able to operate along the length and upper circumference of the forearm, the operating work envelope of the 9-DOF robot was computed based on the derived kinematic equations and the limits of motion for each link. The travel range of the x_r , y_r , and z_r prismatic joints provided a base rectangular work volume of 10 x 10 x 7.5 cm.

Meanwhile, the rotational range of the revolute joints (α : $\pm 90^\circ$ and ϕ : $\pm 30^\circ$) provided an additional hemispherical envelope of $\sim 90 \text{ cm}^3$ from any given position within the base work volume (Fig. 2.25a left). The manipulator added a planar $\sim 14 \text{ cm}^2$ range of motion lying parallel with the axis of insertion (Fig. 2.25a right).

Table 2.6 summarizes the travel ranges of each actuator in the system. In total, the operating workspace allows the robot to cannulate any vein in the anterior forearm (Fig. 2.26), spanning from the wrist to the antecubital fossa region of the elbow. Additionally, unlike earlier generations, the third-gen robot was able to align with significantly angled or varicose veins. The system was also able to reach lateral veins located along the sides of the forearm.

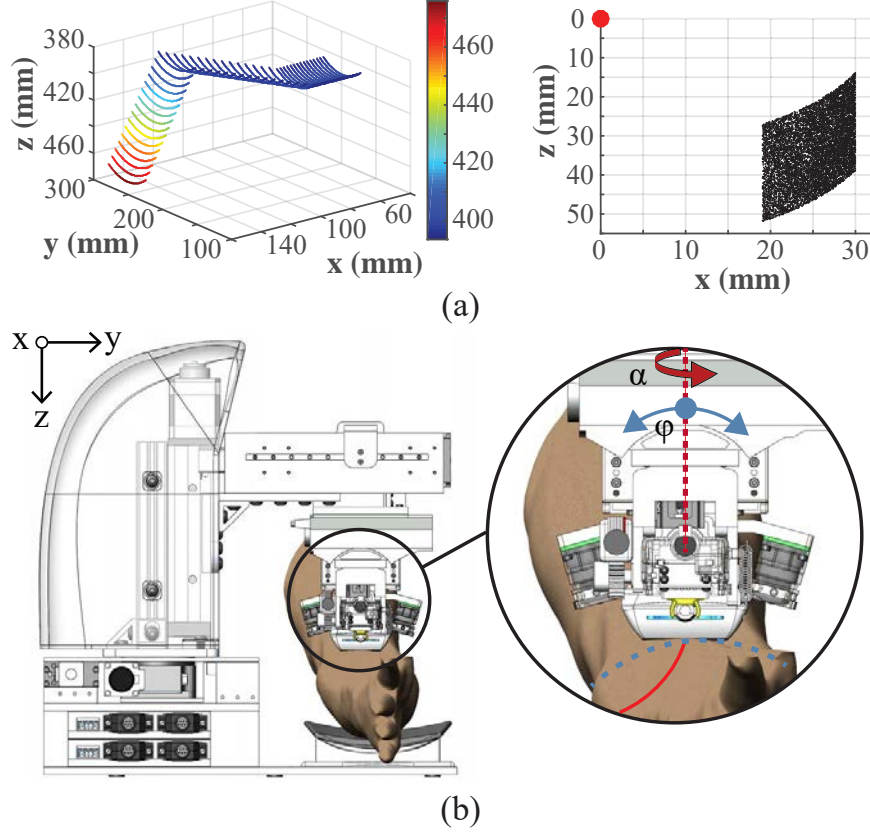


Figure 2.25: (a) Kinematic joint range of the 5-DOF gantry (left), and 3-DOF manipulator (right). Points on the gantry plot indicate the position of the US probe transducer head, whereas the manipulator plot indicates the needle tip position (red dot represents the manipulator origin frame at the θ rotation axle center). (b) Illustration of the two rotational degrees-of-motion in the gantry (α and ϕ) used to align the manipulator unit with the vessel orientation. Figure reproduced with permission from IEEE³ (year of original publication: 2017).

2.3.2.2 Free-space Positioning

Free-space needle positioning experiments were then conducted on a cylindrical calibration platform (Fig. 2.27a) to assess the accuracy and repeatability of the robot over its reachable workspace. The calibration platform comprised 192 circular targets ($\varnothing 4$ mm, 7 mm center-to-center spacing) uniformly spaced over a cylindrical grid, with each target defining a unique, known 5-DOF pose (x , y , z , pitch, and yaw). The sixth-DOF (roll) was varied from -45° – 45° across the circumference of the platform.

To evaluate repeatability, three positioning trials were conducted for each of the circle targets. For each trial, the robot started in its home position, moved the needle tip to the

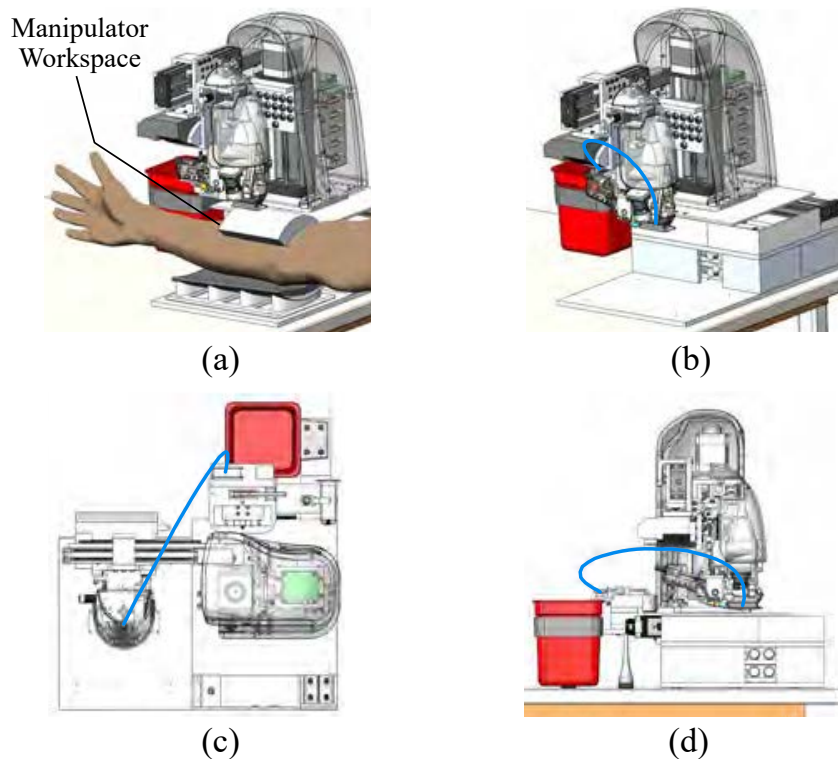


Figure 2.26: (a) Dexterous workspace ($\sim 90 \text{ cm}^3$) of the manipulator highlighted in gray over the forearm. The manipulator workspace may be positioned anywhere within a $10 \times 10 \times 7.5 \text{ cm}$ base rectangular work volume. (b) isometric, (c) top, and (d) side view of the US probe-needle unit trajectory (blue line) during the robotic venipuncture. Figure reproduced with permission from IEEE² (year of original publication: 2015).

desired 6-DOF pose, and returned to the home position. The desired 3D position of each target was obtained from the CAD model of the robot. Target positions were also estimated from the right and left images acquired by the stereo imaging system (Fig. 2.27b). Here, an ellipse detector was implemented to segment and compute the centroid of each target, from which the 3D coordinates were calculated based on the extrinsic camera parameters and the robot kinematic geometry. The needle tip was then extracted manually from each image and used to compute the 3D needle tip location. Actual needle tip positions were then compared to the desired and estimated 3D target positions to determine the error (accuracy) and standard deviation across trials (repeatability).

Fig. 2.27a displays the testing setup with the needle tip positioned at one of the calibration targets. As shown in Fig. 2.27b, the actual needle tip position was manually extracted from the stereo images after applying an ellipse detector to segment the target, and a line

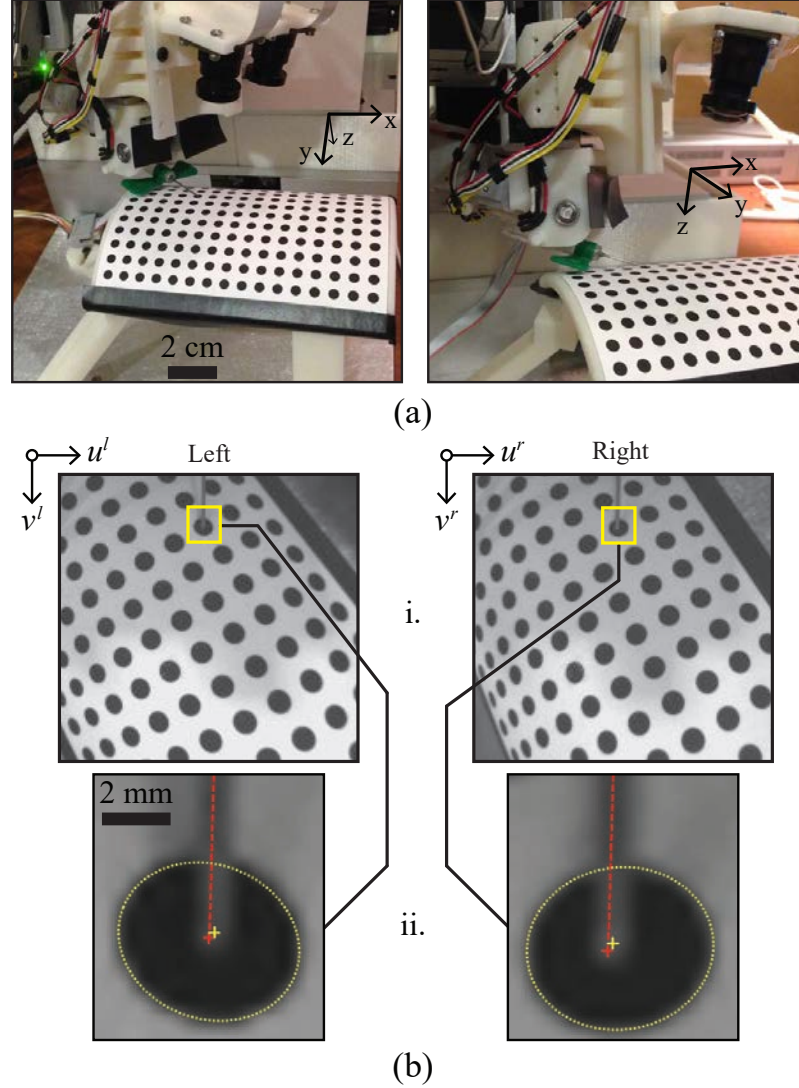


Figure 2.27: Needle tip positioning studies. (a) Experimental setup (with US probe removed). (b) Position estimation of the needle tip and circle target. i. Images acquired and rectified based on the intrinsic camera parameters. ii. Image resolution increased 10x, and an ellipse detector used to segment circular targets (yellow dotted lines) and compute the centroids (yellow crosshairs). The needle is visible in both images (red dotted lines), allowing the needle tip to be extracted manually (red crosshairs). Figure reproduced with permission from IEEE³ (year of original publication: 2017).

detector to highlight the needle. Table 2.8 presents the error between the circle positions in the CAD model and the positions estimated from the stereo imaging (row 1); the error between the desired and actual positions of the needle tip (row 2); the repeatability of the needle tip positioning (row 3); and the repeatability of the needle tip detection alone (row 4). The detection repeatability indicates the error in the manual needle tip extraction

process, which adds to the positioning repeatability.

Table 2.8: Needle tip positioning errors ($n = 3$ trials)—Units in mm. Table reproduced with permission from IEEE³ (year of original publication: 2017).

	dx	dy	dz	3D
Mean – estimated vs. known position	0.05	0.08	0.07	0.13
Mean – needle tip vs. known position	0.09	0.15	0.08	0.22
Repeatability – needle tip positioning	0.05	0.04	0.07	0.05
Repeatability – needle tip extraction	0.02	0.03	0.03	0.03

Over three trials, the 3D positioning error was 0.22 ± 0.05 mm, with the needle tip detection repeatability being 0.03 mm. These results imply that the robot has sufficient accuracy and precision to position the needle tip in vessels as small as $\varnothing 1$ mm. In addition, because these positioning studies were conducted using a cylindrical testing platform that mimicked the curvature of an adult human forearm, we were able to evaluate the performance of the robot over the operating workspace of the needle insertion task. This testing differed from positioning studies conducted on previous prototypes in that each target in the cylindrical calibration grid defined a unique 5-DOF pose for the robot to manipulate the needle. In comparison, previous studies used a planar calibration grid and only specified a 3-DOF Cartesian pose for the robot.

2.3.2.3 Stereo Vision Guidance

Tracking experiments were then conducted to evaluate positioning accuracy under stereo vision-guided servoing. The first set of experiments evaluated the needle pose errors as the robot positioned the needle to follow a moving calibration target (Fig. 2.28a). The calibration target comprised a grid of four circles lying on a plane (Fig. 2.28b). As the target was moved by freehand under the FOV of the cameras, the plane parameters were calculated based on the 3D coordinates of each circle, which were extracted in real-time via an ellipse detector provided in LabVIEW. The plane parameters were then used to compute the 6-DOF pose of the circle target and, in turn, the desired pose of the needle. Fig. 2.29c displays the desired and actual positions of each robot degree-of-motion over a 60 sec period

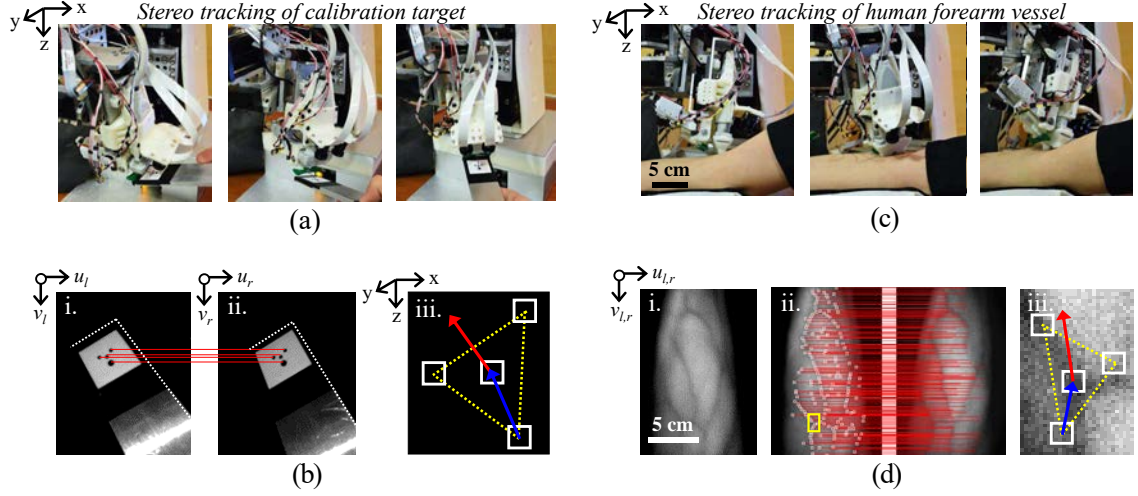


Figure 2.28: Stereo vision tracking experimental setup. (a) Robot tasked with tracking a calibration target moved by freehand under the fov of the cameras. (b) Stereo image pair showing the calibration target (i., ii.); the epipolar correspondence lines between the circular control points (red lines); and the 3D orientation of the target calculated from the plane parameters (iii.). (c) Robot tracking experiments repeated on human subject. (d) NIR contrast image highlighting veins in the forearm (i.); epipolar correspondence lines between SIFT features extracted from the left and right stereo images (ii., red lines); and SIFT feature points used to determine the 3D position and orientation of the vessel target based on the tangent plane parameters (iii.). Figure reproduced with permission from IEEE³ (year of original publication: 2017).

during the experiments.

Fig. 2.29d displays the following errors as a function of the speed of the moving target. Both the linear and rotational errors were observed to increase with movement speed. At speeds of 10 mm/s and 10 °/s, the following errors were 0.4 mm and 0.5° respectively. Particularly at high speeds, state estimation filters (e.g., the extended Kalman filter commonly used in navigation robots^{242,243}) may help to reduce following errors by predicting future positions based on current system states.

Next, tracking experiments were repeated on veins identified on the forearm of a human subject by the NIR imaging system (Fig. 2.28c). To measure following errors over a range of speeds, the subject was asked to move their arm randomly under the device for a 60 sec period. During the experiment, the plane tangent to the forearm surface around the vessel target was estimated from the 3D position of the vessel and the surrounding feature points (Fig. 2.28d). Similar to the previous tracking experiments on the calibration target,

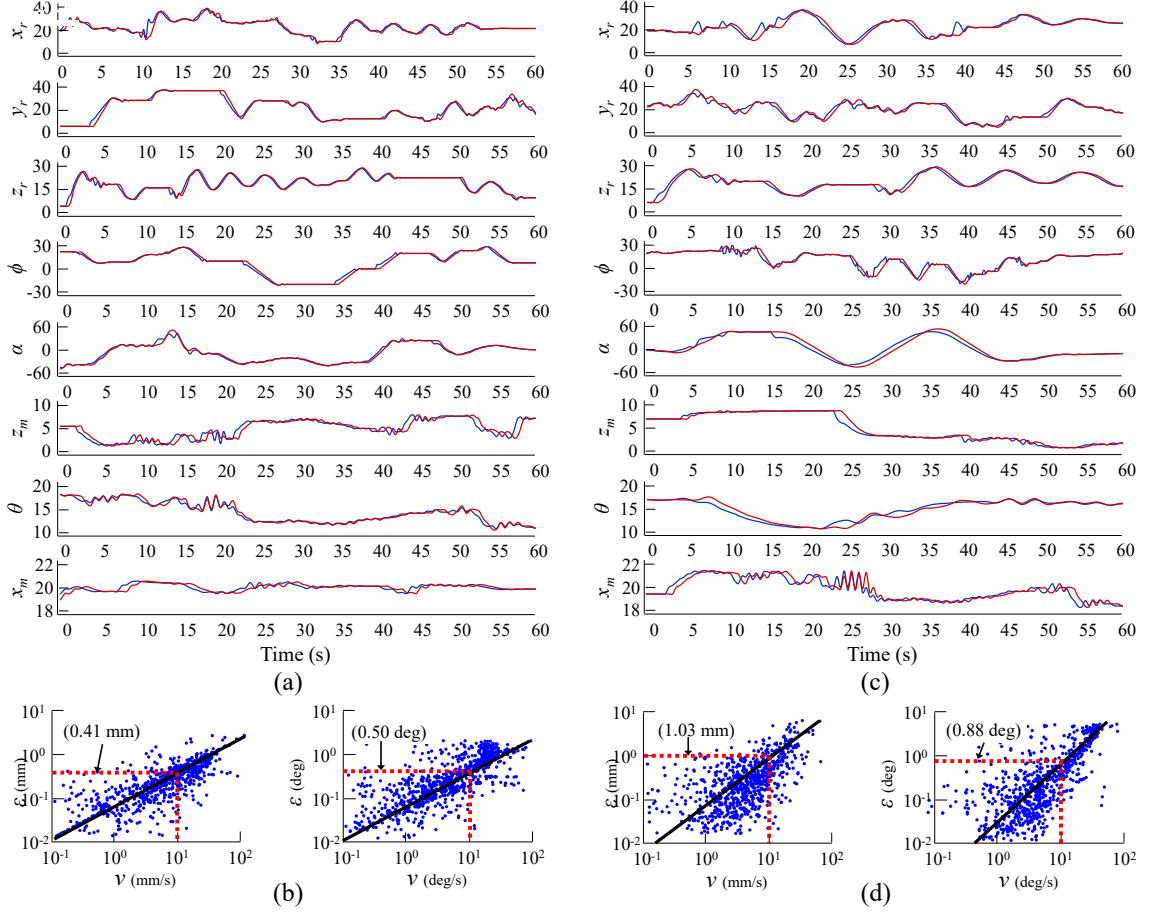


Figure 2.29: Stereo vision tracking results. (a) Desired and actual positions of each robot degree-of-motion over 60 sec of freehand calibration target tracking. (b) Linear (left) and rotational (right) following errors with respect to the speed of the moving target. (c) Desired and actual positions of each degree-of-motion over 60 sec of human vessel tracking. (d) Following errors with respect to forearm movement speed. Figure reproduced with permission from IEEE³ (year of original publication: 2017).

the plane parameters were used to determine the 6-DOF vessel pose and the desired needle pose. Unlike the previous experiments, which relied solely on ellipse detection, the feature points in the forearm images were extracted via SIFT. Only features present along the epipolar lines in both cameras were used in the pose calculations. Meanwhile, the actual vessel target was tracked using optical flow.

The desired and actual positions of each degree-of-motion during the human vessel tracking experiments are shown in Fig. 2.29c, and presented with respect to vessel movement speed in Fig. 2.29d. As before, following errors were higher when the motions were faster. At speeds of 10 mm/s and 10 deg/s, the following errors were approximately 1.0 mm and 0.9

deg respectively. The increased error compared to the calibration tracking experiments is most likely due to errors in the SIFT feature detector and optical flow tracking approach. In future studies, we will evaluate following errors over a range of object tracking algorithms²⁴⁴. We will also assess whether the use of dense stereo correspondence algorithms or active stereo vision approaches—e.g., based on structured lighting, may improve the quality of the 3D reconstruction and thereby reduce errors during tracking.

2.3.2.4 Ultrasound Guidance

In a third set of studies, we evaluated US-based visual servoing in a *in vitro* blood vessel phantom. The phantom consisted of a $\varnothing 3$ mm silicone tube simulating the vessel, embedded within a compliant, fluid-like 0.2% agarose gel simulating the surrounding tissue. The phantom was contained in a 3D-printed enclosure, which was further mounted to the device.

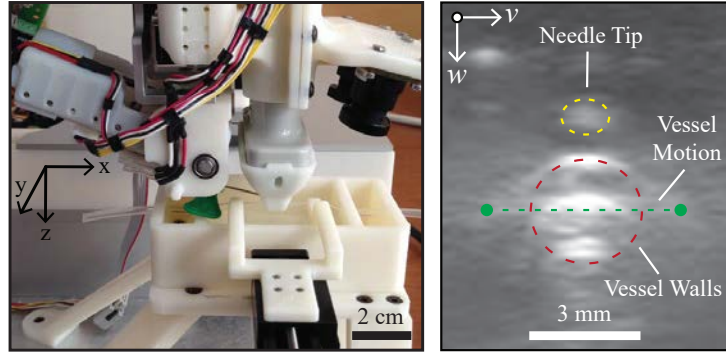


Figure 2.30: US-guided vessel tracking. Left—experimental setup showing the motorized phantom rig used to laterally displace the surrogate vein. Right—transverse US image depicting the vessel cross-section (red) and needle tip (yellow). Figure reproduced with permission from IEEE³ (year of original publication: 2017).

Vessel motions were simulated by moving the vessel laterally (Fig. 2.30, left, *y*-axis) within the phantom over time periods of 60 sec. Controlled motion patterns were generated at varying speeds using a secondary motorized positioning system. The robot was then tasked with maintaining the needle tip position 1 mm above the moving vessel over the duration of the experiment. Frame-to-frame position changes of the vessel wall were tracked in each US image using optical flow. Fig. 2.30, right shows a representative transverse US image of the surrogate vessel within the phantom (red dotted circle) and the tip of the needle passing through the transverse US imaging plane (yellow dotted circle). Also shown

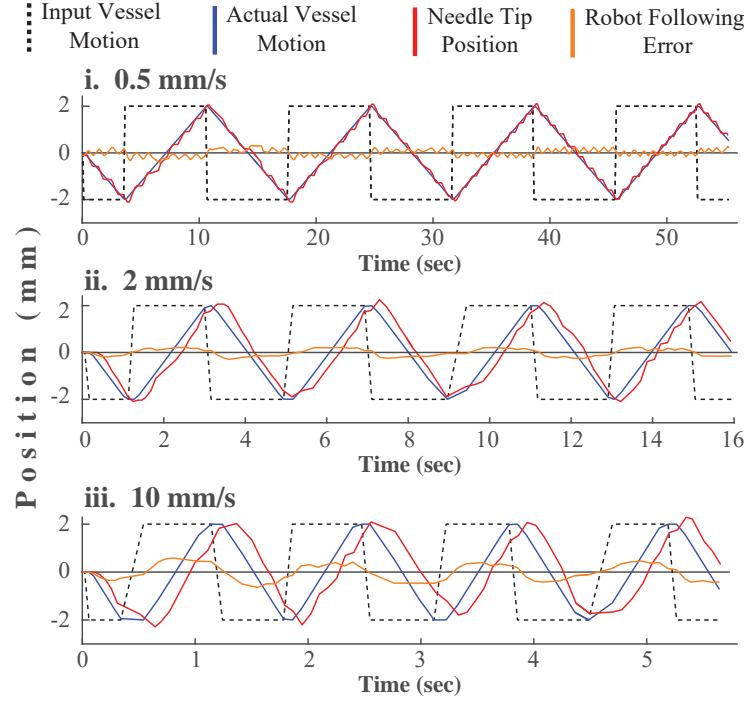


Figure 2.31: US-guided vessel tracking results. Robot following errors observed during side-to-side vessel tracking at i. 0.5, ii. 2, and iii. 10 mm/s. Errors refer to the difference between the known vessel location (determined from the vessel positioning stage) and the needle tip position (computed from the robot kinematics). Figure reproduced with permission from IEEE³ (year of original publication: 2017).

is the vessel's lateral range-of-motion within the phantom (green dotted line).

Fig. 2.31 compares vessel and needle tip positions at three lateral movement speeds (0.5, 2, and 10 mm/s). Table 2.9 summarizes the mean US tracking error (i.e., the error between the known vessel location, as set by the secondary positioning system, and the location estimated from the US images) and the mean robot following error (i.e., the error between the known vessel location and the needle tip position) at each speed. The US tracking errors were negligible at all three speeds, indicating that the frame rate of the US imaging system was sufficient within the tested speed range. Robot following errors, meanwhile, were observed to increase with movement speed; the mean error at 0.5 mm/s (0.003 mm) was about two orders less than the error at 10 mm/s (0.8 mm). As with the vision-based tracking experiments, incorporating state estimation filters may help to reduce the following errors at high speeds.

Table 2.9: US-based vein tracking results averaged over four square wave cycles. Table reproduced with permission from IEEE³ (year of original publication: 2017).

Speed (mm/s)	US Tracking Error (mm)	Following Error (mm)
0.5	0.004	0.003
2	0.006	0.046
10	0.004	0.794

2.3.2.5 Force Sensing

As described earlier, a force sensor was also implemented into the robotic end-effector to provide an added method to estimate needle tip position during the insertion. Our hypothesis was that differences in the mechanical properties of the tissue layers (e.g., tensile and compressive strength) would be reflected in the axial forces applied against the needle as it is inserted through the tissue. The addition of force feedback was incorporated into the device as an additional safety measure to confirm that the needle has first punctured the skin and then the blood vessel, and to ensure that the needle never passes through the opposite vessel wall. Especially in cases where the US image is noisy, the transducer may not be able to receive the acoustic signals back scattered from the metallic needle.

Alternatively, by observing the salient peaks in the force profile during the cannulation, we can determine when the needle pierces the skin tissue, when it is advancing through adipose tissue, and finally when the needle punctures the vein. The mechanism to detect forces encountered during the needle insertion consisted of a sensor, ball bearing linear sliders, and a precision compression spring. As the needle translates along the insertion path, axial forces encountered at the needle tip as well frictional forces along the needle shaft cause the needle holder to move backwards along the linear rails. This causes the spring to compress against the force sensor, generating an analog signal that is analyzed to compute the resulting force. Fig. 2.32 shows the initial concept design to evaluate the force sensing mechanism.

To first test the apparatus, we rapid prototyped an enclosure, used the EM-based needle attach and release system, and mounted the mechanism on a set of linear stages. Phantom skin models designed to mimic the mechanical properties of human tissue were used as a test platform to evaluate the force sensing mechanism. The first translation stage positioned

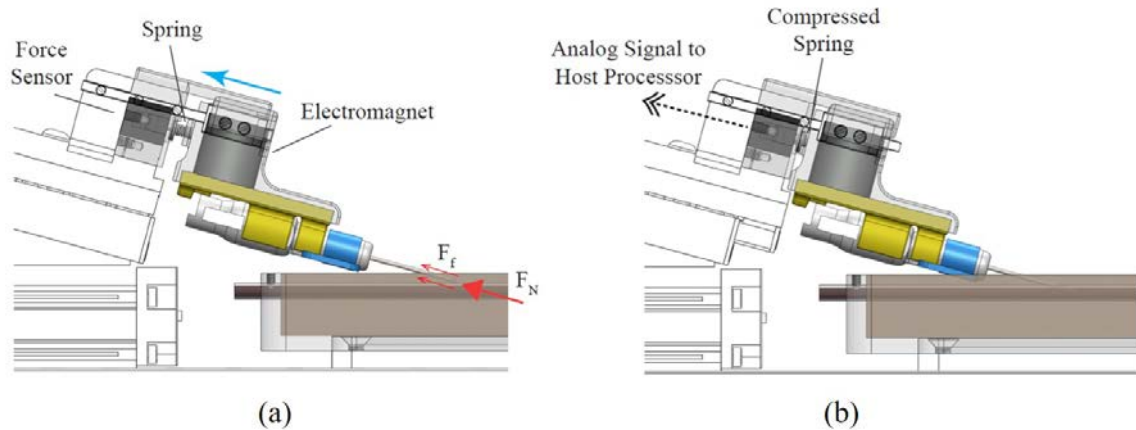


Figure 2.32: (a) CAD model illustrating the forces encountered during a venipuncture, and the mechanism used to detect these forces. F_N and F_f represent the normal force acting at the needle tip and frictional forces along the needle shaft respectively. (b) Depiction of how the needle slides backwards during the insertion, compresses the spring, and applies force against the sensor.

the apparatus along the length of the surrogate vein in the phantom, and the second stage performed the needle insertion. Fig. 2.33 depicts the experimental setup; highlighting the translation stages, tissue phantom, and key components of the force sensing mechanism. Experimental testing consisted of 3 consecutive venipunctures on a 3.18 mm diameter vein using a 21 G butterfly needle. All venipunctures were performed at a 15° insertion angle with a constant speed of 8 mm/s. The needle insertion actuator was programmed to position the needle tip in the center of the surrogate vessel, while the sensor continuously read the force signals. After each insertion, the needle was positioned 10 mm away from the previous injection site along the vein.

Results from the study are shown in Fig. 2.34, where the peaks in the force profile indicate the point in which the needle cannulated the vein wall. The signal-to-noise ratio at each force peak was approximately 13 dB. Further analyzing the force curve of each cannulation trial, we were unable to discern when the needle initially pierced the skin tissue. Expanding on this work, we then experimented with more sensitive force sensors in order to detect when the cannula pierces the skin. Once finalized, this mechanism design was incorporated into the robotic end-effector, and signals from the force sensor were combined with current measurements from the insertion motor to more accurately determine the

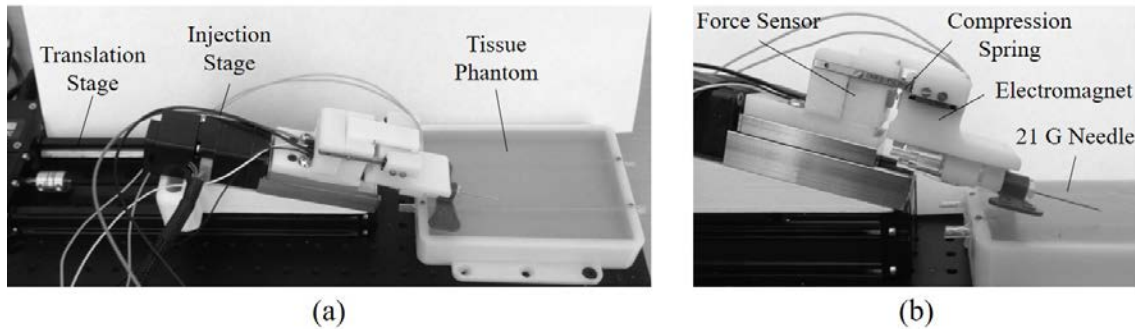


Figure 2.33: (a) Experimental setup used to test the force sensor mechanism on a tissue phantom model. (b) Components of the force sensing apparatus including the sensor, compression spring, and linear sliders.

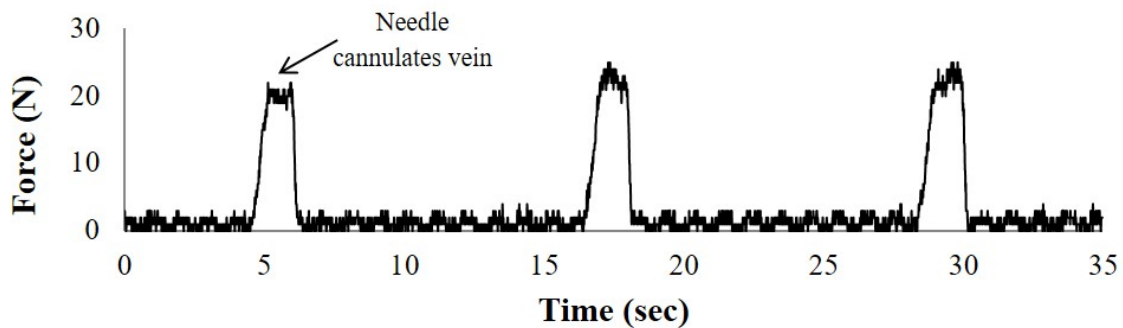


Figure 2.34: Force profile results during venipunctures on a 3 mm diameter surrogate vein. Peaks in the curve signify when the needle has pierced the vein wall, resulting in a successful stick.

needle position during cannulation. As seen in Fig. 2.35, the new force sensing mechanism was able to detect when the needle pierces the skin layer and vessel wall.

2.3.2.6 Force Guidance

In the last set of experiments, we evaluated needle insertion under real-time force guidance using the same blood vessel phantom as described in Section 2.3.2.4. Again, the $\varnothing 3$ mm vein was laterally displaced using the motorized stage (square wave, ± 2 mm, 2 mm/s), and the robot was tasked with following the moving vessel target using the US image. For these studies, the robot positioned the needle tip directly above the vein for three motion cycles, and then the insertion system introduced the needle into the center of the vessel at 10 mm/s and 15° . Both the needle insertion and vein motion were halted once the force

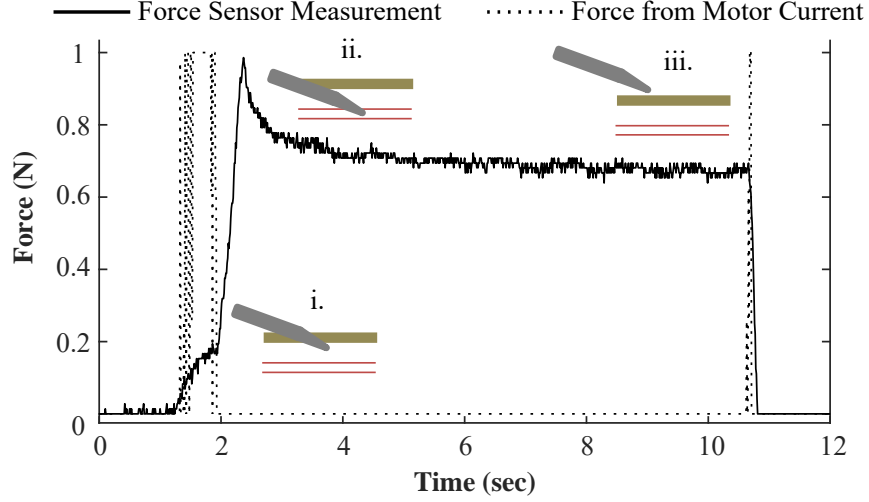


Figure 2.35: Force plot detecting key puncture events during a phantom cannulation on a 3 mm diameter silicon-based surrogate vessel: i. needle pierces top phantom layer; ii. needle pierces surrogate vein wall; and iii. needle is retracted. Figure reproduced with permission from IEEE³ (year of original publication: 2017).

sensor detected the venipuncture. The robot then retracted the needle (at the same speed and angle as the insertion) and moved forward 2 mm in the x -direction to introduce the cannula on a new section of the vessel. In total, this process was repeated over five trials.

Fig. 2.36a displays a series of US image frames depicting the needle insertion steps. In addition to the force and current readings, we also monitored the z -displacement of the vessel from the US images during the needle insertion (Fig. 2.36b). The z -position measurement is the displacement from the original vein position, as measured by optical flow. Thus, a downward vessel movement results in a positive peak in the plot. As seen in Fig. 2.36b, there was no observable latency between the force, current, and z -position readings during the needle insertion. Interestingly, a relaxation phase—commonly seen in force sensing puncture events—was observed in the z -position signal following the venipuncture. Finally, since the needle was inserted along the longitudinal axis of the vein, minimal y -displacement was observed.

2.3.2.7 Phantom Cannulation Testing

Using the thrid-gen device, cannulation accuracy was then assessed in phantom models (Fig. 2.37), where a successful venipuncture was defined as placing the needle in the center

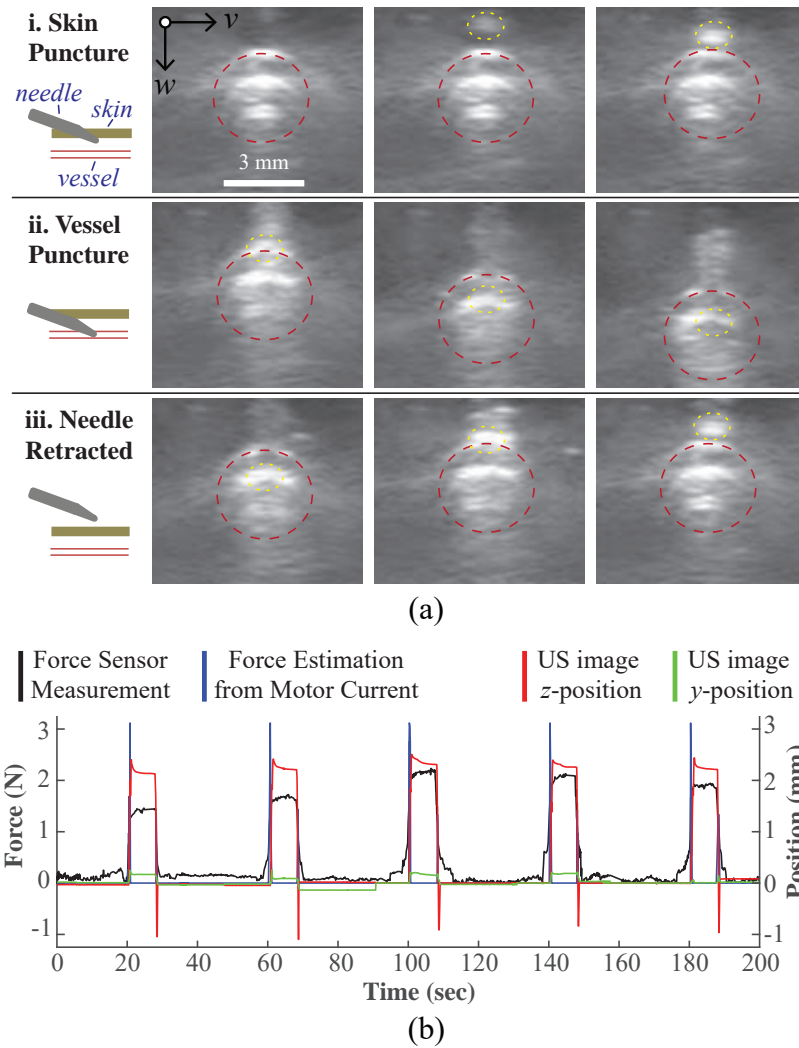


Figure 2.36: Force guided needle insertion. (a) US image frames depicting the needle insertion: i. needle pierces top phantom layer; ii. needle cannulates top vessel wall; and iii. needle is retracted. Vessel wall and needle tip highlighted with a dotted red and yellow border respectively. (b) z -displacement of the vessel extracted from the US images is shown to correlate with the force and current readings during the phantom cannulations (10 mm/s, 15°). Figure reproduced with permission from IEEE³ (year of original publication: 2017).

of the surrogate vessel, and collection of 4 ml of fluid. Phantoms were fabricated based on the protocol described in Chen et al.⁹, and extended by perfusing a viscous solution through the vessels. Briefly, phantoms contained two different sized veins ($\varnothing 3$ and 2 mm) composed of silicone tubing (Silastic silicone, Dow-Corning) embedded in a 10% gelatin matrix. Blood-mimic fluid composed of 45% glycerol and water was then perfused through the surrogate veins at 35 ml/min using a syringe pump (representative of a standard flow rate found in adult forearm vessels).

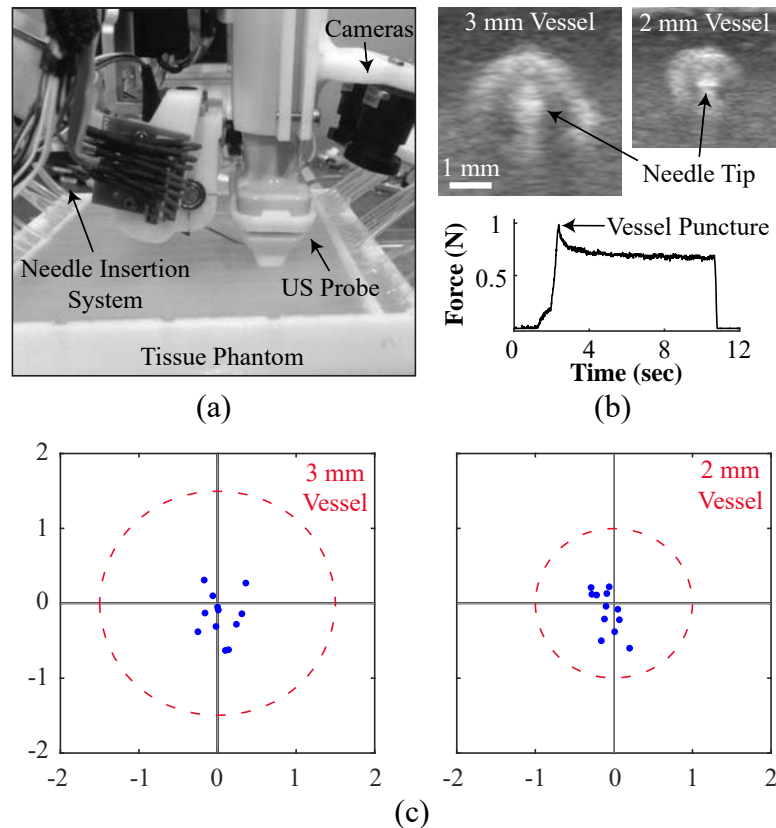


Figure 2.37: Robotic cannulation testing. (a) Experimental set-up highlighting the needle manipulator and tissue phantom. (b) US images of the $\varnothing 3$ and 2 mm surrogate vessel during venipuncture trials, and corresponding force profile observed. (c) Robotic cannulation results (dotted red circle indicates vessel wall, blue dots indicate needle tip position for each trial; units in mm). Figure reproduced with permission from IEEE⁴ (year of original publication: 2016).

The robot located the venipuncture site using the stereo cameras, oriented the end-effector along the vessel, and finally inserted the needle under US image and force guidance. In all trials, cannulation parameters were kept the same. Specifically, a 21 G needle was inserted at a constant 15° angle and a speed of 10 mm/s. The manipulator introduced the cannula into the phantom until a peak in the force profile was observed (as seen in Fig. 2.37b), confirming the vessel puncture. The robot then moved forward 5 mm along the x -axis and repeated this process a total of 6 times for each vein. Figure 2.37 displays the testing setup and cannulation results.

The robot successfully placed the needle into the center of the vessel across all cannulation trials with a needle tip error of 0.3 ± 0.2 mm and 0.3 ± 0.1 mm (mean \pm standard

deviation) for the $\varnothing 3$ and 2 mm vein respectively. Here, positioning error was defined as the distance from the vessel center to the actual needle tip position (extracted from the US image and registered to the robot coordinate frame). As previously discussed, the subtle inaccuracies may have stemmed from errors in the joint kinematics, ultrasound calibration, or assembly of the system. Implementing a state estimation framework to combine measurements from the US image, force sensor, and joint position sensors may improve the localization of the needle tip in future studies.

2.3.2.8 Modeling Needle Tissue Interaction

When introducing the needle into small and fragile veins—such as those common in pediatric and elderly patients—the mechanical forces generated by the needle tip may cause the vein to deform, move, or roll, and this motion may lead to missed insertion attempts³. In such cases, the clinician is required to make subtle real-time adjustments to the needle orientation, oftentimes a challenging task. To further investigate the details of vein motion and needle tissue interaction during the venipuncture, we developed a computational model and validated the results through *in vitro* experiments.

2.3.2.8.1 Computational Models

To simulate the mechanics of needle insertion into a blood vessel, we first modeled the vein as a thin-walled cylinder beam (elastic modulus, $E_v = 10$ kPa; outer diameter, $d_o = 3.2$ mm, inner diameter $d_i = 2.0$ mm, length $l_v = 80$ mm), and calculated displacements based on applying a point load on-axis to cause beam deflection (Fig. 2.38a). Supporting the vein underneath is a distributed load representing the surrounding tissue. Because we were interested in the behavior of the vein prior to the needle piercing the wall, the load was maintained below the minimum puncture force for venous access. Specifically, an applied load of $P = 0.5$ N was introduced at an angle of 15° . Accounting for the distributed load

³Much of the work presented in this section first appeared in: Real-time needle steering in response to rolling vein deformation by a 9-DOF image-guided venipuncture robot. Proceedings of the 2015 IEEE/RSJ International Conference on Intelligent Robots and Systems, pp. 2633–2638². All excerpts represent the original work of Max Balter, whose specific contributions as co-first author included: developing the scope of the paper; designing the experiments; creating figures; writing, editing, and revising the original text; and addressing reviewers' comments.

underneath ($\omega = 0.004$ N/mm), the resulting point load in the axial direction was 0.2 N. Using Eq. 2.26):

$$I_{yy} = I_{zz} = \pi (d_o^4 - d_i^4) / 64 \quad (2.26)$$

where I is the area moment of inertia in y and z , the resulting maximum displacement d_{max} can be calculated from Eq. 2.27:

$$\delta_{max} = \frac{Pl^3}{48EI} \quad (2.27)$$

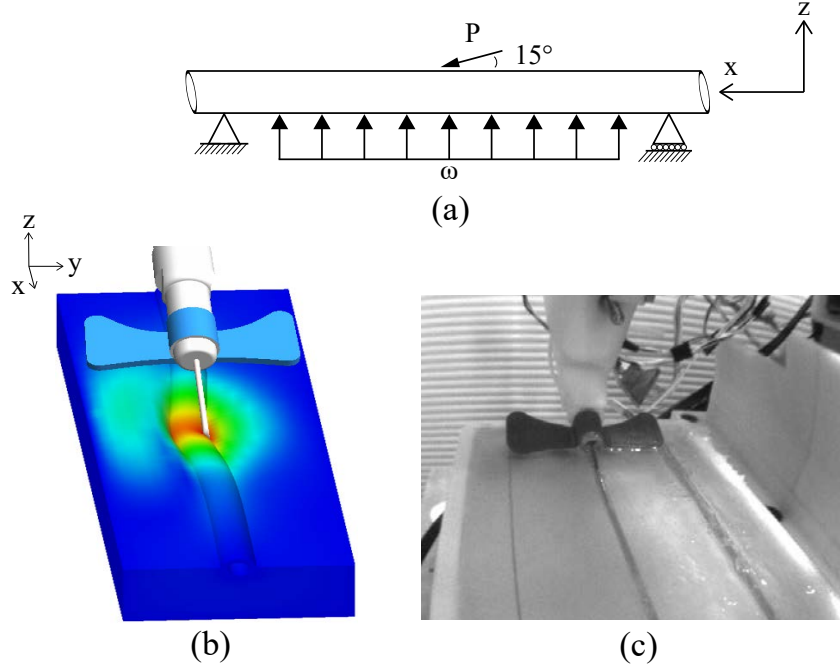


Figure 2.38: (a) Theoretical beam bending model, (b) SolidWorks simulation, and (c) experimental phantom cannulation setup. Figure reproduced with permission from IEEE² (year of original publication: 2015).

Next, to account for the nonlinear behavior of the tissue caused by on- and off-axis loads during needle insertion²⁴⁵, we implemented finite element (FE) models of a typical adult median cubital vein and a dermis/hypodermis support layer (8 x 3 x 1 cm rectangular volume). Table 2.10 summarizes the mechanical properties of the FE models, which were based on literature references of human skin and vessel mechanical properties^{246,247}. Three

different simulations were implemented using the SolidWorks Simulation software package (Fig. 2.38b). In the first simulation, the needle was aligned with the medial axis of the vein. Here, only downward vessel displacements were expected. This condition is representative of an ideal venipuncture. In the second simulation, the needle was positioned off-axis. Slip was allowed at the contact interface between the needle and the vein. This condition, where the vein slides away from the needle tip immediately upon contact, is similarly observed in patients with poorly anchored or rolling veins. The needle was likewise positioned off-axis in the third simulation. However, a no-slip condition was enforced between the needle and the vein. In this condition, which may be observed in patients with hardened veins, high strains are exerted on the vessel wall that may lead to significant deformation or vessel rupture²⁴⁸. In all simulations, the needle gauge was set at 23 G, the angle of insertion at 15°, and the maximum insertion distance at 10 mm. As in the beam deflection model, the applied loads were maintained below the minimum puncture force.

2.3.2.8.2 Experimental Evaluation

Robot cannulation trials were conducted *in vitro* to investigate vessel deformation and device accuracy. Here, phantom models with mechanical properties similar to those of the human forearm were utilized (Fig. 2.38c). To keep consistent with the geometry of the FE models, we fabricated each phantom within an 8 x 3 x 1 cm container. Like the FE models, each phantom comprised a surrogate vein (Dow-Corning Silastic silicone tubing) with the bottom half embedded in support tissue. The support tissue was formed from porcine gelatin, whose mechanical properties can be controlled to resemble those of the dermis and hypodermis. For example, a support tissue with elastic modulus $E \cong 50$ kPa (concentration 20% m/v) may be used to model mechanically rigid tissues such as dermis. In contrast, the phantoms used in this study (Table 2.10) were significantly more compliant ($E \cong 0.5$ kPa, concentration 2.5% m/v) to mimic adipose tissue. Here, rather than provide support, the tissue would more likely deform upon needle contact and thereby allow the vein to roll.

Phantoms were constructed to investigate the three needle insertion conditions simulated earlier, namely: (1) the on-axis condition; (2) the off-axis slip condition; and (3) the

Table 2.10: Mechanical properties used for vein modeling and simulations. Values based on literature references of human tissue mechanical properties^{246,247}. Table reproduced with permission from IEEE² (year of original publication: 2015).

Tissue Layer	Material Parameter	Unit	Finite Element Model	<i>In Vitro</i> Phantom Model
<i>Vein</i>	Material	–	Elastin	Silicone
	Outer vein diameter, d_v	mm	3.2	3.2
	Wall thickness, t_v	mm	0.55	0.6
	Vein length, l_v	mm	80	80
	Elastic modulus, E_v	MPa	10	9.5
	Shear modulus, G_v	MPa	5.2	–
	Poisson ratio, ν_v	–	0.48	0.48
	Compression strength, σ_{cv}	MPa	20	–
	Yield strength, σ_{yv}	MPa	3.1	3.8
	Tensile strength, σ_{tv}	MPa	9	9.3
<i>Dermis, Hypo-dermis</i>	Material	–	Adipose	Gelatin
	Dimensions, l_t, w_t, h_t	cm	8x3x1	8x3x1
	Elastic modulus, E_t	MPa	1	1
	Shear modulus, G_t	MPa	0.5	–
	Poisson ratio, ν_t	–	0.48	0.49
	Compression strength, σ_{ct}	MPa	0.75	1
	Yield strength, σ_{yt}	MPa	–	–
	Tensile strength, σ_{tt}	MPa	–	–

off-axis no-slip condition. In a first set of trials, vessel deformation patterns predicted by the simulations were compared with experimental observations of the three conditions. To ensure that the mechanical properties of the phantom would be affected only by the applied load of the needle, we did not utilize US imaging here. Instead, the robot kinematics were computed directly from the 3D coordinates provided by the stereo NIR imaging. Furthermore, the computational and experimental insertion parameters were kept consistent. That is, the needle was inserted at a constant 15° angle with a 10 mm travel distance and speed of 10 mm/s. Once the 3D coordinate of the vein target was identified, the robotic joints were locked; as such, the linear needle trajectory was unchanged after the cannulation was initiated.

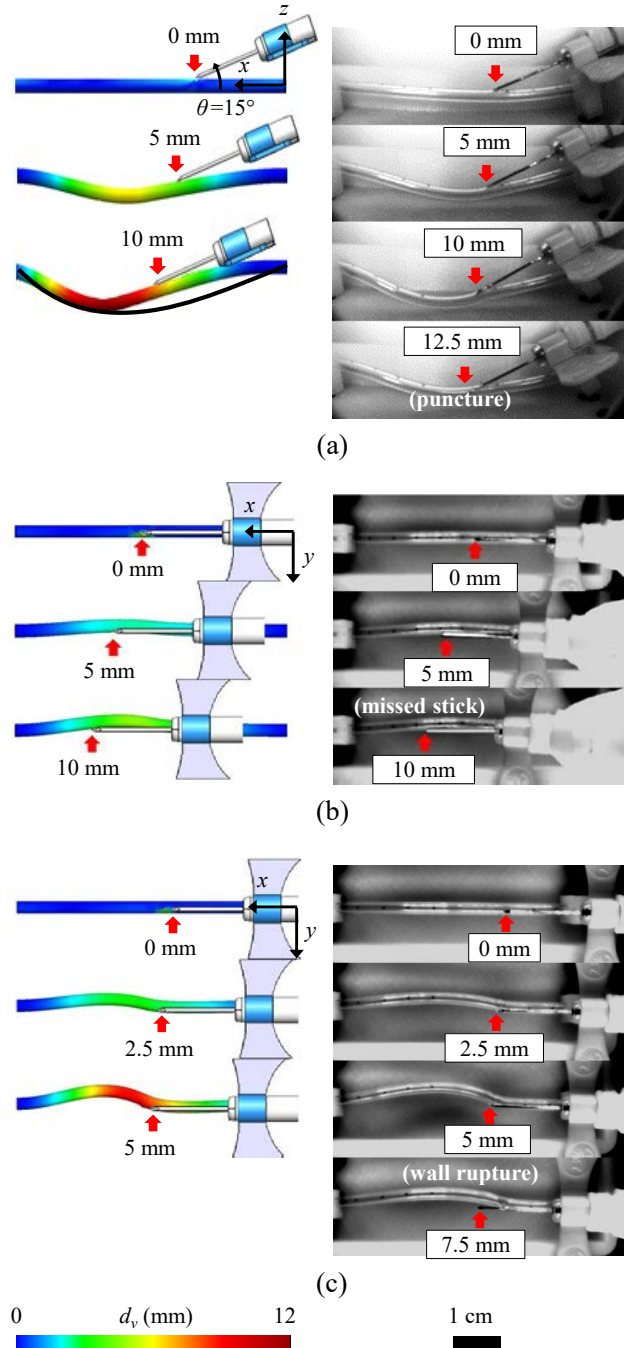


Figure 2.39: Time-lapse images comparing the simulated (left) and experimentally observed (right) vessel deformation patterns for (a) on-axis, (b) off-axis slip, and (c) off-axis no-slip cannulation conditions. Red arrows indicate the needle tip position and total needle insertion distance along the axis of cannulation. Vessel displacement d_v (mm) is also shown via the color map. Insertion parameters between the simulations and experiments were kept consistent, e.g., the needle was inserted at a constant 15° angle with a 10 mm maximum travel distance and speed of 10 mm/s. Figure reproduced with permission from IEEE² (year of original publication: 2015).

In contrast to the comparative studies, we also ran experiments to assess the real-time, image-guided kinematic controls of the robot during the insertion. Here, the US imaging system was fully utilized to locate and track the center of the vein in each image frame. Additionally, the robot was allowed to adjust the position and orientation of the needle tip based on the image feedback. In this way, we were able to evaluate the robot's ability to guide the needle into the vein in the presence of vein movement and deformation.

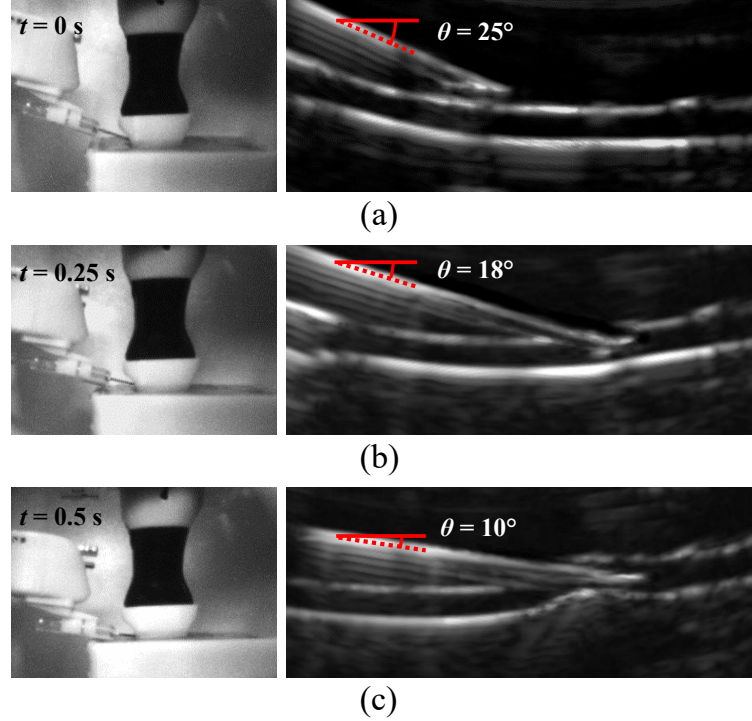


Figure 2.40: Real-time longitudinal B-mode US images showing robotic needle guidance and vessel deformation in a phantom. The adjustment of the needle orientation in response to the moving vein target can be observed. The insertion angle was lowered from its starting angle of $\theta = 25^\circ$ (a) to $\theta = 18^\circ$ upon first contact with the vessel wall (b), and finally to $\theta = 10^\circ$ to allow the needle to be guided into the vessel lumen (c). Figure reproduced with permission from IEEE² (year of original publication: 2015).

Fig. 2.39 shows time-lapse images comparing the FE simulations and experimentally observed vessel deformation patterns for the on-axis, off-axis slip, and off-axis no-slip cannulation conditions. The vessel deflection predicted by the beam bending model for the on-axis applied load is also shown (Fig. 2.39a, solid black line) with maximum displacement $d_{max} = 12.95$ mm. For the on-axis FE and experimental trials, (Fig. 2.39a), vessel

displacement was observed to occur primarily in the longitudinal (x) and vertical (z) directions, whereas minimal vessel displacement was observed in the lateral (y) direction. On the contrary, significant lateral (y) vessel displacement was observed when the needle was introduced off-axis. In the slip condition (Fig. 2.39b), the asymmetrically distributed forces applied to the vein side wall caused the vein to roll under and away from the axis of insertion shortly after initial contact with the vein. Finally, in the no-slip simulation, significant deformations occurred along the distal portions of the vein. In the simulations, the applied stress on the vein side wall was found to exceed the material yield stress after the needle was inserted 5 mm (Fig. 2.39c). Similarly, in the phantom experiment, the vessel side wall was observed to rupture shortly after 5 mm of insertion.

Longitudinal B-mode US images of needle insertion and vessel deformation are shown in Fig. 2.40. The adjustment of needle orientation in response to the moving vein target can be observed. Here, insertion distance within the FOV of the US image was 5 mm (about half the total insertion distance). Likewise, the duration in which the insertion was under US guidance was 0.5 s. In that time, the insertion angle was lowered from its starting angle of $\theta = 25^\circ$ (Fig. 2.40a) to $\theta = 18^\circ$ upon first contact with the vessel wall (Fig. 2.40b), and finally to $\theta = 10^\circ$ to allow the needle to be guided into the vessel lumen (Fig. 2.40c) following an exponential decay trajectory curve. Starting with a steeper angle reduces the amount of dermal tissue punctured by the needle and reduces the axial insertion force at the needle tip. And ending with a shallow angle reduces the likelihood that the needle tip pierces through the other side of the vein. In these studies, the compressive force of the US transducer against the phantoms helped to reduce the extent of vein movement, suggesting that it may be possible to utilize the US transducer to anchor the vein during the cannulation.

2.3.3 Summary and Outline of Future Work

In summary, we designed and built a 9-DOF robotic system capable of cannulating peripheral blood vessels based on stereo vision, US, and force guidance. Kinematic equations were derived to correlate the image frames with the robot joint frames. This allowed us to run a series of workspace simulations to evaluate the reach and pose of the needle based on

joint position commands. Thereafter, we conducted free-space positioning tests on a cylindrical calibration to evaluate errors in the robot that may have resulted from the camera calibration, kinematics, or construction of the device. 3D positioning error was 0.22 ± 0.05 mm, with the needle tip detection repeatability being 0.03 mm. Such a low error gives us confidence that the device can be used to cannulate vessels as small as 1 mm in diameter. Furthermore, these errors can be subtracted from the system by generating error maps—essentially robot calibration.

Next, the control scheme deployed in the venipuncture robot was evaluated through a series of tracking experiments using stereo vision, US, and force guidance. Position-based servoing was implemented as opposed to an image-based approach, because the needle was not in the FOV of the cameras during vision-guided tasks, and was occasionally occluded in the image during US-guided tasks. Though position-based servoing depends on robot kinematics and image calibration parameters, this method worked well for our application, as demonstrated by our results.

Nevertheless, several limitations were observed when we evaluated the effects of motion speed on positioning accuracy. First, the robot lacked true dynamic controls, and instead, relied on set-points for trajectory planning. This was evident in our stereo vision experiments, where increased tracking errors were observed at higher motion speeds. Incorporating a dynamic motion control scheme in addition to the kinematic controls described in this paper may allow the system to rapidly adjust higher-order parameters, such as acceleration, to better adapt to sudden variations in motion speed. It is also possible that state estimation functions (e.g., the Kalman filter) may be implemented to predict future positions based on current trajectories, and that this may help to reduce following errors at high speeds.

A second source of inaccuracy was the 3D localization errors during the stereo reconstruction step. Since the motion control scheme is dependent on the NIR and US imaging, errors in the localization of vessels results in errors in the needle placement. The device relies on a robust stereo matching to identify the 3D positions of the underlying vasculature. By miniaturizing the robotics, the short distance (i.e., approximately 5 cm) between the camera frames and patient’s arm can sometimes impair the 3D reconstruction, resulting in

the device not knowing where to lower the US probe. This is especially important, considering that if the vessel is not initially observed in the US image, the device has no means of automatically searching for the vein without the help of a clinician operating under open loop control. Implementing active methods of stereo vision based on structured illumination may help to improve the 3D reconstruction quality in comparison to traditional passive stereo approaches. Here, we could use an IR pattern projector in conjunction with a single NIR camera for 3D measurements—as seen in the Microsoft Kinect device—to triangulate points in space²⁴⁹.

Moreover, accurately tracking the tissue of interest in 2D US images is a challenging research problem in the visual servoing community, especially when dealing with random, non-linear motions. Part of the challenge is that US imaging is inherently a noisy process, and relies on clean contact between the transducer head and patient. One method to obtain a pseudo-3D image of the vessel is to rapidly servo the probe across a 1 cm length of the vein, using the segmented vessel in the NIR image as an input into the global path planner. Similarly, a localized intensity based servoing scheme using the US image could also be used to sweep across the vein, as demonstrated in Nadeau et al.²⁵⁰. If conventional 2D US imaging is incapable of visualizing vessel features in difficult cases, we may also look into implementing a 3D transducer.

Lastly, we developed an FE model of vessel deformation that occurs during the venipuncture. First using beam-bending mechanics, we modeled the vein as a thin-walled cylindrical pressure vessel and subjected it to point loads at various angles and positions offset from the center-axis. Then using SolidWorks modeling software, we ran a series of simulations to more formally evaluate the stresses, strains, and deformations that occur along the vessel during the needle insertion. This allowed us to observe and quantify the effects of inserting the needle off-axis—a common occurrence with inexperienced clinicians. Future work will focus on refining the FE models to simulate varying human physiological and demographic characteristics. The improved models may then be used to study other factors that affect venipuncture accuracy, such as insertion angle, insertion speed, vein depth, and vein diameter. In addition, the FE models will be expanded to simulate the actual penetration of the tissue by the needle. This will allow us to compare experimentally observed force

profiles with theoretical solutions, and to validate the force sensing component of the robot. Through these studies, we will assess vessel motion speeds due to deflection and deformation during the venipuncture in order to understand whether any changes to the mechanical design of the robot are required.

2.4 Ultrasound Computer Vision Algorithms

With the addition of US imaging to the second and third-gen devices, vein visualization was enhanced through increased penetration depth through skin tissue, and improved image resolution. Complementing the NIR imaging employed in the first-gen device, US imaging provided localized scans of the vessel of interest to guide the needle insertion. In this fashion, the device used a bi-modal imaging scheme, as outlined in Fig. 2.41, which consisted of stereo NIR imaging to coarsely scan the underlying vasculature and select an initial injection site, and US imaging to provide high magnification vein visualization. Image analysis algorithms further segment the vein in the US image, confirm blood flow via Doppler capabilities, and finally detect and track the needle in real-time during the cannulation.

The work of Dr. Alvin Chen included developing algorithms for the first two steps in the process: vessel segmentation and blood flow detection. Several methods were explored for vein segmentation in US images—both in the transverse and longitudinal probe orientation. Specifically, an active-contours based approach and various region grow algorithms were tested on a range of patients¹⁰. The active-contours method proved superior and was selected for implementation in the device. For the second step in the US image processing routine, the device confirmed blood flow in the selected vein to determine whether a vessel is appropriate for cannulation. This safety addition is key to preventing missed sticks in collapsed veins commonly seen in chronically ill and geriatric patients. The most widely known technique used to image blood flow is Doppler velocimetry, where large packets of long transmit pulses are sent and received from the US probe, providing visualization of weak blood echoes.

The conventional approach in blood flow imaging is to overlay the Doppler color data on top of the B-mode scan. However, there are several limitations with this approach.

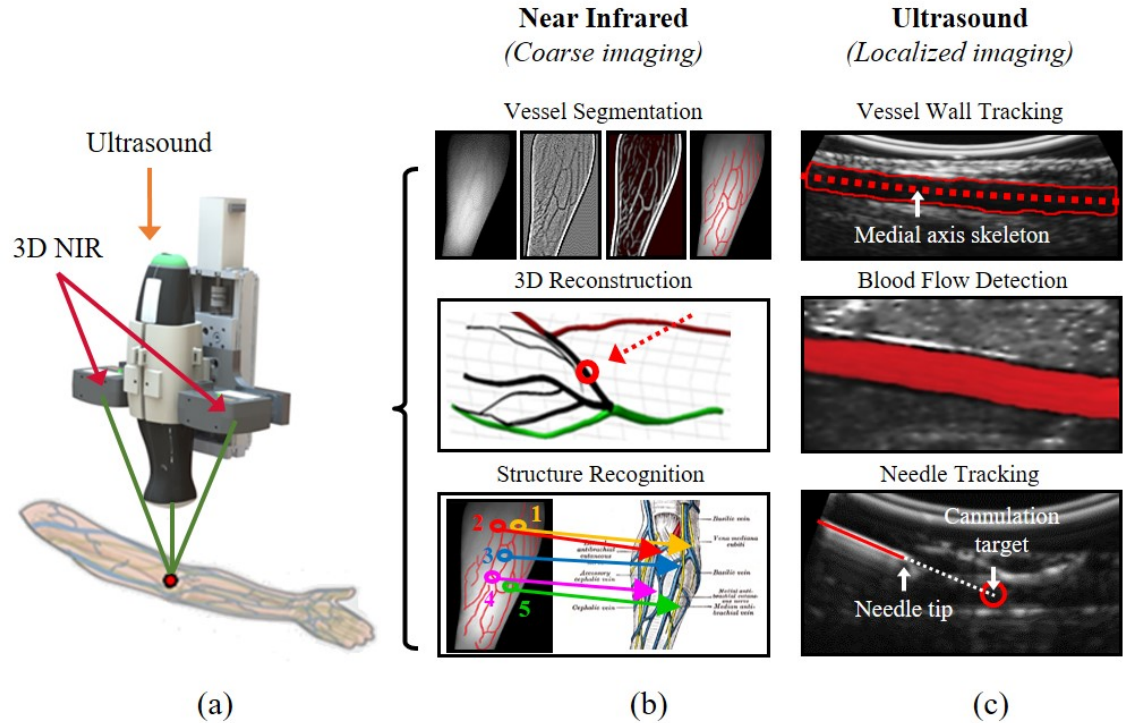


Figure 2.41: (a) Overview of the bimodal imaging system. (b) NIR imaging and analysis (segmentation, reconstruction, structure recognition). (c) US imaging and analysis (vessel wall segmentation, blood flow visualization, and needle tracking). Section 2.4 focuses on the implementation of the US-guided needle tracking software (c, bottom).

Typically, color flow imaging first detects the Doppler shifts of blood flow, and then makes a threshold decision about where to overlay the color pixels on the B-mode image. Since the threshold decision is imperfect, vessel wall overwrite sometimes occurs which may obscure important diagnostic information. In addition, any large tissue motion in the color flow overlay is displayed as a color flash artifact, which overshadows the true flow and anatomical data^{251–253}. Finally, the measured Doppler frequency shift in a blood vessel varies inversely with the cosine of the Doppler angle (i.e., the angle between the incident beam and blood vessel)²⁵⁴. Thus, techniques that do not inherently depend on the Doppler angle, such as B-mode imaging, may be useful for visualizing blood flow²⁵⁵. Instead, we implemented a method—similar to b-flow imaging—to estimate blood flow in real-time. The steps in the algorithm included: (1) contrast enhancement using a Difference of Gaussians technique, (2) feature extraction using a Speeded-Up Robust Features detector, and (3) motion tracking using Lucas Kanade sparse optical flow.

For more details on both the vessel segmentation and blood flow estimation algorithms, the reader is referred to Chen et al.¹⁰.

2.4.1 Needle Localization & Tracking

Tracking the needle tip position throughout the insertion trajectory is critical to the safety of the device. Cannulating through the back of the vein wall can lead to complications such as internal bleeding and nerve injury, whereas failing to reach the center of the vessel can result in extravasation of fluids. Therefore, the goal of this next body of work was to develop a robust needle tracking approach to detect and compute the needle tip position in real-time throughout the venipuncture.

2.4.1.1 Needle Detection & Tracking Methods

With the addition of needle tracking, we created an additional feedback loop to detect when the cannula has reached the center of the vessel. We implemented and tested a range of detection algorithms either in MATLAB, OpenCV, or LabVIEW. B-mode longitudinal US images were acquired using a 12 MHz transducer (Near Field Vascular, 99-5934, Interson Inc.) during robotic cannulations on skin-mimicking phantoms containing surrogate blood vessels. Figure 2.42 illustrates the experimental setup, and an image frame of the B-mode scan. The needle is clearly seen in the US image due to the strong reflections from the metal shaft compared to the surrounding phantom tissue.

In total, 16 cannulation trials were performed on phantom vessels of two different diameters (3.2 mm and 2.0 mm) using a 25 G butterfly needle. The US probe was oriented longitudinally to track the needle as it pierced the phantom, and the needle was manually inserted at approximately a 30° angle in plane with the US probe. For each trial, frame-by-frame image recordings were captured over a 10 second period at 20 fps for a total of 200 acquired images per trial. For each set of images, we selected for analysis the frame corresponding to the time point at which the needle insertion velocity returned to zero, indicating that the completion of the cannulation, with the needle thought to be centered within the vessel. The needle orientation and needle tip positions in each of the selected US image frames were annotated manually, and served as the control for the study.

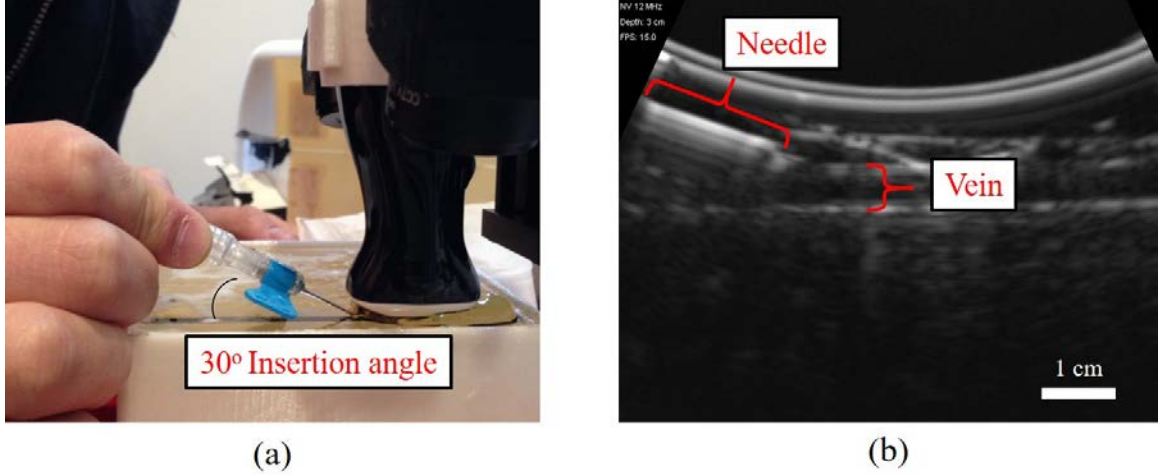


Figure 2.42: (a) Needle tracking experimental setup depicting a manual cannulation of a single layer tissue phantom, and (b) the resulting US image highlighting the simulated vein wall and needle.

Meanwhile, the needle orientation and needle tip positions predicted by the robot kinematics were saved to Excel, and served as the ground-truth information. The needle segmentation and motion tracking algorithms were then applied to each of the images sequentially. Mean error distances were calculated between the robot kinematic predictions and the needle tip positions computed by each algorithm, and between the kinematic predictions and the manually annotated needle tip positions. The same approach was applied to the line segmentation algorithms to determine mean error distances in the estimated angular needle orientation. For the motion tracking algorithms, manual annotation was not performed due to the large number of frames that would have had to be assessed.

Two algorithmic techniques were implemented for needle detection and tracking: (1) a Shi Tomasi corner detector and Kalman filter; and (2) a Gabor filter and Hough Transform. These methods are described in detail in the following sections.

2.4.1.1.1 Corner Detector & Kalman Filter

The first approach utilized a corner detector (Shi-Tomasi) to segment the needle tip and a feature tracker (Kalman filter) to track the tip during the insertion. The implementation included the following. First, to identify the needle in the US image, we applied a second-order filter based on eigenvalues of the Hessian matrix to highlight long, thin, cylindrical

structures^{143,226}. Next, we utilized a modified Shi-Tomasi corner detector algorithm to identify the most prominent corner in the image. This was further used to initialize a point-based feature tracker for the needle tip. Point tracking was then performed using a Kalman filter, which has been shown to be more efficient than direct tracking of raw images²⁵⁶.

To extract the point of interest (i.e., the needle tip), a modified Shi Tomasi corner detector was implemented, which looks for intensity variations in the image²⁵⁷. Essentially, a corner is the intersection of two edges that represents a point where the edge gradients change. Using a 2D grayscale US image, the corner detector algorithm sweeps a 3x3 kernel across the image and looks for the largest variations in pixel intensity. Equation 2.28 was used to calculate the maximum variations in intensity.

$$E(u, v) \approx [u, v] \left(\sum_{x,y} w(x, y) \begin{bmatrix} I_x^2 & I_x I_y \\ I_x I_y & I_y^2 \end{bmatrix} \right) \begin{bmatrix} u \\ v \end{bmatrix} \quad (2.28)$$

Using P to denote the function in parenthesis, the intensity equation becomes:

$$E(u, v) \approx [u, v] P \begin{bmatrix} u \\ v \end{bmatrix} \quad (2.29)$$

Finally, a score (V) is calculated for each window using Eq. 2.30, and thresholded against a specific value to determine if the pixel is a corner.

$$V = \min(\lambda_1, \lambda_2) \quad (2.30)$$

In q. 2.30, λ_1 and λ_2 are eigenvalues of the matrix P. Next, a Kalman filter was implemented to track the detected needle tip. Kalman filtering aims to reduce system error using a least squares method by incorporating measurements from several different sources²⁵⁸. The filter takes in measurements with noise and uncertainty, and outputs estimated values that tend to align better with the true spatial measurements of the target. In our case, that

target is the needle tip position. The Kalman filter was applied to the detected needle tip pixel coordinate based on the algorithm shown in Eq. 2.31.

$$\hat{X}_k = K_k Z_k + (1 - K_k) \hat{X}_{k-1} \quad (2.31)$$

The subscript k 's represent system states which can be considered discrete time intervals (i.e., $k = 1$ means 1 ms). Hence, we can find the estimate of the signal (\hat{X}_k) for each consecutive k value. Z_k represents the noisy measured value in the system. If the measured value were perfect at each state, then it would not be necessary to run the Kalman filter algorithm to track the needle tip. However, US is inherently a noisy process; running a Kalman filter is designed to improve the tracking results. Also, \hat{X}_{k-1} represents the previous estimate of the signal or the predicted value, and K_k is the Kalman gain which is calculated for each consecutive state. The Kalman filter finds the ideal averaging factor (Kalman gain) for each state by remembering information from past states²⁵⁸.

To test the corner detector and Kalman filter, US images were called into a LabVIEW script, cropped, and inputted into the algorithm. This corner detector function was written in C++ using built-in OpenCV functions, and then compiled into a dynamic link library so it could serve as a function block in LabVIEW. Figure 2.43 steps through the process of (a) calling the image; (b–c) cropping to a region-of-interest (ROI), and (d) detecting the needle tip (in red) as well as the Kalman filter estimate (in green) within a secondary ROI (in yellow). Here the center of the secondary ROI is defined by the previously detected needle tip, and the Kalman filter outputs a state estimate of the needle tip position.

2.4.1.1.2 Gabor Filter & Hough Transform

Next, we implemented a Gabor filter in conjunction with a probabilistic Hough Transform algorithm for needle detection and tracking. First, the US image is cropped to restrict the search area to where the needle should be based on the kinematic output by the robot. By registering the US image with the device frame, and using sensors to detect the needle tip location, we can estimate the needle position. This needle tip estimate is used as the reference center target to which we apply the initial ROI to the US image (Fig. 2.44b).

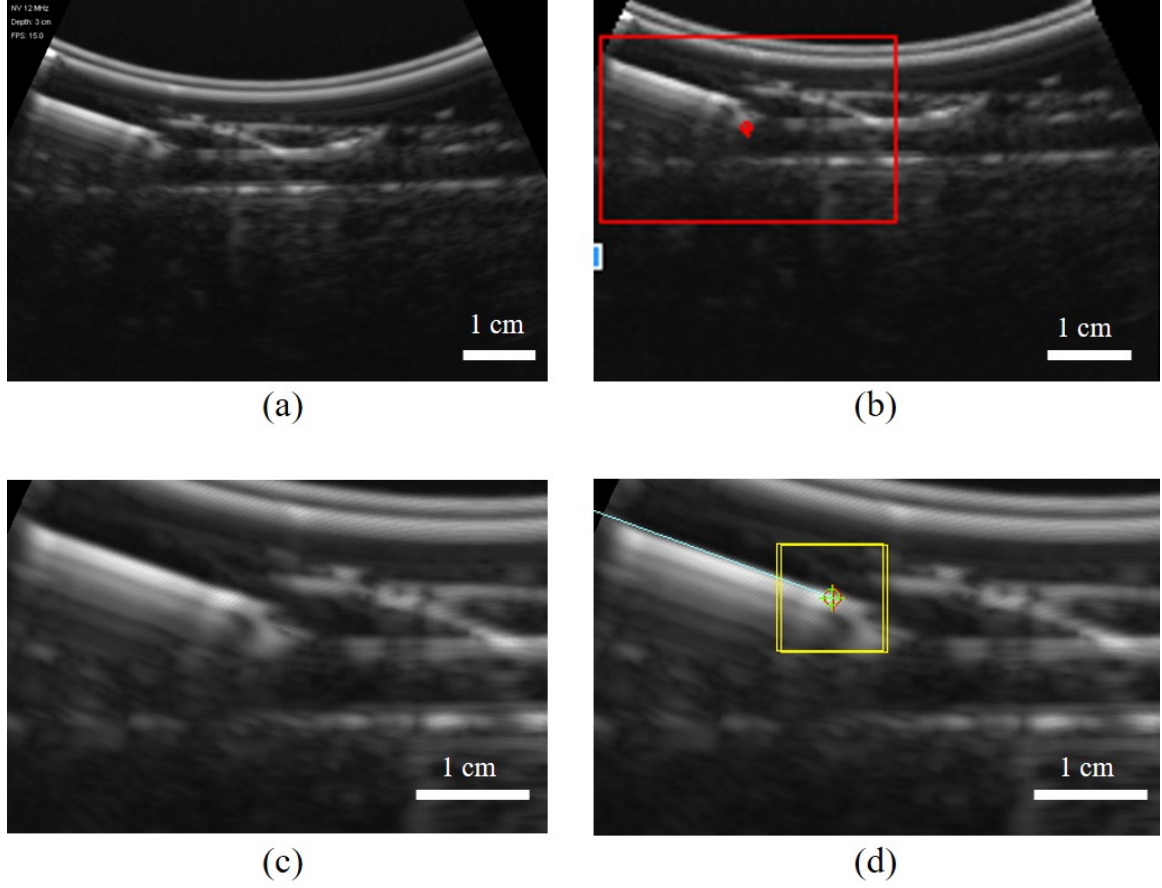


Figure 2.43: Process flow of the Shi-Tomasi needle tip detector and Kalman filter tracking approach. (a) Raw B-mode US image, where the simulated vessel and needle are visible. (b) Cropping to the initial ROI, and (c) the resulting cropped image. (d) Results from the corner detector (red) and KF (green) overlaid on the US image. The yellow box highlights the search ROI for the corner detector.

The Gabor directional filter (as discussed in Kaya et al.²⁵⁹) is then applied to search for intensity gradients along the angle of insertion of the cannula (Fig. 2.44c). A Gabor filter is a rotational filter, which is commonly used for edge detection and feature extraction. The 2D Gabor filter in the spatial domain is a multiplication of a complex carrier sinusoid and a 2D Gaussian. The filter is expressed in Eq. 2.32:

$$g(x, y, \lambda, \theta, \psi, \sigma, \gamma) = e^{-\frac{x'^2 + \gamma^2 y'^2}{2\sigma^2}} * e^{i\left(2\pi \frac{x'}{\lambda} + \psi\right)} \quad (2.32)$$

where

$$\begin{aligned}
x' &= x * \cos(\theta) + y * \sin(\theta) \\
y' &= -x * \sin(\theta) + y * \cos(\theta) \\
\lambda &= 0.25 * \sigma
\end{aligned}$$

And where λ is the wavelength, θ is the angle, ψ is the phase, σ is the standard deviation, and γ is the spatial aspect ratio. Equation 2.32 is the complex representation of the Gabor filter—it can be further split up into real and imaginary components to use as needed. The angle is determined from the device’s position sensor on the insertion system—the filter is continuously updated in real-time to account for the angle of insertion of the needle during the venipuncture.

As shown in Fig. 2.44a, the metallic needle appears as a salient line in the upper left-hand corner of the US image during cannulation with reverberation echoes flowing downward. By filtering the image, extraneous lines are eliminated that may result in false positives for needle detection, and instead, highlight lines that reside along the angle of insertion of the cannula. Finally, to segment the needle, a probabilistic Hough Transform is applied to search for the most prominent and continuous line segment in the image²⁶⁰. If multiple lines are detected, a distance transform is used to select the Hough Transform line whose endpoint is closest to the estimated needle tip position from the kinematics. The Hough Transform line whose endpoint is closest to the needle tip estimate is selected for needle segmentation. Finally, the Lucas Kanade sparse optical flow method is used to track the needle tip position once it is detected in the first frame. In the current implementation, the optical flow tracking algorithm is carried out with each frame during the insertion. The final position is then defined as the estimate that most closely matches the kinematic prediction.

2.4.1.2 Experimental Results

Table 2.11 compares the mean error distances and completion times of 7 line segmentation approaches, 3 needle tip detectors, and 3 tracking algorithms. A combination of the probabilistic Hough Transform with the Gabor filter, Shi-Tomasi corner detector, and

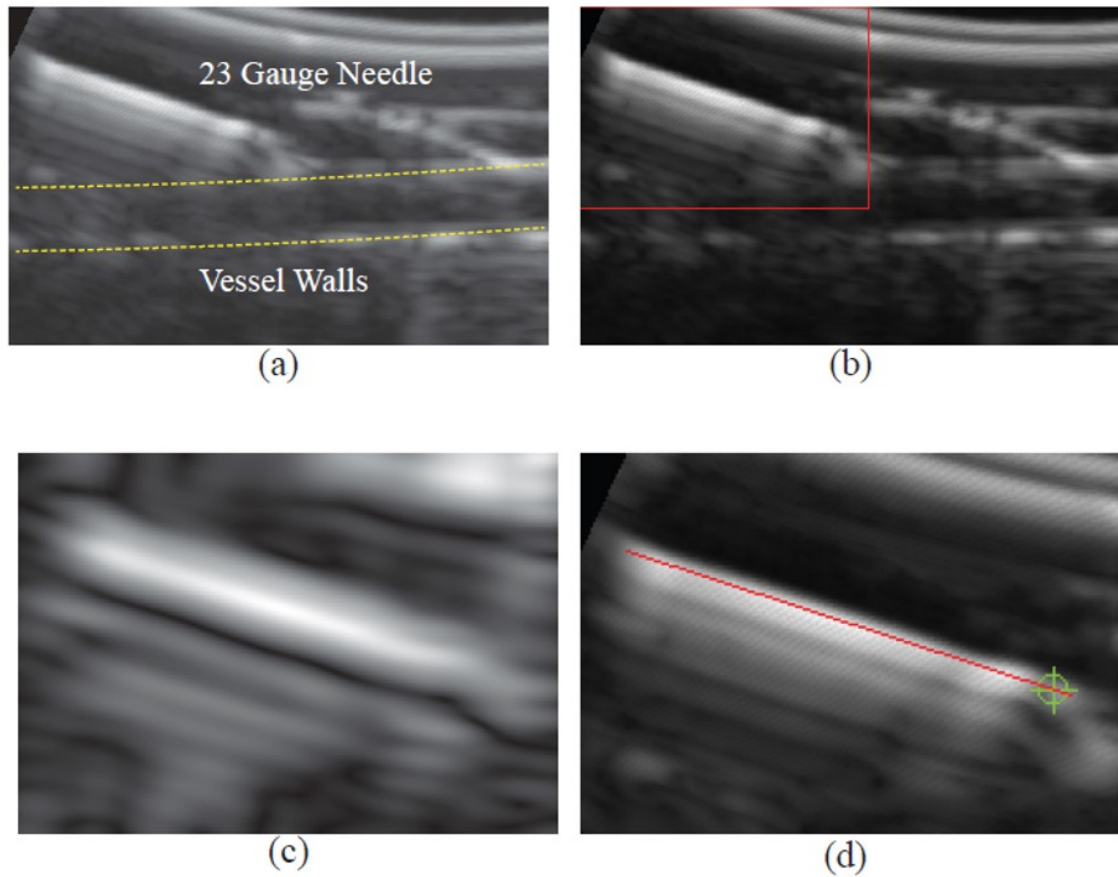


Figure 2.44: Process flow of the Gabor filter and Hough Transform needle detection. (a) Raw B-mode scan during a phantom arm cannulation using a 23 G needle. (b) Highlighted search region in the US image. (c) Gabor angle filter (20°) applied to the ROI in (b). (d) Probabilistic Hough transform (red line) applied to the Gabor filtered image. Green marking indicates needle tip estimate from the device kinematics.

Lucas-Kande sparse optical flow was used in the final software implementation.

Our goal was to identify an approach that would result in minimal error while maintaining a processing rate of 20 fps. The combined use of the probabilistic Hough Transform line detector, Gabor directional filter, Shi-Tomasi needle tip detector, and Lucas Kanade optical flow tracker required a mean processing time of 41.4 ms, with the maximum time unlikely to exceed 52.9 ms. Meanwhile, error distances were still reasonably low: the insertion angle errors were around 1° while needle tip extraction errors were <1 mm.

Table 2.11: Summary of needle segmentation, detection, and tracking algorithms.

Algorithm	Software	Mean Error	SD of Error	Avg Run Time (ms)	SD of Time(ms)
Line Segmentation					
<i>Manual Detection</i>	<i>Manual</i>	<i>0.8°</i>	<i>0.2°</i>	<i>n/a</i>	<i>n/a</i>
Hough Transform w/o Gabor Filter	OpenCV	1.2°	0.6°	160	30
Hough Transform w Gabor Filter	OpenCV	1.1°	0.7°	170	30
Probabilistic Hough Transform w/o Gabor Filter	OpenCV	1.2°	0.8°	28	9
Probabilistic Hough Transform w Gabor Filter	OpenCV	1.0°	0.6°	30	10
Canny Line Detector	LabVIEW	1.6°	0.5°	22	8
Hessian Curvilinear Line Detector	LabVIEW	1.7°	0.67°	13	1
Needle Tip Extraction					
<i>Manual Detection</i>	<i>Manual</i>	<i>0.5 mm</i>	<i>0.3 mm</i>	<i>n/a</i>	<i>n/a</i>
Harris Corner Detector	OpenCV	1.2 mm	0.7 mm	6.2	0.8
Shi-Tomasi Corner Detector	OpenCV	1.1 mm	0.6 mm	5	1
Template Matching	LabVIEW	9 mm	6 mm	8	3
Needle Tracking					
Lucas Kanade Sparse Optical Flow	OpenCV	0.9 mm	0.6 mm	2.3	0.5
Horn Schunck Sparse Optical Flow	OpenCV	0.8 mm	0.5 mm	35	9
Brox Dense Optical Flow	LabView	0.6 mm	0.2 mm	400	100

2.5 Summary and Discussion

Key achievements in this Chapter include the following:

1. A second-gen device was developed that addressed critical limitations of the initial prototype. First, additional degrees-of-motion were added that significantly increased the dexterous workspace and better aligned the needle with the vessel. These new degrees-of-motion enabled joint position feedback for kinematic control programming. Second, US imaging was incorporated into the second-gen device that increased visualization of veins up to 3 cm beneath the skin surface. US also provided a magnified, high-resolution image of the vein; confirming blood flow and vessel patency. Using the US image in our control system, we could track the vessel and needle in real-time during the venipuncture. Overall, this work resulted in a journal publication in the *IEEE Transactions on Robotics*¹ and a poster presentation at the *2014 Biomedical Engineering Society Annual Meeting*.
2. A third-gen device was developed to further improve the mechanical design and functionality of the second-gen device. Specifically, the mechanical structure was completely redesigned. The end-effector on the third-gen device combined the needle insertion system and US probe into one compact unit so the needle could remain in the FOV of the US image throughout the venipuncture. Additional degrees-of-motion were also added to the system that allowed the device to reach cannulation sites on the sides of the forearm. Overall, this work resulted in a journal publication in the *IEEE Transactions on Industrial Electronics*³, an oral presentation at the *2015 Biomedical Engineering Society Annual Meeting*, and three publications in preparation^{6,219,220}.
3. A mechanics-based model and simulation was developed to investigate needle tissue interaction during the venipuncture. These tools allowed us to analyze how the vessel moves, deforms, and rolls during the needle insertion, and how different insertion conditions affect these parameters. This work resulted in a conference paper and presentation at the *2015 IEEE/RSJ International Conference on Intelligent Robots and Systems*².

4. Lastly, a range of needle detection and tracking algorithms were developed to improve the localization of the needle tip throughout the venipuncture. These algorithms were evaluated on robotic phantom cannulations to select the optimal routine to incorporate into the device. The results from this work will be submitted for publication in the coming months⁶.

2.5.1 Merits and Pitfalls of Automated Venipuncture

As with any exciting new technology, there are a number of merits and pitfalls to be considered. Some of the advantages of an automated venipuncture device include the potential for improved first-stick success rates, reduced medical injury, and improved clinical work flow. The device was designed to operate across all patient demographics, especially notoriously difficult cases, such as pediatrics, geriatrics, and obese patients. Here, the device could be used as an alternative to common image-assist devices to obtain rapid venous access. As demonstrated in our studies, the robot has the required accuracy and precision to cannulate a wide range of vessels commonly seen in difficult patients, and has the ability to track the insertion site and dynamically adjust the needle pose in real-time. This offers a unique advantage over manual needle insertion, in that the device can manipulate the cannula in smooth, controlled motions, compared to probing motions occasionally seen in manual venipuncture.

However, despite these advantages, there are limitations that need to be considered. Namely, the current complexity of the system may pose a burden to hospitals and clinics. As with any medical device, the more components, actuators, and parts in a system, the harder it becomes to operate and maintain—especially if the device is to be used on a daily basis. To make the unit more compact, we have begun modeling the device using a passive gantry arm to replace the 5-DOF actuated base positioner. The 3-DOF manipulator would still be used to robotically introduce the needle, but reducing the number of actuators in the system would significantly reduce the complexity of the device. Additionally, a hybrid, semi-automated robotic assist device may be a more clinically feasible approach compared to a fully autonomous system. The device would augment and complement the practitioner’s skills, while also alleviating initial psychological fears of using a robotic venipuncture device.

Chapter 3

Development of Blood Diagnostic Devices

The venipuncture device has the ability to locate and robotically cannulate a suitable vein; however, in the case of a blood draw, the clinician still has to manipulate the blood vials, withdraw the sample, and send it to the lab for analysis. Once the analysis is complete, results are returned to the clinician to guide the intervention. This is a highly segmented and logistically complex process, as outlined below^{15,18,261}.

1. *Pre-analytical*

- Submit the order entry
- Gather phlebotomy materials and supplies
- Prepare and label the blood vials
- Perform the venipuncture
- Transport the sample

2. *Analytical (traditionally performed in a centralized lab)*

- Gather instrument reagents and supplies
- Ensure quality assurance
- Perform the analysis
- Record the results

3. *Post-analytical*

- Report the results
- Bill for the test

Unexpected delays can arise in the transport and analysis of the sample which can result in erroneous test results, potentially leading to inappropriate treatment plans^{15,16,20,24,179,180,262,263}.

Complex hematology analyzers are currently used to perform blood analysis, such as the CBC in conjunction with biochemistry and protein assays, in central lab facilities as there is no commercial POC analyzer that can provide a complete diagnostic read out with one sample^{146,204,213,264,265}. **As such, there is an unmet need for devices that combine the breadth and accuracy of lab-based testing with the speed and convenience of POC analyzers.**

The goal of this Chapter is to integrate the robotic venipuncture device with downstream microdevices, to establish a blood diagnostic platform capable of performing cell, chemistry, and protein assays via optical detection schemes. The presented work will specifically focus on developing three important tests for assessing patient health and disease—WBC differential (cell assay), Hgb concentration (protein assay), and Glu concentration (chemistry assay). Numerous studies have indicated that a WBC count in conjunction with Hgb measurement is an effective screen for predicting the CBC^{218,266,267}. Hence, we believe that focusing on these parameters to start, will create a suitable diagnostic platform that can be adapted for more tests in the future.

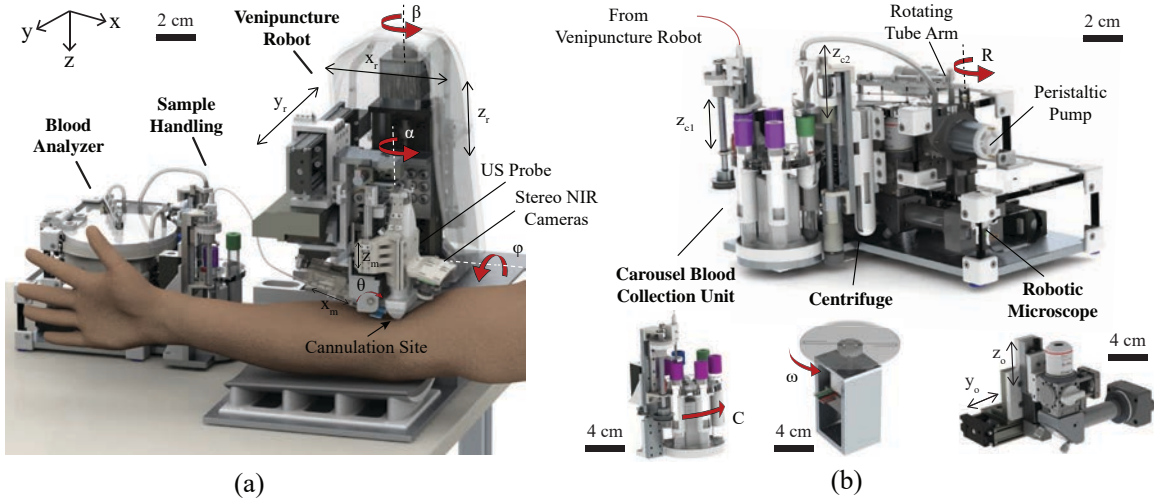


Figure 3.1: (a) CAD rendering of the blood draw and analysis device. (b) Design of the sample handling module integrated with the blood analyzer unit.

This Chapter is segmented into four main sections: (1) the development of a sample handling module to transfer the blood sample from the venipuncture robot to the diagnostic device (Section 3.1), (2) the development of a static WBC-counting device based on fluorescence microscopy (Section 3.2), (3) the development of a photometry module based on optical absorption (Section 3.3) and (4) the development of a centrifuge blood analyzer (Section 3.4). Combined with the venipuncture robot, the integrated device (as seen in Fig. 3.1) is capable of automating the blood draw and analysis.

3.1 Sample Handling Module

The first step in linking the venipuncture robot with a diagnostic device involved designing a method to transfer the extracted sample. A range of ideas were considered including a peristaltic pump and reservoir design (Section 3.1.1), Vacutainer tube storage and robotic syringe pump design (Section 3.1.2), Vacutainer tube storage and peristaltic pump design (Section 3.1.3), and tube switching pump design (Section 3.1.4).

3.1.1 First-generation Design

The first-gen design was based on a two-step pumping method, in which the sample is first driven from the patient's vein to a reservoir open to atmospheric pressure, and then further pumped to the diagnostic device. Specifically, the idea was to replace standard Vacutainer blood collection tubes with a peristaltic pump in conjunction with a microcontroller to modulate the flow rate.

Here, the peristaltic pump would first draw 2 ml of blood from the vein into the reservoir at 2–5 ml/min in the negative direction. Once sufficient volume is drawn, the inlet tube would be closed by a solenoid valve to prevent back flow. Then, the peristaltic pump would induce a positive pressure to transfer fluids from the reservoir to the diagnostic device at a flow rate of 150 μ l/min. In this fashion, 200 μ l of the collected blood sample would be transferred. During this process, the microcontroller would serve as a watchdog, monitoring flow rates, pressures, and sample throughput. Before and after each use, saline buffer would be pumped through the system to remove contaminants, after which the detection microdevice would be disposed.

While in theory this idea sounds feasible, it posed several implementation challenges. First, this design did not take into account how the venipuncture needle tubing would interface with the pumping mechanism. The needle, and its associated tubing, is meant to be disposed after the procedure. Therefore, there needed to be a way for the back-end of the needle tubing to easily connect to the front-end of the peristaltic pump. At the same time, there needed to be a convenient way of flushing the tubing with a wash fluid after the procedure—a non-intuitive process with this design. Second, the open reservoir concept

would have to be cleaned or replaced after each procedure, complicating the protocol from a work-flow standpoint. Finally, this concept lacked a method to interface the back-end of the peristaltic pump with the microdevice in the diagnostic unit to deliver the sample. For these reasons, we designed a new system that utilized a similar two-step approach, but used a Vacutainer tube as the reservoir and replaced the peristaltic pump with a syringe pump.

3.1.2 Second-generation Design and Prototype

For the second-gen design, the sample handling module consisted of two units—a blood collection carousel that housed the Vacutainer tubes and a syringe pump to transfer the sample from one of the tubes to the diagnostic unit. The idea was to design modular components that could be reconfigurable based on the needs of the clinical environment. As an example, the blood collection carousel could be used with the venipuncture robot, even without the diagnostics on the back-end. The device can collect samples in the Vacutainer tubes in an automated fashion and interface with standard butterfly needles.

Moreover, the blood collection carousel could even be used as a standalone device in manual phlebotomy; collecting samples, organizing the vials, and freeing up the hands of the clinician. In the case of central lab testing, the vials can then be packaged and sent to the testing facility. Whereas if the sample were to be tested on the diagnostic device at the POC, the syringe pump could automatically transfer the sample. Even in cases of using the POC analyzer, having the capacity to extract and store extra vials of blood in the collection carousel is a nice feature, considering there may be more esoteric tests that can only be performed in a centralized facility. In the following sections, both the collection carousel and syringe pump are described in detail.

3.1.2.1 Blood Collection Carousel

The initial prototype of the blood collection carousel (Fig. 3.2) consisted of a holder tray for eight 5 ml Vacutainer blood vials seated on a rotary stepper motor along with a linear stage, holding the back-end of the needle, positioned perpendicular to the floor.

Following the venipuncture, the linear stage lowers and pierces the first Vacutainer tube, breaking the vacuum and drawing the appropriate amount of blood. Vacutainer tubes are



Figure 3.2: Prototype of the initial blood collection carousel concept.

manufactured in such a way that allows the internal pressure to only extract the indicated sample volume, in this case 5 ml²⁶⁸. After the vial is full, the linear stage rises, and the carousel rotates to the next vial position. This process then repeats up to eight times (or for as many vials that need to be filled).

The next iteration of the design (Fig. 3.3) focused on miniaturizing the linear motion mechanism and implementing a more stable holder for the back-end of the needle tubing, which pierces the Vacutainer tube. In the previous iteration, the cylindrical cup would often slip from the grips of the holder part, sometimes causing the needle to miss the center of the vial and preventing blood from flowing into the tube. Therefore, there needed to be a better way of stabilizing the needle. To accomplish this, the cylindrical cup was discarded, and instead, an attachment clip was implemented to securely hold the needle in place. Additionally, a custom linear stage was developed using a lead screw design and pulley system to translate the glide nut. The carousel and lead screw were actuated via bipolar stepper motors and controllers capable of high-resolution micro-stepping ($0.028125^\circ/\text{step}$). As in the previous design, the rotary carousel motion utilized a direct drive mechanism to connect the motor axle with the blood vial cartridge.

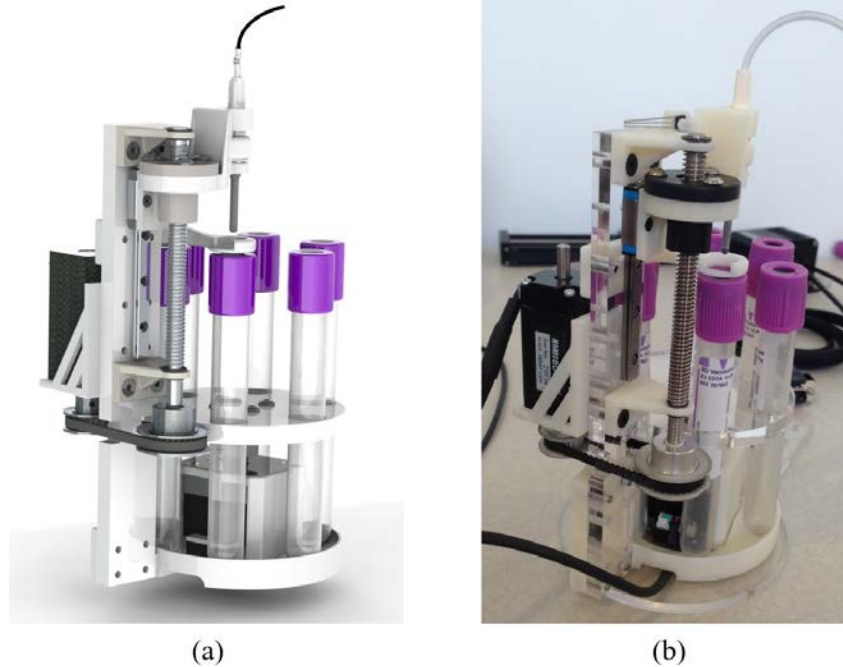


Figure 3.3: (a) Design and (b) prototype of the compact blood collection carousel.

3.1.2.2 Syringe Pump

To then transfer the sample from one of the blood vials to the diagnostic device, a custom syringe pump was designed to interface with the system (Fig. 3.4). The pump was modeled based on a robotic pipette with 2-DOF: vertical and horizontal prismatic motion. Translation in these directions provided a suitable workspace for the pump to travel between the collection carousel and opening of the diagnostic device. In the design, the syringe—10 ml capacity in Fig. 3.4—is a disposable item; the clinician would have to replace this between uses. Furthermore, a right-angle tube connector and syringe needle are also disposable components. Ideally, in a final implementation, the syringe would come packaged with the connector and needle pre-attached.

The syringe was mounted on connectors to ball bearing carriages, parallel to the horizontal translation stage. To actuate the syringe pump, an EM—embedded in one of the ball bearing connectors—activates at two locations along on the linear rails to aspirate and dispense the indicated volume for the diagnostic unit. Steel washers are positioned at these locations for the EM to latch onto. The initial design was further enhanced by replacing the horizontal linear stage with a custom stage using a DC-brushed motor spindle drive

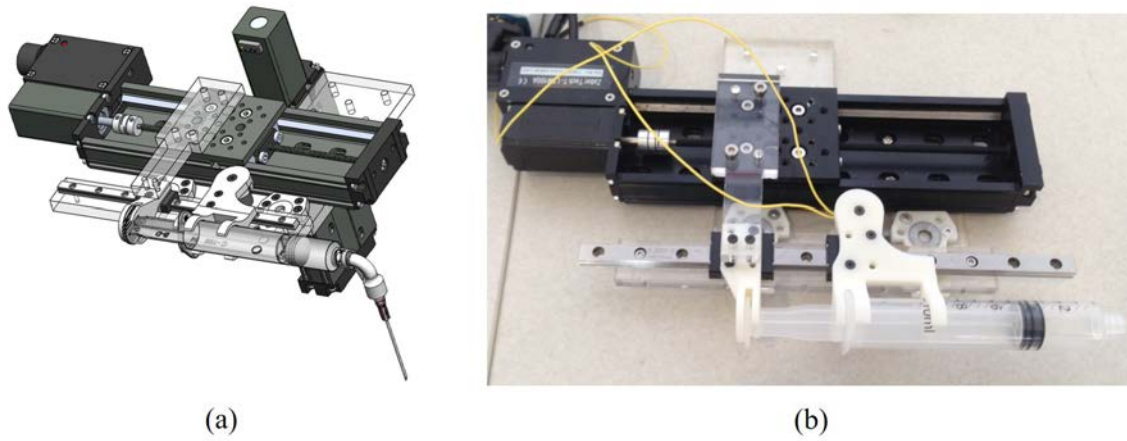


Figure 3.4: (a) Design and (b) prototype of the initial syringe pump.



Figure 3.5: (a) Design and (b) prototype of the miniaturized syringe pump.

(Fig. 3.5). This resulted in a more compact system, though several challenges remained with the syringe pump concept. First, an exposed needle was traversing between the collection carousel and diagnostic device—a distance of around 10 cm. This posed a substantial safety risk, especially considering the syringe pump needle needed to be large enough to pierce the Vacutainer tubes. To accomplish this, we used an 18 G needle. Second, there was a substantial moment arm being placed on the right-angle tube connector piece as the syringe lowered to pierce the blood vial. Several times during preliminary testing of the device, the connector piece snapped, causing the contained liquid to spill. This would pose serious hazards if this were to occur with a blood sample. Third, designing the syringe, connector piece, and needle as disposable components is not a practical solution, both from

a work-flow standpoint and from an economic standpoint. It takes time installing these components on the device, and this may be challenging in time-critical settings. For these reasons, a new concept was designed to replace the syringe pump with a peristaltic pump to reliably transfer the sample to the diagnostic device.

3.1.3 Third-generation Design and Prototype

For the third-gen design, the system again consisted of a two-step approach to deliver the sample to the blood analyzer, as outlined in Fig. 3.6 and 3.7¹. The first phase utilized a similar blood collection carousel, as described in Section 3.1.2.1, to transfer the sample from the venipuncture robot to standard blood vials. The second phase used a peristaltic pump to then deliver the sample to the analyzer unit.

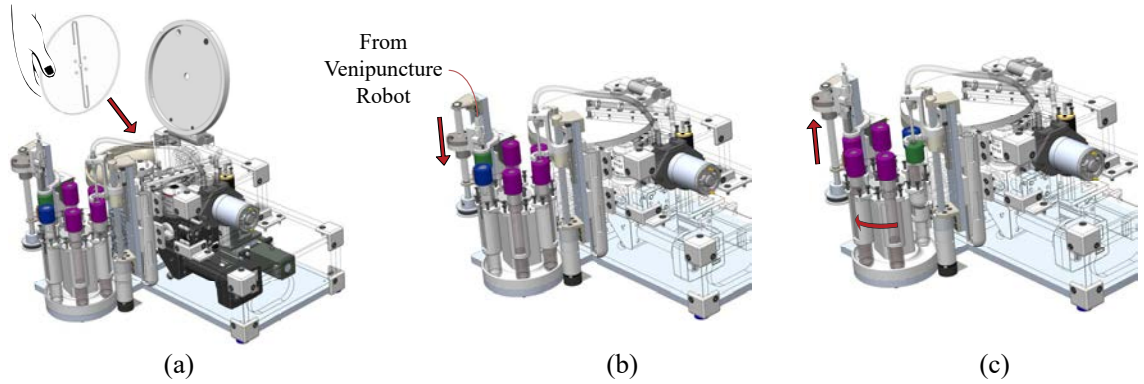


Figure 3.6: Process flow of the sample handling module, steps 1–3. (a) The clinician loads the chip into the analyzer, and closes the lid. (b) After the needle insertion, the z_{c1} -stage lowers the back-end of the needle into the sample collection vial, rapidly filling the tube with blood. (c) The z_{c1} -stage rises and the carousel rotates 60°. At this point, steps a and b are repeated until the green-labeled vial is positioned under the pipette tip (green vial designated for use with our analyzer).

¹Much of the work presented in this section first appeared in: System design and development of a robotic device for automated venipuncture and diagnostic blood cell analysis. Proceedings of the 2016 IEEE/RSJ International Conference on Intelligent Robots and Systems, pp. 514-520⁴. All excerpts represent the original work of Max Balter, whose specific contributions as first author included: designing and conducting the experiments; generating the presented data and corresponding figures; writing, editing, and revising the original text; and addressing reviewers' comments as corresponding author of the original manuscript submission.

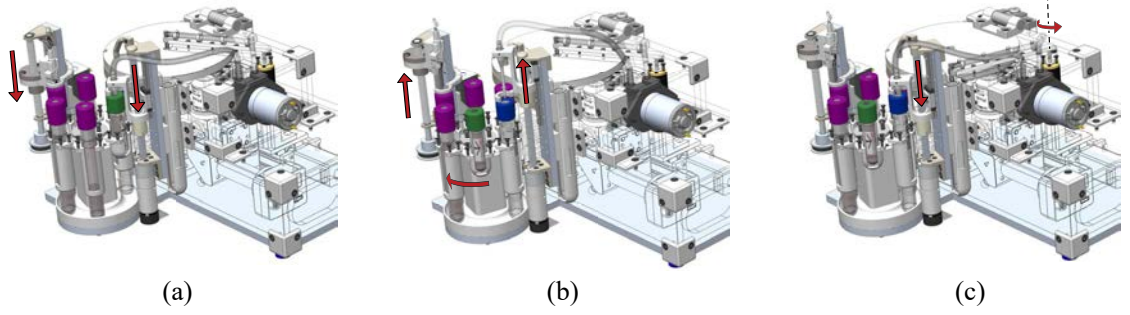


Figure 3.7: Process flow of the sample handling module, steps 4–6. (a) The z_{c2} -stage lowers the pipette tip into the green vial, and the peristaltic pump delivers the sample to the microfluidic chip. (b) Both the z_{c1} and z_{c2} -stage rise, and the carousel rotates 60° . (c) The back-end of the pump tubing rotates over to the waste container, the z_{c2} stage lowers into the saline solution vial stored in the carousel, and wash fluid is pumped through the tubing and into the waste bin.

3.1.3.1 Integrated Blood Collection Carousel

As previously described, the blood draw is controlled via vacuum pressure contained in standard Vactuaainer tubes interfacing with blood collection sets. Before the procedure, the clinician first loads the chip in the analyzer unit (Fig. 3.6a). After the needle insertion, a linear stage (denoted as z_{c1} in Fig. 3.1) connects the back-end of the needle to a blood collection vial (Fig. 3.6b). This causes the needle to pierce the rubber stopper on the Vactuaainer tube, breaking the vacuum and allowing blood to rapidly flow into the vial. Once 4 ml of blood is collected (as confirmed by a compact 780 nm laser diode and photodetector), the z_{c1} -stage rises and the carousel rotates to the next vial (Fig. 3.6c). This process repeats until the requested number of tubes have been filled (Fig. 3.6b–c), at which point the needle is withdrawn from the patient. In total, there are six slots in the carousel—four for standard blood vials (purple caps), one for a custom vial designed for use with our blood analyzer (green cap), and one for a saline wash fluid (blue cap) to clean the peristaltic pump between uses. The standard blood vials are included to allow sample collection for traditional laboratory analysis in addition to on-board measurements by the analyzer.

3.1.3.2 Peristaltic Fluid Delivery

The sample then gets delivered to the analyzer unit via a peristaltic pump. Here, a linear spindle drive (z_{c2}) lowers a metal pipette tip into the green-capped blood vial, the pump is

activated, and approximately 200 μl of sample is aspirated (Fig. 3.7a). The other end of the tubing is attached to a motorized rotating arm (denoted as R in Fig. 3.1) that positions the outlet over the microfluidic chip. Once the sample is delivered, the z_{c1} and z_{c2} stages rise, and the carousel rotates 60° to align the wash container with the metal pipette (Fig. 3.7b). The tubing outlet then rotates over to the waste container on the side of the device, the z_{c2} stage lowers into the saline solution vial, and wash fluid is pumped through the tubing to clean the system (Fig. 3.7c). The spindle drive and rotating tube arm are actuated via DC-brushed motors and position controllers (EPOS 24/2, 390438, Maxon Precision Motors, Inc.). Conversely, the DC-brushed motor driving the peristaltic pump is controlled using a transistor circuit and timing conditions in the software, resulting in a constant flow rate of 12.5 ml/min at a 5 V input. The remaining blood can be stored in standard vials in the event that assays not currently performed on the analyzer are needed, or if the clinician decides that tests should be repeated to achieve a more reliable diagnosis.

3.1.3.3 System Evaluation

For the first set of experiments, we evaluated sample collection time in Vacutainer tubes. Similar blood vessel phantoms as previously described were used for experimental testing. In these trials, collection time was recorded over four variables—needle size, vein diameter, fluid viscosity, and flow rate—all consisting of three levels. A fractional factorial experimental design was implemented (4-variable, 3-level L9 orthogonal array²⁶⁹) to evaluate the effects of these variables on sample collection time. In total, 9 trials were conducted in triplicate, as outlined in Table 3.1.

3.1.3.3.1 Experimental Protocol

After cannulating the phantom vessel, synchronized motions of z_{c1} and C of the blood collection carousel were used to dispense fluid into the Vacutainer tubes (Fig. 3.8a). These vials are evacuated and sealed with a rubber cap, enabling the vacuum to pull the indicated sample volume; in our case, 4 ml. The NIR sensor located on the carousel pump monitored tube volume levels throughout the experiments, allowing us to measure the time needed to fill the tubes.

Table 3.1: Experimental design used to evaluate sample collection time in blood tubes.

Parameter	Levels		
Needle size (G)	21	23	25
Vein OD (mm)	2	3	4.5
Viscosity (%)	35	45	55
Flow (ml/min)	35	45	55

3.1.3.3.2 Results

Analyzing the effect plots in Fig. 3.8b, the fill time increased with increasing fluid viscosities, suggesting that this parameter could potentially be used as an indicator of blood hematocrit and could also be used to tell the y_o -stage on the microscope how far to translate to locate the buffy coat. At 35% glycerol concentration, it took 32.6 sec to fill the collection tubes, whereas for 55% concentration it took 70.9 sec.

Needle size affected sample collection time as well (24.2 versus 79.1 sec for 21 and 25 G needles respectively) with smaller gauge cannulas constricting fluid flow. This implies that smaller gauge needles should only be used when low sample volumes (i.e., <1 ml) are needed; otherwise the cannula risks being dislodged from the vessel due to the long time required for sample collection. Conversely, vein diameter and flow rate had minimal effect on collection time, possibly indicating that collection times may be similar among people with varying blood pressure levels. Finally, once the solution was collected, the peristaltic pump delivered 200 μ l of sample to the microfluidic chip.

3.1.4 Fourth-generation Design and Prototype

Despite the success of the third-gen sample handling module, there were several practical limitations that became apparent during experimental testing. Namely, the system may have been overly complex for the task at-hand. The primary goal of the module is to transfer the extracted blood sample from the venipuncture robot to the downstream diagnostic device. Implementing a two-stage pumping mechanism—using blood vials as a storage reservoir and then a peristaltic pump—may have been unnecessary, especially considering the integrated device is intended to be a portable, POC unit. In this case, the collection

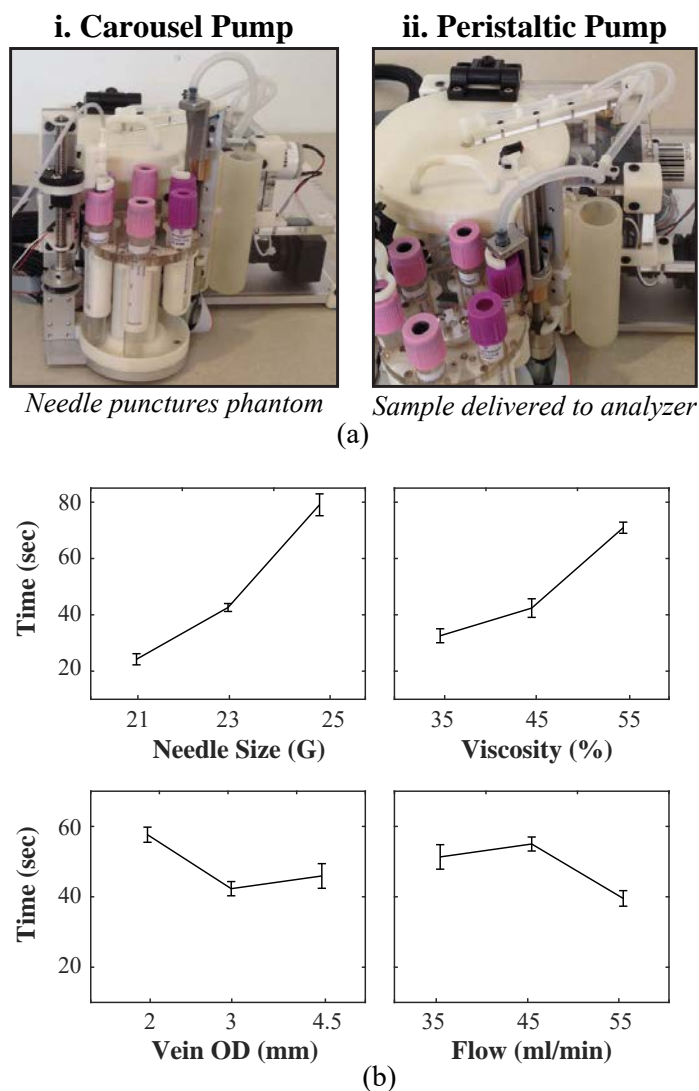


Figure 3.8: Evaluation of the collection carousel and peristaltic pump. (a) Experimental setup of the sample collection study, highlighting the i. carousel pump and ii. peristaltic pump. (b) Effect plots for fractional factorial experimental design, showing sample collection times for each variable and parameter. Data shown as mean \pm standard deviation for each level ($n=3$).

carousel holding the blood vials, could be removed from the sample handling module to bypass that intermediary step. Instead, the blood sample could be pumped directly onto the blood analysis chip using any form of pumping mechanism (e.g., peristaltic, diaphragm, or syringe pump). Not only would this simplify the system, but it would also allow the device to extract blood samples at controlled flow rates and expedite the process from blood draw to analysis.

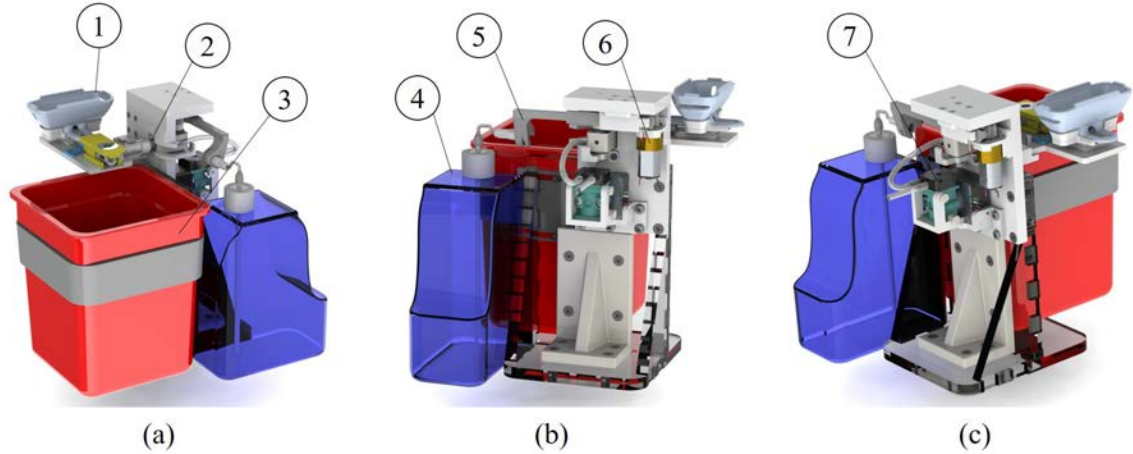


Figure 3.9: Tube switching pump design. (a) Front view, highlighting the: 1. consumables cartridge, 2. butterfly needle tube connector interface, and 3. sharps container. (b) Back-view, highlighting the: 4. saline wash fluid container, 5. wash fluid connector rack, and 6. DC gearmotor to actuate the rack and pinion mechanism. (c) Side-view, highlighting the: 7. peristaltic pump mounted to the back of the unit.

With this in mind, we designed a novel tube switching pump mechanism that utilized a micro-peristaltic pump to deliver blood samples to the diagnostic chip and clean the tubing with a saline wash fluid. Furthermore, this concept was integrated with the automated consumables handling design described in Section 2.3.1.6.2. As seen in Fig. 3.9, the design consists of a base platform which contains the tube switching mechanism, sharps container, and saline wash fluid bottle. At the start of the procedure, the disposable cartridge—containing the butterfly needle and associated clip plus the US gel clip—is loaded into the slot at the front of the module. Once loaded, the back-end of the needle tubing automatically connects to the tube switching mechanism via a press-fit latch in the design. After the venipuncture robot grabs the consumables and performs the needle insertion, the peristaltic pump activates to transfer the blood sample to the fluid dispenser for delivery to the analysis chip. Next, the needle is removed from the patient’s forearm and the robot rotates over to the sharps container in the sample handling module. At this point, the needle and US gel clip are released from the venipuncture device and disposed into the sharps container. At the same time, the DC gearmotor on the tube switching mechanism rotates the needle tubing over a guide rail to release the tube connector from the press-fit, and into the sharps bin. This simultaneously translates a linear rack holding another tube connector interfacing

with the wash fluid container. Altogether, this allows the sample handling module to dispose the contaminated components (i.e., the needle and gel clip), organize the tubing connected to the back-end of the needle, and prepare for the wash step.

Once the rack translates enough so the wash fluid connector is firmly pressed into the tube switching piece, the peristaltic pump activates again, this time, flushing the tubing with saline fluid. The dispenser on the back side of the pump rotates over to a waste fluid container to dispense this fluid appropriately. During this step, the diagnostic device can begin analyzing the blood sample, and the venipuncture device can prepare for the next patient.

3.1.4.1 Design Improvements

After prototyping this concept, it proved difficult to actuate the two degrees-of-motion using a single gearmotor. What's more, since the motor position was being controlled by timing conditions in the software, it was difficult to align the wash fluid connector with the tube switching piece. Oftentimes during testing, the rack would jam against the side of the tube switching piece since the horizontal alignment was slightly off. Consequently, the motor would stall and the mechanism failed to work. Furthermore, after the rack rotated the tube switching piece, it was free to continue rotating, as nothing was there to hold it in place. This resulted in alignment problems as well. In order to resolve this issue, either extra teeth needed to be added to the rack to couple the linear and rotational motions throughout the mechanism, or the tube switching piece needed to be robustly held in position. The first idea was challenging to implement, because the tube switching piece needed to rotate 90° before the rack pressed in the wash fluid connector. This entailed first rotating the tube switching piece and then halting the motion once it reached 90° (i.e., removing gear teeth at the end of the rack). Hence, adding more teeth to the rack was not a practical solution.

On the other hand, a second gearmotor could be added to the design to rotate the tube switching piece, and further hold it in place. With this in mind, components were modified and prototyped, and used to build the final assembly, as seen in Fig. 3.10. Using timing controls in the software, the tube switching piece first rotates 90°, followed by the rack translating the wash fluid connector to be pressed into the tube switching piece. To return

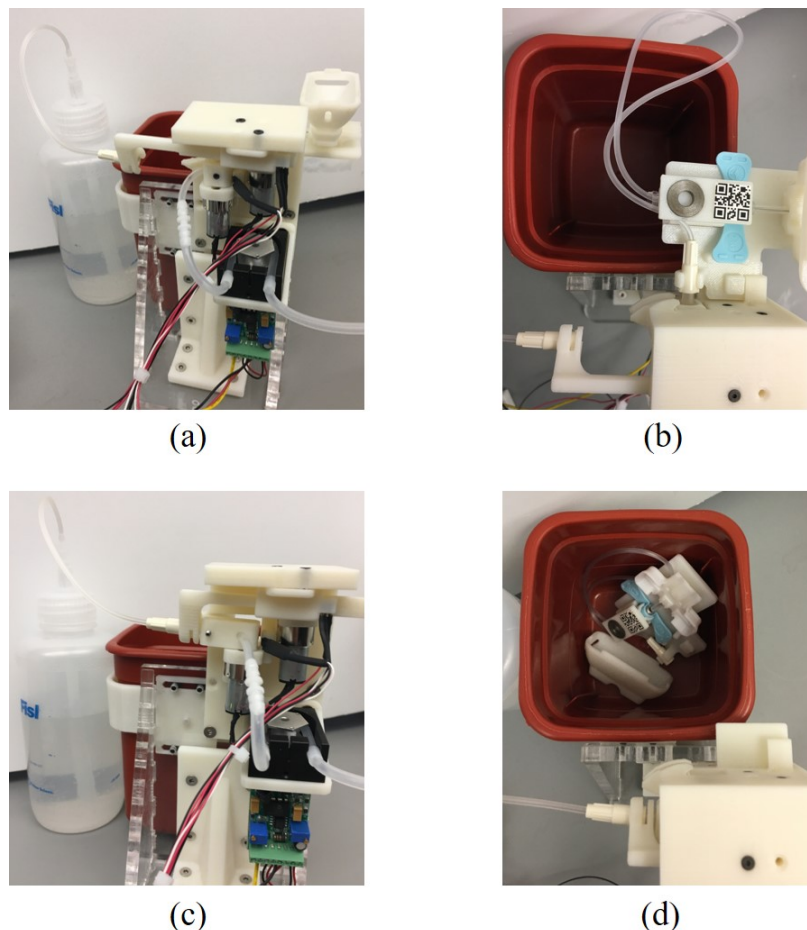


Figure 3.10: Redesign of tube switching pump. (a) Butterfly needle hub connected to the pump via the tube switching piece. (b) Consumables handling for the venipuncture robot, as discussed in Section 2.3.1.6.2. (c) Tube switching piece rotates 90°, and the rack translates to attach the wash fluid connector. Wash fluid can then be pumped through the system using the peristaltic pump (in this design, P625/275.133, Instech Laboratories, Inc.) (d). Consumables disposed in sharps container after procedure.

to the home position, the motions are reversed. Overall, this redesign proved to be reliable, robust, and ready for more rigorous testing.

3.1.4.2 Sample Dispenser Unit

The sample dispenser functions to deliver the blood sample to the analysis chip and aspirate separated fluids and analytes of interest (e.g., blood plasma after centrifugation). The design, as seen in Fig. 3.11, consists of a rotating tube arm, which serves as the main support structure, and a mechanism to lower and raise the dispenser nozzle over the inlet and

outlet holes of the analysis chip. Specifically, a Scotch-yoke mechanism was implemented to convert the rotational motion from the DC gearmotor into linear, vertical motion. This was achieved with a pin wheel that rotated inside a horizontal slot to restrict its motion. Consequently, this caused the dispenser nozzle to translate in the vertical direction. A linear rail and carriage assembly was used to guide this vertical motion, and the dispenser nozzle was locked in place using a press-fit clamp as seen in Fig. 3.11b.

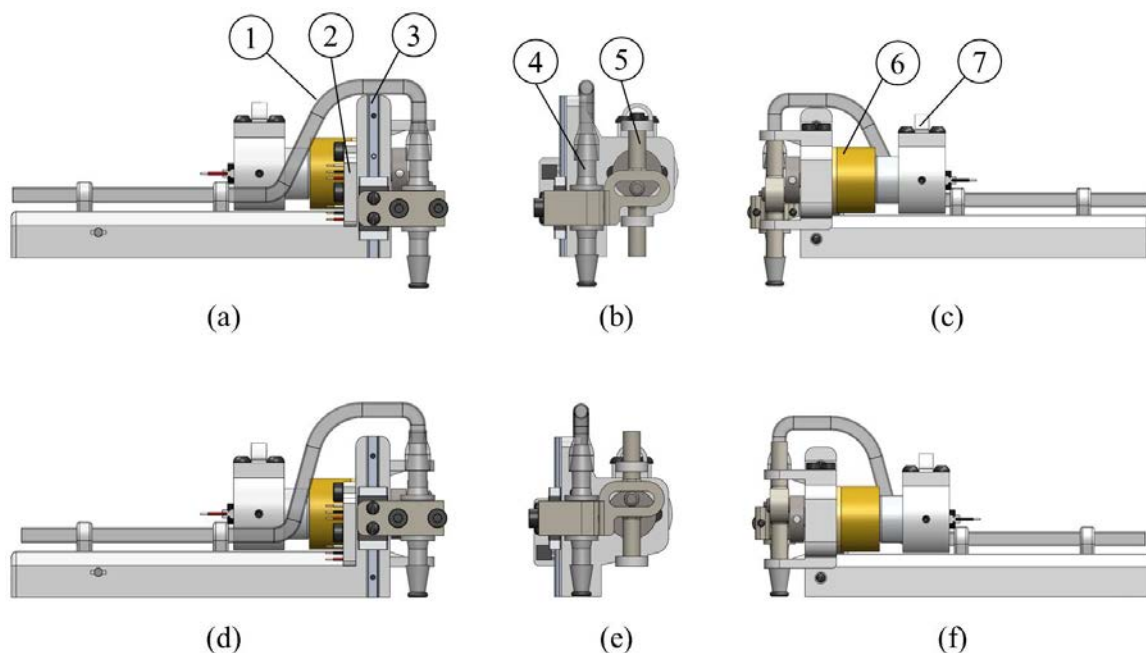


Figure 3.11: Dispenser design—(a–c) when nozzle is lowered and (d–f) when nozzle is raised. (a) Right view, highlighting the: 1. tube leading from the peristaltic pump to the dispenser nozzle; 2. hall-effect homing sensors used to indicate when the dispenser has reached one of two states: raised or lowered; and 3. the linear rail and corresponding carriage used to guide the vertical motion of the nozzle. (b) Front view, highlighting the: 4. plastic nozzle with an O-ring attached to the bottom to achieve a leak-proof seal; and 5. Scotch-yoke mechanism used to convert rotational motion into linear translation. (c) Left view, highlighting the: 6. DC gearmotor to actuate the Scotch-yoke mechanism; and 7. a strain relief for the sensor and motor wires.

Two magnetic-based Hall-effect position sensors were installed behind the linear carriage, and a small magnet was embedded in the dispenser clamp. Together, this formed the hardware of the position control scheme used to lower and raise the dispenser nozzle. Two, discrete system states were programmed into the control software: nozzle raised and nozzle lowered. The gearmotor was programmed to activate until the desired sensor was triggered,

indicating the nozzle has reached the desired position. Utilizing a Scotch-yoke mechanism in this subsystem, the gearmotor only needs to rotate in one direction to achieve either the raised or lowered nozzle state, simplifying the control electronics and programming. The prototyped dispenser unit is shown in Fig. 3.12, with the main components 3D-printed—including the base support structure, sensor mounts, and Scotch-yoke mechanism.

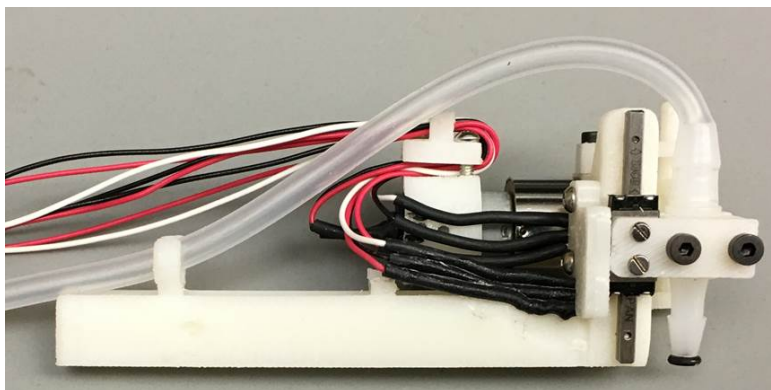


Figure 3.12: Dispenser pump prototype (removed from the diagnostic device).

Overall this mechanism allows the nozzle to translate 5 mm—sufficient for firmly pressing against the blood analysis chip and for clearing the top surface of the diagnostic device as the dispenser rotates to the chip inlet and waste container. As described in Section 3.1.3, the dispenser rotates approximately 60° from the home position (by the waste container) to deliver the blood sample to the analysis chip.

3.2 Static WBC Counting Device

The first approach for WBC counting utilized fluorescent labeling of cells, imaging with a custom microscope, and image processing techniques to segment and enumerate cells. To classify WBC sub-types, features were extracted in the segmentation step and correlated with known physical properties of sub-types (Tab. 3.2).

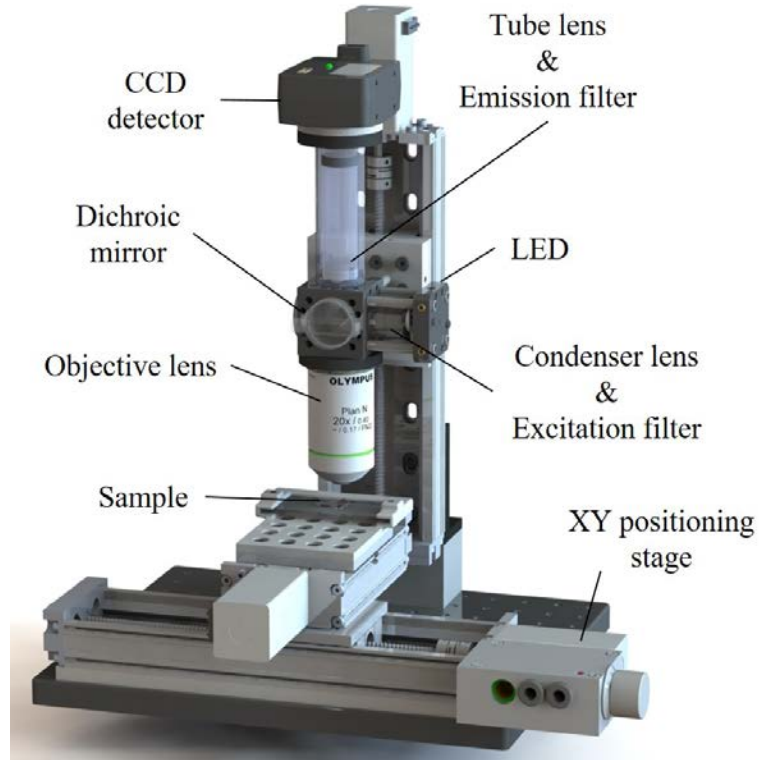
3.2.1 First-generation Microscope Design

The premise of the optical detection system stemmed from the design of a fluorescence microendoscope developed in Dr. Pierce’s lab and validated in numerous *in vitro* and *in vivo* studies^{270,271}. The system enables high-resolution (2 μm), longitudinal imaging *in situ*

Table 3.2: Summary of the physical properties of WBC sub-types²⁰⁵.

Cell type	Concentration (cells/ml)	Diameter(μm)	Volume (μm^3)
WBCs	$0.4\text{--}1.1 \times 10^7$	8–15	160–450
<i>Lymphocytes</i>	$1\text{--}4.8 \times 10^6$	8–15	161–207
<i>Monocytes</i>	$1\text{--}8 \times 10^5$	12–15	382–449
<i>Neutrophils</i>	$2\text{--}6 \times 10^6$	10–12	268–333
<i>Eosinophils</i>	$0.4\text{--}4.8 \times 10^5$	10–12	268–382
<i>Basophils</i>	$0\text{--}1.1 \times 10^5$	12–15	239–321

for a plethora of microscopy applications, ranging from cell culture to protein bio-marker imaging. Designed for use with several fluorescent contrast agents, this microscope can be adapted for multiplexing applications in microfluidic chip sets by incorporating additional light channels, filters, and sensors.

**Figure 3.13:** Design of the single channel miniaturized optical detection system.

Using the optomechanical concept presented in Pierce et al.²⁷⁰, a single channel microscope was designed and built that measures $8 \times 6 \times 6$ cm (Fig. 3.13) for use with 475 ± 35 nm excitation and 500 ± 35 nm emission fluorophores—referred to as the first-gen microscope. Outlined in Fig. 3.13, the components of the microscope, include a high-powered blue LED

(465–485 nm), excitation (475 ± 35 nm) and emission (500 nm long pass) filters, lenses, a dichroic mirror (506 nm) and a CCD sensor (Firefly MV, FMVU-03MTM-CS, Point Grey Research Inc.) All lens and optomechanical components were sourced from Thorlabs Inc.

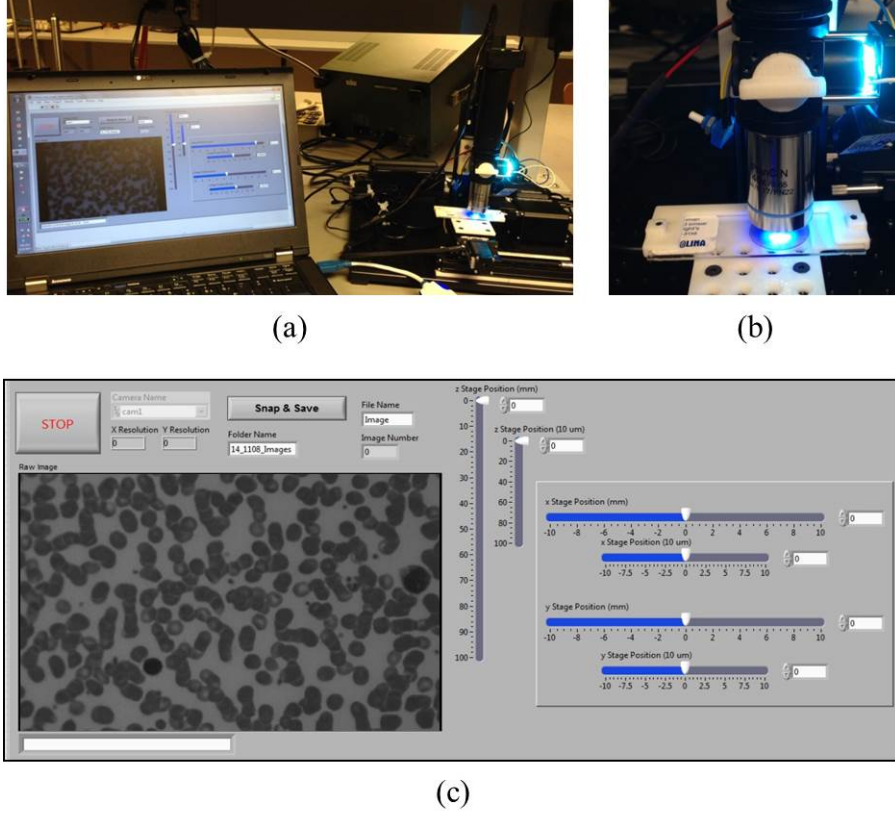


Figure 3.14: Prototype and LabVIEW GUI of the single channel microscope.

The custom-built microscope is displayed in Fig. 3.14 along with the corresponding LabVIEW GUI used to control the motorized linear stages for image focusing and raster scanning the sample, as well the captured image from the camera. Using a 40x objective lens in combination with a 4.5 mm focal length tube lens, the resulting magnification was 22.2x (see Eq. 3.1) with a FOV of 1 mm in the image (see Eq. 3.2).

$$\text{Magnification} = \frac{f_{\text{tube lens}}}{f_{\text{objective lens}}} = \frac{100 \text{ mm}}{4.5 \text{ mm}} = 22.2x \quad (3.1)$$

$$\text{FOV} = \frac{\text{Field Number}}{\text{Magnification}} = \frac{22}{22.2} = 1 \text{ mm} \quad (3.2)$$

The modular design of the microscope allowed it to be adaptable to the contrast agents used for specific blood assays. Additional light channels can be incorporated by adding the corresponding LEDs and filters to test for other fluorochromes.

3.2.2 Sample Labeling & Detection Chip Design

Traditionally, WBC differential counts are performed via flow cytometry, where fluorophore-conjugated antibodies or fluorochrome dye stains are introduced into the assay. This preparation step is typically performed manually and is laborious as well as time consuming. One method to eliminate manual labeling is to store the reagents in dry format on-chip. Using this approach, reagents are rehydrated when the sample enters the reaction chamber, and the labeling step is carried out automatically²⁷².

To accomplish this, the proper amount of RBC lysing agent and nuclear dyes could be stored on-chip to lyse the RBCs and label the WBCs in one step. For the lysing agent, sodium deoxycholate was proposed, which has been shown to be superior in lysing >98% of RBCs while not significantly affecting the WBCs²⁷³. Then, to directly stain the WBCs, a mixture of nuclear dyes could be used, such as fluorescein isothiocyanate (FITC), basic orange 21 (BO21), methylene blue, and propidium iodide.

Using these nuclear dyes, it is then possible to differentiate lymphocytes, monocytes, neutrophils, eosinophils, and basophils based on their respective nuclear content. Previous studies utilizing this technique, have demonstrated highly selective discrimination and strong correlation to bench-top measurements^{209,274,275}. Leukocytes in the detection zone on-chip would then be excited by a dispersed LED, and the fluorescent emission from the cells would pass through a long pass filter to remove residual emission light, before reaching the camera. The relative intensities of each leukocyte from the stains, in addition to the geometrical morphology, can then be used to delineate leukocyte sub-types.

The initial detection device (Fig. 3.15) consisted of a main inlet channel, a bifurcation to partition the sample, and two reservoirs to store dry reagents. After the blood sample is pumped through the channel and reaches the reaction chambers, the sample is ready for imaging.

To fabricate the detection chip, various techniques were investigated. First, chips were

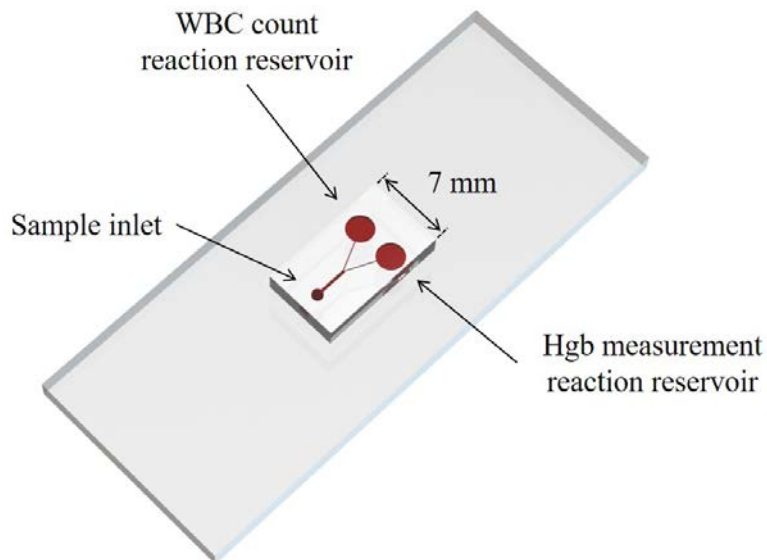


Figure 3.15: CAD rendering of the detection chip illustrating the single inlet, channel bifurcation, and dual detection zones for WBC enumeration and Hgb concentration measurement. Dry reagents stored in the detection zones; reactions occur when blood enters these reservoirs.

3D-printed using a clear resin material. Since channel dimensions were on the $100\ \mu\text{m}$ scale, 3D-printing was sufficient in creating the desired features. However, the resin material was not fully transparent, which presented issues when imaging the chip with the fluorescent microscope. Second, chips were fabricated using a laser-cut acrylic and bonded together using an adhesive. This technique was successful in producing a chip that was fully transparent, and thus capable of working with the microscope. However, as will be discussed in later sections, there were numerous challenges with imaging, counting, and classifying static WBCs. Consequently, a new chip was designed and a new cell counting methodology was implemented in later generations of the diagnostic device.

3.2.3 WBC Segmentation & Subtype Classification

After obtaining WBC images, the next step was to process them via segmentation and feature extraction techniques to enumerate and classify sub-types. For classification, it is crucial to both consistently stain the sample with the optimal reagent concentrations, and properly illuminate the sample to gather consistent images. The processing algorithms highly depend on image quality. Though software can be developed to compensate for

fluctuations in illumination and image quality, it is much easier to segment and analyze cellular features on high SNR images.

3.2.3.1 Background

Segmentation of leukocytes in blood smear images is a well known method used to differentiate sub-types based on the unique geometrical morphology inherent in each sub-class. This technique has been around since the 1900's, when scientists first discovered that WBCs could be segregated based on nuclear stains as well as granule size and distribution in blood smears²⁷⁶. However, to manually image the sample and differentiate each WBC is a tedious and time-consuming process prone to human error.

Oftentimes, the ability to classify leukocytes is a subjective process that depends on the clinician's skill and experience. Even then, it can be difficult to manually recognize one WBC sub-type from another based on subtle color and geometrical differences. Additionally, cell identification metrics are often slightly different among clinicians, resulting in unreproducible counts. Consequently, an automated differential blood counting system that is standardized, repeatable, and consistent over a range of blood samples would result in more accurate counts in less time, compared to traditional manual microscopic analysis.

Even today with faster computer processing, WBC segmentation and classification remains a challenging research problem. The initial WBC segmentation step is critical, because the subsequent feature extraction and sub-type classification heavily depend on a correct segmentation. Several aspects make leukocyte segmentation difficult. Namely, the five WBC sub-types cover a broad range of sizes and geometries that impede segmenting these cells reliably. Specifically, lymphocytes can be as small as 8 μm , while basophils can be as large as 15 μm , and each sub-type also has different amounts of granules. Though these features help in the classification of each sub-type, they can cause problems during segmentation. As alluded to earlier, illumination and staining can also effect the segmentation from uneven light distribution in the image, making it difficult to discern cell boundaries from the background. Finally, compressed WBCs can appear as blurs with hidden edges, causing segmentation methods to miss some cells, resulting in unreliable counts.

To address these problems, researchers have explored numerous filtering, edge detection, feature matching, and binarization techniques for WBC segmentation, all with varied success. Existing approaches are grouped into the following categories: edge-based, contour-based, region-based, and pixel-based segmentation. Edge-based methods extract the cytoplasm and nucleus borders by searching for the largest variations in pixel intensity in the image. Common edge detection algorithms include the Canny edge detector²⁷⁷, and the Teager/Kasier filter²⁷⁸, however both of these schemes alone have trouble segmenting the entire cell/nucleus border. Additionally, they have several parameters that need to be precisely tuned for each image, making them difficult to be robust across different image conditions.

Contour-based approaches iteratively expand a contour/snake from an initial seed point to find the borders of the cytoplasm and nucleus using level-set techniques^{279–281}. These algorithms are robust against images with overlapping cells; however, it can be challenging to identify the initial seed points, especially in noisy images. Similarly, region-based approaches also utilize initial seed points to grow and find the region borders (i.e., cell and nucleus borders). Specific stop criteria for the region grow formula must be incorporated to allow the region to expand to the appropriate borders without leaking outside the desired ROI. Lastly, pixel-based methods operate by grouping pixels into categories (i.e., cytoplasm, nucleus, background) based on intensity, texture, or color features.

In blood smear images, where the sample is stained and imaged under a bright-field microscope, segmenting cells based on color is a popular technique that takes advantage of the blue and pink color of the WBC nuclei and cytoplasm respectively^{282,283}. However, with CCD sensors that capture color images, the resolution is often compromised compared to monochrome sensors. With this lower resolution, it can be difficult to extract WBC features for sub-type classification.

3.2.3.2 Algorithm Development

Our segmentation method combined a global threshold with morphological operations to initially identify the nuclei of WBCs. Then, centroids of the nuclei were used as seed points to initialize an active snake contour model, as discussed in Nativ et al²⁷⁹. The

active contour algorithm functions to segment both the nucleus and cytoplasm from the background of the image based on the varying pixel intensities of the WBCs. Here, it is important to isolate the WBCs by removing extraneous noise in the image that may have resulted from RBC/PLT fragments. In this fashion, a clean image of the WBC cytoplasm and nucleus can be obtained in order to extract the morphological features necessary for sub-type classification. An overview of the segmentation scheme is summarized in Fig. 3.16.

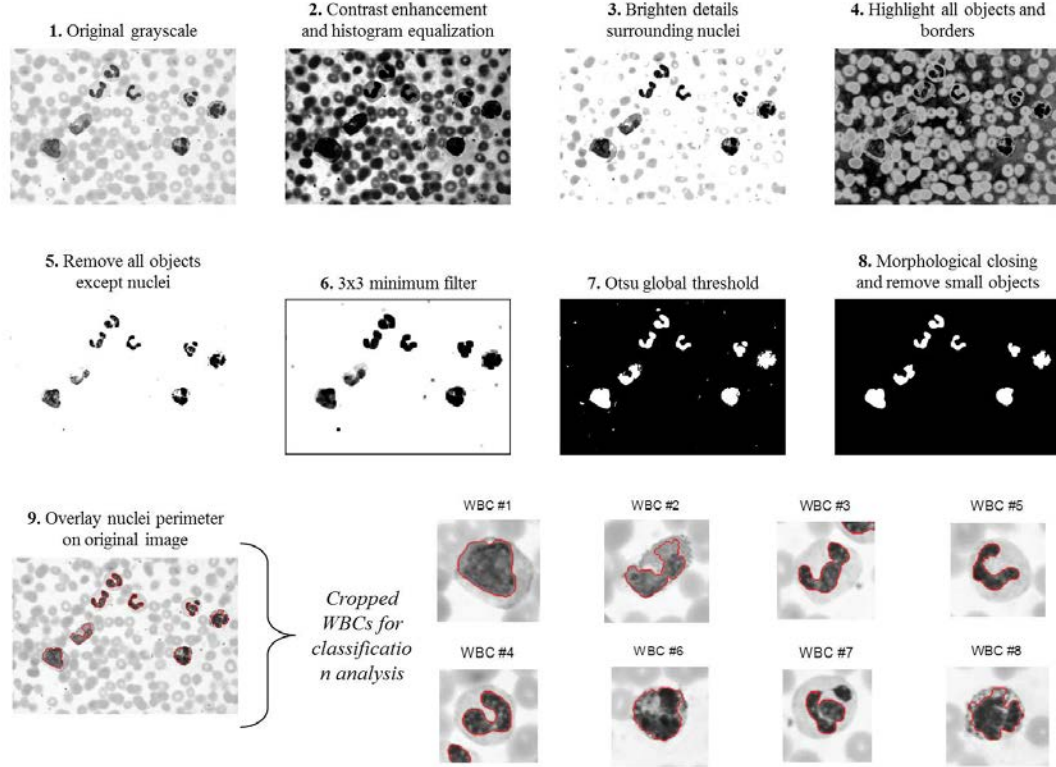


Figure 3.16: Overview of the WBC segmentation scheme: (1) original grayscale image; (2–6) image filtering via built-in MATLAB functions to highlight cell nuclei; (7–8) global thresholding and morphological operations; and (9) overlay of segmented nuclei on original image. Segmented nuclei serve as seed points for sub-type classification using extracted features. Original image obtained from Sangle et al.²⁸⁴; processed images illustrate preliminary results on a blood smear.

In order to visualize and analyze each cell in the detection chip, the sample had to be scanned in a raster-like trajectory. This was accomplished via x and y motorized linear stages as shown in Fig. 3.13 and 3.14. The linear stages were controlled in LabVIEW to scan and capture images at each location. The segmentation algorithms as well as the

subsequent feature extraction and sub-type classification scheme were run in parallel as the microscope scanned the sample.

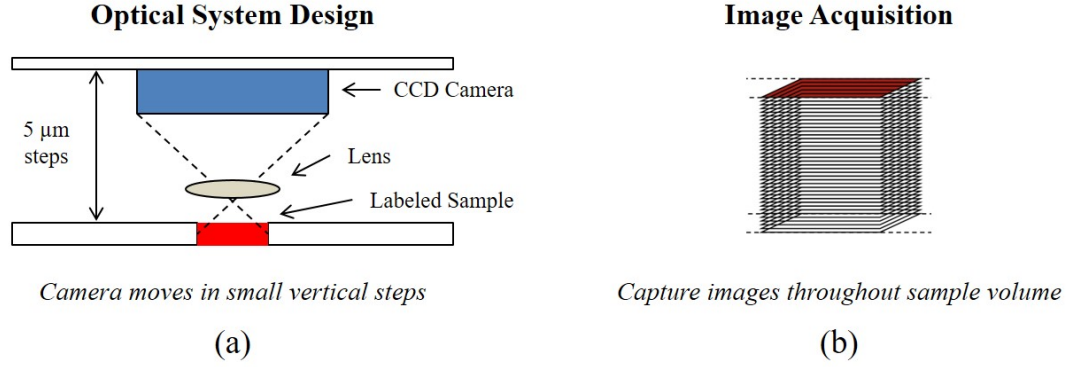


Figure 3.17: (a) Optical system design and (b) microscope image acquisition scheme.

Additionally, since the detection chip was a flat substrate on which the blood sample sat, it was necessary to image the sample at a range of depths to capture all the WBCs in the sample. Even after letting cells settle to the bottom of the substrate, there still may be some that are floating. To compensate for this, the optical detection system was designed to image the sample at various heights. As seen in the microscope design in Fig. 3.13, the vertical linear stage actuated via a stepper motor can precisely focus the camera at various depths. In our case, a step size of 5 μm was used, because WBCs are on average, around 10–15 μm in spherical diameter. Figure 3.17 illustrates the concept of translating the camera in small vertical steps to capture images throughout the sample volume.

3.2.3.3 Classification of WBC Subtypes

As the acquired images are processed and cropped to the WBC ROI, a set of separate 20 morphological features were extracted (e.g., area, perimeter, intensity, texture variance, aspect ratio, convexity, and Euler number) from both the cell and nucleus. This approach takes advantage of the unique geometrical properties of the WBC sub-types inherent in the cytoplasm and nucleus (Fig. 3.18). Principal component analysis (PCA) was then implemented to reduce the morphological data-set into the key differentiating parameters by converging on a linear solution²⁸⁵. The selected data-set was then computed for each sub-type to collect sufficient data for classification. To differentiate sub-types, a K-means

gating method was implemented to cluster the data based on cellular morphology²⁸⁶.

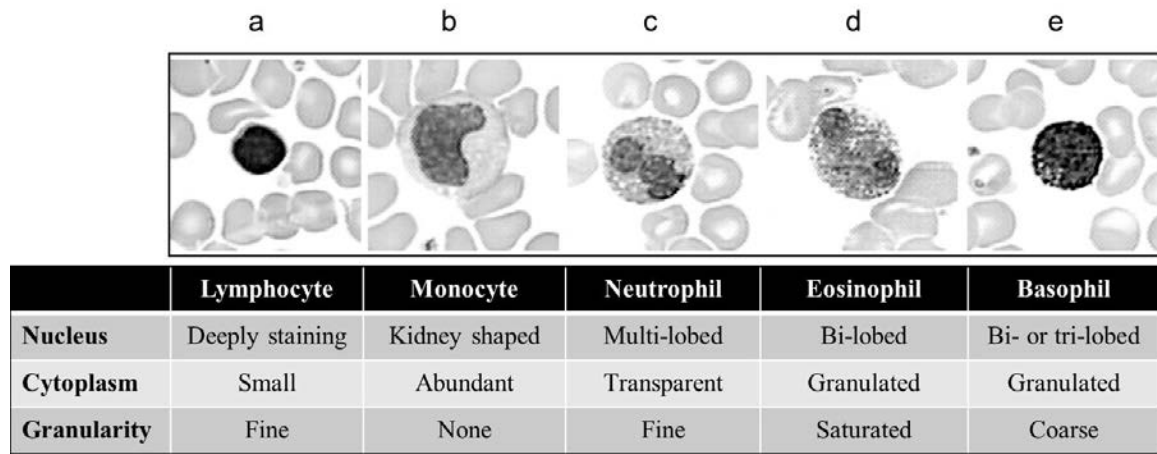


Figure 3.18: Blood smear WBC images obtained from Kovalev et al²⁸⁷.

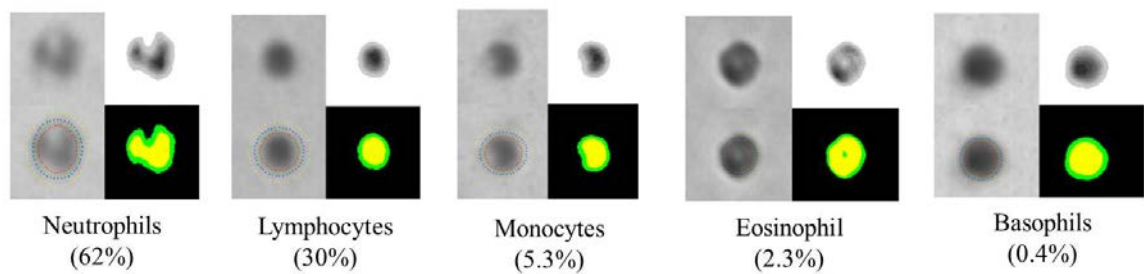


Figure 3.19: WBC feature extraction. Images obtained from Lindberg et al²⁸⁸.

A similar approach is utilized in the HemoCue WBC Diff device in which cell images are acquired under fluorescence and bright-field, then segmented to extract key morphological features for sub-type classification²⁰⁹. Figure 3.19 outlines the various image processing steps used to extract these morphological features. The specific algorithms implemented in the device are unclear, but the company claims that the system is capable of performing a 5-part differential—a challenging task considering the low percentage of basophil and eosinophil sub-types in blood (i.e., approximately 2.5% and 0.5% of the total WBC population respectively). What's more is that the device counts cells using miniscule blood samples (i.e., 10 μ l), meaning there may only be a couple of eosinophils or basophils to even count. If for some reason the image processing routine is unable to extract these sub-types, then the device could report inaccurate cell counts.

3.2.4 Experimental Testing

3.2.4.1 Lab Microscope

To first evaluate the segmentation scheme, bright-field images of WBCs were acquired on an inverted microscope (Olympus IX81) at 40x and 10x magnification, and then the previously described algorithms were run in MATLAB on a separate PC (Intel Core i5-2450M, 2.50 GHz). Porcine blood sample controls (HC WBC Hematology Controls, R&D Systems) were used in conjunction with plastic microcuvettes designed for use with the HemoCue automated WBC counting device. Control samples consisted of three levels—low (3.1×10^3 cells/ μl), normal (7.7×10^3 cells/ μl), and high (21×10^3 cells/ μl). Moreover, the chips contained a RBC lysing agent to prevent these cells from interfering with the absolute WBC count, plus a methylene blue nuclear stain.

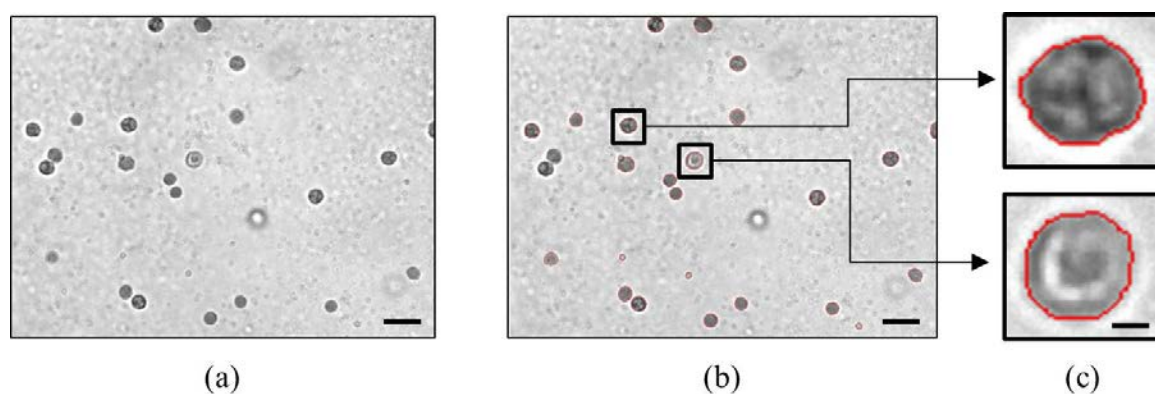


Figure 3.20: WBC segmentation in 40x microscopy images. (a) Original bright-field image of porcine WBCs (7.7×10^3 cells/ μl) imaged in a plastic HemoCue WBC microcuvette. (b) Segmentation results show 21/23 WBCs isolated from the image processing routine. (c) Zoomed-in images of segmented WBCs, highlighting the cell border extraction. Scale bar in (a) and (b) is $30 \mu\text{m}$; scale bar in (c) is $4 \mu\text{m}$.

With this approach, the segmentation routine was evaluated on clean, robust images, with evenly distributed light throughout the sample. Fig. 3.20 and 3.21 display microscopic images of the blood smears at 40x and 10x respectively, as well as the associated results from the segmentation algorithm. At both magnifications, the algorithm extracted $>90\%$ of WBCs present in the images.

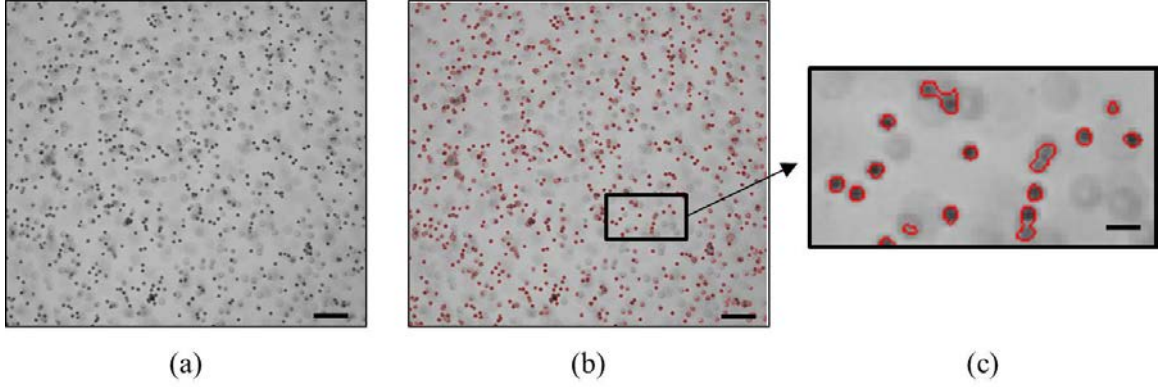


Figure 3.21: WBC segmentation in 10x microscopy images. (a) Original bright-field image of porcine WBCs (21×10^3 cells/ μl) imaged in a plastic HemoCue WBC microcuvette. (b) Segmentation results from the image processing routine. (c) Zoomed-in images of segmented WBCs, highlighting the cell border extraction. Scale bar in (a) and (b) is $100 \mu\text{m}$; scale bar in (c) is $20 \mu\text{m}$.

3.2.4.2 Custom-built Microscope

Next, the custom-built microscope was evaluated on the same porcine blood sample controls housed in the microcuvettes. Similar segmentation results were expected to be observed if the images clearly displayed the WBCs. Though not pictured in the design in Fig. 3.13, a bright white LED was placed underneath the 2-DOF linear gantry to illuminate the sample from below and enable bright-field imaging. The same optics, as described in Section 3.2.1, were used for collecting the transmitted light (e.g., dichroic, tube lens, and camera).

As seen in Fig. 3.22a and c, the original images acquired at low magnification (10x objective lens) were not as evenly illuminated as those acquired from the lab microscope (Fig. 3.21). As a result, it was difficult to delineate some cells from the background, which in turn, affected the subsequent segmentation (Fig. 3.22b and d). Moreover, cells had a tendency of floating in and out of the image, especially in the high concentration control samples. Cells could translate horizontally out of the image or even vertically out of the image plane. In both cases, this posed challenges to the image processing routine. The resulting segmentation, displayed in Fig. 3.22b and d, show a number of false positive (where the algorithm predicts a WBC is present, but is not) and false negative cases (where the algorithm fails to segment a WBC that is present).

Similarly, as seen in Fig. 3.23a and c, images acquired at higher magnification (40x

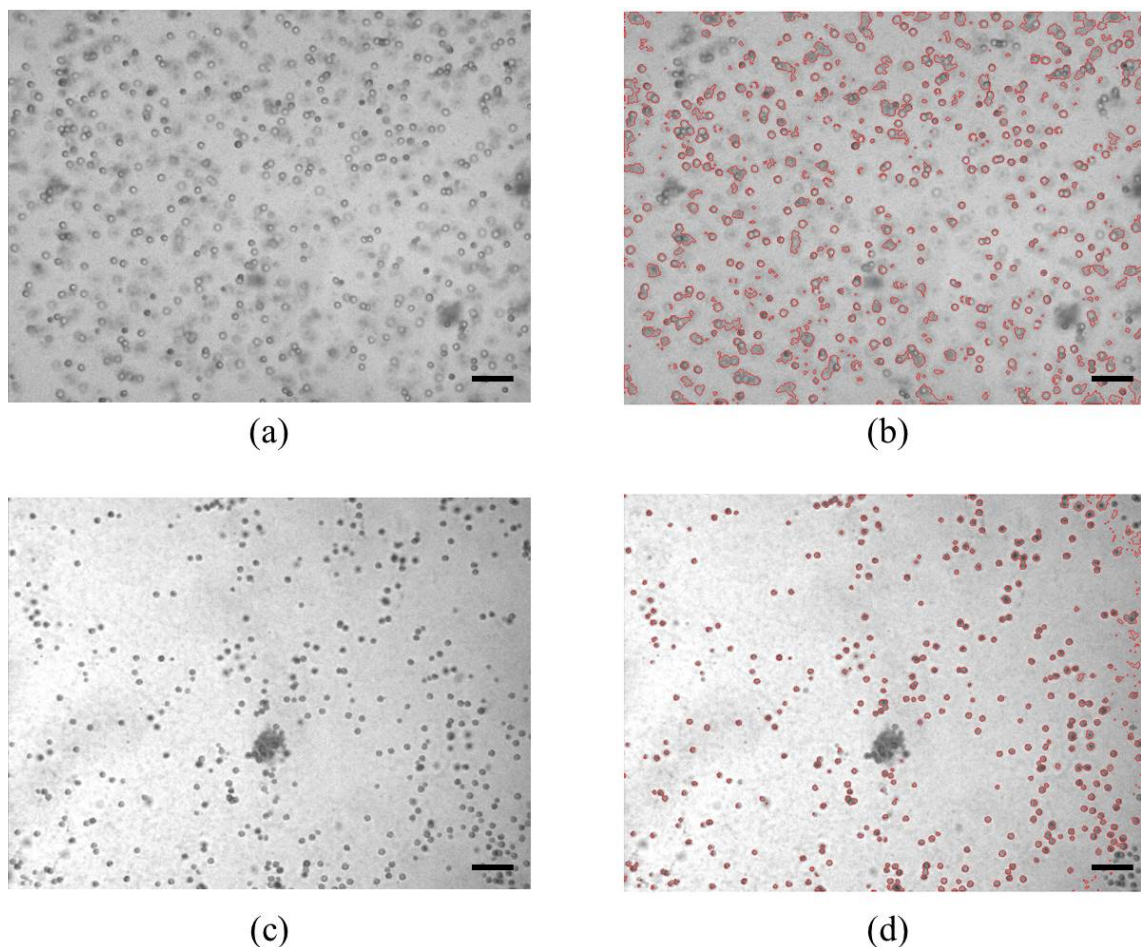


Figure 3.22: WBC images obtained from the custom-built microscope using a 10x objective lens (total magnification = 5.5x). (a) Original bright-field image of porcine WBCs (21×10^3 cells/ μl) imaged in a plastic HemoCue WBC microcuvette. (b) Segmentation results from the image processing routine. (c) Original bright-field image of porcine WBCs (7.7×10^3 cells/ μl). (d) Segmentation results from the image processing routine. Scale bar in all images is 70 μm .

objective lens) also had an uneven distribution of light throughout the sample. It was also even more challenging to focus cells on a single image plane in this case. Even a slight vertical displacement of the cell (e.g., 5 μm) would cause the microscope to lose focus. In order to count this moving cell, the microscope would end up chasing it around, continuously translating the gantry—a challenging task when trying to enumerate all the cells in the sample. Nevertheless, it would be close to impossible to count every cell using this static imaging approach. Looking at the segmentation results in Fig. 3.23b and d, there are still a number of false positive and negative cases that result from a noisy background,

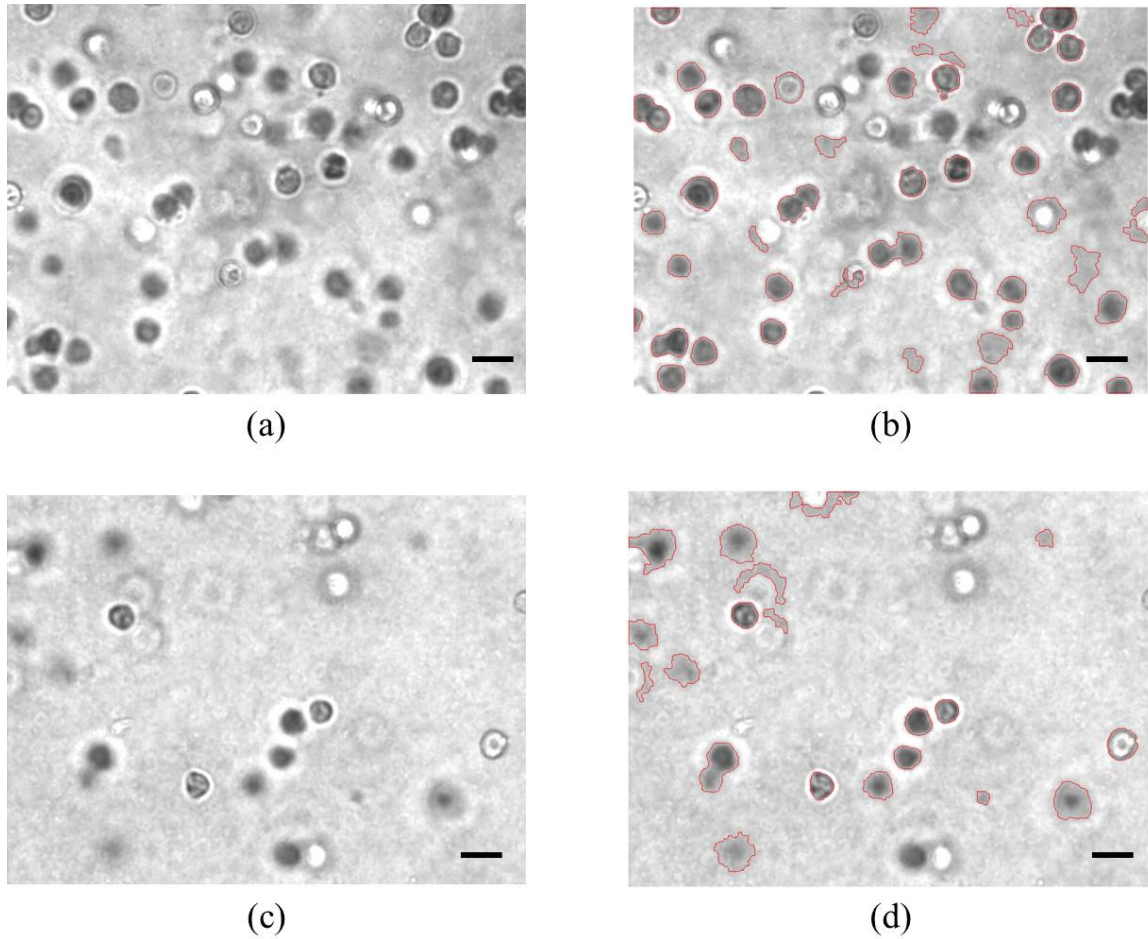


Figure 3.23: WBC images obtained from the custom-built microscope using a 40x objective lens (total magnification = 5.5x). (a) Original bright-field image of porcine WBC's (21×10^3 cells/ μl) imaged in a plastic HemoCue WBC microcuvette. (b) Segmentation results from the image processing routine. (c) Original bright-field image of porcine WBC's (7.7×10^3 cells/ μl). (d) Segmentation results from the image processing routine. Scale bar in all images is 20 μm .

and from cells not being clearly in focus at that particular image plane. One issue with slightly adjusting the focusing distance, is that the segmentation algorithm may extract cells that have already been accounted for. Increasing the vertical increments to say 10 or 15 μm would resolve this issue, but at the expense of missing cells that may be on an image plane in between those increments.

3.2.5 Limitations with Static Cell Counting

Despite the proof-of-concept results demonstrating the feasibility of the static cell counting method via image segmentation, there were numerous limitations observed in this approach. First, cells had a tendency to float out of the image plane while the microscope was scanning the sample. This made it challenging to focus the microscope initially, and to reliably segment cells in the images. Even after letting the WBCs settle for 5 min at the bottom of the substrate, they still moved around when observed under high magnification. This could have resulted from the substrate not lying perfectly parallel with the table, or there being too much sample volume in the detection chamber. The more sample in the chamber, the more likely cells will float around. The caveat about using a lower sample volume is that then there are fewer WBCs to image, and thus the consequences of missing a handful of cells in the segmentation routine have a greater impact on the resulting cell count. Another way to ensure cells remain flat on the substrate is to create a thin blood smear before imaging. Given the complexity of automating this task, and the associated limitations with blood smear imaging, this method is not a practical solution.

A second limitation with this method, is that it was a time-consuming process having to raster scan the sample, while at the same time, incrementing the z -stage in small steps to image cells. Even when processing the images simultaneously while the microscope was acquiring new images, the system took over 10 minutes to output an absolute WBC count using the 40x objective lens. An alternative approach would be to use the 10x objective lens so that a larger FOV of the sample could be acquired, but then the resolution of the images would be compromised. With lower resolution, we may lose some of the morphological detail needed to differentiate sub-types.

A third limitation was even at the higher magnification using a 40x objective lens, it was challenging to extract meaningful information from the segmented cells. The proposed idea was to first segment WBCs in the image, and then further classify them by analyzing their subtle differences in size, nuclear content, granularity, etc. However, after segmenting WBCs, the image processing routine had trouble gathering more detailed data for use in the K-means classifier. This made it extremely difficult to generate a differential WBC count

using this approach. Although providing an absolute WBC count is important for clinical diagnosis, there are already numerous POC devices on the market that can accomplish this, and there is more clinical value in providing at least a 2-part differential count—separating granulocytes (i.e., neutrophils, basophils, and eosinophils) from lymphocytes and monocytes.

For these reasons, an alternative approach for WBC counting was pursued, based on a bulk-cell analysis approach using centrifugal microfluidics and fluorescent microscopy. The details of this method and a series of more rigorous evaluation studies are presented in Section 3.4.

3.3 Optical Absorption Device

To quantify Hgb concentration in whole blood, the proposed method was to adapt an azide methemoglobin reaction as demonstrated in the HemoCue Hb201 device^{164,289,290}. First, RBCs would be lysed using sodium deoxycholate, which causes the RBC membranes to rupture, thereby releasing Hgb. Then the addition of sodium nitrate converts Hgb to methemoglobin by bringing Hgb iron from the ferrous to the ferric state. This solution further mixes with azide, resulting in azide methemoglobin. All reagents would be stored in dry format on-chip, and would be hydrated upon sample contact. The full reaction equation is summarized below.



The microscope would then measure the absorbance of azide methemoglobin based on the reflectance of the sample at 465 and 625 nm to calculate the Hgb concentration. Including two wavelengths in the photometric detection, allows the system to compensate for turbidity, ensuring proper Hgb readouts.

When trying to implement this design, we found that adapting the microscope to perform this absorption assay was unnecessarily complex, considering we were just trying to measure the amount of light being transmitted through the sample. To capture the transmitted light,

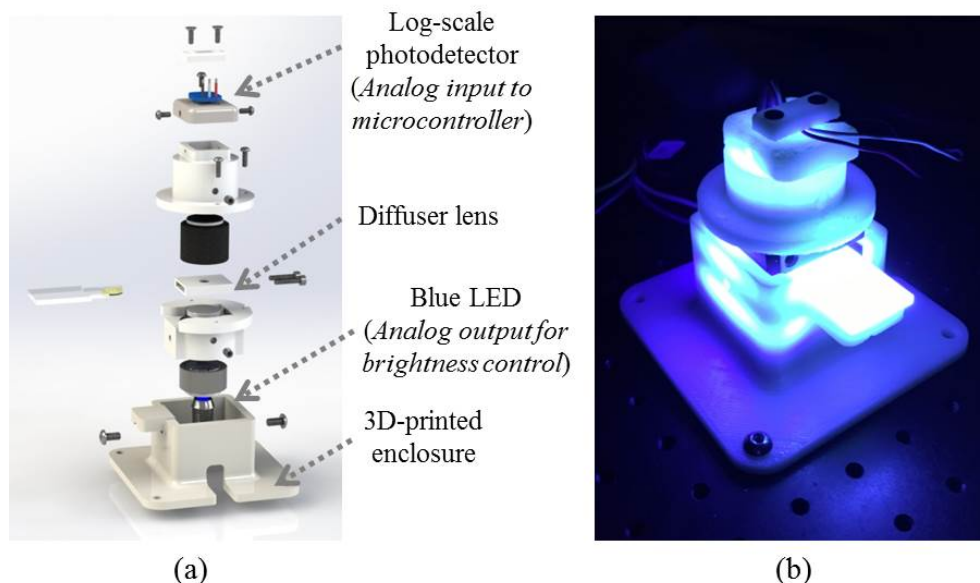


Figure 3.24: (a) Design and (b) prototype of the photometry module.

a photo-diode light sensor could be used instead of a camera. Along the same lines, using a high-powered LED to excite the sample was not necessary. Rather, a simple 5 mm low-powered LED could be used instead. With this in mind, a separate photometry module was designed, built, and tested using Hgb control samples (Fig. 3.24). Developing a separate module to evaluate absorption-based assays, allowed us to test both the WBC and Hgb assay at the same time in two independent devices. Using this approach, a new detection chip (Fig. 3.26) was developed to be used specifically for the photometry module.

3.3.1 Absorption Methodology

To quantify the concentration of Hgb, transmitted light that passed through the sample was measured, and using Beer-Lambert's law, this value was correlated with absorption. If the amount of transmitted light through the sample is compared to the amount of light transmitted through a blank (i.e., DI water), then a measure of absorption can be computed as outlined in Beer-Lambert's Law. Explicitly, the law states that absorbance linearly depends on the molar extinction coefficient of the solution, initial concentration, and optical path length. This is expressed in Eq. 3.3:

$$A = \log \frac{I_0}{I} = \ln(10) * \epsilon(\lambda) * c * l_{abs} \quad (3.3)$$

where A is absorption, I_0 and I is the transmitted light intensity through the blank and sample respectively, ϵ is the molar extinction coefficient at wavelength λ , c is the analyte concentration, and l_{abs} is the path length of light through the sample (defined as the thickness of the detection chamber). A blue LED (465 nm) was selected to illuminate the sample, corresponding to the max absorption peak in the Hgb spectra, as seen in Fig. 3.25.

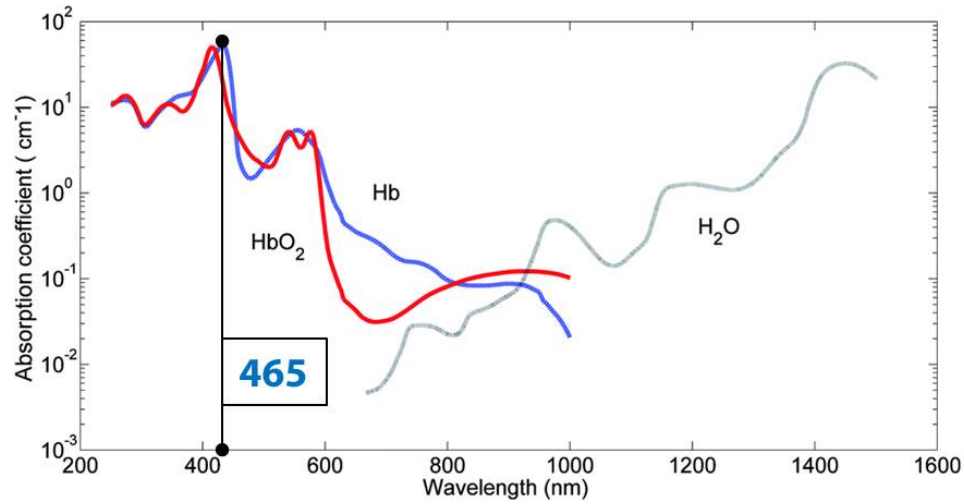


Figure 3.25: Absorption coefficients for Hgb and water, highlighting the wavelength used (465 nm) for the Hgb absorption studies, corresponding to the peak absorption.

3.3.2 Absorption Testing Instrument

The photometry module was designed to be a compact unit, capable of testing absorption across a broad range of LED wavelengths and intensities, accomplished via interchanging the LED and modulating the voltage input respectively. As pictured in Fig. 3.24a, the instrument consists of a 3D-printed enclosure, which houses the main optical components. This includes the LED, diffuser lens, and 0.5 in. lens tube.

The LED intensity is controlled via an analog output from a data acquisition board (USB DAQ-6009, National Instruments, Inc.) where 5 V and 0 V corresponds to the max and min intensity respectively. Sitting atop the main enclosure is a sample holder for the

detection chip. In the case of Fig. 3.24, a HemoCue Hgb microcuvette is used for preliminary testing. Lastly, a log-scale photodetector is mounted on a series of 3D-printed components, and is used to capture the transmitted light through the sample. The photodetector outputs an analog signal corresponding to the amount of light hitting the sensor, which is then read by the host processor via an analog input pin on the data acquisition board. Using a log-scale sensor, the system can operate at extremely high and low brightness conditions without saturating. This is important when trying to detect small amounts of analyte in the sample.

3.3.2.1 Detection Chips

Two different chip designs were evaluated: commercial cuvettes (Fig. 3.26) and custom acrylic chips (Fig. 3.27). The commercial cuvettes served as an initial baseline to which results from the custom chips could be compared against. The commercial cuvettes were sourced from HemoCue, which contained dry reagents to lyse RBCs and convert the Hgb to methemoglobin, as described in Section 3.3.

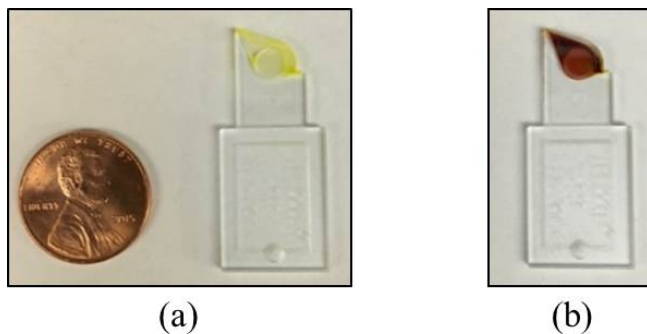


Figure 3.26: (a) HemoCue Hgb microcuvette with reagents in yellow, and (b) after placing 10 μl of blood in the inlet. The chip uses capillary action to disperse the sample throughout the detection chamber.

On the other hand, the custom chips consisted of five layers: three pieces of laser-cut acrylic and two pieces of double-sided adhesive. Using a 3D-printed alignment rig, the layers were pressed together to create fully leak-proof channels and detection chambers, as seen in Fig. 3.27. There were several important differences between the commercial microcuvettes and the custom chips. First, the custom chips contained significantly more sample volume (i.e., 50 μl vs 10 μl). This resulted from using a 1.5 mm thick acrylic piece for the channel

layer in the custom chips. Typically, the longer the path length—the distance the light travels through the sample—the higher the resolution in the absorption measurement¹⁹⁴. That is, a more sensitive measurement, because absorption scales linearly with the optical path length as governed by Eq. 3.3.

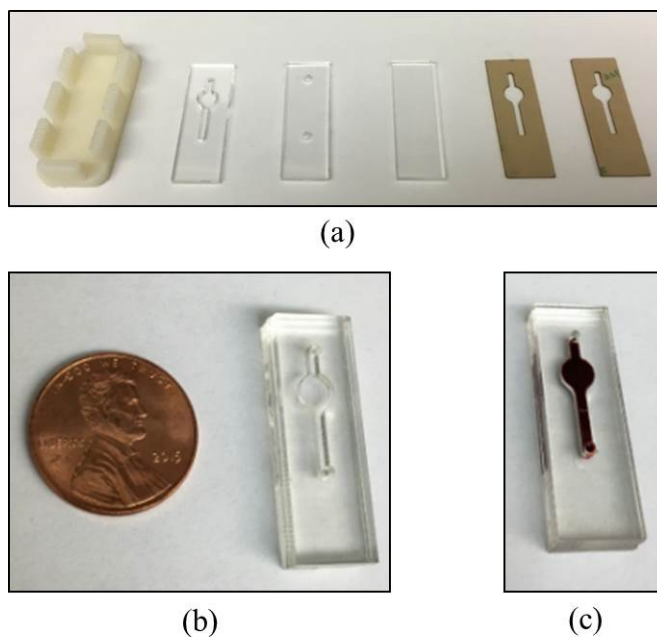


Figure 3.27: (a) Five-layer chip design. From left–right: alignment rig, acrylic channel layer, top acrylic layer, bottom acrylic layer, double-sided adhesive, and another piece of double-sided adhesive. (b) Assembled chip, and (c) chip filled with 50 μl of blood.

Second, the custom chips used no reagents; instead, the absorbed light is a measurement of the Hgb contained within RBCs. This technique has been shown to be an accurate and reliable method of determining Hgb concentrations, especially in situations where storing reagents on-chip is not practical, like in low-resource settings²⁹¹. Although this is more of an indirect method of measuring Hgb, it is a simplified approach that does well in approximating the analyte concentration in the sample.

3.3.2.2 Experimental Methods

To evaluate the absorption module, we tested four conditions: two chip designs (commercial and custom, as previously described) and two LEDs (a standard 5 mm LED and a high-powered LED used in the microscope—both in the blue wavelength). Three blood sample

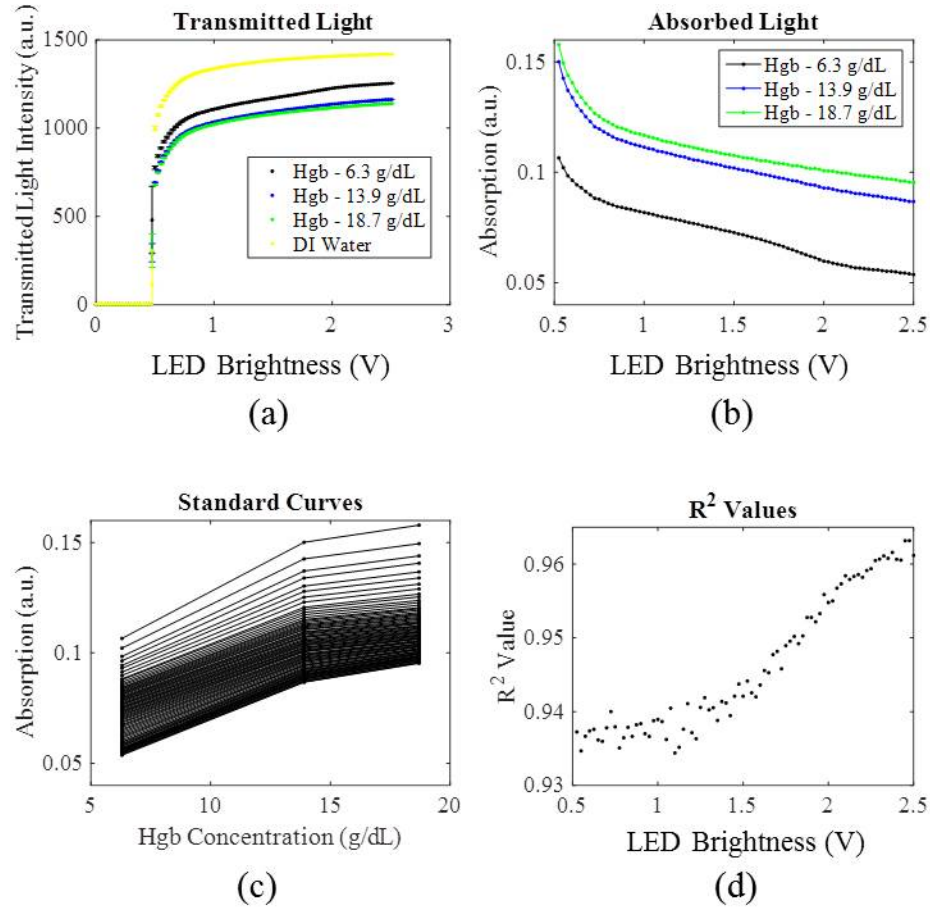


Figure 3.28: Hgb absorption results using HemoCue chips and a bright LED. (a) Transmitted light, (b) absorbed light, (c) standard curves for each intensity level, and (d) R^2 values for each intensity level standard curve.

control levels with known Hgb concentrations, corresponding to low (6.3 g/dl), normal (13.9 g/dl), and high values (18.7 g/dl), were used for testing. For each test condition, three experimental trials were run, and LED intensity sweeps were performed in attempts to extract trends in Hgb absorption at various intensities to optimize LED lighting conditions.

3.3.3 Experimental Testing

Results from the experiments are displayed in Fig. 3.28, 3.29, 3.30, and 3.31 for the HemoCue chip + bright LED condition, HemoCue chip + standard LED condition, custom chip + bright LED condition, and custom chip + standard LED condition respectively.

For each results figure, the original transmitted light data is plotted in (a), where 1500 refers to the max value on the light sensor (i.e., fully saturated). The absorbed light

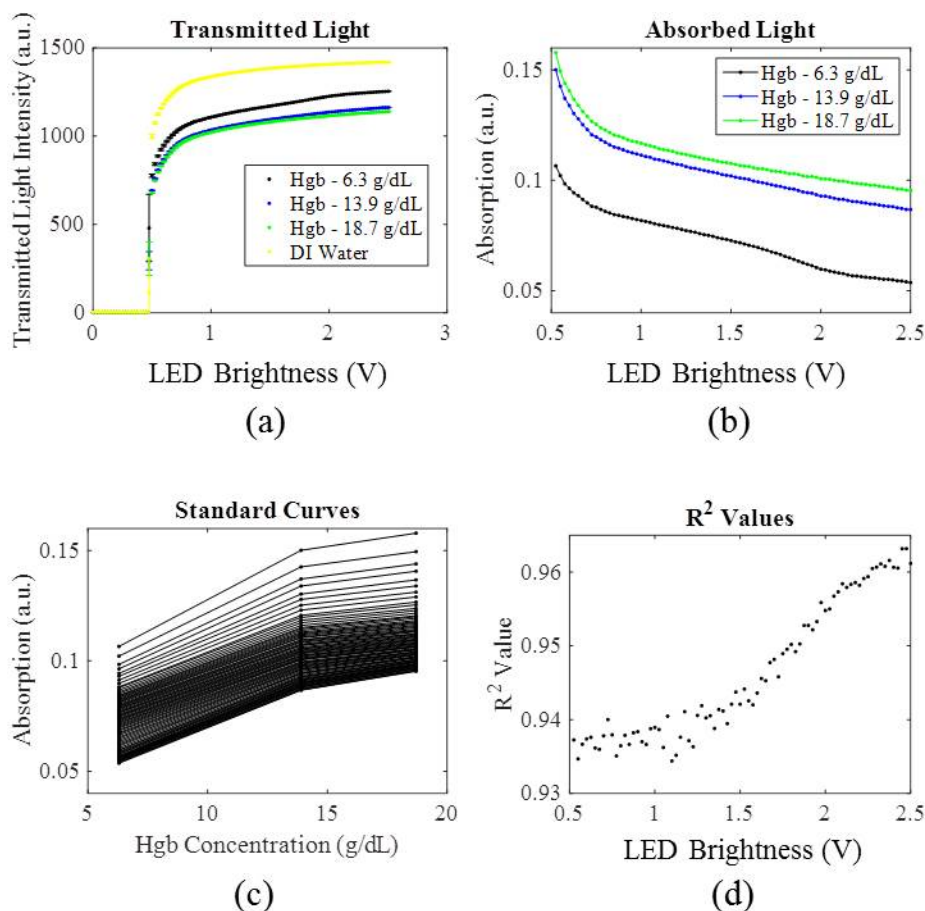


Figure 3.29: Hgb absorption results using HemoCue chips and a standard 5 mm LED. (a) Transmitted light, (b) absorbed light, (c) standard curves for each intensity level, and (d) R^2 values for each intensity level standard curve.

is plotted in (b), which takes into account the transmitted light on the blank sample. Standard curves for each LED intensity value are plotted in (c), and lastly, R^2 values for each standard curve are plotted in (d). Analyzing the plots for the HemoCue chip condition, some interesting trends in the R^2 values for both the bright and standard LEDs were observed. For the bright LED condition, R^2 values were observed to increase with increasing LED intensity, implying that illuminating the sample with brighter light may improve the sensitivity of the measurement. Overall, the R^2 value increased from about 0.94 to 0.96 when increasing the LED intensity. Although an R^2 value >0.9 is an indicator of a reliable assay, it is still far from perfect, especially considering there are numerous POC Hgb analyzers that report R^2 values of at least 0.98.

Conversely, for the standard LED condition, the R^2 value started off high around 0.997

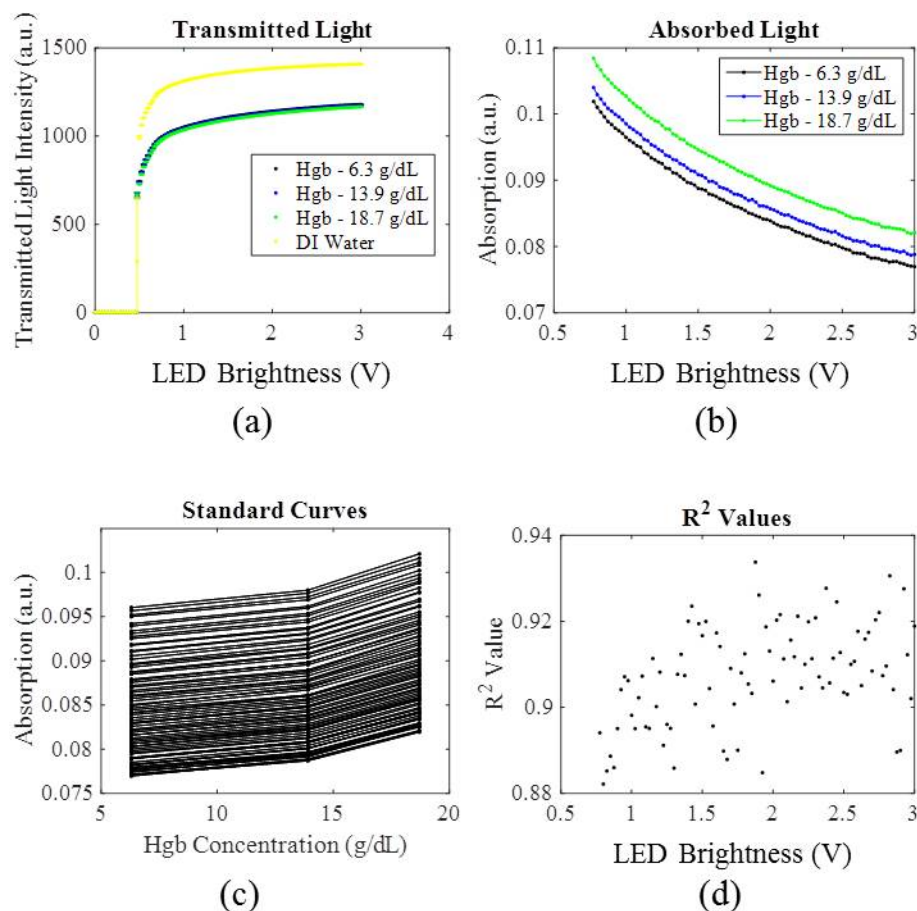


Figure 3.30: Hgb absorption results using custom chips and a bright LED. (a) Transmitted light, (b) absorbed light, (c) standard curves for each intensity level, and (d) R^2 values for each intensity level standard curve.

at low LED intensities, dropped to around 0.993 as the LED intensity increased, and finally increased again to around 0.997 as the LED intensity increased even more. The exact reason for this trend is unclear, though it most likely had something to do with the reagents stored in the chips. Nonetheless, the R^2 values remained above 0.99 throughout the tested LED intensities, indicating accurate and reliable standard curves using this approach.

Analyzing the plots for the custom chips, the LED intensity had negligible effects on the resulting R^2 values using the bright LED. Overall, R^2 values in this case were fairly scattered around the 0.92 range. For the other test condition—using the standard LED— R^2 values were observed to increase with increasing intensity values, similar to what was seen in Fig. 3.28d. Towards the maximum LED intensity, R^2 values were around 0.98. This

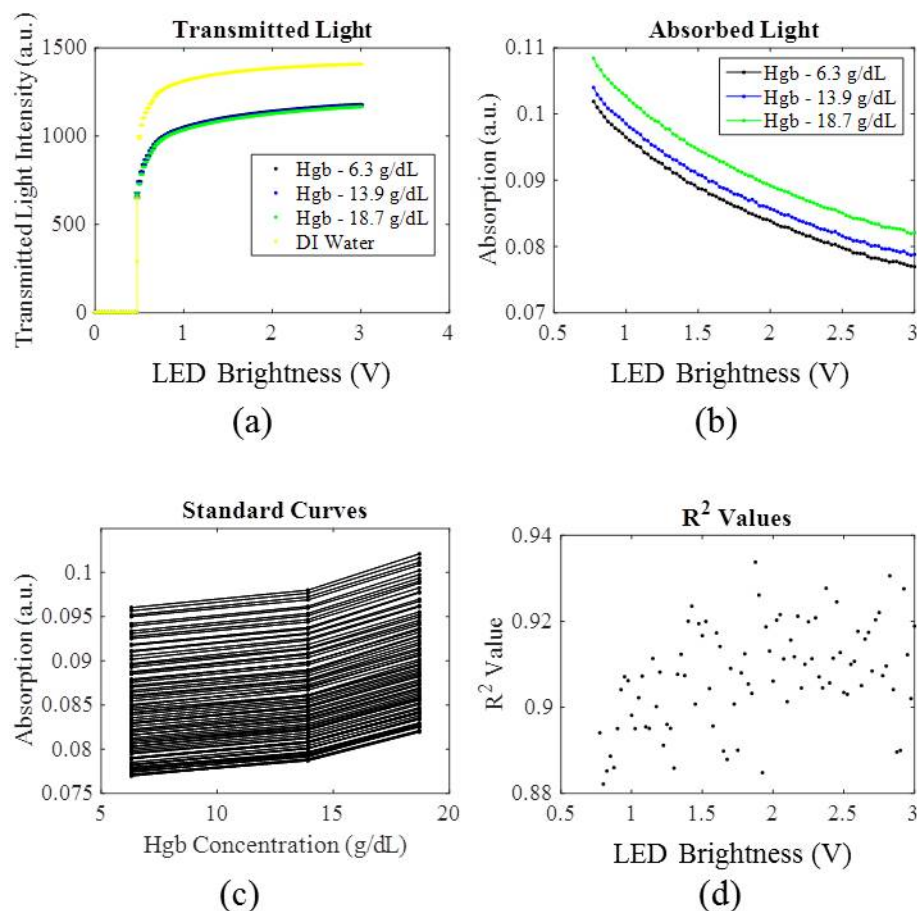


Figure 3.31: Hgb absorption results using custom chips and a standard 5 mm LED. (a) Transmitted light, (b) absorbed light, (c) standard curves for each intensity level, and (d) R^2 values for each intensity level standard curve.

implies that the custom chips—fabricated with acrylic sheets and double-sided adhesive—serve as a reliable detection chamber for measuring the concentration of Hgb in whole blood samples. Interestingly, the strong R^2 values seen in the custom chips, especially when using the standard LED, indicate that lysing the RBCs and converting the released Hgb to methemoglobin may be not be a necessary step for accurate Hgb measurements.

As a final comparison, absorption results for both detection chips were plotted on Fig. 3.32 to evaluate the sensitivity of the measurement. Here, the change of absorption (denoted $dAbsorption$) for each blood control level to the next is plotted at each LED intensity level. Fig. 3.32a and b shows the results from using the standard LED and bright LED respectively. In both cases, the HemoCue chips exhibit larger changes in absorption for each control level, indicating a more sensitive detection chip for small changes in Hgb

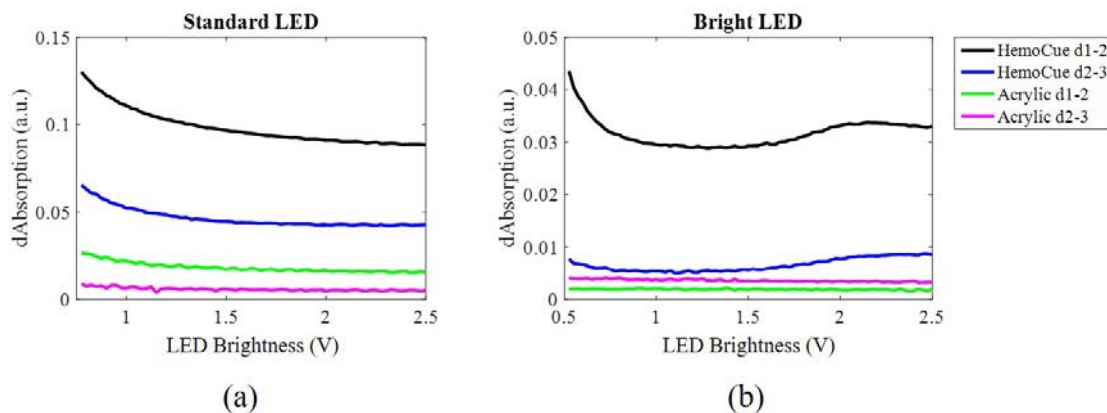


Figure 3.32: Comparing the change in absorption, for each blood sample control level, and both types of chips. (a) Testing with the (a) standard LED and (b) bright LED.

concentration. Additionally, the trend for both LEDs is that a lower light intensity results in greater measurement sensitivity.

3.3.4 Summary and Future Work

In summary, there are three main conclusions from these studies.

1. The light sensor is extremely sensitive, repeatable, and low-cost (\$3.95 from a hobby electronics store).
2. The custom chips produced reliable standard curves ($R^2 \approx 0.98$).
3. The HemoCue cuvettes were more accurate ($R^2 \approx 0.995$).

Future development of this photometry module and absorption assay include the following. First, additional data points should be added to the standard curves. In the presented data, only three control samples were tested. However, to more formally evaluate this approach, more data points need to be considered. This can be accomplished by serially diluting the Hgb control samples and running these samples on the test instrument.

Moreover, other homogeneous absorption-based assays can be evaluated on this module. Some examples include Glu and ALP—both of which are small molecules in blood that are frequently tested for in hospital visits. Evaluating these assays is simply a matter of exchanging the LED to match the peak absorption coefficient of the analyte of interest,

and modifying the detection chip to include the necessary reagents. For proof-of-concept, Glu was evaluated on the test instrument using a 660 nm LED in conjunction with the HemoCue Glu microcuvettes. These chips contained the necessary reagents for a modified Glu dehydrogenase chemistry method after hemolyzing the RBCs with saponin. Figure 3.33 displays the absorption results and corresponding R^2 values for each LED intensity level, using Glu blood sample controls. The controls contained three levels: low— 55 ± 15 , normal— 121 ± 30 , and high— 348 ± 50 .

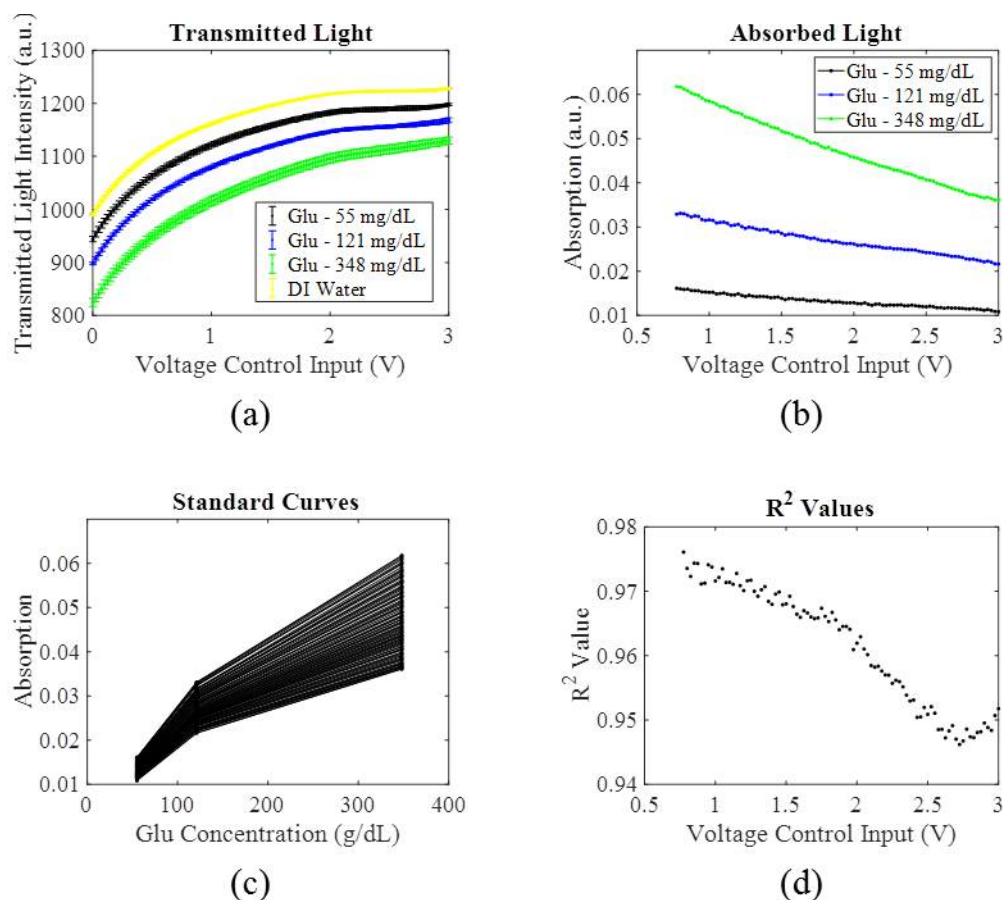


Figure 3.33: Glu absorption results using HemoCue chips and a standard 5 mm LED (660 nm). (a) Transmitted light, (b) absorbed light, (c) standard curves for each intensity level, and (d) R^2 values for each intensity level standard curve.

Finally, future work will focus on integrating this assay with the cell counting assay into one, compact device. Ideally, these analytes could be detected in parallel with the possibility of incorporating additional assays into the blood analyzer in the future.

3.4 Centrifuge Blood Analyzer

After preliminary testing of the single-cell static WBC counting approach and photometry module, it became apparent that it would be difficult to extend these concepts to detect other analytes of interest in blood. As stated earlier in Section 1.5.1, oftentimes in the ED, multiple blood tests are ordered for a range of symptoms, indicating the need for a POC analyzer that can perform multiple assays at once. To accomplish this—and improve upon our WBC counting and homogeneous absorption-based assays—we transitioned to a centrifuge-based approach. With this technique, biological constituents can be isolated via density separation, fluids can be transported via centrifugal forces, and a range of large and small molecules can be detected.

In this section, the development of the centrifuge blood analyzer is presented, highlighting designs from the first-gen 3.4.1, second-gen 3.4.2, and third-gen 3.4.3 device with a focus on evaluating the WBC assay using this approach.

3.4.1 First-generation Analyzer

The design of the initial prototype is pictured in Fig. 3.34. This concept was at first developed independently of the venipuncture robot and sample handling module to establish preliminary evidence of this approach. Hence, the device, as pictured in Fig. 3.34, is contained within a testing enclosure.

The system has four main components to achieve a WBC count: disposable microfluidic chips to house the sample, a custom-designed centrifuge to hold the chips and fractionate the sample, a fluorescent microscope for cell imaging, and LabVIEW software to run the device and output diagnostic results. The main components of the system are summarized in Fig. 3.35.

The operating protocol includes the following steps. First, the blood sample is introduced in the disposable chip, which is preloaded with acridine orange (AO)—a fluorescent dye that stains the nuclei of WBCs. The chip is then placed inside the centrifuge and spun for five minutes at 1500 RCF. Next, the motor decelerates and an RC servo motor mounted underneath the centrifuge rotates a magnetic arm, which latches onto the centrifuge chip

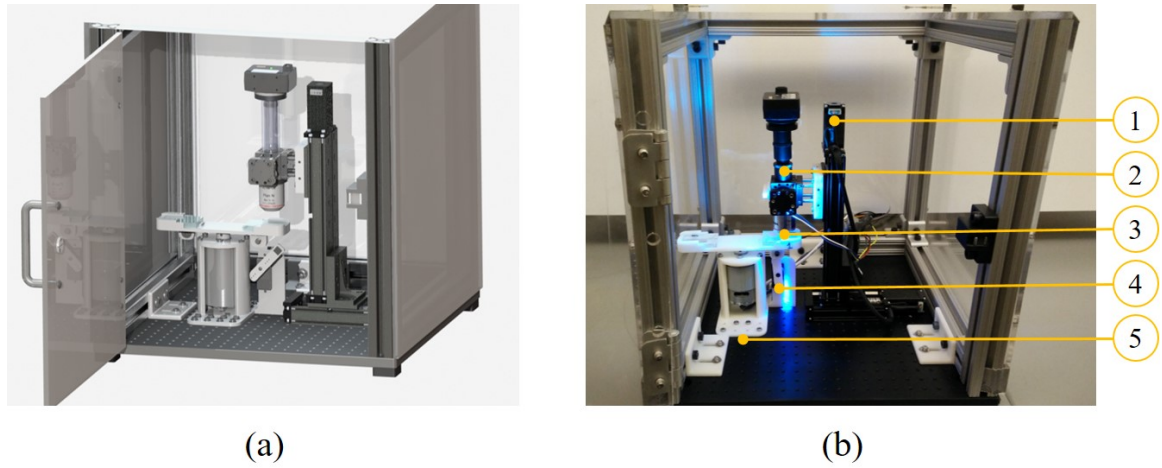


Figure 3.34: (a) Design and (b) prototype of the first-gen centrifuge analyzer, highlighting the: 1. stepper-based linear stages, 2. fluorescent microscope, 3. disposable chips, 4. RC servo alignment lock, and 5. mini centrifuge.

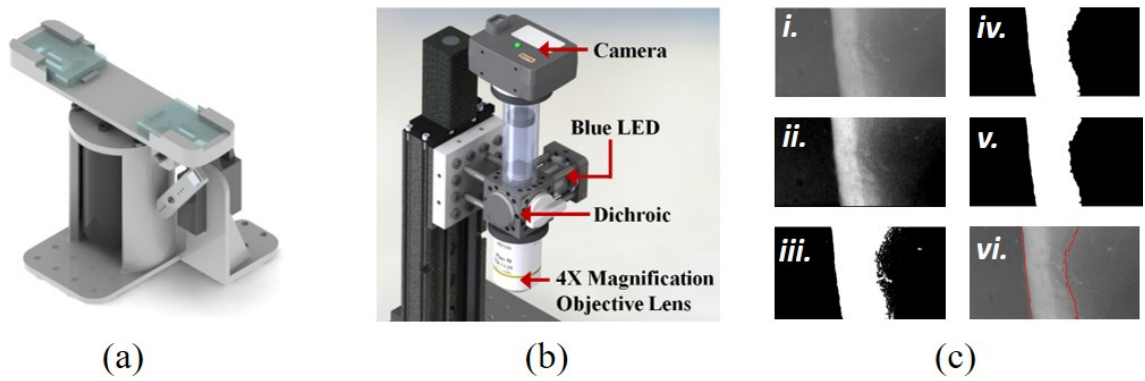


Figure 3.35: Main components of the first-gen centrifuge analyzer. (a) The custom-designed centrifuge. (b) The miniature fluorescent microscope comprised a high sensitivity CCD camera, a blue LED for excitation, a dichroic filter, and a 4X objective lens. (c) Image analysis routine for buffy coat segmentation and area quantification. The original image (i) was processed in LabVIEW using contrast enhancement and filtering (ii) and thresholded to obtain a binary image (iii). Morphological processing filters (iv) were then applied to fill unwanted areas inside and surrounding the buffy layer to obtain the final segmented image (v). Finally, the outline of the segmented area was overlaid on top of the original image to clearly show the buffy region (vi).

holder to position the blood samples directly underneath the microscope for imaging. At this point, the fluorescent microscope focuses on the separated WBC layer—which resides above the packed RBCs and below the plasma after centrifugation.

The optical detection system uses similar components, as the first-gen microscope (described in Section 3.2.1). Here, the blue LED is used to excite the AO that is now bound

to the WBCs, but in this design, a 4x objective lens is used as well as 0.5 in. diameter tube lens components. A digital camera then captures the reflected green light and transmits the images to the host processor for analysis in LabVIEW. Finally, the software segments and measures the WBC layer in the image, correlating this area to a cell count referencing a standard curve.

3.4.1.1 Chip Design and Fabrication

One of the main facets of the analyzer was developing a disposable to contain the blood sample. The unit had to be optically transparent for imaging, leak-proof at high centrifugal speeds, and geometrically consistent to ensure repeatable results. Early designs included a glass capillary tube and a polydimethylsiloxane (PDMS) chip, as seen in Fig. 3.36a and b respectively.

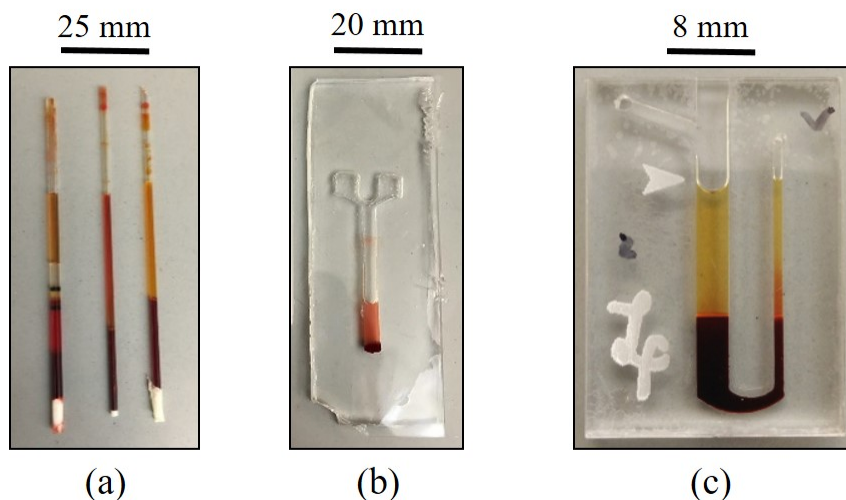


Figure 3.36: Evolution of disposable chip design. (a) Initial designs utilizing commercially available capillary tubes demonstrated difficulties with fluid handling and imaging under the microscope. (b) Chips fabricated in PDMS allowed for significantly improved imaging, but required labor and time-intensive manufacturing and were easily damaged under centrifugation. (c) The third design utilized three-layers of acrylic fabricated via a precision laser-cutting process, were mass producible, had ideal transparent optical properties with channels that could be easily positioned within the microscope's depth of focus, and were easily sustained at >10,000 rpm during centrifugation.

Capillary tubes are widely available and have consistent dimensions, however they can be challenging to image due to their curved surface. Conversely, PDMS chips have favorable

optical properties and are consistent in size, but are ultimately not robust enough for use. Specifically, during preliminary testing, PDMS fragments tended to disintegrate at high centrifugation speeds.

Moving away from the soft elastomer PDMS design, hard plastic chips were then investigated. The example pictured in 3.36c, is a 36 x 26 mm three-layer laser-cut acrylic chip design. The top and bottom layers were cut from 1.5 mm clear cast acrylic sheets, while the middle layer was cut from 1.0 mm stock acrylic. After cutting, layers were bonded together using acrylic solvent, ensuring leak-proof channels. The chip also includes a fill line engraved on the top, and a side channel for reagent pre-loading.

3.4.1.2 Experimental Methods & Results

The device was evaluated on porcine blood sample controls consisting of low ($3.2 \pm 0.8 \times 10^3$ cells/ml), medium ($7.9 \pm 1.2 \times 10^3$ cells/ml), and high ($21.2 \pm 2.5 \times 10^3$ cells/ml) concentrations. Approximately 200 μ l of sample was mixed with AO, and then manually introduced into the acrylic chip. The channel design includes a pressure outlet, obviating the need to surface treat the substrate. However, because of the curved channel design, the WBCs are split between the two sides of the curve. On one hand, this provides another buffy coat measurement to improve the quantification of WBCs in the sample, though on the other hand, the cells may not evenly disperse between the two sides. This issue will be further addressed in later chip design iterations. For preliminary evaluation studies, the current design was sufficient.

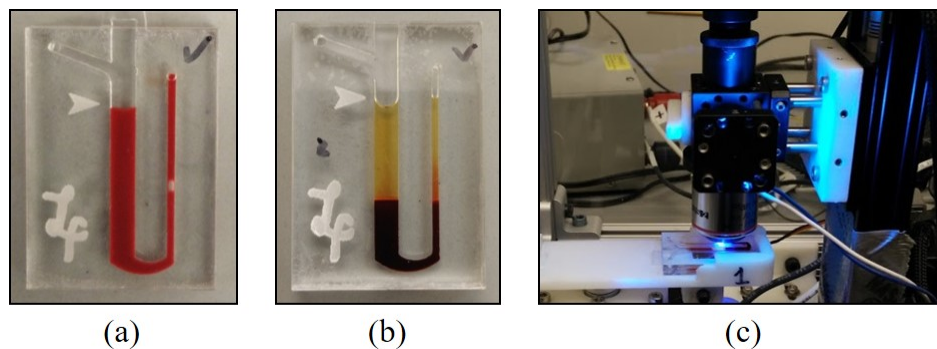


Figure 3.37: Experimental setup during testing of the first-gen centrifuge analyzer. The acrylic chip (a) before and (b) after centrifugation. (c) The fluorescent microscope aligning over the chip and imaging the isolated buffy coat.

After placing two chips in the centrifuge holder and spinning the samples for 5 min, the buffy coat was imaged, segmented, and measured. These results were used to generate a standard curve. Figure 3.37 displays the chip before and after centrifugation, and the microscope imaging the buffy coat. In total, three experimental trials were conducted for each control level. As seen in the standard curve of Fig. 3.38, a strong linear fit is observed between the buffy coat pixel area and cell count. Standard deviation from the experiments (expressed as vertical error bars in Fig. 3.38) were appreciably smaller than the inherent standard deviation reported in the control samples.

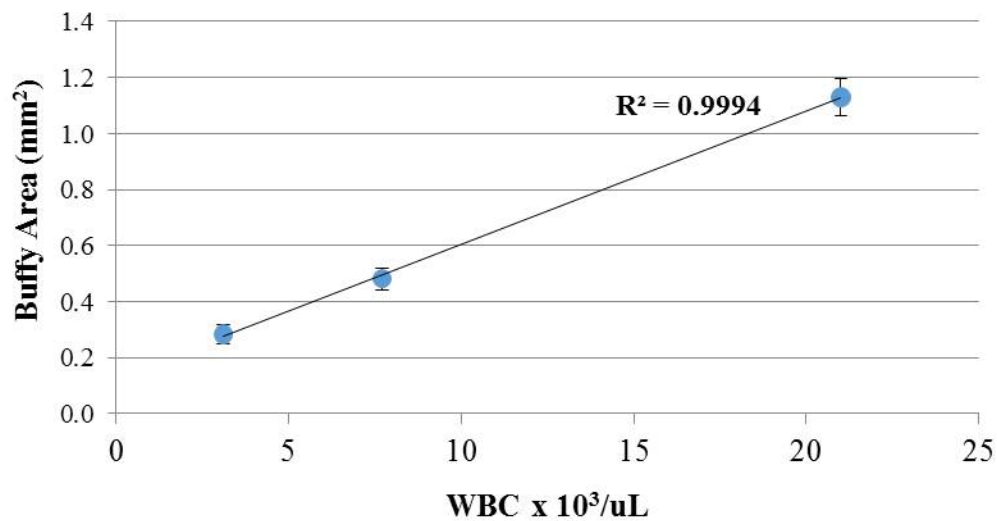


Figure 3.38: Standard curve generated using porcine blood sample controls. Data represents the mean \pm standard deviation ($n = 3$).

3.4.1.3 Limitations

Despite promising results obtained from using the initial centrifuge analyzer, there were numerous design flaws that needed to be addressed in subsequent prototypes. First, the system was excessively large and bulky. The size of the device stemmed from the orientation of the microscope relative to the centrifuge. In the design, the microscope was positioned above the spinning disc, which resulted in a substantial amount of empty space in order to mount the imaging system.

Second, the centrifuge was actuated by a large, hobby-type DC-brushed motor that made a significant amount of noise when running, tended to heat up when operating for

more than 60 sec, and had trouble reaching speeds >5000 rpm. At times, the centrifuge motor sounded like a lawnmower, causing severe vibrations to the microscope and to the entire device itself.

Third, the device was contained in a square box enclosure, prototyped using 80/20 aluminum bars and acrylic panels. Due to the height and orientation of the microscope, the enclosure was quite large (i.e., 12 x 12 x 12 in). Although it served the purpose of protecting the users in case a chip slipped off the centrifuge, the design could be simplified to better contain the components.

3.4.2 Second-generation Analyzer

Similar to the initial prototype, the second-gen analyzer consists of the following components: a centrifuge to fractionate the blood sample, a microfluidic chip to house the sample, and an optical detection system to quantify the WBCs².

3.4.2.1 Centrifuge

A miniaturized centrifuge (Fig. 3.1b) was used to spin the microfluidic chip at 10,000 rpm to separate the cellular components from plasma. The centrifuge was driven by a brushless servo motor (EC i-40, Maxon Precision Motors, Inc.) with an attached encoder to provide position and velocity control. Motor torque and power calculations governed the selection of the servo, assuming a required centrifugal force of 1,500 RCF for 5 min to fractionate the blood sample. Machined brackets were used to mount the motor to an aluminum base, which also served as the mounting plate for the enclosure.

Compared to the motor in the previous prototype, this one was substantially more robust, made less noise while operating at high speeds, and provided position and speed feedback via the attached encoder. Moreover, this servo was capable of achieving much

²Much of the work presented in this section first appeared in: System design and development of a robotic device for automated venipuncture and diagnostic blood cell analysis. Proceedings of the 2016 IEEE/RSJ International Conference on Intelligent Robots and Systems, pp. 514–520⁴. All excerpts represent the original work of Max Balter, whose specific contributions as first author included: designing and conducting the experiments; generating the presented data and corresponding figures; writing, editing, and revising the original text; and addressing reviewers' comments as corresponding author of the original manuscript submission.

higher speeds (i.e., up to 15,000 rpm) and did not heat up during periods of high torque, as was observed in the initial centrifuge motor. Despite all of these advantages in the servo itself, the control electronics were more complicated because of the brushless motor configuration. This required electrical switching of the input current to the motor windings, as opposed to direct DC voltage control implemented in brushed motor control applications.

3.4.2.2 Microfluidic Chip

The single-use disposable chips housed the blood sample and were fabricated using three layers of cast acrylic sheets which were laser cut and bonded into $\varnothing 72$ mm chips. The top and bottom layers were 1.5 mm thick, whereas the middle layer was 0.8 mm thick. Plasma activation was used to enhance the wettability of the substrate, allowing the sample to easily flow into the channels once introduced into the chip. Layers were bonded using pressure-sensitive adhesive and pressed together under 5 MPa of pressure at 65 °C for 5 min to ensure leak-proof channels. To differentially label nucleated white blood cells, 5 μ g of dry acridine orange fluorescent stain (A3568, Life Technologies) was pre-loaded in the chip during fabrication.

Compared to the initial acrylic chip prototype described in Section 3.4.1.1, this new design combined the two smaller chips into one, transitioning to more of a disc-based unit. The chip geometry consisted of a wide inlet in the chip center and two parallel channels (3 mm wide) that curve back to the middle with pressure outlets at both ends. These parallel channels also served as the detection chambers. Similar to the initial acrylic chip design, the curved channels provided additional locations to measure the packed WBC layer.

3.4.2.3 Optical Detection System

To image the blood sample, the miniaturized fluorescent microscope developed in the first-gen centrifuge analyzer was redesigned to position the objective lens underneath the microfluidic chip. This resulted in a more compact design and made it easier to introduce and remove the chip from the device. To briefly review the main elements of the microscope, the system included a high-powered blue LED (465–485 nm), excitation (475 ± 35 nm) and emission (500 nm high pass) filters, a dichroic mirror (506 nm), lenses (4x objective and $f=50$

mm tube lens), and a CMOS sensor (Firefly MV, FMVU-03MTM-CS, Point Grey Research Inc.) to capture the reflected light in an 8-bit grayscale image. The camera update rate was 30 fps for image capture and 20 fps for the subsequent processing. The microscope was further mounted on two linear stages (LSM025 and LSA25, Zaber Technologies Inc) to provide horizontal and vertical translation (denoted as y_o and z_o respectively in Fig. 3.1b).

After the centrifuge fractionated the sample, the motorized stages positioned the microscope over the fluorescing white cell region using a pre-determined trajectory. The location in the y -dimension can be estimated from typical hematocrit levels (i.e. $\sim 45\%$) and the known sample volume, while the z_o -stage automatically translated upwards a set distance to get within focusing range. The z_o -stage then made further adjustments to auto-focus the light by maximizing image contrast along the borders of the buffy coat (i.e., sharp transitions between the black background and white fluorescing region). Once in focus, an image thresholding step was performed based on Otsu's method²⁹², and the thickness of the white cell region was quantified. The software then compared this measured thickness with pre-determined values to compute the total WBC count. Pre-determined values would be obtained from generating a standard curve using samples with known cell concentrations.

3.4.2.4 Blood Analysis of Simulated White Cell Count

To demonstrate feasibility of the second-gen centrifuge analyzer, experiments were conducted using a simulated white cell assay, in which the area of the buffy coat was correlated with a cell count to generate a standard curve. We used *in vitro* human blood samples spiked with fluorescently labeled beads ($\varnothing 15\ \mu\text{m}$) to simulate white cells. The bead counts per μl of sample were 100, 200, and 300.

3.4.2.4.1 Experimental Protocol

First, 200 μl of sample was manually pipetted into the microfluidic chip and loaded into the analyzer unit. The centrifuge was then spun at 10,000 rpm for 5 min. Following centrifugation, the microscope auto-focused (z_o) and scanned the detection channel (y_o) for the fluorescing buffy coat. The y_o -stage translated until it found the salient layer of packed beads, at which point a series of image processing steps were implemented to enhance,

segment, and measure this region.

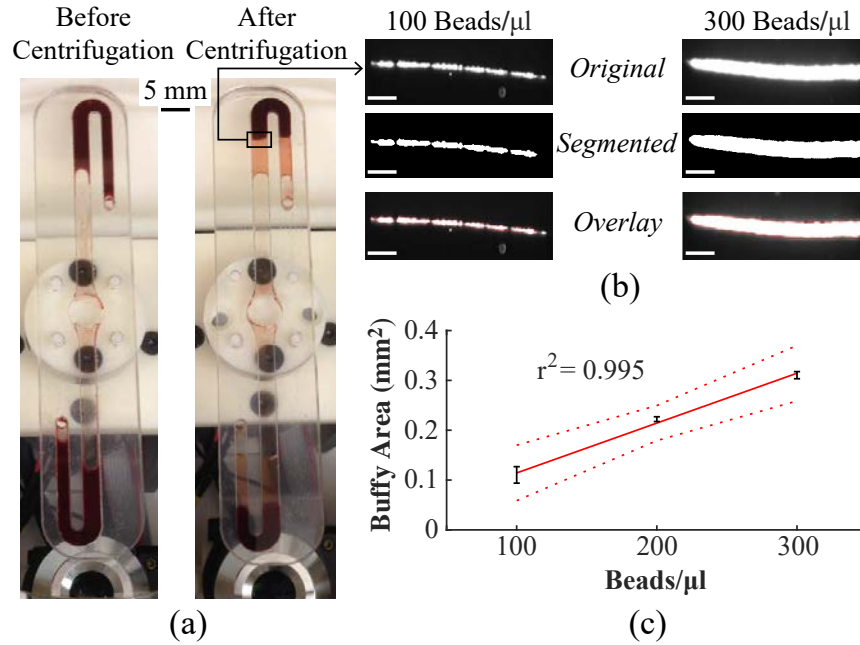


Figure 3.39: Simulated WBC count on the centrifuge analyzer. (a) Chip before and after centrifugation. (b) Original and processed images of the buffy layer used to quantify the number of beads in the sample (scale bar = 0.5 mm for all images). (c) Standard curve for the bead-simulating white cell assay. Error bars show standard deviation for each level ($n=3$); red line shows the linear fit ($r^2=0.995$); dotted red lines show 90% confidence bounds. Figure reproduced with permission from IEEE⁴ (year of original publication: 2016).

3.4.2.4.2 Results

The chip is displayed before and after centrifugation in Fig. 3.39a, and the image processing used to quantify the buffy coat area is shown in Fig. 3.39b. The standard curve (Fig. 3.39c), produced from plotting the measured buffy coat area with the known number of beads in each sample, resulted in a coefficient of variation of 0.995, indicating a near linear fit. The image processing algorithms were able to successfully segment and quantify the buffy coat for all trials. Standard deviations in the measured area (i.e., 15.10%, 2.16%, and 2.32% of the mean for 100, 200, and 300 beads/ μ l respectively) were more likely due to inherent variations in manual sample preparation than to the segmentation algorithms.

3.4.2.5 Limitations

By inverting the microscope and positioning it underneath the chip for imaging, the analyzer was substantially more compact compared to the initial prototype. Nonetheless, the centrifuge motor was 40 mm in diameter, so the microscope could only image samples towards the periphery of the chip. This proved to be a fairly significant limitation, especially considering the device was designed to measure the buffy layer, which resides approximately in the middle of the sample after centrifugation. In some cases, the large centrifuge motor prevented the microscope from imaging the WBCs.

Furthermore, the current microscope design had only one excitation and emission light channel, limiting the diagnostic capabilities of the system. Specifically, the analyzer could only perform an absolute WBC count. At the very least, the device should be capable of differentiating between WBC sub-types. To accomplish this, additional light channels needed to be added to the microscope.

3.4.3 Third-generation Analyzer

In the third-gen analyzer, the optical detection system was modified to allow for the differentiation of WBC sub-types³. Similar to previous analyzers, leukocyte counting was performed using a bulk-cell analysis approach (Fig. 3.40). However, to more fully evaluate this technique, two approaches were tested. In the first method, glass capillary tubes were used to house the blood sample as a control group. Samples were then fractionated using a bench-top centrifuge and the leukocytes were analyzed using the fluorescent microscope. In the second method, layered acrylic chips were used, but in this case, samples were spun on a miniaturized centrifuge which was further integrated with the microscope. The capillary tube control group allowed the acrylic chip results to be compared against an established method.

³Much of the work presented in this section first appeared in: Differential leukocyte counting via fluorescent detection and image processing on a centrifugal microfluidic platform. *Analytical Methods* 2016; 8(47):8272–8279⁵. All excerpts represent the original work of Max Balter, whose specific contributions as first author included: designing and conducting the experiments; generating the presented data and corresponding figures; writing, editing, and revising the original text; and addressing reviewers' comments as corresponding author of the original manuscript submission.

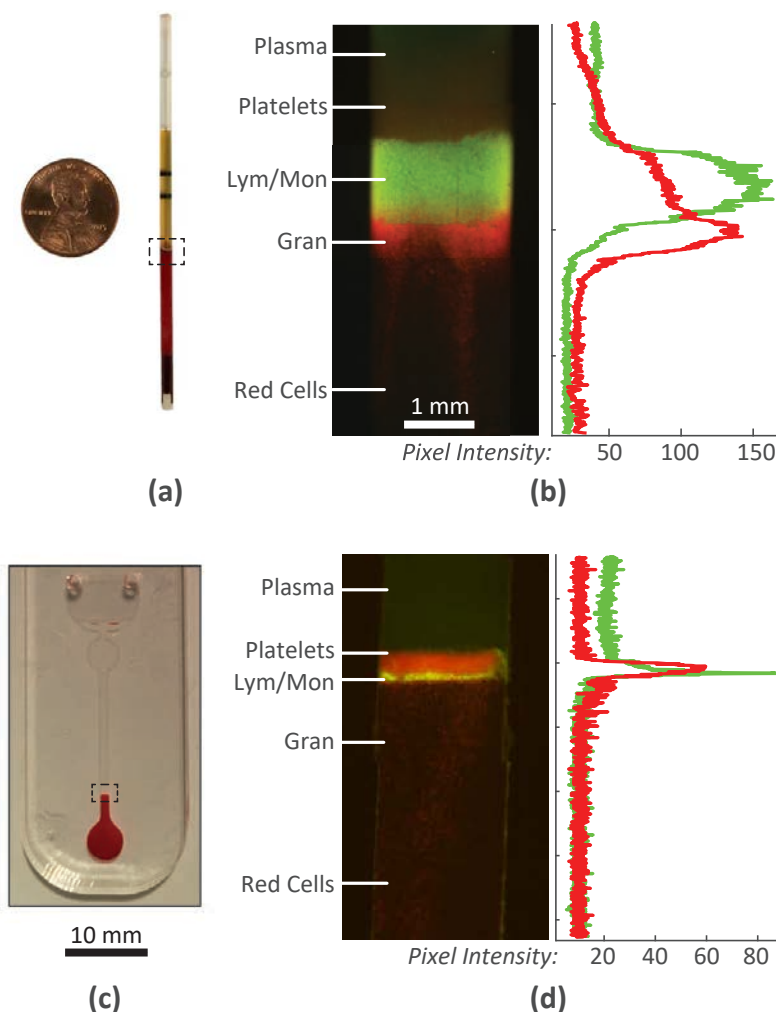


Figure 3.40: Methods for differential leukocyte counting using a bulk-cell analysis approach. (a) Capillary tube after centrifugation with the buffy coat outlined. (b) Microscopic image of the buffy coat, highlighting the separated blood layers, and corresponding green and red fluorescent profiles. (c) Acrylic chip after centrifugation, and (d) microscopic image of the buffy coat with corresponding fluorescent profiles. Balter et al. /citeBalter2016a - reproduced by permission of The Royal Society of Chemistry.

A more detailed description of the third-gen analyzer and associated experiments is presented in the following sections. First, Section 3.4.3.1 introduces the leukocyte staining methodology, designs for the fluorescent microscope, and image processing steps implemented to extract and measure the leukocyte region (i.e., the buffy coat). Section 3.4.3.2 presents the results, comparing the buffy coat areas with measured cell counts to generate a set of standard curves for absolute leukocytes and a 2-part differential (i.e., lym/mon and

gran) using capillary tubes and acrylic chips. We also demonstrated the use of pixel clustering to separate lymphocytes from monocytes, extending the bulk-cell analysis approach to a 3-part differential. Finally, section 3.4.3.3 discusses various ways to enhance the accuracy and repeatability of this approach.

3.4.3.1 Experimental Materials & Methods

Our approach for cell counting utilizes density centrifugation to isolate and enumerate leukocyte sub-types. After centrifugation, distinct bands are formed where cells are layered from most to least dense. Since leukocytes contain nuclei, it is possible to differentially stain them and analyze the distinct layers using fluorescence imaging. The imaged layers can then be correlated to cell counts with the capacity to perform a 2-part differential, and potentially a 3-part differential, by separating monocytes from lymphocytes based on their fluorescence intensity profiles.

Some advantages of the bulk-cell analysis approach include the following. First no dilution step is required; therefore, it is possible to use whole blood. Second, minimal sample processing is needed with the use of a single nuclear stain—AO. Third, results can be obtained in under 5 min (i.e., the time needed to fractionate the blood sample).

3.4.3.1.1 Leukocyte Staining Methodology

AO has several unique biochemical characteristics that make it simple to use and enable the differentiation of leukocyte sub-types based on nuclear content. Specifically, AO has a natural affinity for nucleic acids, so it can stain both DNA and RNA of live cells. Bound dye fluoresces more intensely than unbound dye, obviating the need for a wash step. Finally, the use of AO allows leukocyte sub-types to be identified based on chemical rather than morphological differences in cells²⁹³. When excited under blue light, DNA emits green light and RNA emits red light, which enables the classification of sub-types using a single nuclear dye. As summarized in Tab. 3.3, this approach can be thought of as color-coded leukocyte counting: in which lymphocytes emit an intense green, granulocytes emit mostly red, and monocytes emit a moderate amount of both green and red—all under blue excitation.

Table 3.3: Color-coded leukocyte counting approach for a 3-part differential.

WBC sub-type	Concentrated DNA (Green Fluorescence)	Concentrated RNA (Red Fluorescence)
Lymphocytes	strong	minimal
Granulocytes	minimal	strong
Monocytes	moderate	moderate

3.4.3.1.2 Second-gen Fluorescent Microscope

To image the buffy coat, a miniaturized fluorescent microscope was developed for use with AO stain (i.e., blue excitation and green/red emission). The system, as pictured in Fig. 3.41a, is mounted on two linear stages (LSM025A and LSA25A, Zaber Technologies Inc) to provide translation along y and z . The excitation optics include a high-powered blue LED (465–485 nm, CreeXPE-Blu-1, LED Supply), excitation filter (475 ± 35 nm, FF01-475/35-12.5, Semrock, Inc), condenser lens ($f=8$ mm, 0.78 NA, ACL12708U, Thorlabs, Inc.), dichroic mirror (506 nm beam splitter, FF506-Di03-12.5m, Semrock, Inc), and an objective lens (Olympus Plan Achromatic, Thorlabs, Inc.). For capillary tube experiments, a 4x objective (0.1 NA, RMS4x) was used, whereas a 10x objective (0.25 NA, RMS10x) was used for acrylic chip experiments due to sizing and sample volume differences between the two methods.

After illuminating the sample, the reflected light passes back through the objective lens and dichroic mirror, and then reflects off a right-angled mirror to redirect the light through a tube lens (Achromatic Doublet, $f=50$ mm, AC127050A, Thorlabs, Inc.). Next, the light passes through a motorized filter-wheel which rotates a green (529 ± 24 nm, FF02-529/24-12.5, Semrock, Inc) and red (684 ± 24 nm, FF02-684/24-12.5, Semrock, Inc) filter in front of the camera. The filter wheel is actuated via a DC-brushed gearmotor (GM22, Solarbotics Ltd.) using an H-bridge motor driver (COM-00315, SparkFun Electronics) and a microcontroller to set the speed and switch the direction via digital output signals (EPOS 24/2, 390438, Maxon Precision Motors, Inc.).

As seen in Fig. 3.41(b), the filter wheel contains a motor mount connector plate, filter

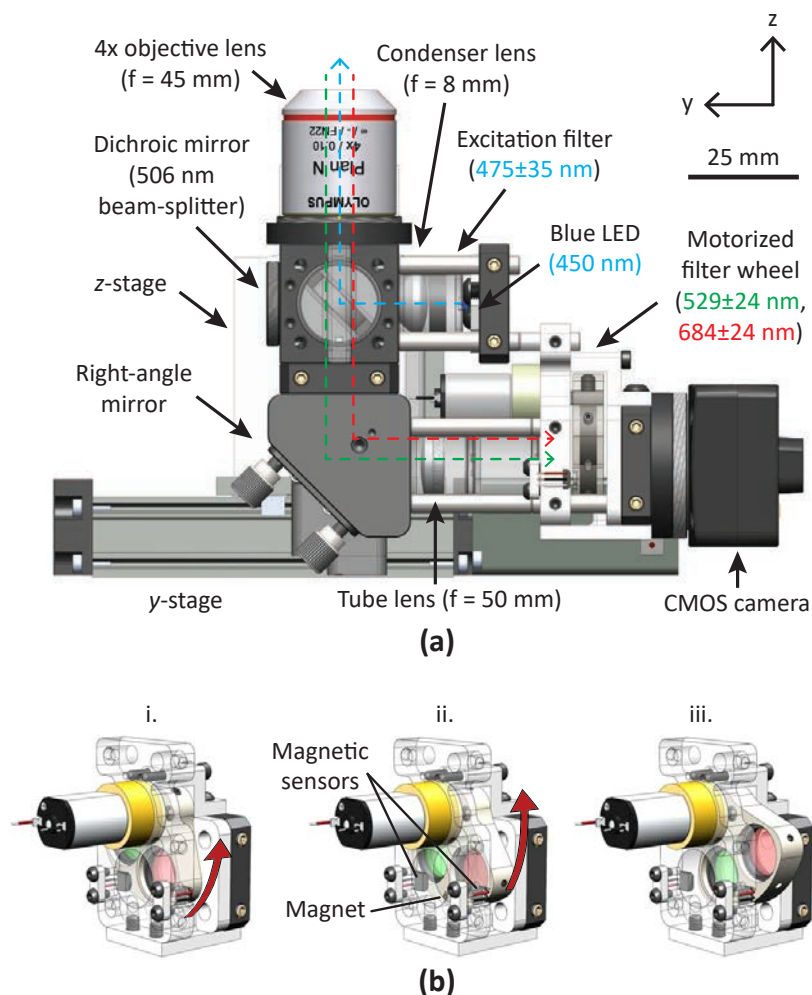


Figure 3.41: Second-gen fluorescent microscope. (a) Conceptual design of the microscope, highlighting key components in the system. Dotted lines indicate excitation (blue) and emission (green/red) light paths. (b) Illustration of the motorized filter wheel mechanism: i. red filter positioned in light path; ii. filter wheel rotating until magnetic sensor is triggered; and iii. green filter positioned in light path. Balter et al. /citeBalter2016a - reproduced by permission of The Royal Society of Chemistry.

holder, and support brackets—all custom designed and rapid prototyped out of acrylonitrile butadiene styrene (ABS) plastic using a 3D printer (Mojo, Stratasys, Ltd.). The motor mount also contains slots for two magnetic-based hall effect sensors (A1120, Allegro MicroSystems, LLC). Embedding a small magnet (D101-N52, $\varnothing 1/16 \text{ in.}$, $1/32 \text{ in.}$ thick, K&J Magnetics, Inc.) in the filter holder, the green and red filters can be alternated using a switching control scheme. Filtered light is captured by a CMOS monochrome camera (Firefly MV, FMVU-03MTM-CS, Point Grey Research Inc.), which transmits captured images

to the host processor (Intel i5-2450M CPU, 2.5 GHz) for analysis.

3.4.3.1.3 Glass Capillary Tube Testing

Glass capillary tubes pre-stained with AO (23-900-105, Fisher Scientific) were used for the first set of experiments to evaluate the microscope and bulk-cell analysis approach. This product also included a plastic float, which was placed in the tube after pipetting in the sample. Use of the plastic float expands the buffy coat tenfold for enhanced visualization²¹². Porcine blood sample controls (424304 and 424305, Drucker Diagnostics) were used to establish standard curves for lym/mon, gran, and absolute leukocyte counts. Blood cells in porcine and human samples have similar densities, which allows us to test the feasibility of the centrifugation approach. The controls included four different levels, corresponding to the values reported in Tab. 3.4. In total, 48 experimental trials were performed (i.e., 4 control levels x 3 replicates x 4 tube orientations).

Table 3.4: Porcine blood sample control levels with reported ranges (cells x $10^3/\mu\text{l}$; monocytes comprise approximately 2% of the lym/mon grouping).

	Level 1	Level 2	Level 3	Level 4
Lym/Mon	2.6 \pm 1.5	3.9 \pm 1.5	6.2 \pm 2.2	7.5 \pm 2.2
Gran	5.3 \pm 2.2	6.5 \pm 2.2	8.5 \pm 3.9	11.1 \pm 3.4
WBCs	7.9 \pm 3.7	10.4 \pm 3.7	14.7 \pm 6.1	18.6 \pm 5.6

The experimental protocol was as follows. First, 70 μl of blood was pipetted into the capillary tube and then the tube was inverted six times to ensure adequate mixing. Next, the plastic float was inserted and the bottom of the tube was capped with a rubber stopper. To fractionate the sample, tubes were placed in 15 ml vials, which were then spun in a bench-top centrifuge (Allegra X-22R, Beckman Coulter) for 5 min at 1500 RCF.

3.4.3.1.3.1 Image Acquisition and Processing To image the buffy coat, capillary tubes were mounted on a test stand above the microscope (Fig. 3.43a). Motorized stages, as seen in Fig. 3.41, were then adjusted through a program written in LabVIEW to obtain a clear image of the fluorescing white cell region. Images were acquired along

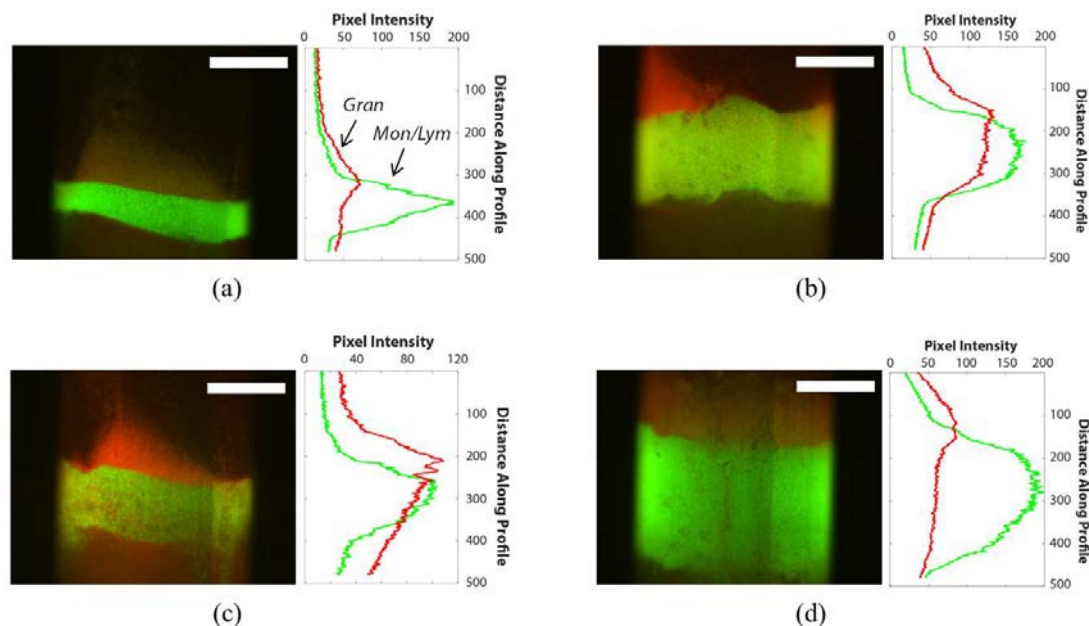


Figure 3.42: Expanded buffy coat in capillary tubes, highlighting the fluorescent signatures of lymphocytes/monocytes and granulocytes. Images and corresponding intensity profiles show the buffy coats for control levels 1–4 (a–d). Scale bar in all images is 1 mm and units for the *distance along profile* on the y-axes are in mm.

the full length of the tube and stitched together post-testing in MATLAB. Four sets of images were acquired along different tube orientations (in 90° increments) to analyze intra-run variability in the buffy coat measurements. Figure 3.42 displays representative images of the fluorescent buffy coat for each blood sample control level.

A preliminary measurement step was first performed, in which the lym/mon and gran layers were manually measured in the green and red channel images respectively using MATLAB. Correlating these pixel lengths to reported cell counts, a series of standard curves were generated for lym/mon, gran, and absolute WBCs. This data served as a baseline before moving on to more complex buffy coat measurement techniques.

An image processing routine was then written in MATLAB to quantify the fluorescing regions in the green (lym/mon) and red (gran) channel images (Fig. 3.43c and d). Beginning with the grayscale image from the green channel, the buffy coat was cropped and intensity values were adjusted via linear contrast stretching. A global threshold was then applied using Otsu's method,²⁹² and morphological operations were used to remove small pixel groups. Fig. 3.43c, ii. shows the segmented border overlaid on the original image.

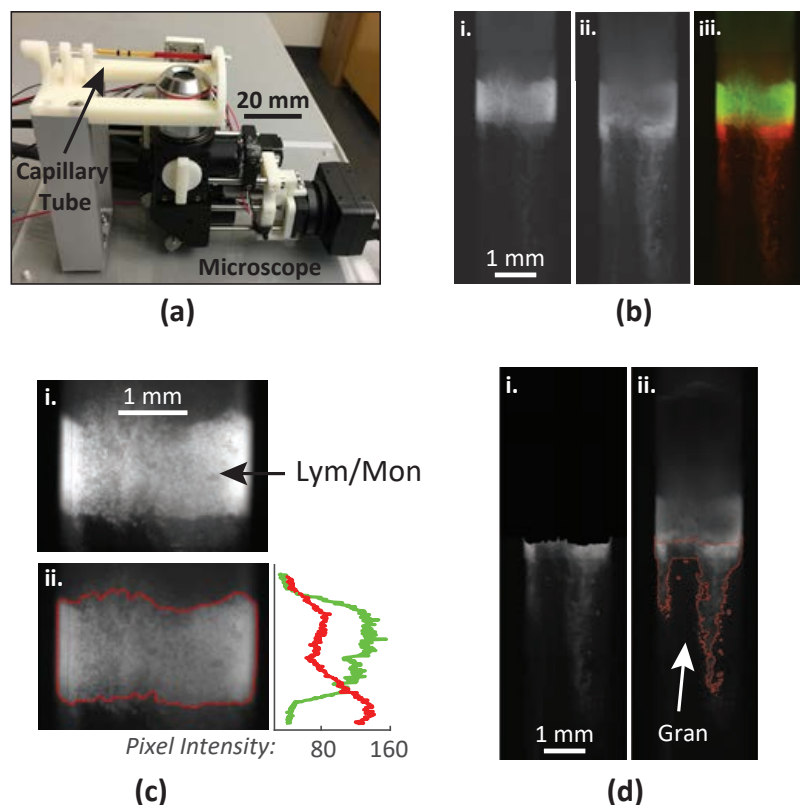


Figure 3.43: Buffy coat image acquisition and processing in capillary tubes. (a) Imaging test platform. (b) Original grayscale images from the i. green and ii. red channels, with iii. displaying the merged image. (c) Processing of green channel image, including: i. cropping and ii. segmentation (intensity profile on the right used to separate lymphocytes from monocytes). (d) Processing of red channel image, including: i. masking to black out the lym/mon layer and ii. segmentation. Balter et al. /citeBalter2016a - reproduced by permission of The Royal Society of Chemistry.

Next, to isolate the granulocyte layer, the segmented region in the green channel was used as a mask in the red channel, preventing the lym/mon layer from interfering with the granulocyte segmentation. Similar to the previous segmentation step, a global threshold was then applied. In this case, however, minimal morphological operations were used in order to preserve cell clumps that may have drifted away from the granulocyte layer. The resulting segmentation is displayed in Fig. 3.43d, ii..

Once the lym/mon and granulocyte layers were segmented, pixel areas were quantified and plotted against measured cell counts to generate standard curves. Cell counts were measured using the QBC Star Analyzer (n=3) and the accuracy of the cell counts was compared against measurements from a flow cytometer (Abbott CD-3700, n=3). A more

detailed description of the image processing routine is provided in Appendix B.1.1.

3.4.3.1.4 Acrylic Chip Testing

In the next set of experiments, acrylic chips were spun on a miniature centrifuge. Custom chips were fabricated using two layers of 1.5 mm-thick cast acrylic sheets (8560K171, McMaster-Carr) and 100 μm -thick pressure sensitive adhesive (PSA) film (DFM 100, FLEX-con) sandwiched in between (Fig. 3.44a). The acrylic sheets were cut using a laser engraver (Zing 24, 60 W, Epilog Laser), whereas channels in the PSA were shaped with a vinyl cutter (SV-8, Roland DGA). The acrylic pieces were surface treated via corona discharge (BD-10A, Electro-Technic) to enhance wettability. Top and bottom layers were then aligned and bonded using a heat press (Clam shell, PowerPress). Altogether, the raw materials cost is $< \$0.10/\text{chip}$.

The design contains an inlet and air vent in the top layer (Fig. 3.44b). When manually pipetting in the sample, it fills the inlet reservoir via capillary action until the air vent is blocked by the fluid. A capillary valve below the inlet reservoir prevents blood from flowing into the sedimentation channel. The combination of the valve and air vent allows the inlet reservoir to trap 5 μl of sample.

Upon centrifugation, the centrifugal force (F_c) exceeds the forces due to surface tension (F_s), allowing the sample to pass through the valve at approximately 1700 rpm. The sedimentation channel width was selected to be 1 mm so that approximately 85% of the channel width could be within the microscope's FOV using a 10x objective lens. Finally, the diameter of the red cell reservoir was selected to balance the sample volume in the inlet reservoir pre-centrifugation, with the sample volume in the sedimentation channel post-centrifugation.

In these experiments, a miniature centrifuge was integrated with the optical detection system (Fig. 3.44e). The centrifuge was driven by a brushless servo (EC-16, 400161, Maxon Precision Motors, Inc.) which contains a mounting hub to securely attach the acrylic chip. A secondary camera (Grasshopper3, GS3-U3-32S4M-C, Point Grey Research Inc.) and strobe light (DT-311A, Shimpo) were positioned above the centrifuge for real-time monitoring of fluid flow in the channels.

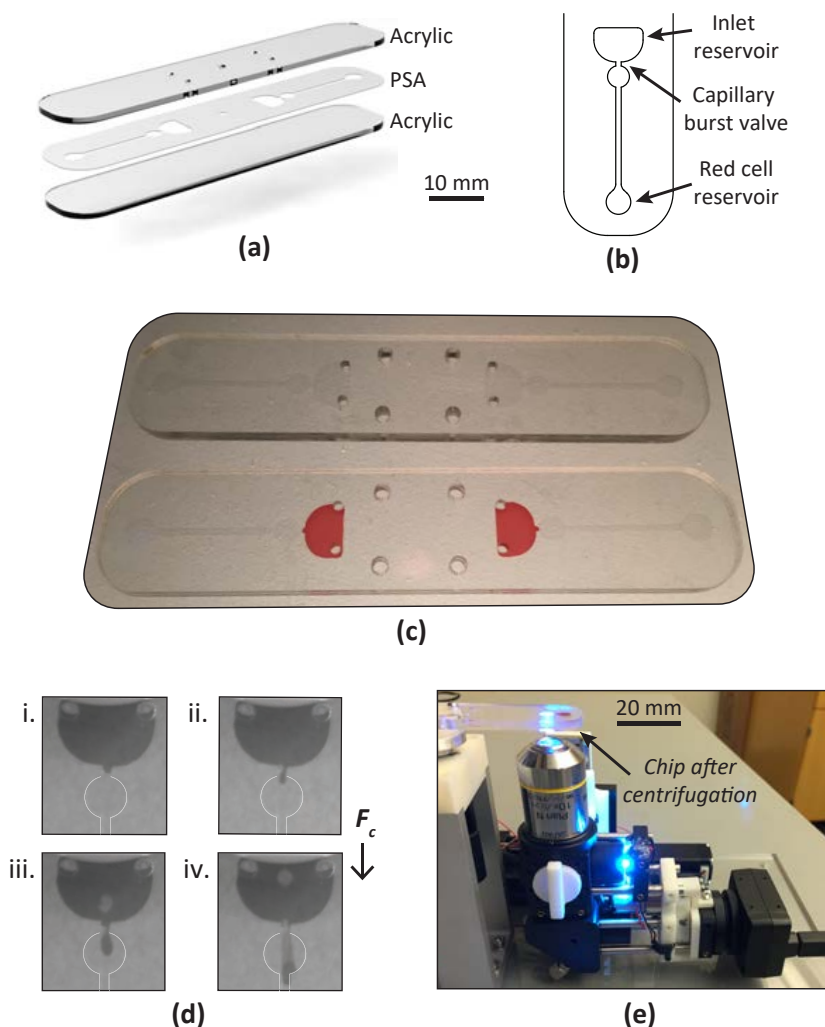


Figure 3.44: Acrylic chip leukocyte testing. (a) Three-layer design—top and bottom: acrylic; middle: PSA. (b) Channel layer consists of an inlet reservoir ($5 \mu\text{l}$ volume), capillary burst valve, sedimentation channel, and red cell collection reservoir. (c) Assembled chip (top); blood sample introduced into the inlet reservoir (bottom). (d) Image sequence of capillary burst valve (channel edges highlighted for clarity): i.–ii. sample held in inlet ($F_c < F_s$); iii.–iv. valve bursts ($F_c > F_s$) and sample flows into sedimentation channel (width: 1 mm). (e) Experimental setup showing the microscope imaging the chip after centrifugation. Balter et al. /citeBalter2016a - reproduced by permission of The Royal Society of Chemistry.

As in the capillary tube experiments, porcine blood sample controls were used for testing; but in this case, samples were manually stained with AO off-chip and no float was used. A much lower sample volume of $5 \mu\text{l}$ was used with the acrylic chips, because of the thin PSA layer (i.e., $100 \mu\text{m}$) and 1 mm wide sedimentation channel. Fig. 3.44c depicts the assembled chip before and after pipetting in the sample.

3.4.3.1.4.1 Image Acquisition and Processing Following centrifugation, the detection channel of the acrylic chip was aligned with the microscope, and the image was focused by adjusting the motorized stages in the LabVIEW interface. A series of images were then acquired along the length of the channel in set increments using a pre-programmed routine (only one image set was acquired for each run). Similar to the image processing scheme used for capillary tube experiments, green and red channel images were stitched together in MATLAB.

A global threshold was again applied to extract and measure the lym/mon layer from the green channel image, however in this case, we used a different approach to quantify the granulocytes. Since granulocytes tended to drift-off into the packed red cell layer (even more pronounced with small sample volumes) it can be challenging to reliably segment a region of cells. Instead, we used a summation of pixels approach in the red channel image to quantify granulocytes—a simplified method in which the intensities of each pixel are summed together to produce a total intensity value describing the level of fluorescence.

3.4.3.2 Experimental Results

3.4.3.2.1 Glass Capillary Tube Testing

Our objectives for the first set of experiments using capillary tubes were to: (1) extract the leukocyte sub-type layers from analyzing intensity profiles of the green and red images; (2) evaluate the variability to see if tube orientation results in different buffy coat measurements and thus different cell counts; (3) evaluate the accuracy and precision of the bulk-cell analysis approach through generating standard curves; and (4) separate monocytes from lymphocytes based on pixel intensities and cluster analysis.

Computing the intra-run standard deviation for each experimental trial, little variability was observed in the lym/mon pixel area. However, there was a substantial amount of variability in the granulocyte pixel area based on the orientation of the tube on the imaging platform (Fig. 3.45). Granulocytes had a tendency to clump to one side of the tube, resulting in a radially non-uniform distribution. This motivated our decision to image on all four sides of the tube when extracting data to generate standard curves. Imaging on only

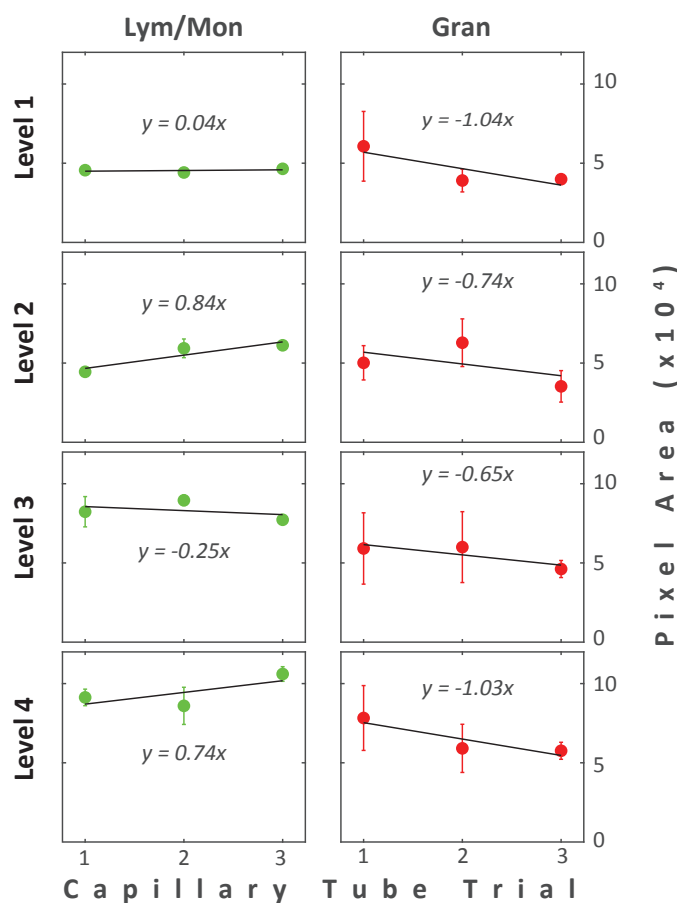


Figure 3.45: Variability in buffy coat measurements in capillary tubes. 4 image sets were captured for each tube. Data points represent the average segmented area; error bars represent SD (n=4). Linear fits show inter-run variability due to different tubes/samples used for each control level and error bars show intra-run variability due to tube orientation. Balter et al. /citeBalter2016a - reproduced by permission of The Royal Society of Chemistry.

one side, like the QBC analyzer does, can give misleading granulocyte counts if it happens to be the wrong side.

The first set of standard curves were generated from manually measuring the length of the lym/mon and gran layer in the green and red channel images respectively, and plotting these values against reported cell counts. The curves, displayed in Fig. 3.46, exhibit strong linear fits for each cell count (i.e., $r^2 = 0.987$, 0.961 , and 0.977 for lym/mon, gran, and absolute WBCs respectively). However, there was some variability observed in the granulocyte measurements. Specifically, our measurements indicated lower amounts of granulocytes compared to lymphocytes/monocytes, which does not correlate with the reference cell counts.

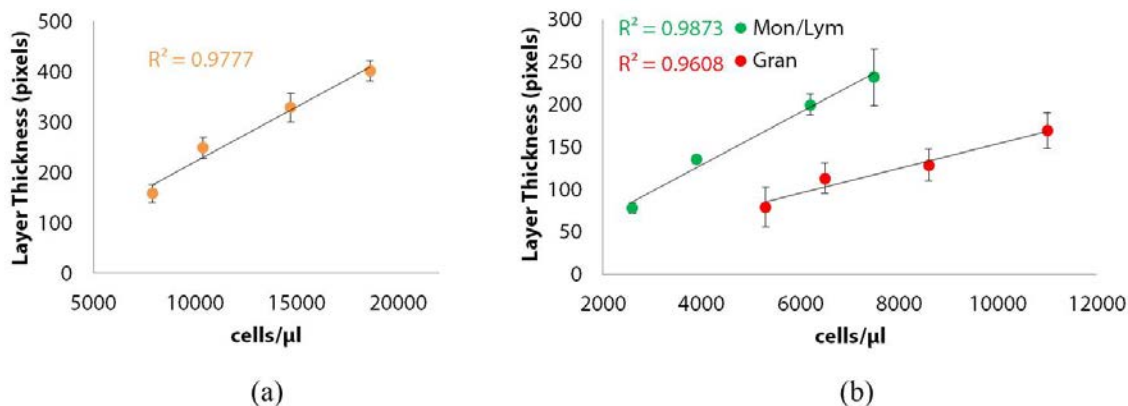


Figure 3.46: Capillary tube standard curves for (a) total WBCs and (b) lym/mon and gran. Buffy coat lengths plotted on the y -axes (mean of $n=3$; error bars represent standard deviation) are compared against reported cell counts plotted on the x -axes. Solid black lines represent linear fits.

Next, analyzing the standard curves in Fig. 3.47, the linear regressions in each plot demonstrate strong linear fits between measured pixel areas and known cell counts (i.e., $r^2 = 0.993$, 0.990 , and 0.993 for lym/mon, gran, and absolute WBCs respectively). Interestingly, the pixel area of the lym/mon layer was consistently greater than that of the gran layer across each control level, despite there being a greater percentage of granulocytes in the samples. Inter-run variation (computed as the standard deviation between separate experimental trials for each control level) was also much lower in our studies compared to the reported variations for the samples listed in Tab. 3.4. These reported variations from the manufacturer of the controls were most likely determined from experimental testing on the QBC analyzer. One explanation for the large ranges is that the analyzer only images tubes at one orientation, potentially resulting in inaccurate cell counts if cells, particularly granulocytes, are clumped to one side.

In some cases, these cells were observed to drift away from the granulocyte band into the packed red cell layer. The plastic float placed in the capillary tube before centrifugation may have contributed to the uneven spreading of granulocytes. There were also times when cells clumped around the ends of the plastic float, serving as a barrier and preventing these cells from reaching their respective density band.

Finally, we attempted to isolate lymphocytes from monocytes by analyzing the pixel intensities from the green and red channel images within the segmented lym/mon layer.

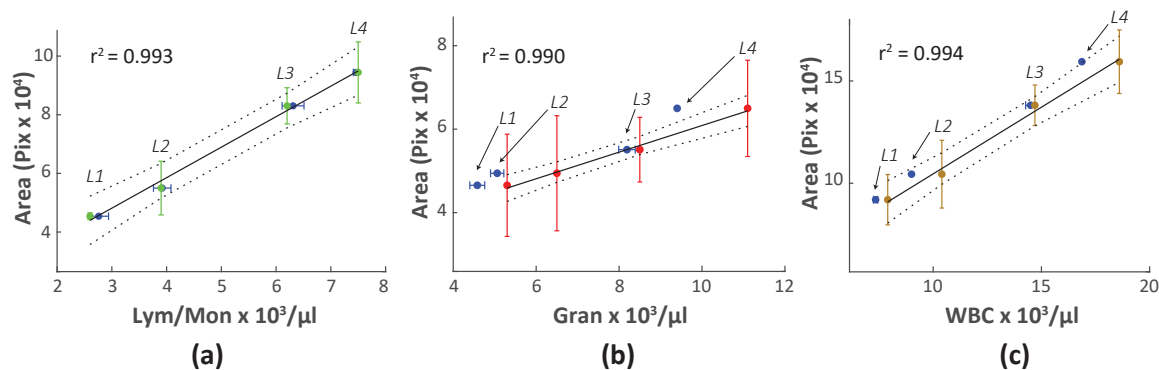


Figure 3.47: Capillary tube standard curves for (a) lym/mon, (b) gran, and (c) total WBCs. Buffy coat areas plotted on the y -axes (mean of $n=12$: 3 samples per level, 4 tube orientations; error bars represent SD) compared against measured cell counts using the QBC Analyzer plotted on the x -axes. For the 4 blood control levels (labeled L1–4), solid and dotted black lines represent linear fits and 95% confidence intervals respectively. Accuracy of cell counts compared against flow cytometry measurements plotted on the x -axes (blue points, mean of $n=3$, error bars represent SD). Balter et al. /citeBalter2016a - reproduced by permission of The Royal Society of Chemistry.

In human samples, lymphocytes typically outnumber monocytes 5–6:1, and monocytes are difficult to distinguish from lymphocytes because of their similar size, density, and appearance²⁰⁵. However, these sub-types exhibit different relative proportions of DNA and RNA, and thus will fluoresce differently when stained with AO. Lymphocytes emit more green when excited under blue light compared to monocytes, whereas monocytes also emit a moderate amount of red. Analyzing the lym/mon segmented region in the green and red channel images, Fig. 3.48 shows evidence for isolating monocytes from lymphocytes ($n = 1$). Here, pixel intensity values from the green and red channel images are plotted against each other to create scatter plots.

Table 3.5: Estimated mon from the lym/mon region computed via pixel clustering, compared to measured values via flow cytometry (cells $\times 10^3/\mu\text{l}$). Balter et al. /citeBalter2016a - reproduced by permission of The Royal Society of Chemistry.

	Level 1	Level 2	Level 3	Level 4
Estimated	7.4	12.4	22.6	7.7
Measured	5 ± 2	7 ± 4	5 ± 1	7 ± 3
Reported	2.0	2.0	2.0	2.0

Analyzing these results even further, we investigated a clustering technique based on

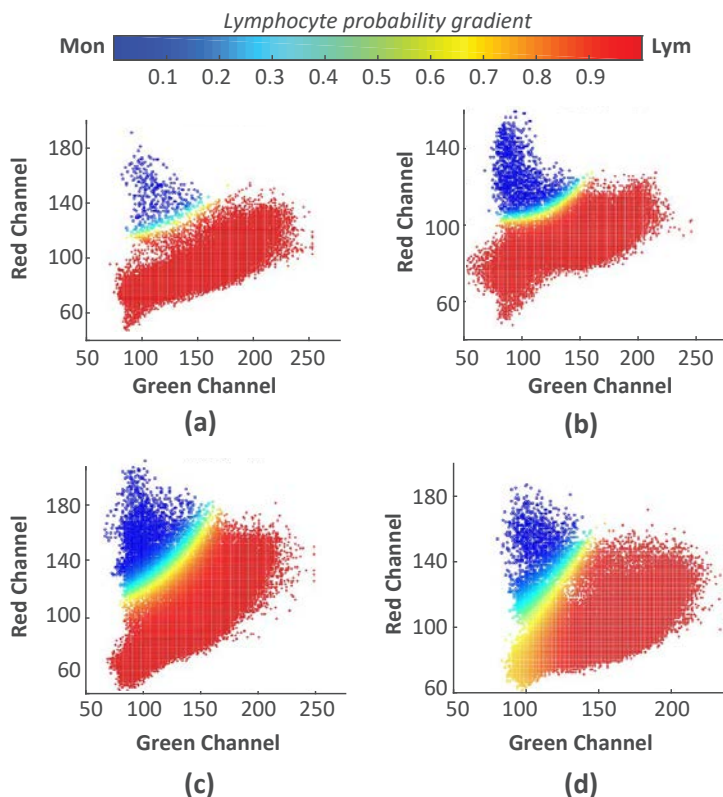


Figure 3.48: Representative scatter plots of green and red channel image pixel intensities for blood control levels 1–4 (a–d) using capillary tubes. A GMM was implemented for data clustering to separate monocyte regions (blue) from lymphocyte regions (red). Color map shows the posterior probability of each pixel data point assigned to the lymphocyte cluster. Balter et al. /citeBalter2016a - reproduced by permission of The Royal Society of Chemistry.

Gaussian mixture models (GMM) to separate the two groups of cells based on their chemical fluorescence profile. GMM clustering can accommodate regions with various sizes and correlation structures within them. GMM operates by assigning every data point to a multivariate normal component (i.e., cluster) by maximizing component posterior probability²⁹⁴. Cluster results are displayed in Fig. 3.48, with heat maps indicating the likelihood of a pixel belonging to the lymphocyte cluster. Tab. 3.5 shows results from estimating the number of monocytes in each control sample via cluster analysis. For each control level, pixel clustering was able to estimate the number of monocytes to within a 2% difference from reported values.

3.4.3.2.2 Acrylic Chip Testing

As we discovered in the previous experiments, imaging on only one side of the capillary tube can give misleading cell counts if it happens to be the wrong side. By housing the sample within a flat, rectangular channel, the need to repeatedly rotate and image the tube is avoided. Additionally, imaging on a flat plane avoids having different focusing distances, as was encountered in the round capillary tubes. Focusing on the top part of the tube required a different working distance from the objective lens, compared to focusing on the sides of the tube. Thus to image the buffy layer on the acrylic chips, the objective lens was kept at a fixed distance from the acrylic chip.

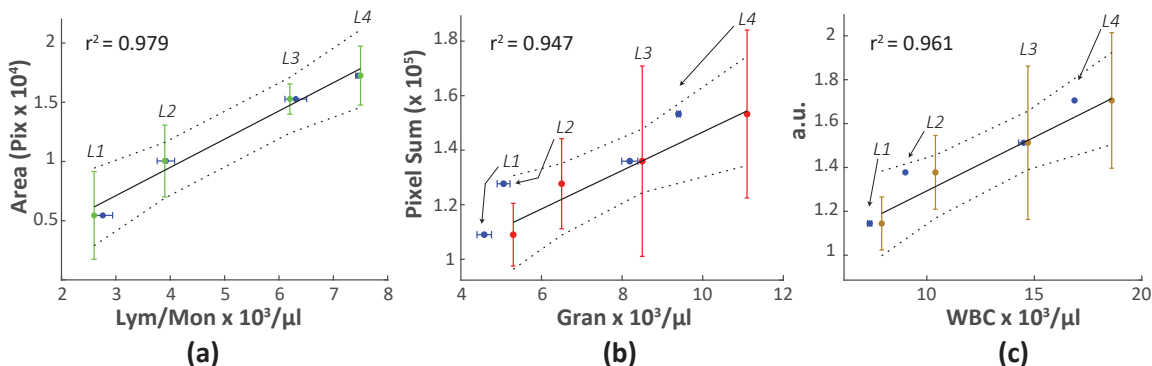


Figure 3.49: Acrylic chip standard curves for (a) lym/mon, (b) gran, and (c) total WBCs (a.u. indicates the summation of pixel areas and intensities from the lym/mon and gran data respectively). Buffy coat measurements (mean of $n=3$, error bars represent SD) are compared against measured cell counts using the QBC Analyzer. For the 4 control levels (labeled L1–4), solid and dotted black lines represent linear fits and 95% confidence intervals respectively. Accuracy of cell counts was compared against flow cytometry measurements (blue points, mean of $n=3$, error bars represent SD). Balter et al. /citeBalter2016a - reproduced by permission of The Royal Society of Chemistry.

Standard curves are displayed in Fig. 3.49, where the results show strong linear fits (i.e., $r^2 = 0.969$, 0.858 , and 0.899 for lym/mon, gran, and absolute WBCs respectively); however, more variability is observed compared to results obtained using capillary tubes. Possible explanations for the increased variability include: the lack of a float to expand the buffy coat, low-sample volumes, and poor separation between blood cell layers after centrifugation. Although the use of a plastic float expands the buffy coat, it can also cause clumping of cells around the ends. In the case of the acrylic chips, no float was used due to the small channel layer thickness (i.e., $100\ \mu\text{m}$).

As was expected, granulocytes tended to drift off into the packed red cell layer considerably more than those from the capillary tube experiments. This introduced a significant amount of noise when trying to quantify the granulocytes through segmentation. Instead, we used a summation of pixels approach which worked well in estimating the number of granulocytes. After masking out the lym/mon region and areas above (i.e., platelets and plasma), the remaining fluorescence observed in the red channel was assumed to be from the granulocytes. In the current configuration, the optical detection system captured monochrome, 8-bit images, where pixel values can range from 0–255. Considering black pixels with a value of 0 indicate areas where no cells are present, summing image pixels is an interesting method to isolate and enumerate granulocytes.

3.4.3.3 Discussion

In conclusion, two methods for differential leukocyte counting on a centrifugal microfluidics platform were demonstrated, evaluating the bulk-cell analysis approach by generating standard curves for a 2-part differential and absolute WBC count. Preliminary evidence for isolating lymphocytes from monocytes and obtaining a 3-part differential by analyzing pixel intensities in the green and red channel images was also presented.

More accurate and repeatable leukocyte counts were observed in the capillary tube control compared to the acrylic chip group. However, capillary tubes required larger sample volumes (i.e., 70 μ l vs. 5 μ l per test) and more expensive consumables from a raw materials standpoint. Specifically, the cost of one capillary tube could range from \$1.15 to \$5.75, based on an 80% or 0% profit margin respectively from the listed price²¹¹. Conversely, the raw materials cost for one acrylic chip is \$0.10. Conversely, the acrylic chips provided a flat imaging plane for measuring the buffy coat and a low-cost design that can easily be modified to enhance leukocyte spreading, and thus, improve cell count accuracy and repeatability. Specifically, raw materials cost for one acrylic chip is <\$0.10, and the manufacturing process to produce these devices is highly automated through the use of a laser and vinyl cutter. Using this process, it takes approximately 10 and 20 seconds to cut one layer of acrylic and PSA respectively. In one hour, 360 acrylic chips and 175 PSA layers can be produced with our current setup. For scaling, industrial cutters can be used that have larger workspaces

and faster operating times.

Ordering raw materials in higher volumes (i.e., enough to manufacture hundreds of chips) would likely reduce these costs to <\$0.10/chip. Similarly, the size and cost of the centrifugal and optical detection systems may also be reduced with further development. Overall, the strength of this approach is the ability to obtain accurate leukocyte counts using simple low-cost hardware, one nuclear stain, no dilution, no density medium, minimal sample preparation, no flow focusing, and no complicated image analysis.

Nevertheless, several limitations with the bulk-cell analysis approach remain. As previously mentioned, the capillary tube method allowed misleading cell counts due to imaging on only one side of the tube—the curved surface of which also required different focusing distances. Our solution was to fabricate a flat acrylic chip, in which we chose to exclude a plastic float: the trade-off being that the granulocytes were allowed to spread evenly without clumping around the float, but at the expense of not expanding the buffy layer. In future work, we could instead use a density medium to better isolate the granulocyte layer from the packed red cell layer. Additionally, experimenting with different density media could potentially compensate for the lack of buffy layer expansion. Adjusting the channel geometry and reducing the channel height to 50 or 10 μm is another approach to enhance buffy layer expansion and reduce variability. Similarly, channels with non-uniform heights can be machined into the acrylic substrate using micro-milling techniques²⁹⁵.

Overall, for both the capillary tube and acrylic chip studies, more rigorous testing needs to be done with human blood samples. This includes generating another set of standard curves using discarded patient samples and more formally validating cell counts via flow cytometry. Standard curves can then be stored in the software of the device and referenced when outputting diagnostic cell counts during run-time. Moreover, to further evaluate the 3-part leukocyte differential approach via pixel clustering, more rigorous testing and data analysis needs to be conducted in future studies. Scatter plots displayed in Fig. 3.48 demonstrate promising results for one sample in each control level, but this method needs to be validated with larger sample sizes.

Auto-focusing algorithms will also be explored so the microscope can automatically localize and measure the buffy coat without user input. In this fashion, the system could

make fine position adjustments along the vertical axis to maximize contrast in the image. This could also enable real-time image processing and buffy coat quantification immediately after centrifugation. Although the image processing routines were able to estimate cell counts in these studies, more robust segmentation approaches will be tested in the future. Using the summation of pixels approach to enumerate granulocytes, the microscope had to scan the length of the packed red cell layer to collect images of granulocytes that drifted away from the buffy coat area. With the addition of density medium, we expect granulocytes to form a more cohesive band, thereby improving the cell estimation approach, either through summation of pixels or segmentation.

Finally, we would like to expand the diagnostic capability of the acrylic chip by expanding the design to automate the sample processing steps and simultaneous detection of other analytes. For example, incorporating additional reservoirs and valves would allow for the storage and release of AO, obviating the need for manually mixing the sample off-chip. In addition, we could implement centrifugo-pneumatic pumping to extract leukocytes for further off-line processing (e.g., genomic analysis). Through the use of pneumatic siphoning, plasma can be isolated to allow for the detection of other analytes on-chip, including chemistries and proteins. Altogether, the integration of multiple blood panels on one chip has the potential to simplify the process of diagnostic blood sample analysis and reduce costs associated with POC testing.

3.4.4 Detection of Cells, Proteins, and Chemistries On-chip

Building off the work described in Section 3.4.3, the centrifuge analyzer was redesigned to incorporate the detection of multiple blood analytes in one device. This was accomplished by creating a CD-like chip (herein referred to as the disc) and integrating the photometry module introduced in Section 3.3.2 into the analyzer. With this setup, as seen in Fig. 3.50, the device is capable of detecting cells, proteins, and chemistries in blood via fluorescence detection and optical absorption.

As previously described, the centrifuge regulates fluid flow in the disc, allowing the sample to sediment, mix with the appropriate reagents, and move to the indicated detection chambers. Reagents can be stored in dry format or in miniature stick-packaging, as discussed

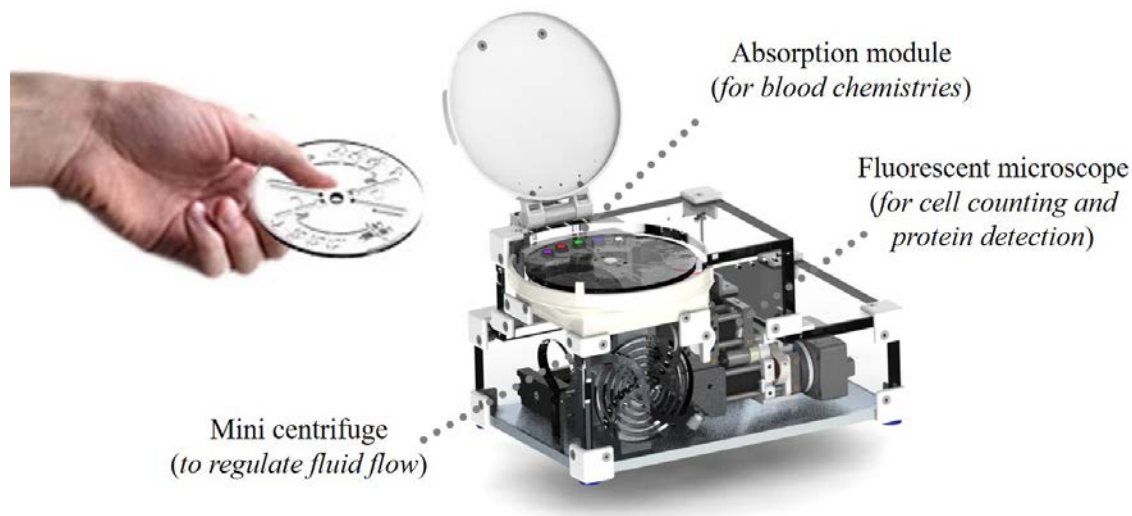


Figure 3.50: Centrifuge-based blood analyzer design concept.

in^{181,296}. Here, reagents can be pre-packaged, integrated in the disc during fabrication, and released at a specific centrifuge spin frequency during run-time.

For analyte detection, the fluorescent microscope shown in Fig. 3.41 is used to quantify WBCs by measuring the buffy coat area, and can also be utilized to quantify targeted proteins in the sample. As an example, if implementing a bead-based immunoassay where the detection antibody fluoresces under blue light, the microscope can monitor the emitted light intensity, and thus quantify the amount of protein in the sample. To detect small molecules, like blood chemistries, the photometry module is situated on the periphery of the disc, where the LEDs are oriented underneath, and the photodetectors are placed above (embedded in the door used to access the centrifuge). In the current setup, there are 5 LEDs, though the number can be increased, space requirements permitting.

To integrate the components and create a compact device, it was necessary to design an enclosure to store all the associated electronics and develop an efficient method to route cables to and from each system. Figure 3.51 and 3.52, shows the design and implementation of the centrifuge analyzer respectively, with the electronics stored in the device. Acrylic panels were shaped using a laser cutter and assembled using joint connectors and screw fasteners for easy assembly. Moreover, this new design also includes the dispenser pump positioned on the top of the device. As stated earlier, this unit functions to deliver blood

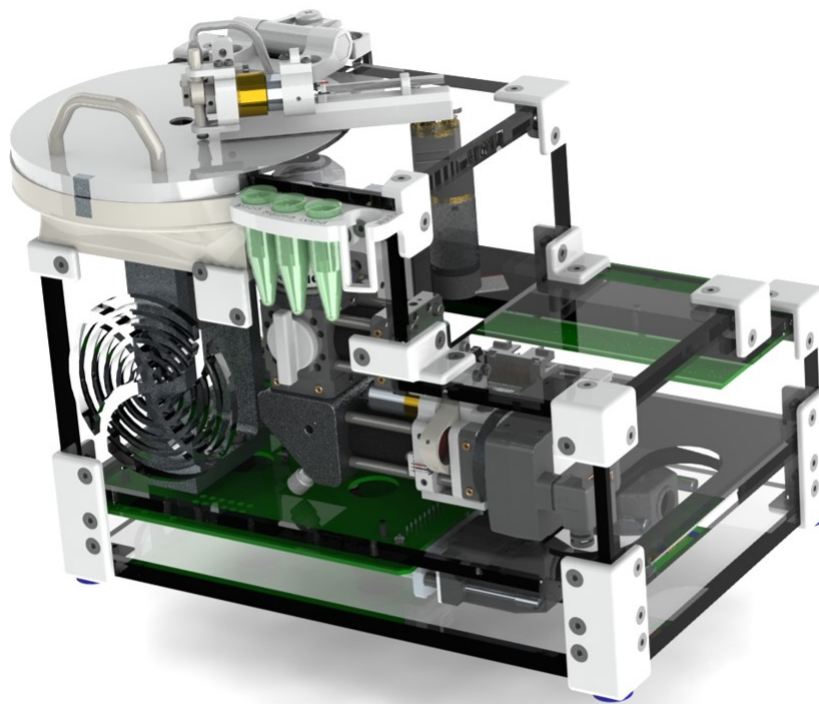


Figure 3.51: Centrifuge blood analyzer design with electronics contained in the device. The design includes the dispenser pump, and 1.5 ml tubes located on the front panel are included for dispensing blood, isolated plasma, and lysed RBCs.

from the venipuncture robot to the disc through an opening in the top lid. The nozzle lowers over the inlet in the disc, creating a leak-proof seal to deliver the sample. The nozzle then rises and the dispenser rotates over to a waste container to flush the tubing with a saline wash fluid.

After the procedure, the dispenser can rotate back over to the disc, collect isolated biological constituents in the sample (e.g., plasma and lysed RBCs), and dispense them in indicated vials stored on the side of the device. This allows for off-line processing of blood components, in addition to the assays provided in the system. This flexibility allows the device to be used in multiple settings: in clinical and research environments.

In total, the device contains 6-DOF: three in the microscope, one in the centrifuge, one in the dispenser, and one in the rotary arm. The linear stages actuating the microscope are controlled by a two-axis stepper motor driver (X-MCB2, Zaber Technologies Inc). As seen in Fig. 3.51, the casing for the motor driver was removed to conserve space, and is

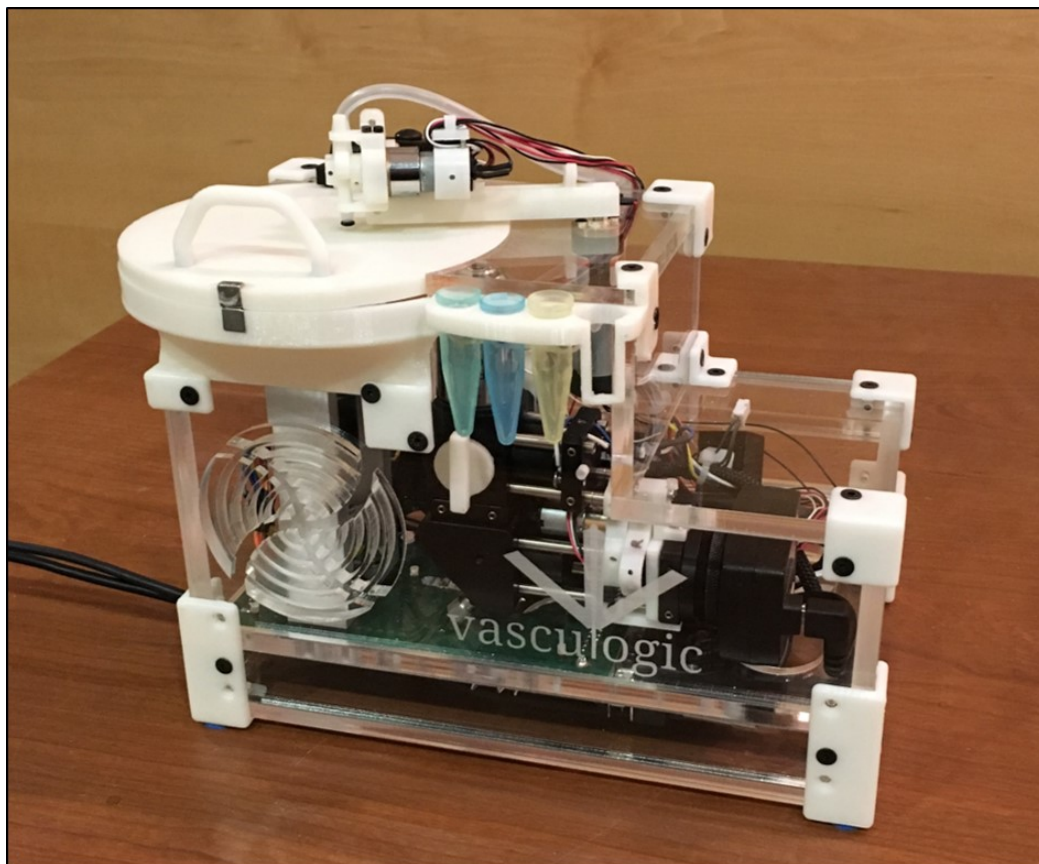


Figure 3.52: Centrifuge blood analyzer prototype.

placed underneath the base platform of the centrifuge. The driver communicates with the host processor via USB and takes an input of 24 V (using an AC to DC power adapter). This voltage supply is then routed to the motor controller driving the centrifuge motor (360665 and 407582, Maxon Precision Motors, Inc.). From there, the voltage pins connect to a custom designed electrical adapter board that regulates the input voltage down to 12 V to power the microscope LED, peristaltic pump, and motor driver for the dispenser rotary arm (390438, Maxon Precision Motors, Inc.). The Maxon motor drivers connect to each other via a communication area network (CAN) protocol, and talk to the host processor via USB in a master-slave configuration.

To power the small DC gearmotors implemented in the microscope filter wheel and dispenser unit, the supply voltage is further regulated down to 5 V on the circuit board, and is routed to bi-directional motor drivers (sn754410, SparkFun Electronics). These motor drivers are controlled via digital output signals from the on-board microprocessors.

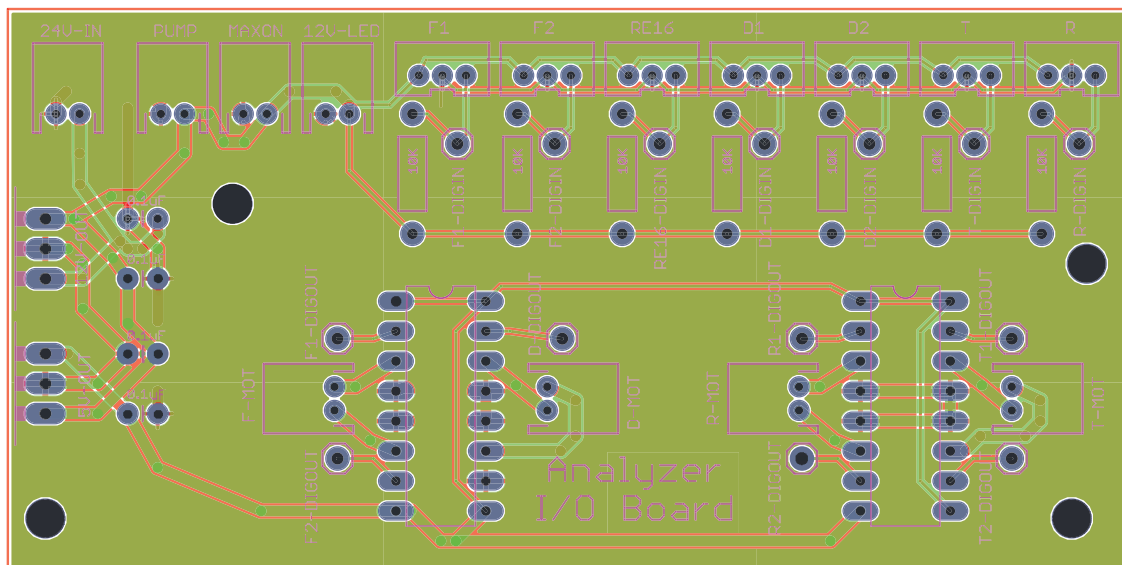


Figure 3.53: Centrifuge analyzer PCB design for routing power and DIO lines.

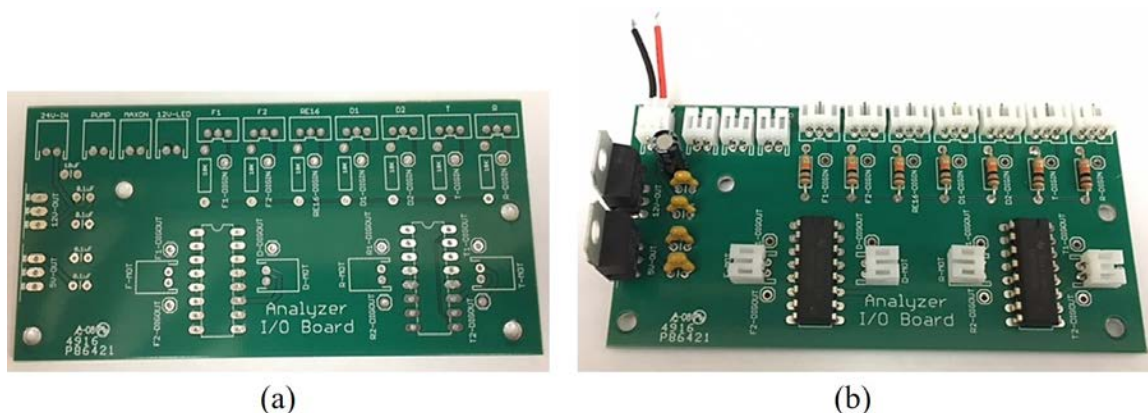


Figure 3.54: Fabricated PCB: (a) before and (b) after assembling the components.

In addition to handling the power lines, the circuit board also routes digital input and output (DIO) lines from the microprocessors to the associated motors for positioning and homing control. Both the Zaber and Maxon motor drivers include DIO lines. The printed circuit board design and fabricated assembly is shown in Fig. 3.53 and 3.54 respectively, with a more detailed schematic and bill of materials included in Appendix B.1.2.

With the construction of the analyzer and the contained electronics, it is a true plug-and-play module. All one needs to do is simply connect the power line to an AC outlet and the USB cables to the host processor in order to use the system. The software controlling the device is written in LabVIEW, where each module in the analyzer can be controlled

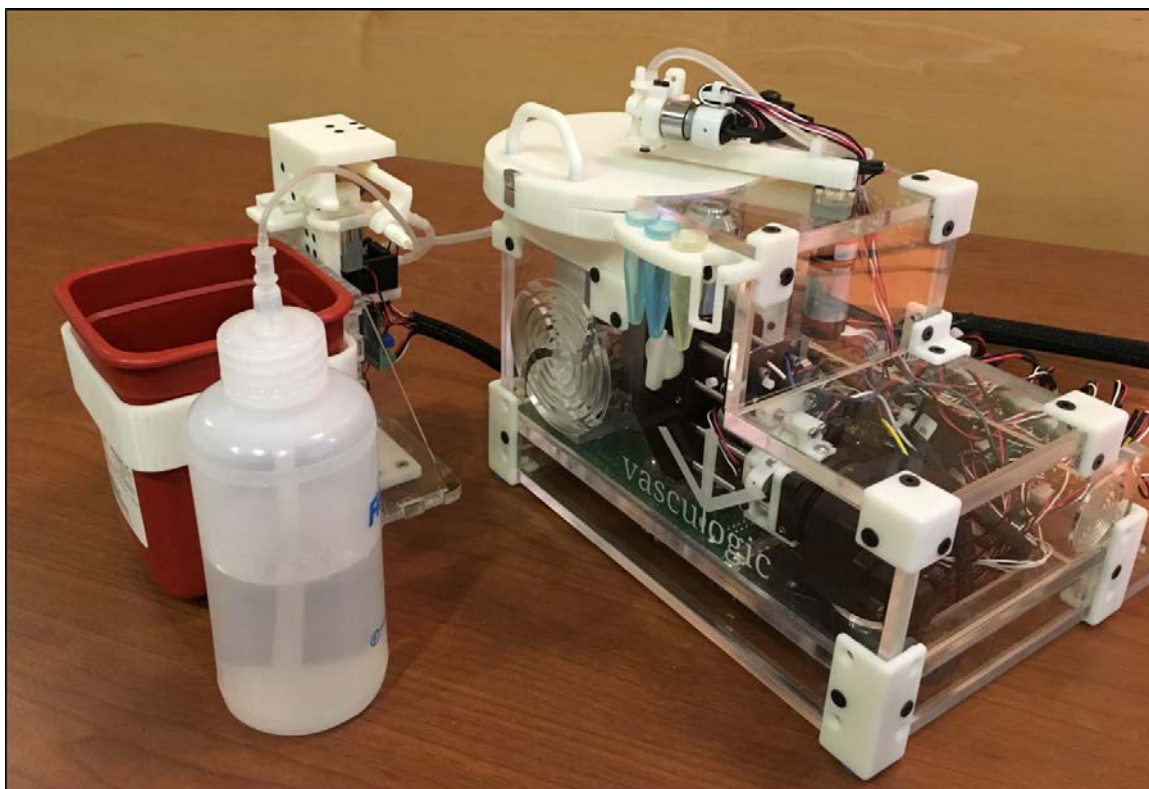


Figure 3.55: Blood analyzer prototype integrated with the tube switching pump.

independently, or a spin protocol and detection routine can be programmed using the pre-built control blocks. Furthermore, Fig. 3.55 shows the analyzer integrated with the tube switching pump for automatic sample loading, dispensing, and cleaning of the tube lines.

Altogether, this system is a platform device that has the potential for detecting a range of analytes: both large and small molecules. Another reason for building this self-contained device was to open up opportunities for future research projects, making it easy for new students to operate the system. My thesis work for this part of the project specifically focused on the detection of WBCs on the centrifuge platform, but the following sections describe how to extend this approach for the detection of proteins and blood chemistries. Finally, preliminary work for achieving this is presented.

3.4.4.1 Chip Design

The key factor in running multiple blood panels in a single device lies in the chip design. Using centrifugal microfluidics, the sample can be manipulated on-disc simply by varying

the speed of the centrifuge. In this fashion, the sample preparation and analysis can be fully automated. Looking at the concept disc in Fig. 3.56, the following analytical processes can be achieved. First, reagent storage and release. A range of techniques have been proposed and tested, all with varying success^{193,198,297–299}. In our design, capillary burst valves were implemented, evaluated, and characterized, in which the sample is held within a reservoir until a certain burst frequency is achieved, at which point the sample flows past the valve. This is achieved once the centrifugal forces exceed the capillary forces in the microchannel.

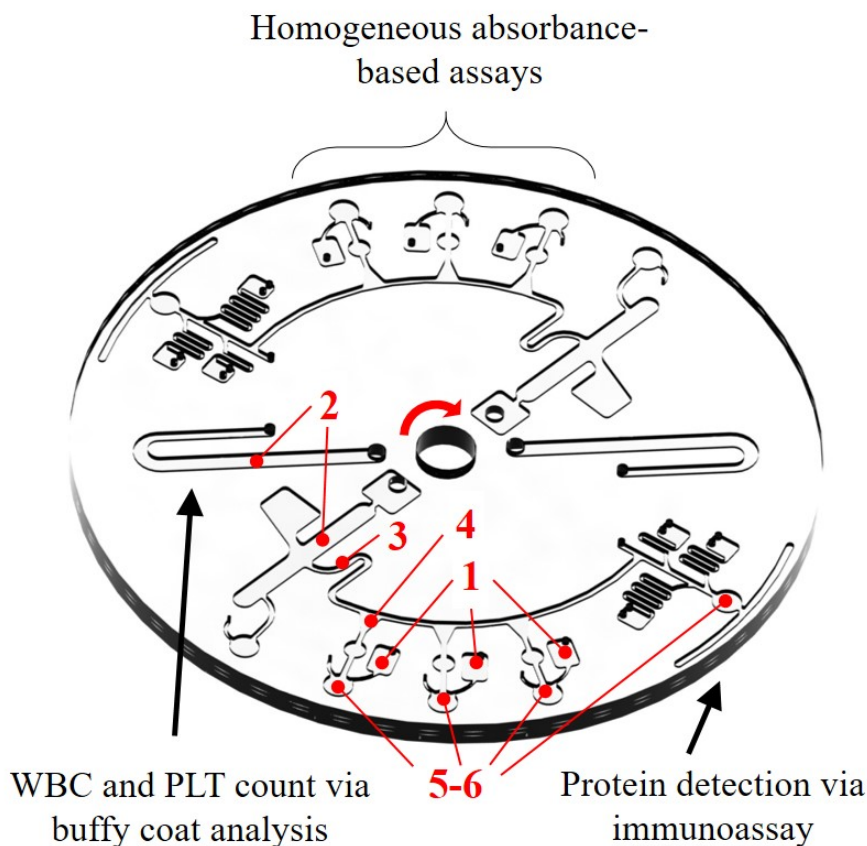


Figure 3.56: Blood analyzer CD-like disc concept for the detection of cells, proteins, and chemistries. Numbered analytical processes: 1. reagent storage and release, 2. sedimentation, 3. liquid transport, 4. metering, 5. mixing, and 6. detection.

Second, sedimentation. The centrifugal platform lends itself to this analytical process, and plasma extraction is a critical step for protein and blood chemistry assays. In these cases, the sensitivity of the measurement is highly dependent on the purity of the extracted plasma^{182,183}. Third, liquid transport, which is critical to route samples to the appropriate

reaction and detection chambers³⁰⁰. Fourth, metering, that is, controlling how much sample volume is flowing to these reaction and detection chambers¹⁸⁵. Fifth, mixing—a key step for antigen-antibody binding reactions and blood chemistry assays¹⁸⁸. Finally, detection, which in our case is optical-based in which a fluorescent microscope and photometry module are situated on the periphery of the disc.

To fabricate the disc, channels are first shaped in acrylic and PSA via laser and vinyl cutting respectively. The number of layers varies based on the chip design. For the concept disc displayed in Fig. 3.56, five layers are used, in which the top acrylic layer contains inlets, outlets, and air vent holes; the middle PSA layers contain the microchannels; the middle acrylic layer contains the reservoirs; and the bottom acrylic layer serves as a base. Then, using a 3D-printed alignment rig, the layers are aligned and pressed together using a heat press to ensure a leak-proof seal at high spin speeds. A more detailed description of the fabrication protocol of the five layer chip design is presented in Section 3.4.4.3.2.

Due to the modular nature of the disc design and rapid fabrication process, the aforementioned analytical processes can be evaluated independently and linked together once fully tested. This allows for the systematic evaluation of each component and solving isolated problems in the channel designs before integration. As an example, this was demonstrated in our evaluation of the WBC assay, where only the specific microchannels needed for the test were implemented in the chip. To extend upon this work, a series of experiments were then performed to evaluate capillary burst valves and rapid plasma extraction via centrifugo-pneumatic pumping.

3.4.4.2 Capillary Burst Valves

Valving is a critical function in microfluidic applications and is typically accomplished through the use of active mechanisms^{301–304}. The most common being an electrical switch valve to open or close a passageway to allow liquid to flow through or be blocked. An interesting concept in the field of centrifugal microfluidics is the use of capillary burst valves—a passive valving approach based on the interaction between centrifugal and capillary forces. This technique relies solely on the geometry of the channel and the spin frequency of the centrifuge motor; no complicated electrical switches and associated control electronics are

needed. Concretely, capillary burst valves can be designed to release fluid at certain motor spin frequencies, allowing for the timed release of sample and reagents^{187,305}. This is particularly important when integrating multiple assays on one chip, where numerous analytical steps need to seamlessly operate in parallel or in serial. In this section, we first present a numerical analysis, outlining the theoretical burst frequencies for different valve geometries. Then, a series of experiments were conducted to validate the numerical analysis.

3.4.4.2.1 Numerical Burst Frequency Calculations

The derivations discussed below are based on the concepts presented in Chen et al¹⁸⁷. The burst frequency (ω) can be computed based on a pressure balance between the centrifugally induced pressure (Δp_c) and the barrier pressure at the liquid front (i.e., the burst pressure— Δp_b). When p_c exceeds p_b , the valve breaks, allowing liquid to flow through. The centrifugally induced pressure is expressed in Eq. 3.4:

$$\Delta p_c = \rho \omega^2 \Delta r r_m \quad (3.4)$$

where ρ is the liquid density, ω is the angular speed (in Hz), Δr is the distance from the disc center to the reservoir (r_1) minus the distance from the disc center to the valve (r_2), and r_m equals $(r_2 + r_1)/2$. The dimensions of r_1 and r_2 are displayed on the chip in Fig. 3.58. Conversely, the burst pressure is expressed in Eq. 3.5:

$$\Delta p_b = 4\gamma_{la} \sin\theta_c / D_h \quad (3.5)$$

where γ_{la} is the surface tension at the liquid-air interface, θ_c is the contact angle, and D_h is the hydraulic diameter of the capillary burst valve channel (in our case, the channel width, when analyzing 1D geometry). Setting p_c equal to p_b and solving for ω , burst speeds were calculated with varying dimensions of D_h (0.5–2 mm), r_1 (5–16 mm), and r_2 (12–23 mm), using Eq. 3.6, and assuming a θ of 90°.

$$\omega = \sqrt{\frac{4\gamma_{la}}{D_h \rho (r_2 - r_1) \left(\frac{r_1 + r_2}{2}\right)}} \quad (3.6)$$

3.4.4.2.2 Experimental Testing

3.4.4.2.2.1 Test Platform Theoretical burst speeds were then experimentally validated by fabricating acrylic chips (similar to those discussed in Section 3.4.3.1) and spinning them on a custom-designed test platform. As outlined in Fig. 3.57, the platform consisted of four main components: a centrifuge, high-speed camera, enclosure, and strobe light.

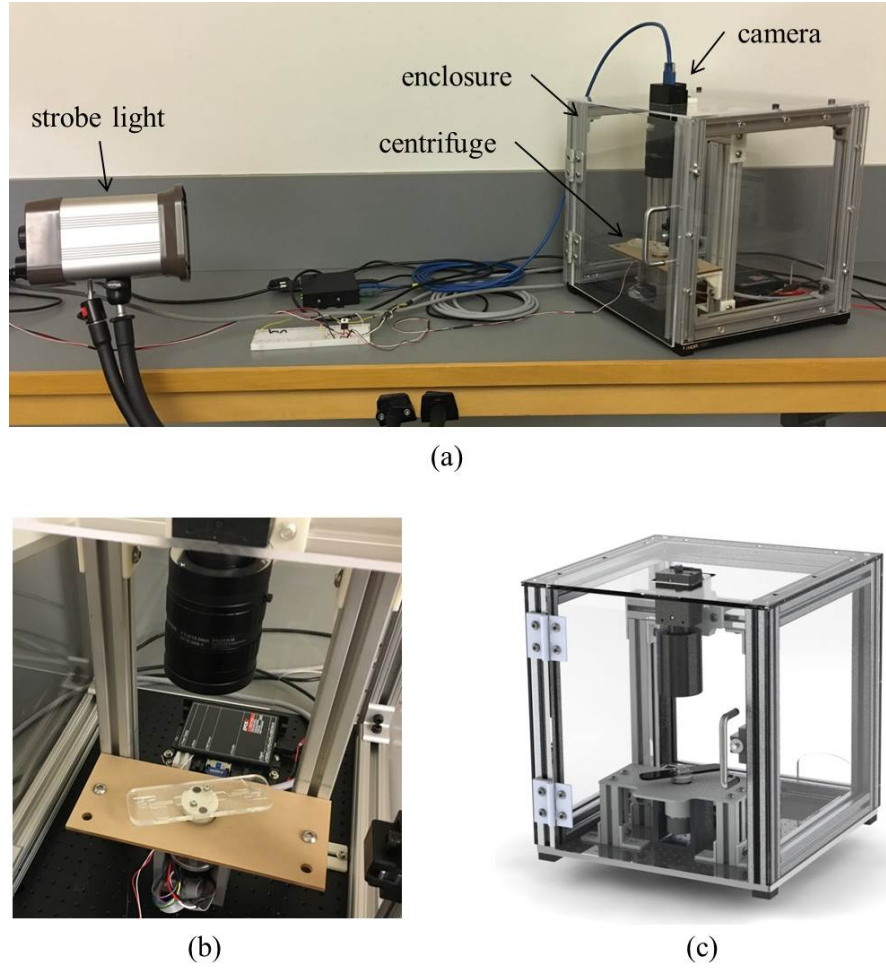


Figure 3.57: Centrifuge test platform for monitoring on-disc fluid manipulation. (a) Image of the test platform with key components labeled. (b) Close-up view of the high-speed camera imaging the chip. (c) Design concept of the system used to guide fabrication of the prototype.

The centrifuge was actuated by a brushless DC motor with an attached encoder for

position and velocity feedback (EC-16, 400161, Maxon Precision Motors, Inc.), capable of spinning chips $>10,000$ rpm. An enclosure was fabricated in case liquid accidentally leaked out of the chips during experimentation. Using a combination of 80/20 extruded aluminum, acrylic panels and 3D-printed brackets, the enclosure was built surrounding the centrifuge. Moreover, an 80/20 aluminum frame was used to mount the high-speed camera (Grasshopper3, GS3-U3-32S4M-C, Point Grey Research Inc.) and corresponding lens (LENS-125F6C, Fujinon) directly above the centrifuge to monitor fluid flow. To image the spinning disc in real-time a strobe light (DT-311A, Shimpco) was mounted 2 ft away from the system, as seen in Fig. 3.57, and triggered to flash light once per revolution on the centrifuge motor. This had the effect of freezing the spinning disc, when in fact, it could be rotating at speeds in excess of 5000 rpm.

To trigger the strobe light, a magnetic-based hall effect position sensor (A1120, Allegro MicroSystems, LLC) was placed on the centrifuge mounting bracket, while a small magnet (D101-N52, $\varnothing 1/16$ in., $1/32$ in. thick, K&J Magnetics, Inc.) was embedded in the axle adapter. Furthermore, the digital input signal of the position sensor was wired into the strobe light. Every time the magnet passed the sensor, it would trigger the strobe to pulse a beam of light for approximately $10\ \mu\text{s}$. Using the encoder on the centrifuge motor to monitor the spin speed, the frame rate of the camera was adjusted to match the spin frequency in order to capture a live video stream.

To mount the microfluidic chips on the centrifuge, a simple adapter was designed and 3D-printed, which allowed chips to be fastened to the mounting hub via M2 screws. Ideally, there would be a quick attach/release adapter on the centrifuge hub to avoid having to screw in chips for each test. In fact, several designs have already been conceptualized and prototyped for this mechanism. Nonetheless, using screw fasteners is a safe method to reliably secure the chips to the centrifuge, and to ensure the chips remain on a flat plane during experiments. An insecure fastening approach may result in the chip flying off the centrifuge, potentially damaging the test platform.

Altogether, the test platform is a system for evaluating analytical processes in chip designs by monitoring fluid flow in channels. Not only can it be used to evaluate capillary

burst valves, but it can also be utilized to test pumping mechanisms, mixing, and sedimentation. In this fashion, the test platform can easily be used by future students continuing the project. An intuitive GUI was designed in LabVIEW to assist new students in designing centrifuge spin profiles, setting up the camera, and analyzing the captured video streams.

3.4.4.2.2.2 Numerical and Experimental Results Figure 3.58 displays the sequential steps of the capillary valve opening to allow fluid to pass through. In this case, the width of the valve is 1 mm, and black India ink was used for the test fluid to enhance visualization. As seen in the first two images in the figure, the capillary forces (F_s) are greater than the centrifugal forces (F_c), thus the liquid remains in the valve. However, as the speed is increased past 1700 rpm, the centrifugal forces exceed the capillary forces, and consequently, the liquid flows past the valve towards the periphery of the chip (as seen in the second two images).

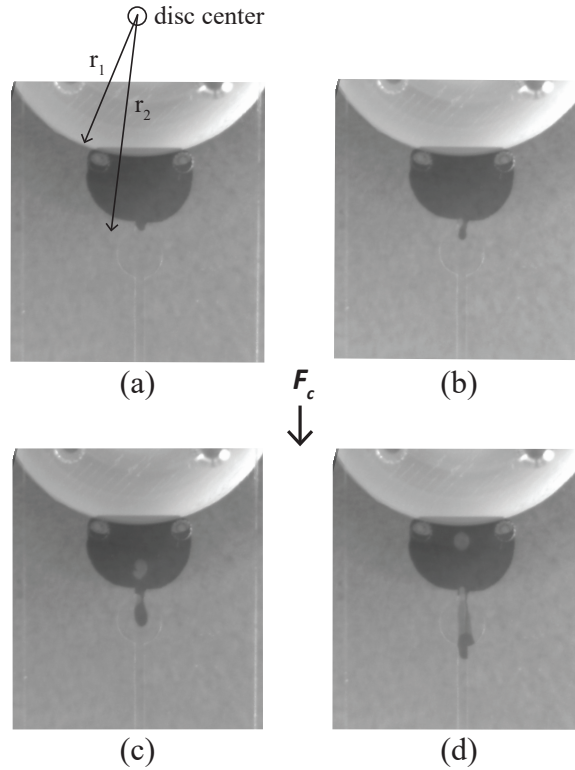


Figure 3.58: Capillary burst valve visualization using black ink. (a–b) Fluid held in inlet ($F_c < F_s$). (c–d) valve bursts ($F_c > F_s$) and fluid flows towards the periphery of the chip (valve width: 1 mm). Valve burst at approximately 1700 rpm.

Quantitative burst frequency results from the numerical calculations and experimental trials are displayed in Fig. 3.59. The plots illustrate how the burst frequency changes with respect to valve geometry (i.e., D_h , r_1 , and r_2). For the experimental trials, a sample size of $n=3$ was used for each of the four test levels. As expected, increasing the channel width, decreased the burst frequency, whereas increasing r_1 , increased the burst frequency. Additionally, increasing both r_1 and r_2 caused the burst frequency to decrease. These trends were valid for both the numerical calculations and experiments. In fact, the error between the numerical and experimental results was — mm, averaged over all tests.

In summary, this work evaluated capillary burst valves on our centrifuge platform, and generated a design guide which can be referenced when designing chips in the future. If a certain burst frequency is needed to store and release a reagent or control flow from one reservoir to another, the plots in Fig 3.59 can be referenced. Finally, this work demonstrated how we can evaluate modular components of the disc design on the test platform.

3.4.4.3 Plasma Extraction via On-chip Pumping

Another critical step in blood chemistry and protein assays is isolating and extracting plasma from the sample. Blood cells, in particular, RBCs, can introduce noise in the detection of analytes, potentially compromising measurement accuracy. Consequently, the first step in these assays is centrifugation, followed by extraction of the plasma. In the lab, this process is typically done on large bench-top centrifuges that spin 5 ml blood vials. Once the biological constituents are separated, either a technician manually pipettes the plasma or a robotic system collects it for downstream analysis. In either case, this approach is not suitable for POC environments.

On the other hand, the centrifuge analyzer can accomplish the same task in a compact device, in less time, and with equal, if not better extraction efficiency. Compared to other plasma separation approaches—for example, size-based filtering^{306,307}, inertial focusing^{308,309}, and channel bifurcation designs^{310,311}—centrifugal microfluidics offers several unique advantages. Namely, faster sample processing, higher purity in the extracted plasma, and the ability to process large volumes of sample (i.e., >2 ml). With this in mind, the main objective here was to develop channel features in the disc design capable of extracting

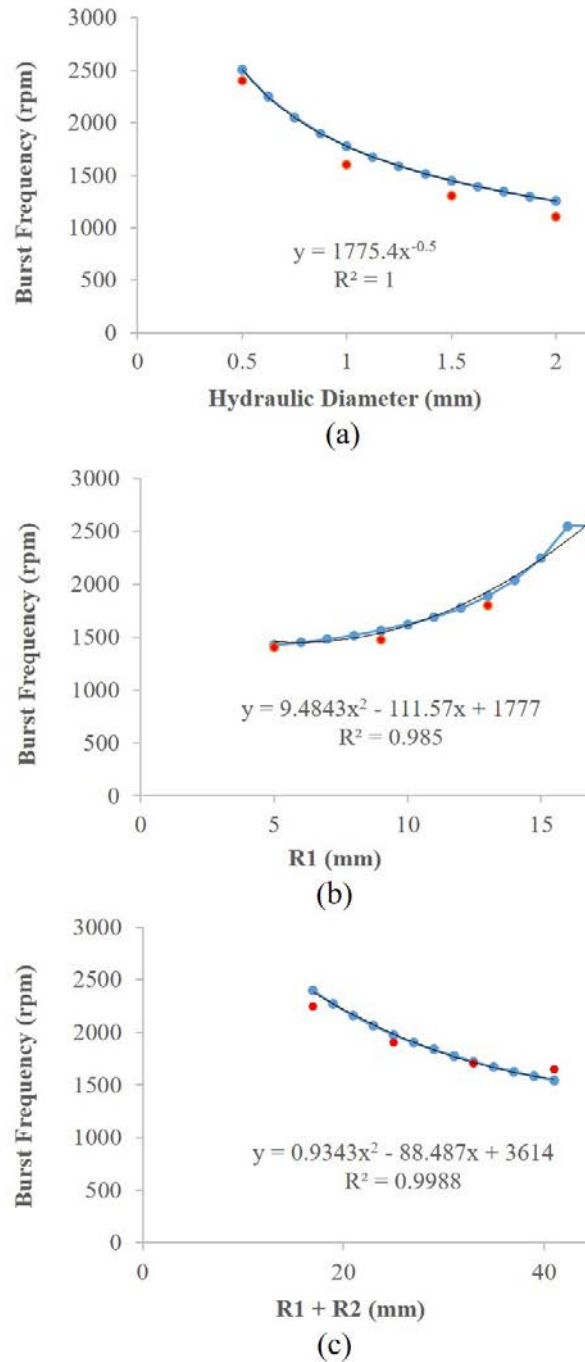


Figure 3.59: Capillary burst valve results, varying: (a) hydraulic diameter, (b) R_1 , and (c) $R_1 + R_2$. Theoretical results from numerical calculations shown in blue; experimental values shown in red. Polynomial fits in black are for the numerical calculations.

plasma using the interplay between centrifugal, capillary, and pneumatic forces.

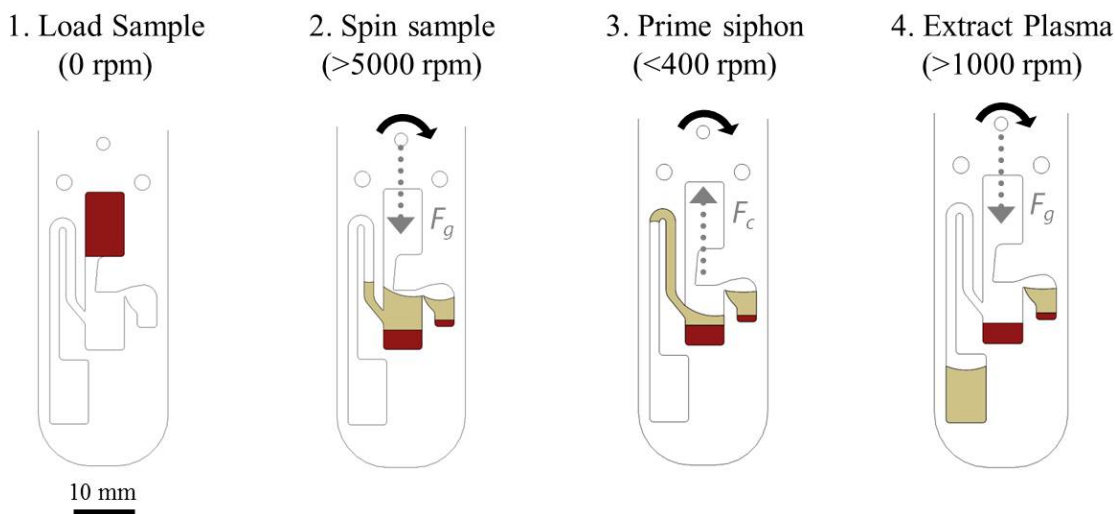


Figure 3.60: Capillary-based pumping for plasma extraction using centrifugal microfluidics. As outlined in the graphic, the following steps are achieved solely by varying the centrifuge spin speed: 1. sample loading, 2. sedimentation, 3. siphon priming, and 4. plasma extraction.

3.4.4.3.1 Chip Design

The first design, as outlined in Fig. 3.60, was based on capillary action to prime the siphon valve after sedimentation. Specifically, the main steps in the process include: 1. loading the sample—this could be done manually or dispensed from a robotic pipetter; 2. spinning the sample—this could be done manually or dispensed from a robotic pipetter; 3. slowly decelerating the disc at 5000 rpm for 2 minutes to fully sediment the sample; 4. slowly decelerating the disc down to 400 rpm so the capillary forces overcome the centrifugal forces and push the plasma radially inward on the disc over the siphon crest (referred to as siphon priming); and 5. increasing the speed to 700 rpm to transport the plasma to the extraction reservoir. At this point, the plasma can either be aspirated for off-chip analysis, or it can be further routed to mixing and detection chambers for downstream analysis on-chip. The latter approach would be used in our case for the detection of blood chemistries and proteins.

What's more, each step in the aforementioned protocol is solely controlled by the motor spin speed; no need for external pumping or valving devices³¹². However, this chip design relies on capillary forces, and thus the acrylic chip surface that comes in contact with the sample, must be hydrophilic. Acrylic is a naturally hydrophobic material, and to render the surface hydrophilic, it must be pre-treated with Corona discharge. Surface treatment adds complexity to the fabrication procedure, and more importantly, the surface energy on

acrylic can decrease over time, on the scale of days²⁹⁹. Moreover, capillary-induced fluid motion is extremely slow, because it relies on energy on the surface for propulsion. For example, transferring 2 ml of separated plasma to a collection reservoir can take up to 2.5 min. Hence, we transitioned to a new design that did not rely on capillary forces.

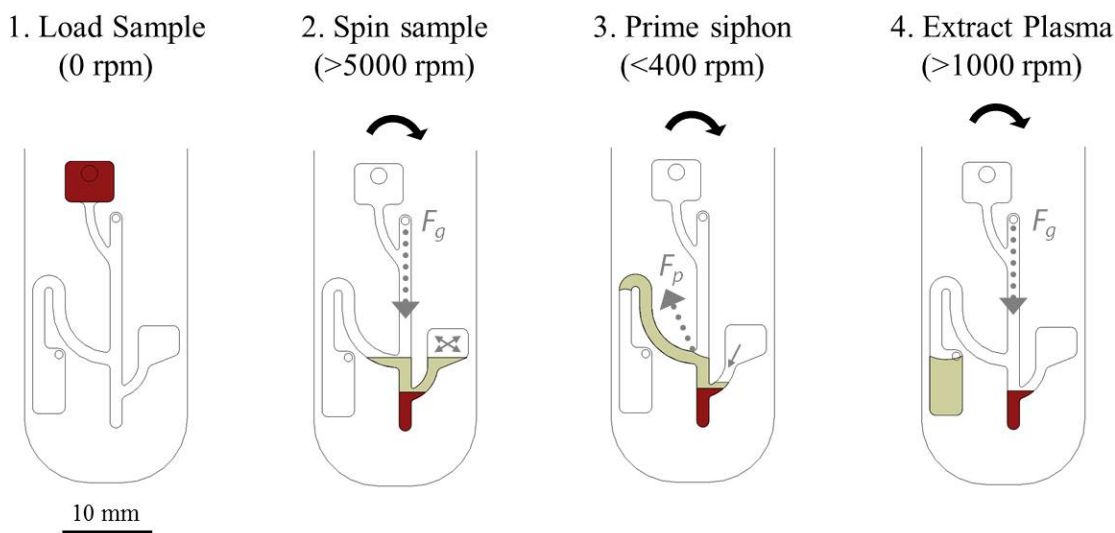


Figure 3.61: Centrifugo-pneumatic pumping for rapid plasma extraction. As outlined in the graphic, the following steps are achieved by varying the motor spin frequency: 1. sample loading, 2. sedimentation, 3. siphon priming, and 4. plasma extraction.

The next concept utilized pneumatic forces to pump fluid inward towards the center of the disc, over the siphon crest. In this case, the interplay between centrifugal and pneumatic forces was utilized (herein referred to as centrifugo-pneumatic pumping). As seen in Fig. 3.61, the process involves similar steps as the capillary-based pumping. The key difference is that the centrifugo-pneumatic chip design relies on a build-up of pressure inside the pneumatic chamber during centrifugation (Fig. 3.61, step 2). Upon lowering the centrifuge speed, this pneumatic pressure releases and pushes the plasma over the siphon crest. Once over the crest, the speed is then increased, allowing the rest of the plasma to flow into the collection reservoir. This technique does not rely on surface treatment to render the acrylic hydrophilic and provides rapid plasma extraction via the release of pressure from the pneumatic chamber.

Fig. 3.61, presents the original five-layer centrifugo-pneumatic chip design (three acrylic, two PSA layers). However, there were numerous limitations which motivated our decision

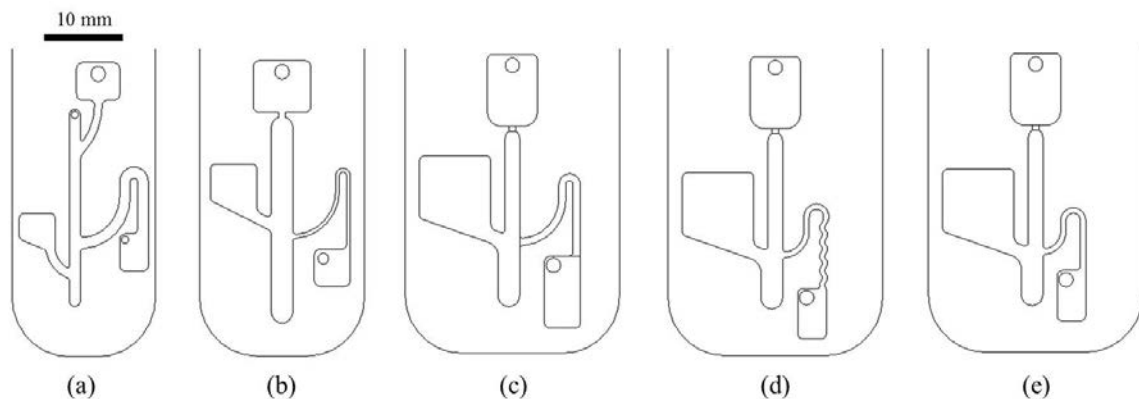


Figure 3.62: Centrifugo-pneumatic pumping chip design iterations.

to modify channel features and dimensions. A series of design iterations are shown in Fig. 3.62, illustrating the adjustments made in each chip. The main adjustments included the following. First, the size of the pneumatic chamber needed to be expanded to increase the pneumatic force used to push the plasma over the siphon crest. In the final design, the chamber volume is $140 \mu\text{l}$. Second, the position of the pneumatic chamber needed to be brought closer to the bottom of the sedimentation chamber to better align with the blood-plasma interface. Third, the height of the siphon needed to be reduced, so that a lower pneumatic force could be used to push the plasma over the crest. Finally, a capillary valve needed to be implemented below the inlet reservoir to prevent the sample from flowing back up the sedimentation channel, helping the plasma flow into the siphon, instead.

3.4.4.3.2 Chip Fabrication

Similar to the fabrication method discussed in Section 3.4.3.1.4, a laser cutter was used to shape channels in acrylic layers, whereas a vinyl cutter was used to shape channels in PSA layers. Here, the fabrication process was more complex due to the five-layer chip design. Figure 3.63 shows an exploded view of the layers used to assemble the chip.

The top acrylic layer contains inlets, outlets, and air vents; the middle acrylic layer contains reservoirs (i.e., inlet chamber, sedimentation chamber, pressure chamber, and outlet chamber); and the bottom acrylic layer serves as a support. Conversely, the PSA layers serve a multipurpose function. One, they bond the acrylic layers together and provide a

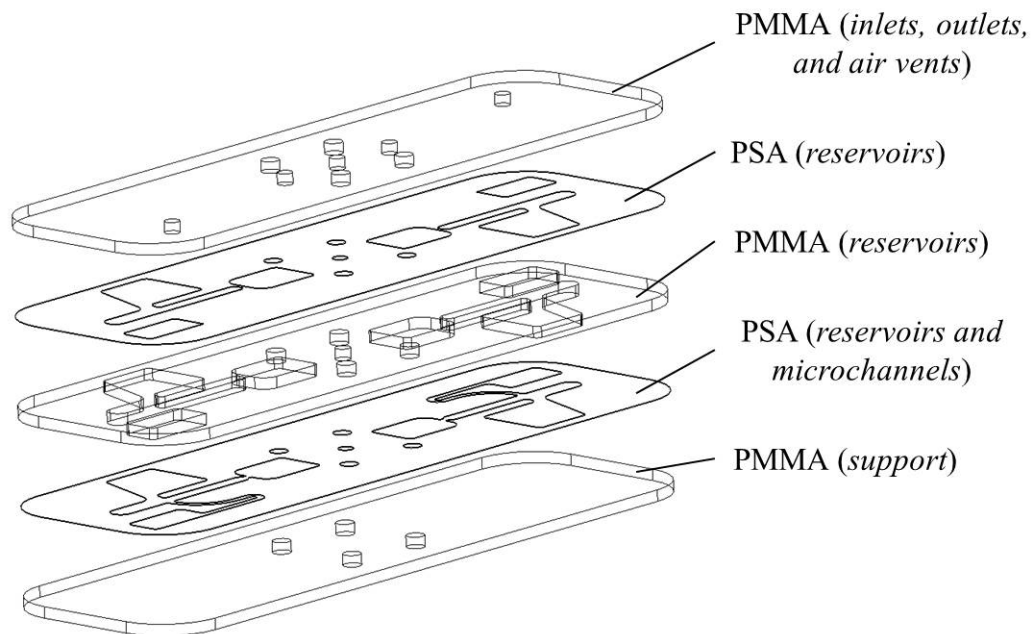


Figure 3.63: Centrifugo-pneumatic pumping chip design exploded view.

leak-proof seal at high centrifugation speeds. Two, they contain microchannels and conduits, in which the sample flows through. As seen in Fig. 3.63, the top PSA layer contains the same channels as the middle acrylic layer, whereas the bottom PSA layer contains microchannels for the capillary burst valve and siphon.

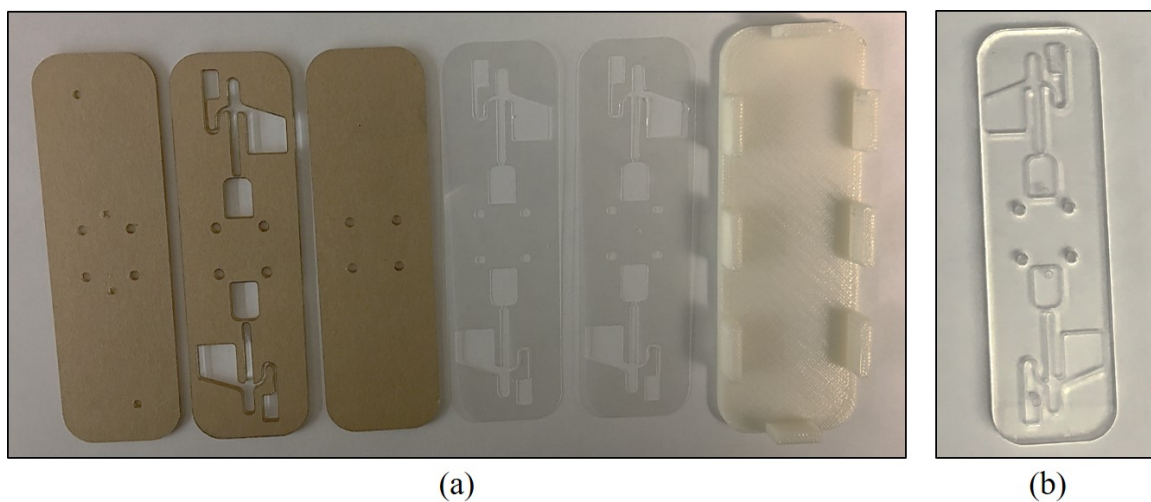


Figure 3.64: Five-layer chip fabrication and assembly. (a) Individual shaped layers after cutting, and the alignment rig used for assembly. From left-right: top acrylic layer, middle acrylic layer, bottom acrylic layer, two layers of PSA, and the alignment rig. (b) The final assembled chip, with layers bonded together.

Figure 3.64a displays the five cut layers and 3D-printed alignment rig used for assembly. Layers are aligned in the rig and pressed together manually, assembling the chip layer-by-layer. Once complete, the chip is placed in a heat press to ensure a leak-proof bond. The resulting chip is shown in Fig. 3.64b.

3.4.4.3.3 Experimental Testing

To evaluate the pumping mechanism on-chip, trials were first run using colored water, and then using porcine blood after the channel designs were optimized. After manually pipetting in the sample, chips were placed in the centrifuge test platform for analysis. Watching the live video stream from the camera placed above the centrifuge, fluid flow through the channels was monitored in real-time. In this fashion, we could determine when the siphon primed, how much fluid got pushed through the siphon channel, and how much fluid got routed to the collection reservoir. This mode of testing also allowed us to optimize the spin profile of the disc (i.e., velocity, acceleration, and deceleration). The optimized spin profile is listed in Tab. 3.6. In our case, the same spin profile was used for testing both water and blood, however, the sedimentation time and speed could be reduced without affecting the pumping mechanism.

Table 3.6: Centrifuge spin profile for inward pumping on-disc.

Step	Speed (rpm)	Spin Time (s)	Acceleration (rpm/s)
Sedimentation	5000	120	1800
Siphon Priming	400	10	1800
Collection	700	20	1800

Evaluating the capillary chip design, numerous limitations were observed, including unreliable siphon priming and slow operation. Consequently, minimal fluid was pumped into the collection reservoir, which prompted our decision to transition to the centrifugo-pneumatic pumping technique. Using this approach, the maximum amount of fluid was transferred to the collection reservoir throughout our trials. The collected volume can be controlled by modifying the dimensions of the collection reservoir. Figure 3.65 displays

images of the key centrifugo-pneumatic pumping events: (a) sample loading, (b) sedimentation, (c) siphon priming, and (d) sample collection.

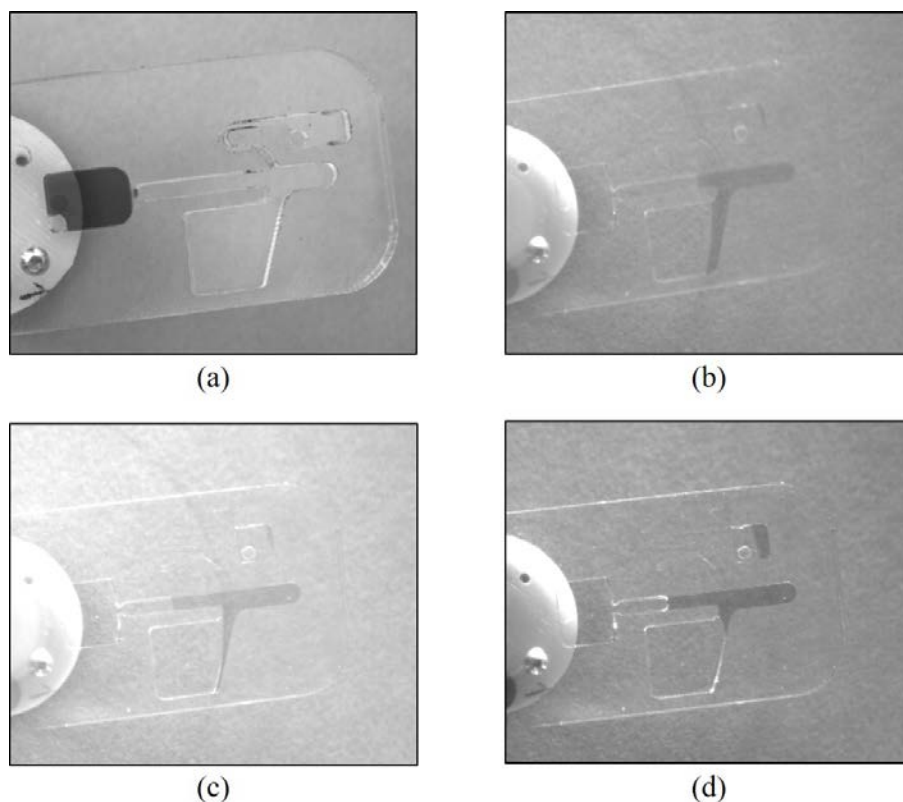


Figure 3.65: Centrifugo-pneumatic pump testing using colored water. Tested chip corresponds to (c) in Fig. 3.62. (a) Sample loaded in inlet reservoir, (b) sedimentation and build-up of pressure in the pneumatic chamber, (c) release of pneumatic pressure and siphon priming, and (d) sample flowing in collection reservoir.

Overall, this work demonstrated preliminary evidence of how plasma can be siphoned off using centrifugal microfluidics. Future work entails more rigorously validating this technique—evaluating the purity of the extracted plasma (i.e., how few RBCs were transferred) and the efficiency (i.e., the quantity of extracted plasma relative to the known volume). Both evaluation metrics could easily be conducted on-chip. For example, to quantify the purity of the isolated plasma, one could measure Hgb absorbance using a similar photometry module as discussed in Section 3.3.2. In this case, the LED could be placed underneath the chip, whereas the photodetector could be positioned directly above—both within the centrifuge test platform. Alternatively, the extracted plasma could be collected and analyzed off-chip using a bench-top flow cytometer to quantify the number of RBCs in

the sample.

To evaluate the extraction efficiency, one could measure the plasma volume in the collection reservoir via segmentation in the acquired images. The segmentation could either run while the disc is in motion, similar to the approach discussed in³¹³, or could run immediately after the disc stops spinning. Combining the segmentation information and the known dimensions of the disc, the volume of extracted plasma can be computed and compared with known values for an efficiency metric.

3.5 Summary and Discussion

Key achievements in this Chapter include the following:

1. Three sample handling modules were designed and prototyped to integrate the robotic venipuncture device with a blood analyzer to enable rapid diagnostic testing at the POC. Designs included a blood collection carousel, robotic syringe pump, peristaltic pump, and tube switching pump. Altogether, pieces of this work resulted in a conference paper and presentation at the *2016 IEEE/RSJ International Conference on Intelligent Robots and Systems*⁴.
2. A static WBC counting device was developed using a custom-designed microscope for fluorescence detection, and a range of image processing algorithms to segment, classify, and enumerate WBC subtypes. Key insights derived from this work were implemented in the design of the centrifuge blood analyzer.
3. A photometry module was created for optical absorption studies of blood chemistries (e.g. Hgb and Glu). Elements of this module were later incorporated in the centrifuge blood analyzer.
4. A blood analyzer was built using centrifugal microfluidics and fluorescence microscopy. The concept was designed for the detection of cells, proteins, and chemistries on one chip, in one machine. Three generations of devices were prototyped and evaluated using a WBC assay on porcine blood sample controls. A bulk cell analysis approach was implemented, in which the thickness of the buffy coat was correlated with cell

counts. Microfluidic chips were designed using acrylic, spun on a miniature centrifuge, and buffy coats were imaged and measured using an integrated fluorescence microscope. Overall, this work resulted in a journal publication in *Analytical Methods*⁵.

5. Lastly, various analytical processes were tested on the centrifuge platform, including capillary burst valves and centrifugo-pneumatic pumping. This work demonstrated how fluidic modules can be evaluated independently before final integration into a complex system such as this. The results from this work will be submitted for publication in the coming months⁷.

Chapter 4

Conclusion

4.1 Summary

In conclusion, this dissertation focused on the development of a fully automated platform for end-to-end POC testing, combining robotic venipuncture with a centrifuge blood analyzer. This work resulted in a compact, easy-to-operate, electronically connected unit to provide critical patient information rapidly at the site of the blood draw. The overall approach to automate the entire pipeline from blood draw to diagnostic readout fills a major gap in POC testing.

The device, once translated, will have the potential for impact across multiple domains, including pediatric, geriatric, emergency, and military use. The device will be particularly suited to address challenges of blood testing in children, for whom difficult venipuncture and low sample volume requirements greatly affect the quality of care. Finally, the underlying technological advancements covered a spectrum of research disciplines, including hematology and diagnostic medicine, optics and microfluidics, as well as robotics and medical device development.

To briefly summarize the key parts of this dissertation, Chapter 2 discussed the development of a second-gen and third-gen venipuncture robot, both of which substantially improved the usability, functionality, and accuracy of earlier devices, while at the same time, miniaturizing the system. Both robots were custom-designed in SolidWorks, built using rapid prototyping techniques such as 3D-printing, laser cutting, and CNC-machining, and programmed using LabVIEW. Kinematic models were created to evaluate the operating workspace and a range of sensors (i.e., stereo cameras, ultrasound, and position plus force sensors) were integrated to guide accurate needle placement. Robotic prototypes were evaluated through a series of free-space needle positioning tests to measure the accuracy, precision, and repeatability of each system. Furthermore, *in vitro* phantom cannulations were performed using customized, multilayered tissue phantoms developed by Dr. Alvin

Chen. These phantoms simulated the optical, mechanical, and acoustic properties of human skin tissue, providing a realistic test model—even more so than phlebotomy training arms—for evaluating the insertion accuracy and precision of the venipuncture devices. Altogether, this work resulted in three journal publications^{1,3,8}, two conference proceedings^{2,9}, plus three publications in preparation^{6,219,220}.

Chapter 3 discussed the development of POC blood diagnostic devices and their integration with robotic venipuncture via pumping and sample handling modules. Taking into account the need to integrate multiple assays into one device from a clinical perspective, a blood analyzer was built using centrifugal microfluidics and optical detection techniques—specifically, fluorescence and absorption. Several designs were conceptualized and prototyped, along with corresponding disposable chips to house the sample. A custom-designed two-channel fluorescence microscope was fabricated alongside a miniaturized centrifuge. Together, this system allowed for the automation of analytical processes—including sedimentation, valving, pumping, mixing, and metering—and the detection of analytes on-chip. Microfluidic chips were prototyped using a rapid fabrication protocol, consisting of acrylic and adhesive layers, shaped using a laser and vinyl cutter respectively. This protocol made it easy to quickly iterate and test designs, compared to photolithography fabrication methods, which can be time-consuming, unreliable, and require the use of a clean room^{314,315}.

To evaluate the device, I chose to focus on the detection of leukocytes on-chip using a bulk-cell analysis approach—a challenging assay to pursue that has still yet to be proven using centrifugal microfluidics. Using porcine blood sample controls, a set of standard curves were generated for lymphocyte/monocyte, granulocyte, and absolute leukocyte counts that demonstrated strong linear fits against measurements from an established method: flow cytometry. Results indicated that this is a promising approach that uses one nuclear stain, no dilution, no density medium, minimal sample preparation, simple low-cost hardware, no flow focusing, and no complicated image analysis.

To merge robotic venipuncture with the downstream diagnostics, various pumping schemes were explored including a syringe pump, peristaltic pump, and tube switching pump, along with various designs to extract, store, and deliver samples to the analyzer. In the end, a tube switching mechanism in conjunction with a peristaltic pump was implemented. This

mechanism interfaced with the automated consumables unit for the venipuncture robot, and also provided an efficient method for washing the peristaltic pump tubing between uses without having to dispose and replace pumping components. Altogether, this work resulted in one journal publications⁵, one conference proceeding⁴, plus one publication in preparation⁷.

4.2 Future Directions

4.2.1 Venipuncture Robot

Beyond these initial clinical studies, there are several factors that need to be addressed moving forward to bring a device like this into the clinic.

4.2.1.1 Human Factors Engineering

First, the device must integrate with the existing phlebotomy work-flow. This means that the device must be easy-to-use and intuitive for the clinician (or technician) to operate. It cannot over-complicate the procedure. If, for example, it takes a long for the device to be set up (e.g., loading the needle, US gel clip, and other consumables) then this distracts the clinician and interrupts the work-flow. Similarly, if there is a long learning curve to operate the device (e.g., a complicated GUI), then clinicians would prefer manually performing the venipuncture. Therefore it is critical that the device integrate seamlessly within the existing clinical work-flow and provide a means to assist the clinician, not replace them (at least just yet). Venipuncture sounds relatively straightforward: locate a suitable vessel and introduce a needle into the vein. However, oftentimes it requires a high degree of dexterity and clinical skill, especially when cannulating a vein on a difficult patient. In these cases, imaging technology is brought in to help with locating a suitable vein to cannulate, however numerous clinical studies highlight the fallacies of these devices. They are non-intuitive to use, require a long learning, and in some cases, they do not improve first-stick success rates compared to manual techniques. For a robotic solution to improve clinical care, it must address these limitations, while at the same time, appear comforting and non-intimidating to the patient from a psychological perspective.

The first thought that typically comes to mind when the word *robot* is mentioned, is an industrial robotic arm. Trusting a robot to successfully insert a needle into a vessel can be scary for some people. Therefore, it is critical that the device be compact, sleek, and friendly-looking. To accomplish this, our group collaborated with a local design firm—HS Design—to help with the human factors engineering of the device. This included the design of arm rest and consumables, as discussed in Section 2.3.1.6. Future work entails redesigning the exterior of the device and eliminating auxiliary features in the system that detract from the main value the device offers to patients (improve first-stick success rates), clinicians (reduce the likelihood of an accidental needle-stick injury), and healthcare facilities (reduce venipuncture-related complications and costs).

4.2.1.2 Maintenance Considerations

Second, the maintenance of the robot must be considered. Though the third-gen venipuncture device has 9-DOF, each motion is necessary in allowing the system to reach blood vessels located throughout the forearm. These include branched, non-linear, and rolling vessels, commonly encountered in difficult patients. The corresponding image sensors localize blood vessels in 3D and relay this spatial position information to the robot to guide the needle insertion. The NIR and US image sensors complement each other and play a critical role in directing the robot. NIR provides a coarse scan of the underlying vasculature, whereas US provides a magnified view of the blood vessel. An embedded force sensor in the end-effector then monitors puncture events during the needle insertion, serving as an additional safety feature.

Looking into the future and considering how the device would be manufactured, all sensors would be pre-calibrated during assembly—a common practice in medical robots such as the Da Vinci surgical system and the Lasik ablation system. All motors, actuators, and electronics used in the device were sourced based on durability and reliability to minimize maintenance requirements, and have lifetimes of 150,000 cycles or greater. Moreover, all of these components have been previously used in FDA-approved medical robotic systems. Nevertheless, the device would have to be properly maintained over its lifetime, and detailed analysis would be required to identify components of the device that would require annual

maintenance. Our current model suggests a life-cycle of 7 years for each device before replacement with a new unit.

4.2.1.3 Cost Considerations

Third, the medical costs associated with venipuncture in normal and difficult patients must be considered. In the case of a hospital, these costs are typically reimbursed by insurance (i.e., the payers). However, the amount of reimbursement varies depending on the medical procedure, payer, and health insurance plan. Concretely, how these factors control reimbursement rates is a gray area. For example, the amount reimbursed by a private payer for a peripheral catheter insertion is more than the amount reimbursed for a blood draw, even though both procedures are so similar.

Further complicating the issue is difficult cases, where the actual costs needed to perform the procedure may exceed the reimbursement rate. For a healthcare facility, these losses can represent a substantial economic burden. As discussed earlier, costs due to difficult venipuncture include wasted materials/supplies and extra personnel time needed to complete the procedure. Additionally, in the case of a blood draw, costs may be associated with compromised specimen quality that can result from difficulties and delays during the venipuncture and sample collection¹⁷⁹. Finally, costs can be incurred resulting from unintended complications and adverse events, including accidental needle-stick injuries to clinicians and injury to the patient. Ultimately, the adoption of robotic venipuncture in the clinic, either to address challenging scenarios or to replace standard techniques, will be determined by the extent to which the technology can minimize these costs and improve patient care.

4.2.1.4 Device Miniaturization

Fourth, the robotic mechanisms utilized in the device must be miniaturized. To begin addressing this, we have started to develop alternative *semi-automated* prototypes that reduce the number of degrees-of-motion in exchange for a substantially miniaturized form factor (Fig. 4.1). These alternative systems are much simpler, smaller, and more lightweight in their design, but as a result, will require some amount of human positioning before the

automated component completes the procedure.

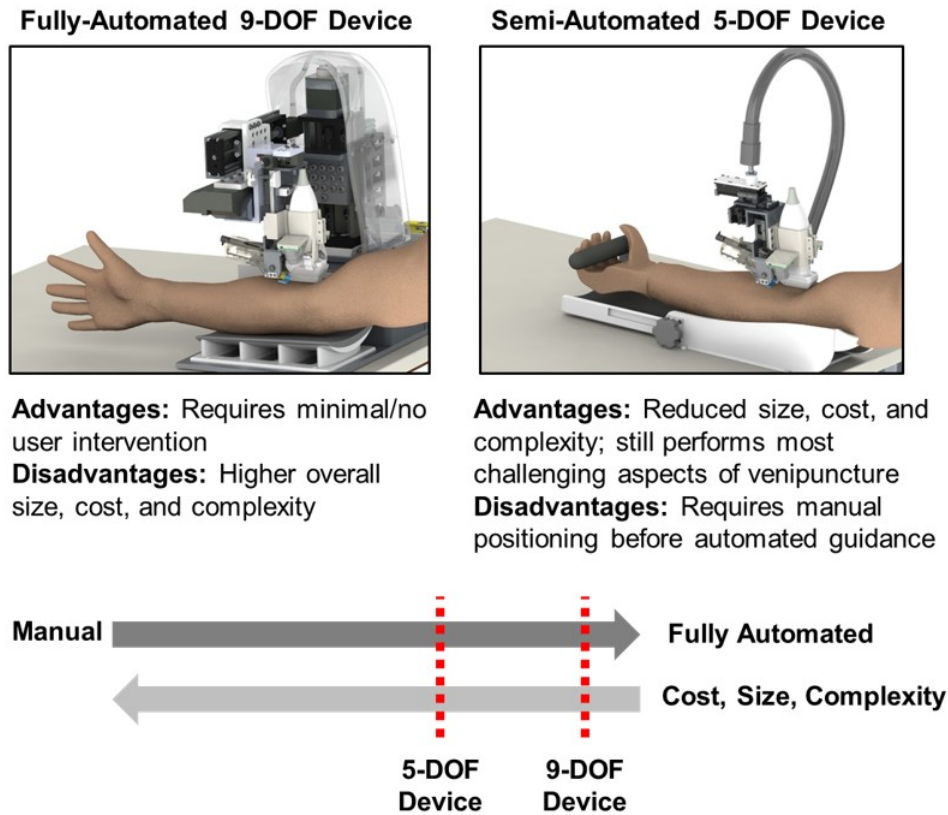


Figure 4.1: Comparison of automated versus semi-automated venipuncture devices.

Further miniaturization to the main device will entail, primarily, the implementation of custom mechanical stages and a custom US transducer. Currently the use of commercially available off-the-shelf stages, electronics, and transducers has limited further miniaturization. However, we believe it is better to commit resources to custom hardware development only after demonstrating human feasibility.

4.2.1.5 Embedded System Design

Lastly, the control architecture of the device needs to be transitioned from a laptop computer to an embedded system-on-chip. Currently, the device is controlled on a laptop computer running the Windows operating system. The control software, developed in LabVIEW, is compiled to the laptops CPU, and parallelizable graphics computations are directed to a

GPU (Nvidia Quadro K2100M). With this architecture, the computer can perform the imaging and robotics computations at real-time frame rates using of 800 MB of CPU memory and 500 MB of GPU memory. Approximately 100 MB/s of data is communicated between the laptop and the robot via a single USB3 cable. Inside the robot, a USB3 receiver hub splits the input cable into five independent outputs that connect respectively, to the cameras, LED circuitry, US system, base positioning robot, and manipulator robot. Significant changes in the memory or processing requirements are not expected upon transition to an embedded system design. In addition to the added stability and determinism provided by the system-on-chip architecture, the elimination of the Windows operating system will reduce the memory load, hardware complexity, and cost of the device. Several chip design platforms have been considered:

1. National Instruments platform (e.g., the Single-Board RIO): The SBRIO platform runs on Linux and contains a reconfigurable field-programmable gate array (FPGA) that can be programmed using LabVIEW.
2. Dedicated FPGA platform (e.g., the Xilinx chip architecture): Recent Xilinx chips have begun to combine ARM and FPGA architectures and are compatible with a large library of optimization, power management, and security features for dedicated FPGA systems.
3. Dedicated GPU platform (e.g., the Nvidia Tegra chip architecture): A number of core vision algorithms currently used in the device (e.g., vessel segmentation, stereo reconstruction, and US needle tracking algorithms) are already optimized for NVIDIA GPUs. Thus keeping with the NVIDIA platform would greatly reduce the time needed to re-develop these software components.

4.2.2 Medical Robotics

Robotics has finally entered the realm of modern medicine over the past decade with the success of the da Vinci surgical system by Intuitive Surgical. The robot, used to assist surgeons in performing complex surgical tasks in a minimally invasive fashion, is ubiquitous across all major hospitals in the U.S., and is poised to gain even more acceptance in more

procedures in the years to come. Currently, the da Vinci system is most commonly used in gynecologic (48%), general (28%) and urologic (20%) surgeries, with the overwhelming majority of these systems deployed in the U.S. (71%)³¹⁶.

Other big players in the technology and medical device space—Medtronic as well as Google and Johnson & Johnson—have realized the future of surgery may reside in the hands of robots and have invested substantial resources to develop surgical robots of their own. In both cases, these companies are focusing on procedures that Intuitive Surgical has little presence. Interestingly, Medtronic is planning to launch their surgical robot outside of the U.S., and instead, in India. Time will tell whether these companies will be able to compete with Intuitive Surgical in the future, and which procedures will be targeted.

One of the central hypotheses of this dissertation was that the combination of imaging and robotic technology, as implemented in surgical robots, can be applied outside the operating room to address the challenges with routine medical procedures, like venipuncture. Automation of common surgical tasks, such as suturing^{93,317–321}, has received much attention in the robotics community over the years, and these same concepts in deep learning and artificial intelligence can be applied to automated venipuncture. In our case, algorithms can be developed to teach the robot how to identify optimal insertion sites by training the system to recognize major blood vessels across patients, for example with deep neural networks³²². Furthermore, patient information such as medical history, demographic, and previous insertion sites can be stored and referenced in future procedures. This data could even be used to optimize needle insertion parameters, including speed, orientation, and trajectory to reduce tissue deformation during the insertion and potentially reduce pain and discomfort for the patient.

4.2.3 Diagnostic Blood Testing

Large diagnostic companies, like LabCorp and Quest, have recently invested substantial resources in automating central lab processes including, sample handling, preparation, and analysis. This robotic technology has expedited throughput of commonly requested blood tests, such as the CBC; however, the central lab testing approach is still prone to errors. Even more so, in emergency environments, where rapid diagnostic results are critical, a

paradigm shift towards testing at the POC has emerged. But is POC testing, in its current state, the best approach for providing information on patient health? Could robotic technology be implemented in POC devices to automate the sample handling, preparation, and analysis of blood tests? And does this make sense from an economic perspective?

4.2.3.1 POC Technology

These are just a few of the question being posed—and explored—by the diagnostic testing community. For example, Theranos—the controversial start-up company developing technology to run multi-analyte tests using blood from the fingertip—is attempting to miniaturize key instrumentation used in centralized labs, and combine these modular units into a portable system for POC settings^{323,324}. Despite all the media hype and attention surrounding Theranos, there are serious flaws in the science, engineering, and strategy of their approach, claimed to supposedly *disrupt, revolutionize, and democratize* lab testing^{11,325–333}.

First, blood from a finger is *not* the same as blood from a vein. Theranos claims their machine can run multi-analyte detection using blood from a finger-prick, yet from a basic physiological standpoint, large molecules—like proteins and cells—have difficulty traveling through small capillaries to reach the finger-tips. Second, the device itself is bulky (14 x 22 x 18 in) and contains complicated, sensitive, and expensive electrical and optical components. Using this system at the POC would likely require a dedicated room and a highly trained technician to operate—aspects that POC technology is hoping to eliminate. Third, the economics of their strategy were ill-conceived. The majority of blood tests are cheap to perform and the expensive ones (e.g., esoteric tests) are proprietary. As succinctly stated by Bryan Roberts in Time magazine in the May 16, 2016 issue³³⁴:

Why would you start a business in a super-low margin commodity space.

Considering the details of this argument, medicare reimbursement for a CBC with a 5-part differential is \$10.94. If consumables (e.g., blood collection devices, reagents, sample trays, etc.) used with the device cost close to \$10, it can be extremely difficult to create a sustainable business. These are just a few of the issues that Theranos will need to address

if they are serious about *revolutionizing* the lab testing industry. It remains to be seen if they have the capabilities to accomplish this.

One reason why the central lab testing infrastructure still exists is because of economies of scale. Automating the processing and testing of simple assays (with low reimbursement rates) at high-throughput is a logical solution, compared to running these assays one at a time, as is commonly done in POC devices. Translating robotic technology to POC settings is also challenging, especially if complex components are implemented in the system. These components can be challenging to operate, troubleshoot, and maintain for clinicians. Device ease-of-use was one of the main reasons we chose to pursue a centrifugal blood analyzer for a diagnostic system. It can provide multi-analyte detection of both small and large molecules in blood in an automated fashion using a single disposable chip, all within a portable unit.

4.2.3.2 Common Versus Esoteric Testing

The centrifugal analyzer also has the capacity to perform esoteric tests, such as the detection and enumeration of circulating tumor cells^{200,335–337} and CD4+ cells^{201,338,339}, among others. In these cases, a separate disc can be placed in the analyzer, but the same centrifuge and optical detection scheme can be used for the processing and analysis respectively.

Recently, there have been two emerging trends in POC testing research. First, in developed countries, there has been a shift towards developing POC devices for more esoteric assays, which have higher reimbursement rates, compared to common tests. The large diagnostic companies have leveraged their economies of scale for common blood tests, making it difficult for new entrants to compete in this market. Second, in developing, low-resource countries, researchers are trying to bring simplified versions of central lab testing equipment to these communities—a challenging endeavor considering the harsh environments typically found in these settings. Overall, POC testing offers tremendous value for patients, clinicians, and healthcare facilities; however, this added value needs to be put in perspective and evaluated against other practicalities, including the economics, device ease-of-use, and operation in various clinical environments. The future of POC testing will be exciting to watch, especially as robotic technology continues to enter the realm of modern medicine.

4.2.4 Robots of the Future

Many of the concepts presented in this dissertation—related to image-guided robotics and diagnostics—are directly applicable to other industries outside of healthcare. In essence, robots are all around us; from manufacturing to transportation to energy to defense. This technology often raises similar questions regarding the role of robots in the future: how will humans interact with robots and should robots be fully autonomous? Transportation, in the form of self-driving vehicles, has been the central avenue for discussion in recent years, regarding the impact of robotics in the future. As technology development accelerates, ethical, legal, and economic issues will continue to be raised. Robots are here to stay. I strongly believe there is no longer a questions of if this technology will improve society, but a matter of when. And with that, I would like to thank you, my dear reader, for taking the time to sift through this dissertation.

Appendix A

Venipuncture Robot

A.1 Derivation of Kinematic Equations—Gen-2 4-DOF Manipulator

The DH parameters specified in Tab. 2.1 link the manipulator origin frame to the wrist frame at the distal end of the end-effector. The needle tip position is then computed utilizing a wrist-to-tool transform. Once the end-effector grabs the cannula, the location of the needle tip is offset from the wrist frame by 28 and 23 mm in the x and y directions respectively. Equation A.1 shows the kinematic transform from the manipulator origin to the wrist frame, and Eq. A.6 is the resulting transformation matrix.

$${}^0_W T = {}^0_1 T(\theta_1) * {}^1_2 T(\theta_2) * {}^2_3 T(\theta_3) * {}^3_W T(L_3) \quad (\text{A.1})$$

$${}^0_1 T = \begin{bmatrix} c_1 & -s_1 & 0 & 0 \\ s_1 & c_1 & 0 & 0 \\ 0 & 0 & 1 & 0 \\ 0 & 0 & 0 & 1 \end{bmatrix} \quad (\text{A.2})$$

$${}^1_2 T = \begin{bmatrix} c_2 & -s_2 & 0 & 0 \\ 0 & 0 & -1 & 0 \\ s_2 & c_2 & 0 & 0 \\ 0 & 0 & 0 & 1 \end{bmatrix} \quad (\text{A.3})$$

$${}^2_3 T = \begin{bmatrix} c_3 & -s_3 & 0 & L_2 \\ s_3 & c_3 & 0 & 0 \\ 0 & 0 & 1 & 0 \\ 0 & 0 & 0 & 1 \end{bmatrix} \quad (\text{A.4})$$

$${}^3_W T = \begin{bmatrix} 1 & 0 & 0 & L_3 \\ 0 & 1 & 0 & 0 \\ 0 & 0 & 1 & 0 \\ 0 & 0 & 0 & 1 \end{bmatrix} \quad (\text{A.5})$$

$${}^0_W T = \begin{bmatrix} r_{11} & r_{12} & r_{13} & p_x \\ r_{21} & r_{22} & r_{23} & p_y \\ r_{31} & r_{32} & r_{33} & p_z \\ 0 & 0 & 0 & 1 \end{bmatrix} \quad (\text{A.6})$$

where

$$p_x = c_1(c_2(L_2 + c_3L_3) - L_3s_2s_3)$$

$$p_y = s_1(c_2(L_2 + c_3L_3) - L_3s_2s_3)$$

$$p_z = s_2(L_2 + c_3L_3) + c_2L_3s_3$$

$$r_{11} = -c_1(s_2s_3 - c_2c_3)$$

$$r_{12} = -c_1(c_2s_3 + c_3s_2)$$

$$r_{13} = s_1$$

$$r_{21} = -s_1(s_2s_3 - c_2c_3)$$

$$r_{22} = -s_1(c_2s_3 + c_3s_2)$$

$$r_{23} = -c_1$$

$$r_{31} = c_2s_3 + c_3s_2$$

$$r_{32} = c_2c_3 - s_2s_3$$

$$r_{33} = 0$$

A.2 Gen-2 Manipulator Motor Torque and Power Calculations

The following pages describe the torque and power calculations used to guide the selection of motors in the Gen-2 serial manipulator arm. A similar approach was used to select motors in the Gen-3 manipulator. The presented computations can also be utilized when designing a motorized mechanical system of your own.

- **Motor 3:**

- Revolute joint connecting bottom and top arms
- Rotating bottom arm, needle holder, needle, and linear injection system
- Length of bottom arm (fully extended—rotational axis to needle tip) according to model: 104.91 mm.
- Total volume of parts:
 - * 19931 mm^3 – Bottom arm
 1. Lower Arm Inj 1: 3740 mm^3
 2. Lower Arm Inj 2: 16190 mm^3
 - * 1014 mm^3 – Needle Holder
 - * 1575 mm^3 – Needle
 - * $TOTAL = 22500 \text{ mm}^3 = 2.25 \times 10^{-5} \text{ m}^3$
- Density of ABS plastic: $1.04 \times 10^3 \text{ kg/m}^3$
- Assume everything is made out of ABS plastic
 - * Total mass = $(2.25 \times 10^{-5} \text{ m}^3) * (1.04 \times 10^3 \text{ kg/m}^3) = 0.023 \text{ kg}$
- Maxon spindle drive actuator mass = 0.01 kg
 - * Total mass motor 3 rotates = $0.023 \text{ kg} + 0.01 \text{ kg} = \underline{0.033 \text{ kg}}$
- Assume center-of-mass of bottom arm is 0.75 its length from point of rotation
 - * Motor 3 experiences max torque when bottom arm is parallel with floor
- Torque on motor 3 = $(0.328 \text{ N}) * (0.079 \text{ m}) = 0.026 \text{ N-m} = \mathbf{2.58 \text{ N-cm}}$
- **Motor 3 must have a Max Torque of at least 2.58 N-cm**

- Motor 3 must also satisfy the required mechanical power output

$$* P = T_{out} * \omega_{out}$$

$$* P = (0.026 \text{ N-m}) * (1.047 \text{ rad/sec}) = 0.027 \text{ W}$$

- **Motor 3 must have a Power Output of at least 0.027 W**

- **Motor 2:**

- Revolute joint connecting top arm to rotation bracket
- Rotating bottom arm, needle holder, needle, linear injection system, top arm, and motor 3
- Length of top arm (from axes of rotation) according to model: 40 mm
- Total volume of parts:
 - * 22500 mm^3 – from motor 3 calculations
 - * 6370 mm^3 – Top Arm
 - * $TOTAL = 28900 \text{ mm}^3 = 2.89 \times 10^{-5} \text{ m}^3$
- Assume everything is made out of ABS plastic
 - * Total mass = $(2.89 \times 10^{-5} \text{ m}^3) * (1.04 \times 10^3 \text{ kg/m}^3) = 0.030 \text{ kg}$
- Maxon spindle drive actuator mass = 0.01 kg
- Maxon anti-backlash motor assembly mass = 0.039 kg
 - * Total mass motor 2 rotates = $0.030 \text{ kg} + 0.01 \text{ kg} + 0.039 \text{ kg} = \underline{0.079 \text{ kg}}$
- Assume center-of-mass at the bottom and top arm is 0.5 its length from point of rotation
 - * Motor 2 experiences max torque when bottom and top arms are parallel with floor
- Torque on motor 2 = $(0.775 \text{ N}) * (0.073 \text{ m}) = 0.0562 \text{ N-m} = \mathbf{5.62 \text{ N-cm}}$
- **Motor 2 must have a Max Torque of at least 5.62 N-cm**
- Motor 2 must also satisfy the required mechanical power output
 - * $P = T_{out} * \omega_{out}$
 - * $P = (0.0562 \text{ N-m}) * (1.047 \text{ rad/sec}) = 0.059 \text{ W}$
- **Motor 2 must have a Power Output of at least 0.059 W**

- **Motor 1:**

- Revolute top joint
- Motor rotates a flywheel at a variable radius, depending on how far both arms are stretched out
- Assume this motor is rotating a cylindrical object

$$* T = \frac{J}{9.55 \times 10^4} * \frac{N}{t} \text{ (N-m)}$$

1. J = moment of inertia (kg-cm²)

2. N = speed (rpm)

3. t = time to accelerate to N (sec)

$$* J = \frac{1}{8} * W * D^2 + W S^2$$

1. W = mass of rotating object (kg)

2. D = cylinder diameter (cm) – 2 cm (based on model)

3. S = turning radius (cm) – 8.5 cm (center-of-mass)

- Calculate total mass that motor 1 rotates

* Total volume of parts:

1. 28900 mm³ – from motor 2

2. 6210 mm³ – top rotation bracket

3. $TOTAL = 35100 \text{ mm}^3 = 3.51 \times 10^{-5} \text{ m}^3$

- Assume everything is made out of ABS plastic

$$* \text{Total mass} = (3.51 \times 10^{-5} \text{ m}^3) * (1.04 \times 10^3 \text{ kg/m}^3) = 0.037 \text{ kg}$$

$$* \text{Maxon spindle drive actuator mass} = 0.01 \text{ kg}$$

$$* \text{Maxon anti-backlash motor (M2) assembly mass} = 0.039 \text{ kg}$$

$$* \text{Maxon anti-backlash motor (M3) assembly mass} = 0.039 \text{ kg}$$

$$* \text{Total mass motor 1 rotates} = 0.037 \text{ kg} + 0.01 \text{ kg} + 0.039 \text{ kg} + 0.039 \text{ kg} = \underline{0.1245 \text{ kg}}$$

$$* J = \frac{1}{8} * W * D^2 + W S^2 = (1/8) * (0.1245 \text{ kg}) * (2 \text{ cm})^2 + (0.1245 \text{ kg}) * (8.5 \text{ cm})^2 = 9.06 \text{ kg-cm}^2$$

$$* T = \frac{J}{9.55 \times 10^4} * \frac{N}{t} \text{ (N-m)} = \frac{9.06}{9.55 \times 10^4} * \frac{10}{1} = 9.48 \text{ E}^{-4} \text{ N-m}$$

– **Motor 1 must have a Max Torque of at least 0.095 N-cm**

– Motor 1 must also satisfy the required mechanical power output

$$* P = T_{out} * \omega_{out}$$

$$* P = (9.45 \text{ E}^{-4} \text{ N-m}) * (1.047 \text{ rad/sec}) = 9.93 \text{ E}^{-4} \text{ W}$$

– **Motor 1 must have a Power Output of at least 9.93E⁻⁴ W**

Appendix B

Blood Diagnostic Devices

B.1 Centrifuge Blood Analyzer

The following pages describe the details of the image processing routine from Section 3.4.3.1.3.1 used to enhance, segment, and quantify the buffy coat area on the centrifuge platform¹.

B.1.1 Image Processing for Quantifying Buffy Coat Areas

The image processing routines (i.e., *mergeImages.m*, *sort_nat.m*, *segmentLym_Mon.m*, and *segmentGran.m*) were written using MATLAB 2015b and require the installation of the Image Processing Toolbox to function. Acquired images (and example images) can be placed in either the same or a different folder. If located in a different folder, be sure to change the file paths in the code, otherwise, errors will occur.

B.1.1.1 Image Acquisition and Image Loading

In this study, green and red channel images were acquired length-wise along the capillary tube and stored in separate folders. These programs were written under the assumption that multiple images were acquired, however, the code also works for single images. For example, if one image fully captures the buffy coat region, then only one image is needed for processing. Furthermore, the green and red channel images can be placed in the same folder, but again, the file paths need to be updated in the code before running. All images stored in a specific folder can be processed during one run of the code. This is accomplished with a for loop, iterating through each image via the *imread* function.

¹This work first appeared in the electronic supplementary information of the following publication: Differential leukocyte counting via fluorescent detection and image processing on a centrifugal microfluidic platform. *Analytical Methods* 2016; 8(47):8272–8279⁵. All excerpts represent the original work of Max Balter.

B.1.1.2 Grayscale Conversion

A monochrome camera was used for this study, in which captured images were represented as 8-bit grayscale images. If color images are acquired instead, the code can still run; the images just need to be converted to grayscale before processing. This can be added to the code itself, or a separate pre-processing routine can be created using the `rgb2gray` function.

B.1.1.3 Merging Green and Red Channel Images

This code allows the user to input the trial number (s) and the number of image sets acquired (v). In our case, four image sets were acquired: one for each tube orientation, rotating the tube 90° for each set. This code also operates under the assumption that each image set, for both the green and red channel, is stored in a separate folder (*sort_nat.m* sorts images based on the natural order of a cell array of strings).

The montage function is used to separately stitch green and red channel images together, where the length of the montage corresponds to the number of images stored in the respective folder. Once individual montages are created for the green and red channel, the images are normalized to the maximum intensity value to correct for lighting differences across image sets. Finally, the images are fused together using the `imfuse` function to obtain a composite. Intensity values from the green image are colored green, and intensity values from the red image are colored red. At this point, the code saves images in a results folder (2-Processed Images) before moving on to the following processing steps.

B.1.1.4 Image Processing and Quantification of Buffy Coat

A number of processing steps are performed on the images before segmentation. Each image is processed and segmented sequentially based on the order specified by the filename strings.

B.1.1.4.1 Green Channel Images

1. **Crop Images:** By means of the `imcrop` function, the user is prompted to manually select the region of interest (i.e., the approximate location of the buffy coat). An interactive rectangle object appears on the image which can be dragged and/or moved

until the desired area is selected. The user then must either double click the area or press enter to execute the image crop and proceed with the code.

2. **Linear Contrast Stretching:** The function `imadjust` is used to adjust pixel intensity values for a more even distribution.
3. **2D Order-statistic Filter:** A 3x3 minimum filter is applied to the image using a for loop with three iterations. The filter size and number of loop iterations can be adjusted as needed.
4. **Segmentation:** A global threshold is applied to the image based on Otsu's method, using the function `graythresh` to automatically compute a threshold level. This level is selected to minimize intra-class variance between black and white pixels. At this point, the image is converted from grayscale to black/white, in which the white region indicates the lym/mon region of the buffy coat.
5. **Morphological Operations:** Holes in the segmented region are filled using the function `imfill`, and small pixels are removed via the `imopen` function.
6. **Identify Connected Objects:** Using the `bwconncomp` function, connected objects are located and analyzed for outlier segmented regions (e.g., abnormally large or small pixel areas away from the buffy coat region). The area (in pixels) of the segmented buffy coat region is quantified via the `regionprops` function.
7. **Overlay Segmented Boundary:** A mask is created from the binary image and the region is then overlaid over the original grayscale image. Data from the overlay boundary, including area, perimeter and location obtained from the `bwboundaries` function, is saved for use in processing the red channel images.

B.1.1.4.2 Red Channel Images

1. **Image Masking:** Segmented boundary data from the green channel image processing is loaded and converted to a mask using the `poly2mask` function. This is used to black out the lym/mon region so this area won't interfere with segmentation of the

granulocytes in the red channel images. Moreover, all regions above the buffy coat (i.e., platelets and plasma) are also masked out.

2. **Median Filter:** The function `medfilt2` is applied to the image to reduce noise.
3. **2D Order-statistic Filter:** Similar to the processing step for the green channel images, a statistic filter is also applied here. But in this case, a smaller 2x2 filter is used instead to better preserve pixel information.
4. **Segmentation:** Again, a global threshold is applied based on Otsu's method.
5. **Morphological Operations:** Holes in the segmented region are filled and small pixels are removed. In this case, a smaller disk object is used for cleaning operations to preserve segmented regions that drifted away from the buffy coat.
6. **Identify Connected Objects:** Connected objects are located and analyzed for outlier regions and the segmented buffy coat region is measured.
7. **Overlay Segmented Boundary:** A mask is finally created from the binary image and the region is overlayed over the original grayscale red channel image.

Buffy coat measurements are displayed at the end of *segmentLym_Mon.m* (`greenBuffyArea` is the lymphocyte/monocyte area) and *segmentGran.m* (`redBuffyArea` is the granulocyte area). These area measurements can then be collected for generating a standard curve, as demonstrated in this study, or used to reference a standard curve to output diagnostic leukocyte counts.

Image processing and segmentation steps for the acrylic chip data is identical to that previously described for the green channel images. However, in the case of the red channel images, pixel intensity values were summed after masking out the lym/mon buffy coat region.

B.1.2 Printed Circuit Board Design Details

As discussed in Section 3.4.4, a custom circuit board was designed to route power and DIO lines to and from the various electronic components in the analyzer (i.e., the microscope,

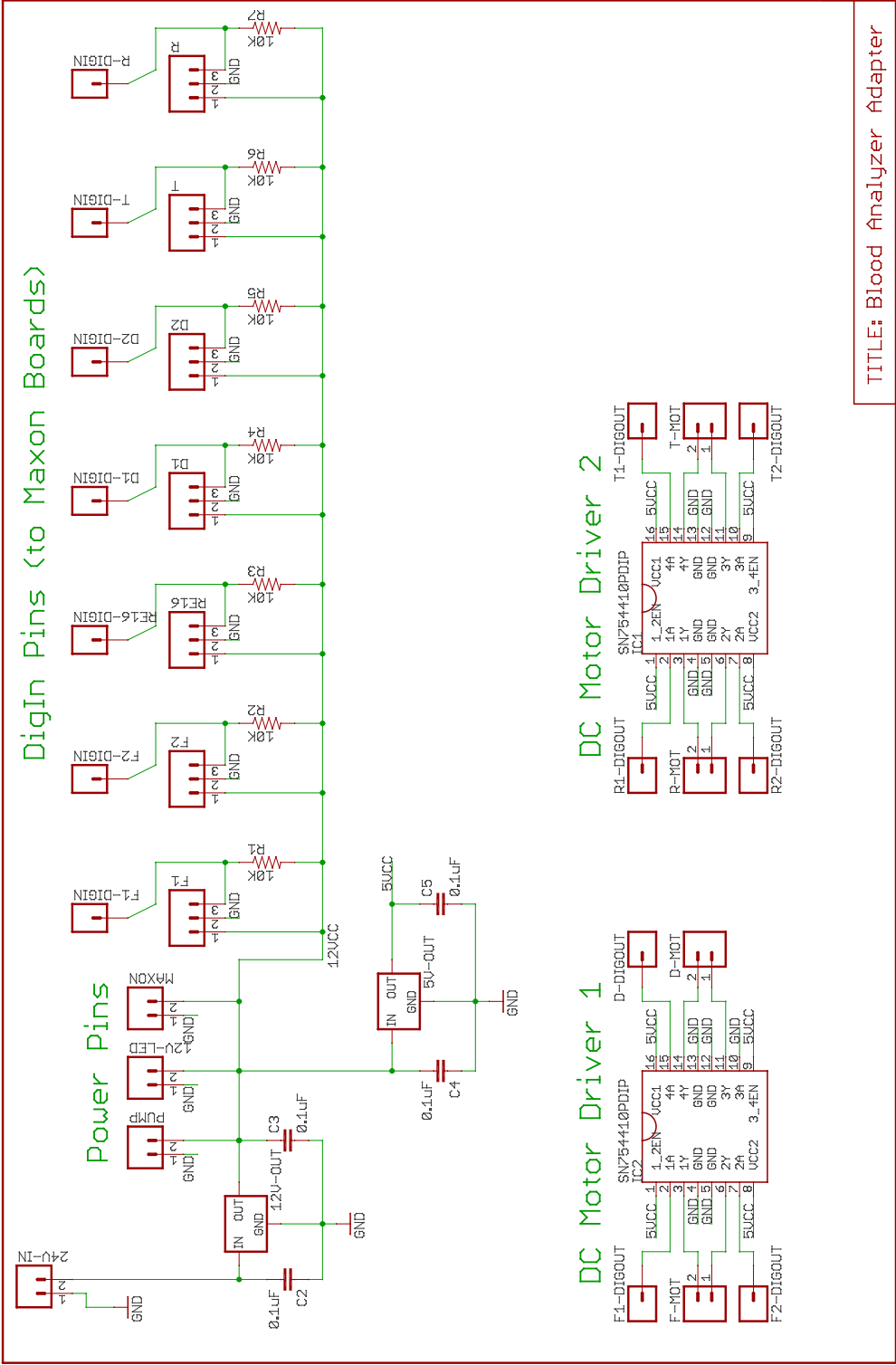


Figure B.1: Electronic circuit board schematic with labeled components.

centrifuge, and photometry module). Figure B.1, displays a detailed schematic of the board and Tab. B.1 lists the corresponding descriptions for each part.

Table B.1: Electronic circuit board components

Component	Description	Value	Part Number
5V-OUT	1.5A Voltage Regulator	—	L7805
12V-LED	2-pin 0.1 in. header	—	SFE-09914
12V-OUT	3A Voltage Regulator	—	LT1085CT-12
24V-IN	2-pin 0.1 in. header	—	SFE-09914
C2	Capacitor	0.1 μ F	399-4266-ND
C3	Capacitor	0.1 μ F	399-4266-ND
C4	Capacitor	0.1 μ F	399-4266-ND
C5	Capacitor	0.1 μ F	399-4266-ND
D-DIGOUT	Header 1	—	—
D-MOT	2-pin 0.1 in. header	—	SFE-09914
D1	3-pin 0.1 in. header	—	SFE-09915
D1-DIGIN	Header 1	—	—
D2	3-pin 0.1 in. header	—	SFE-09915
D2-DIGIN	Header 1	—	—
F-MOT	2-pin 0.1 in. header	—	SFE-09914
F1	3-pin 0.1 in. header	—	SFE-09915
F1-DIGIN	Header 1	—	—
F1-DIGOUT	Header 1	—	—
F2	3-pin 0.1 in. header	—	SFE-09915
F2-DIGIN	Header 1	—	—
F2-DIGOUT	Header 1	—	—
IC1	Dual motor driver	—	SN754410
IC2	Dual motor driver	—	SN754410
MAXON	2-pin 0.1 in. header	—	SFE-09914
PUMP	2-pin 0.1 in. header	—	SFE-09914

R	3-pin 0.1 in. header	—	SFE-09915
R-DIGIN	Header 1	—	—
R-MOT	2-pin 0.1 in. header	—	SFE-09914
R1	Resistor	10 K Ω	SFE-11508
R1-DIGOUT	Header 1	—	—
R2	Resistor	10 K Ω	SFE-11508
R2-DIGOUT	Header 1	—	—
R3	1/6W Resistor	10 K Ω	SFE-11508
R4	1/6W Resistor	10 K Ω	SFE-11508
R5	1/6W Resistor	10 K Ω	SFE-11508
R6	1/6W Resistor	10 K Ω	SFE-11508
R7	1/6W Resistor	10 K Ω	SFE-11508
RE16	3-pin 0.1 in. header	10 K Ω	SFE-09915
RE16-DIGIN	Header 1	—	—
T	3-pin 0.1 in. header	10 K Ω	SFE-09915
T-DIGIN	Header 1	10 K Ω	—
T-MOT	2-pin 0.1 in. header	10 K Ω	SFE-09914
T1-DIGOUT	Header 1	10 K Ω	—
T2-DIGOUT	Header 1	10 K Ω	—

Appendix C

Device Troubleshooting

Similar design, prototyping, and programming techniques were used to develop all the devices described in this dissertation. Specifically, SolidWorks 2015 was used for design modeling; parts were fabricated via 3D-printing, laser-cutting, vinyl-cutting, and CNC-machining; and software was written in MATLAB and LabVIEW.

C.1 Design and Prototyping

If you encounter problems in the initial design stage, there is an extensive online help forum for SolidWorks users and a long list of YouTube tutorials. To help get started with the prototyping equipment in the lab, I provided a brief user manual in Appendix D. For the most part, these machines are fairly intuitive to use after you get acclimated with the basics. As you prototype, however, there are a few tips and tricks that are important to remember.

First, we use screw fasteners for attaching parts together—we found this is the best approach for robust, non-permanent assemblies, while also allowing for quick alignment adjustments of parts, if needed. In order to use screws in the assemblies, clearance and tapped holes are designed in SolidWorks, and tapped holes are manually threaded after prototyping. One of the nice features in SolidWorks is the *Hole Wizard* function, which automatically creates and dimensions holes based on the type of screw selected. For example, if you are designing threads for an M3 screw, you can simply select *tapped hole* and *M3* screw size, and the program will automatically create an M3 tapped hole with the appropriate diameter (i.e., 2.5 mm) at the specified location; no need to reference a tap chart. After building the part, for example via 3D-printing, the screw threads are formed using a manual tap. There is an extensive toolbox of hand taps in the lab for a wide range of metric and inch screw types.

Second, when designing, always be cognizant of how you plan on making the part: whether it is via 3D-printing, laser cutting, or machining, each have their respective design

requirements. This process is also known as design for manufacturing. As an example, 3D-printing is great for fabricating complex 3D objects, however, CNC-machining is not. Likewise, CNC-machining and laser cutting are great for fabricating large flat panels, however, 3D-printing is not.

Third, keep in mind that prototyping is a process. Creating the *perfect* part is a never-ending pursuit and going through 10+ design iterations for an important part is common. With the rapid prototyping equipment in the lab, the process is expedited, but the process of editing features and sketches in parts can be time-consuming.

C.2 Motor and Sensor Integration

Once the mechanical parts of a device are prototyped and assembled, actuators, motors, and sensors can be integrated into the system. In the devices described in this dissertation, linear and rotary stages were sourced from Zaber Technologies, Inc. and National Aperature, Inc.; motors were sourced from Maxon Precision Motors, Inc.; and sensors were sourced from DigiKey, SparkFun, Pololu, and Adafruit. Each website provides detailed information regarding the various products and troubleshooting.

One sensor in particular, the Hall-effect position sensor (A1120, Allegro MicroSystems, LLC—sourced from DigiKey), is worth noting since it was used extensively in our devices for homing motors. Paired with a small magnet (D101-N52, $\varnothing 1/16$ in., $1/32$ in. thick, K&J Magnetics, Inc.), it provides a robust, reliable, and effective means for homing motors. When the magnet is positioned <2 mm from the front face of the sensor, the signal pin on the sensor outputs a high-pulse (i.e., 5 V), indicating that the sensor is on. Conversely, if the magnet is >2 mm from the front face of the sensor, the signal pin on the sensor outputs a low-pulse (i.e., 0 V), indicating that sensor is off. The signal pin can then be routed to a microcontroller for analysis and device control on the host processor. However, the magnet needs to be placed in a particular orientation (i.e., the magnetic side facing up) in order to trigger the sensor. The correct face of the magnet is colored gray, and is also magnetic when picked up with tweezers. Figure C.1 shows the magnet with the magnetic side facing up, and the Hall-effect position sensor. If the magnet is implemented in the wrong orientation,

the corresponding motor will fail to *home* and this may damage the hardware of the device. When using these position sensors, it is critically important to place the magnet in the proper orientation on the device. This was one of the most common hardware bugs we encountered during device development, yet it is one of the easiest to resolve.

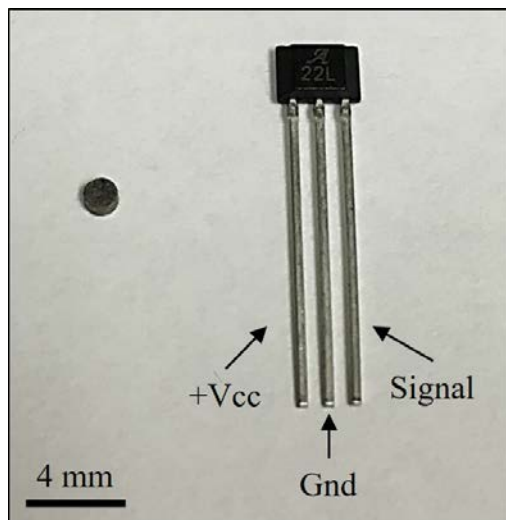


Figure C.1: Magnet (left) and hall-effect homing sensor (right). When connecting the sensor pins to the EPOS microcontroller from Maxon Precision Motors, a 10K Ω needs to be placed between the +Vcc and signal pins. +Vcc can range from 3–24 V, and the signal line is routed to a digital input pin.

C.3 Motor Control

To control the actuators and motors, third-party drivers were deployed that interfaced with the LabVIEW programming environment. Specifically, the X-MCB2 series motor drivers from Zaber Technologies were used to control the stepper-based linear actuators, whereas the EPOS series drivers from Maxon Precision Motors were used to control DC-brushed motors. Both drivers have an extensive user manual online as well as example LabVIEW code for positioning control and DIO handling. When interfacing the Zaber driver in LabVIEW, be sure to specify the appropriate COM port when initializing the device; otherwise errors will occur in the software. When switching USB ports, the COM port also changes, and this needs to be updated in the code. This is another common (and avoidable) error if LabVIEW is unable to *find* the device.

The EPOS drivers are more challenging to operate and more error prone. To control

multiple DC-brushed motors, the drivers must be daisy-chained to enable the USB2CAN communication protocol. This entails manually linking the Tx and Rx pins together with wire and specifying a unique node ID for each driver. Commands from the host processor will then specify which motor to control using this node ID. Powering the devices can be accomplished by connecting the power pins in a parallel circuit, ensuring each device receives the same input voltage (in our case 12 V). Upon power up, the status LED on each driver should be blinking green. Oftentimes, however, the status LED on the first or last driver in the chain will be a constant red, indicating an error. Don't be alarmed! This is simply an unexplainable error, called the *CAN passive mode error* and is a bug in the motor driver firmware. To get rid of the error, open the EPOS Studio software, create a project, right-click on the error in the status window, and hit *clear all errors*. This will resolve the issue, and the indicator LEDs on all the drivers should now be flashing green. When controlling the DC-brushed motors, either in LabVIEW or EPOS Studio, *activating* the specified axis will cause the LED indicator on that particular driver to turn a constant green.

The EPOS drivers also provide *auto-tuning* of parameters (i.e., current, speed, and position control gains) in EPOS Studio. Before using the DC-brushed motors, they **MUST** be tuned! Otherwise, you risk damaging the motors and the device hardware. The tuned parameters can then be exported for use in LabVIEW. The parameters for each axis only need to be uploaded once. If the wrong parameters are loaded onto the wrong driver, errors may occur.

Appendix D

Equipment User Manuals

This section explains how to operate the various prototyping equipment in the Yarmush lab (BME-123). If you do not understand the following instructions or have any questions regarding the equipment, please do not hesitate to contact me. These machines can be tricky to operate at first, but the protocol becomes fairly intuitive with practice. As with any equipment, proper maintenance is a must! When in doubt, you can always refer to the user manuals included with the equipment or contact the technician.

D.1 Stratasys Mojo 3D-Printer

Contact: Gary Lavieri (glavieri@alleghenyedusys.com, (570) 401-2389)

Figure D.1 shows the Mojo 3D-printer. It is capable of printing parts as large as 5 x 5 x 5 in., and operates using fused-deposition modeling—that is, it prints parts layer-by-layer. From my experience, the printer works great on part features >0.1 mm; anything less, runs the risk of not accurately resembling the model. If finer print resolution is required, the rapid prototyping facility, in the D-wing of the mechanical engineering department, has a PolyJet, resin-based printer that has a resolution of $30\text{ }\mu\text{m}$. If interested in this service, you can contact John Petrowski (petrows@rci.rutgers.edu).

To use the Mojo 3D-printer, first, prepare the machine. This includes cleaning out the scraps of plastic in the blue bins, the brushes, and throughout the enclosure; removing plastic from the build and support material nozzles; and placing a build plate in the device. The build plate should securely lock in-place if properly inserted. Once complete, the inside of the printer should look like that displayed in Fig. D.2.

Next, in the software, import the .stl file into the *Print Wizard* program (Fig. D.3). Double clicking the .stl file also works to open the model in the program. You can add as many parts as you want, given they all fit within the build plate dimensions (5 x 5 x 5 in.). If all the parts do not fit on one build plate, the program populates extra parts on a



Figure D.1: The Mojo 3D-printer from Stratasys

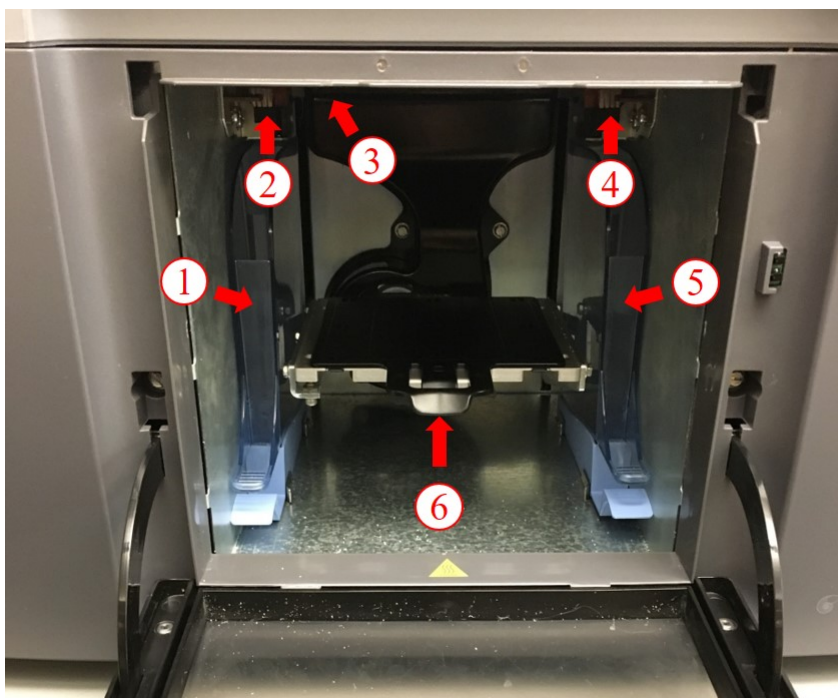


Figure D.2: Step 1: Prepare the machine for printing by cleaning plastic debris from the blue bins (1 and 5), brushes (2 and 4), and print nozzles (3). Afterward, securely attach a build plate to the platform (6).

second plate. In this case, the printer makes two runs, which requires you to exchange out the build plate with a new one after the first run.

In my experience, the *sparse* print support setting works best, though feel free to change it as needed. At this stage, it is important to figure out the optimal orientation to print your part(s). Typically, you want the largest flat surface to be facing down on the build plate. Changing the part orientation in the *Print Wizard* program can affect the final build. This is important if you plan on printing the same part multiple times. Once the settings and part orientation(s) are set, press *Print* (Fig. D.4).

This creates a build path for the part(s) and loads the file into the *Mojo Control Panel* software. From here, select the build from the drop down menu (Fig. D.5) and press *Print*. The printer then calibrates and prints the parts, providing an indicator for the current layer being printed and the estimated time to completion.

Once the part(s) is finished printing, remove the build plate from the machine and gently remove the part(s) from the plate. Sometimes the part(s) can be difficult to take off the plate, in which case, you can bend the plate and/or use pliers to snap off the part(s). Also note, the build plates are one-time use disposables.

Then, place the part(s) in the washer (Fig. D.6) to dissolve away support material. The washer must first be prepared by filling the tank with water and dissolving a wash tablet, as pictured in Fig. D.6c. Enough liquid should be placed in the tank to fully cover the part(s). The washer runs for an 8-hour cycle—sufficient to completely remove the support material. Once complete, remove the parts (wear lab gloves and try not to let fluid contact your skin!), store the wash liquid in containers, and clean out the tank. Chemicals in the wash fluid can damage the insides of the washer and limit the life-cycle of the agitator components (Fig. D.6c).

Table D.1: Components and associated part numbers for the Mojo 3D-printer.

Components	Description	Part Number
QuickPack P430 Ivory (80 ci)	Model material	350-80100
QuickPack SR-30 Support (80 ci)	Support material	350-80200
Modeling Bases 5 x 5 in. (case of 24)	Build plates	350-10000
Cleaning Agent Tablets (case of 24)	Wash tablets	300-00104
WaveWash 55 Replacement Bushing	Agitator bushing	540-10402

And that is it! Please be sure to continuously maintain both the printer and washer,

especially if using these machines on a daily basis. Table D.1 lists the parts used in the printer and washer if additional/replacement components are needed. Please refer to the user manual on how to replace print material in the machine. Figure D.7 shows a view underneath the hood of the 3D-printer, highlighting the model and support print engines. The *Mojo Control Panel* monitors how much material is left in both the build and support material cartridge, and provides an indication of when more material should be ordered. The printer only works with the *Mojo QuickPack* ABS material from Stratasys—*DO NOT* use any other ABS (or other plastic) with the machine; otherwise you risk damaging the equipment.

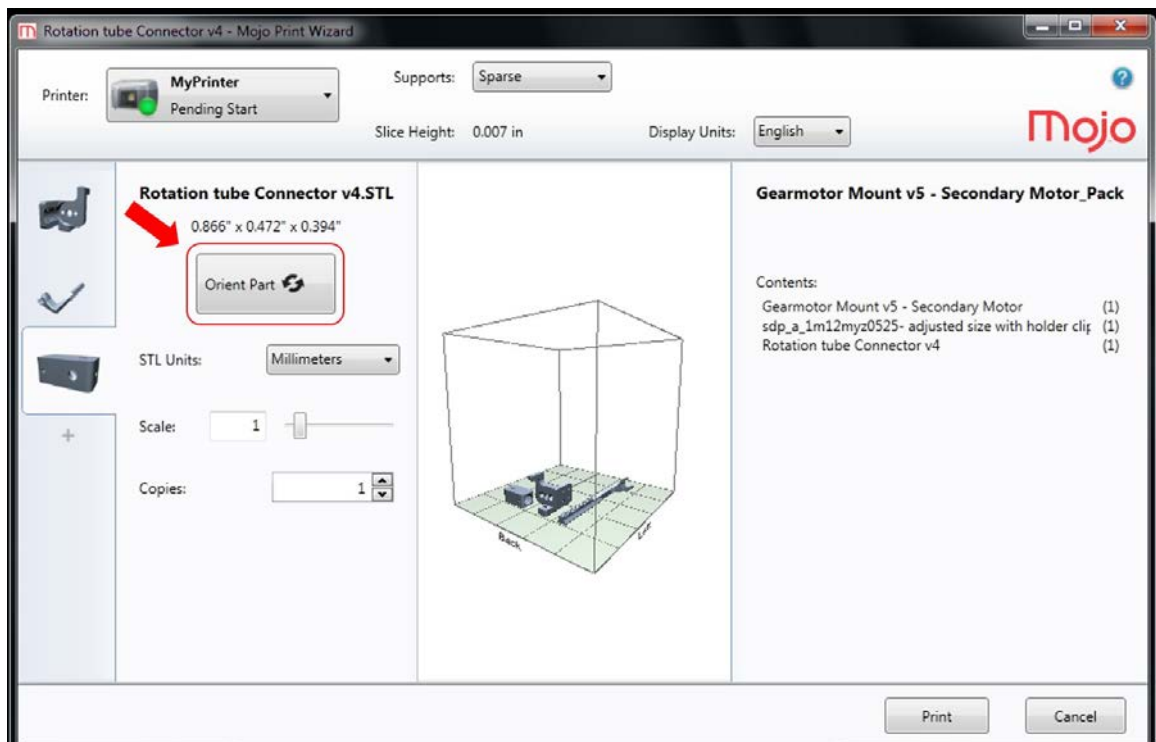


Figure D.3: Step 2: Import the .stl file(s) into the Print Wizard and orient part(s).

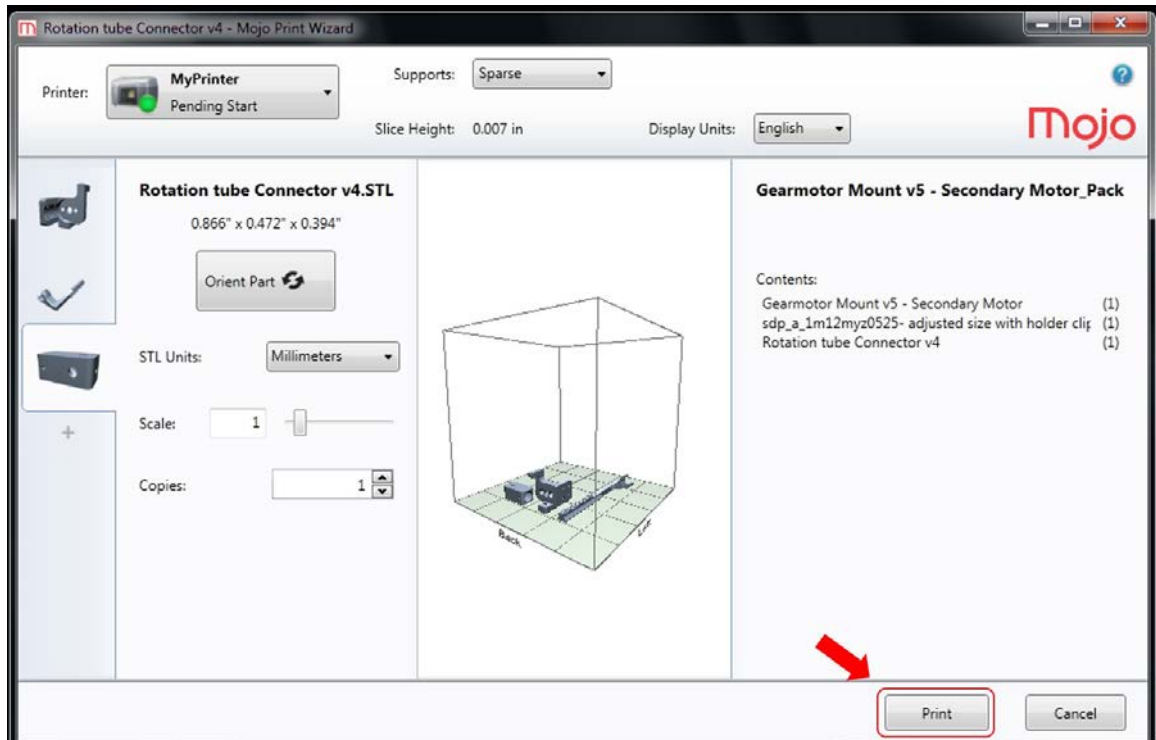


Figure D.4: Step 3: Press print to send the build file to the Mojo Control Panel.

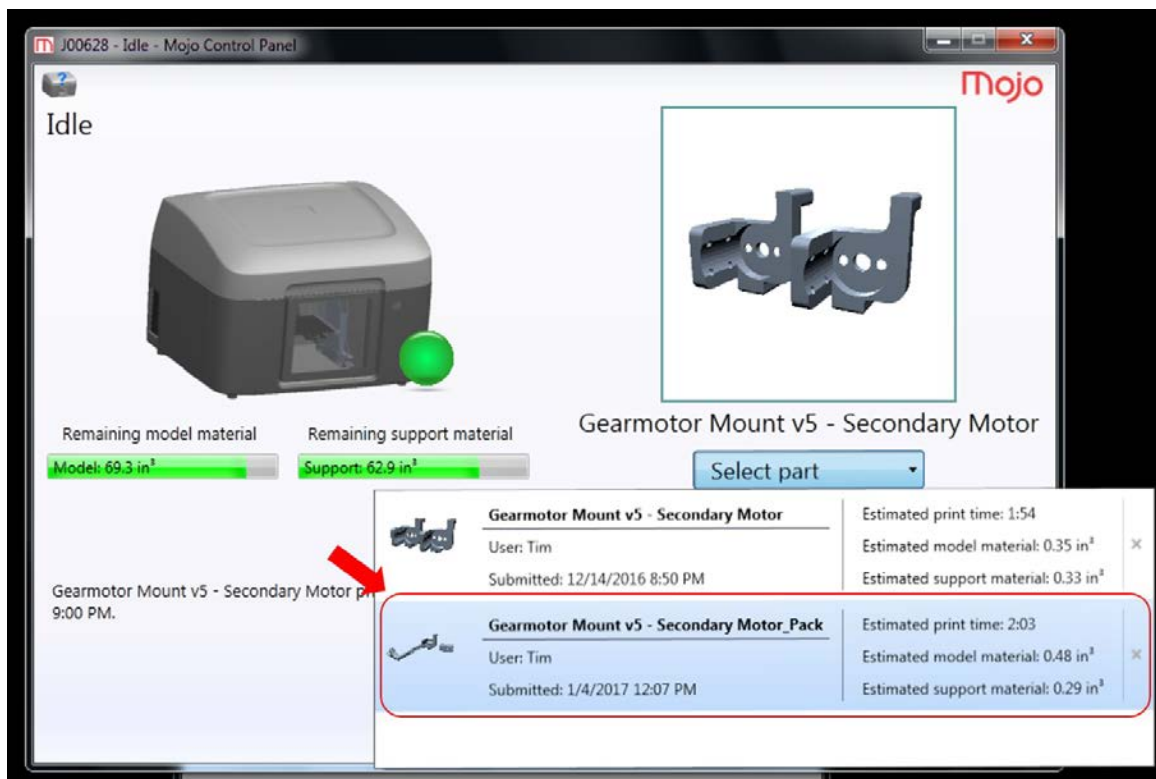


Figure D.5: Step 4: In the Mojo Control Panel, select the build from the drop down menu, and hit print.

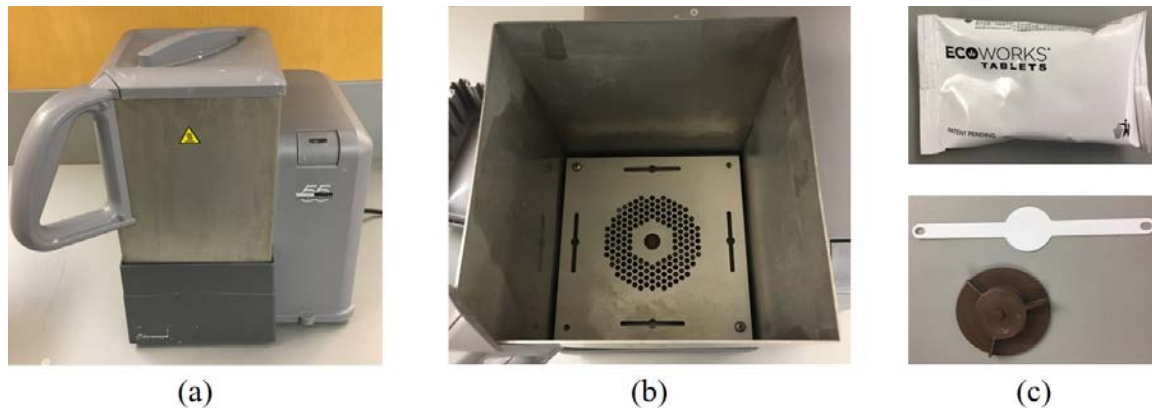


Figure D.6: Step 5: Place printed part(s) in the washer to dissolve support material. (a) Outside and (b) inside of the washer. (c) Top: wash tablet that needs to be placed in the washer and dissolved in water. Bottom: replacement bushing and agitator components.

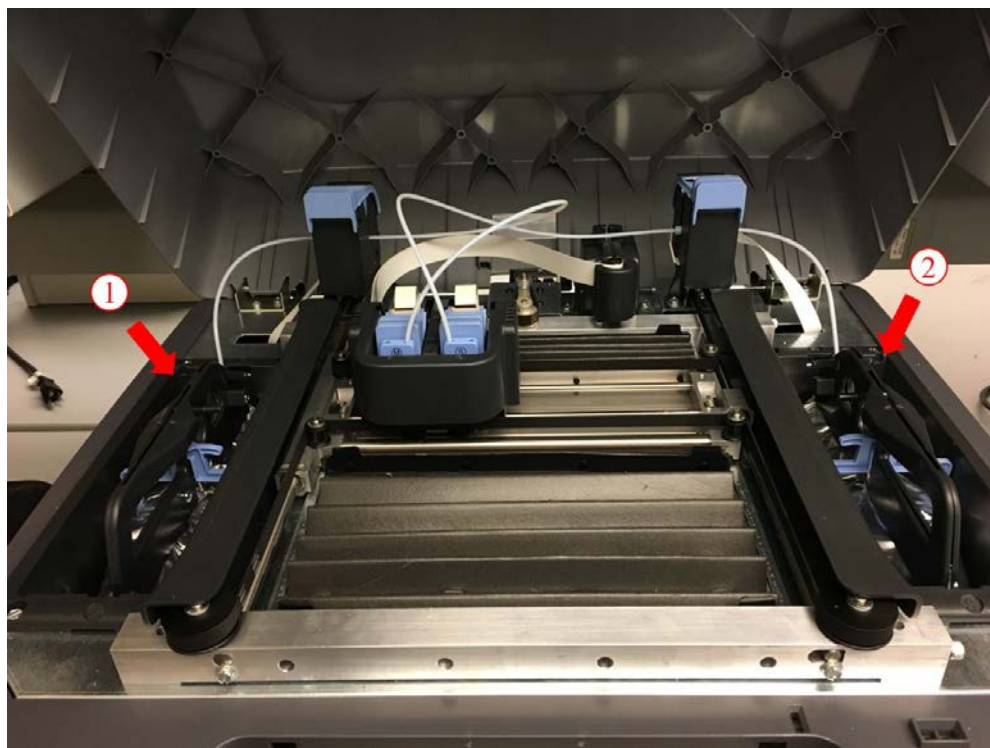


Figure D.7: View underneath the top lid of the 3D-printer: 1. modeling material print engine, 2. support material print engine.

D.2 Epilog Zing 24, 60 W Laser Cutter

Contact: Brian Koskuc (bkoskuc@alleghenyedusys.com, (917) 757-1322)

Figure D.8 displays the Epilog laser cutter; underneath is the air filtration system, and above is the air pump. To use the machine, you must first turn on *ALL* three devices. It is absolutely critical to turn on the air filtration system and air pump to ensure harmful particulates are appropriately removed, and to reduce the risk of fire during operation.



Figure D.8: Epilog laser cutter (60 W, 24 x 12 in. workspace).

After turning on the machines, the laser cutter will proceed to home the two axes on the gantry. At this time, the controls on the user interface are disabled as not to interrupt the homing. Once this process has finished, the laser needs to be manually focused based on the thickness of material you are cutting and/or engraving. This is accomplished by opening the top lid of the laser cutter, placing the material in the workspace (the top left corner is best) pressing the *focus* button on the control panel, and pulling out the focusing peg, as seen in Fig. D.9.

Using the up and down arrows on the control panel, adjust the height of the platform so the focusing peg gently presses against the surface of the material (Fig. D.10). It does not have to be perfect, but the peg should be in contact with the material without the

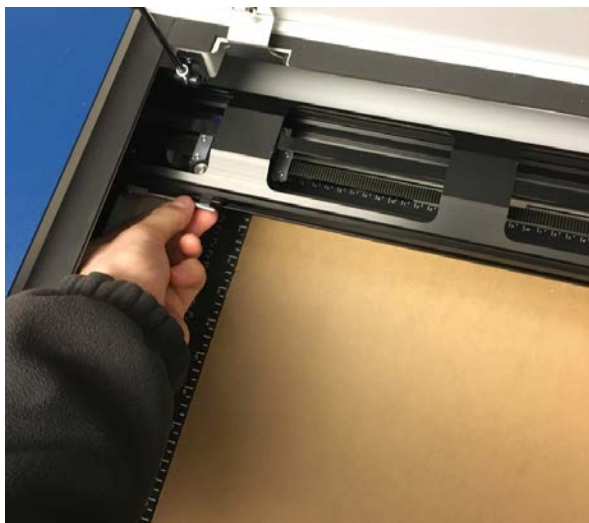


Figure D.9: Step 1: Press the *focus* button on the control panel and pull out the peg.

spring bending. When using cast acrylic sheets—which we use for fabricating microfluidic chips—oftentimes, the thickness will vary throughout the sheet. This is just a result of the acrylic manufacturing process on the supplier’s end; it has nothing to do with the platform being imbalanced.



Figure D.10: Step 2: Focus the laser by adjusting the vertical height of the platform.

At this point, the laser cutter is all set and calibrated. Next, the design file needs to be configured in Adobe Illustrator by first importing a vector formatted design file (e.g., .dxf). The software will prompt you to select the appropriate import settings. It is critically important to remember the units used when designing the part. For example, if millimeters were used when dimensioning the part in a CAD program, then millimeters must be selected

in Illustrator, with a scale of 1 (Fig. D.11).

Then, the extraneous text that comes with the imported file must be deleted, otherwise the text will be cut/engraved into the material (Fig. D.12). A new file must then be created using the pre-made template: *Epilog Zing 24 Laser Cutter Template* (Fig. D.13). This file has a 24 x 12 in. art board, which corresponds to the area of the laser cutter workspace.

Next, copy the designs from the imported .dxf file to the new Illustrator file, and adjust the stroke size to 0.07 pt. for cutting (Fig. D.14). This is an extremely important step. Any geometry with a stroke size >0.07 pt. will be engraved in the material, whereas, geometry with a stroke size <0.07 pt. will be cut. When wondering why the laser engraved a design when you intended to cut the material, the issue is likely due to a large stroke size. After aligning the pieces to cut (can be aligned fairly close to each other to preserve material), select File → Print → Setup (Fig. D.15).

This opens up a dialog box to select the printer (Fig. D.16); in this case the *Epilog Engraver WinX64 Zing*. Make sure the status of the printer is *Ready*. Sometimes the status can read *Offline*, which indicates that either the power on the laser cutter needs to be cycled, or Illustrator needs to be restarted. In some instances, a *copy* of the *Epilog Engraver WinX64 Zing* will appear in the printer section. Selecting this as the printer works fine. Next, select *Preferences* which opens up the printing preferences for the laser cutter. Under the *General* tab, speed, power, and frequency settings can be manually set (Fig. D.17). Note, the *Raster Setting* is for engraving, whereas, *Vector Setting* is for cutting (this is just the nomenclature Epilog uses).

If cutting acrylic, saved parameters are found under the *Advanced* tab (Fig. D.18). Here, speed, power, and frequency were experimentally optimized for the various acrylic thicknesses we have in stock in the lab (i.e., 1/32, 1/16, 1/8, and 1/4 in.—all sourced from McMaster-Carr). If using these settings, please do not change them after loading. After loading the appropriate settings, return to the *General* tab to double check key parameters. Specifically, make sure the horizontal and vertical piece size are 24 and 12 in. respectively. If these values are different, the dimensions of the cut will be offset.

Once everything looks correct, you can then select *ok*, which returns you to the original print dialog box (Fig. D.20). Notice how the designs do not appear in the print preview box,

and instead, it is a blank, white sheet. This indicates that the orientation of the document needs to be adjusted. To do this, select the leftmost orientation so the print preview area is displayed as a canvas. If the problem persists, and you do not see the designs in the print preview box, then you need to select Setup → Print again (Fig. D.21).

As seen in Fig. D.22, the designs are now displayed in the print preview box. You are now all set to send the file to the laser cutter! The file name will then appear on the laser cutter control panel (Fig. D.23). The job number refers to how many files have been uploaded to the laser cutter while it has been powered on. If multiple files have been uploaded, you can cycle through the various print jobs on the control panel. Once you select the job, press *GO* and watch the laser cut your designs.

It is critically important to watch the laser cutter while it is operating. Flare-ups do occur while the laser is cutting through material. Typically, the thicker the material, the more likely flare-ups will occur. If a fire does happen to break out (this has never happened to me before) unplug the power cord, call 911, and use the fire extinguisher sitting next to the cutter. To maintain the machine, the platform should be removed from the laser cutter in order to dispose the scraps and debris. If using the laser on a daily basis, it should be cleaned once a week.

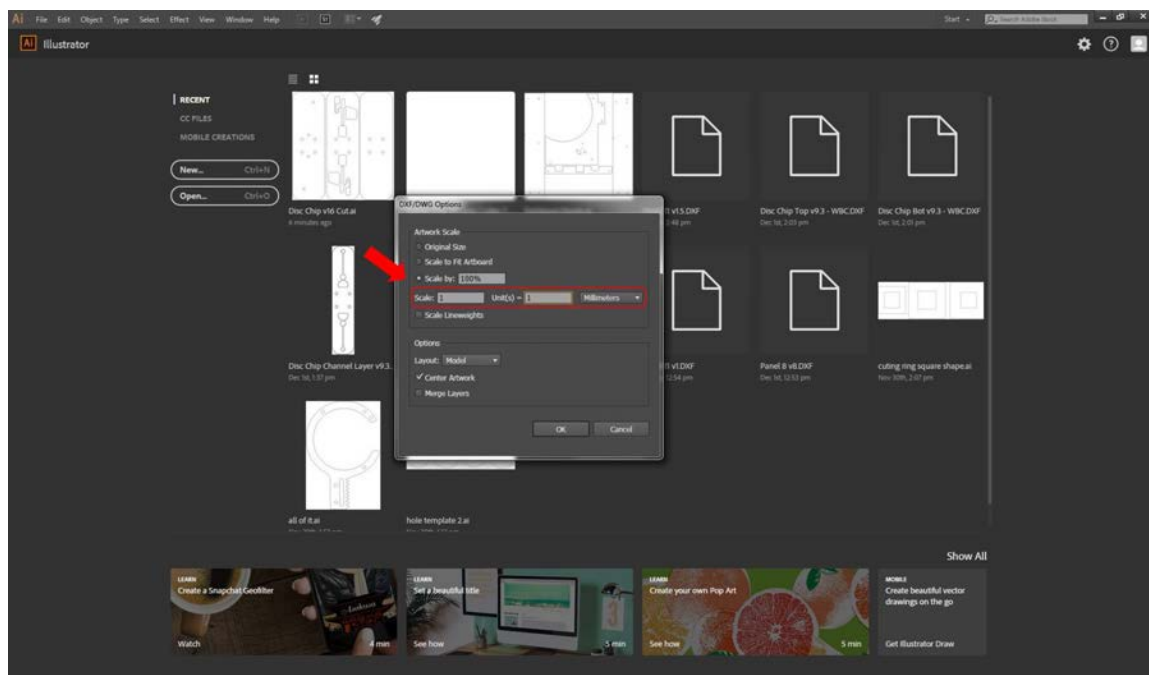


Figure D.11: Step 3: Import the .dxf file into Illustrator.

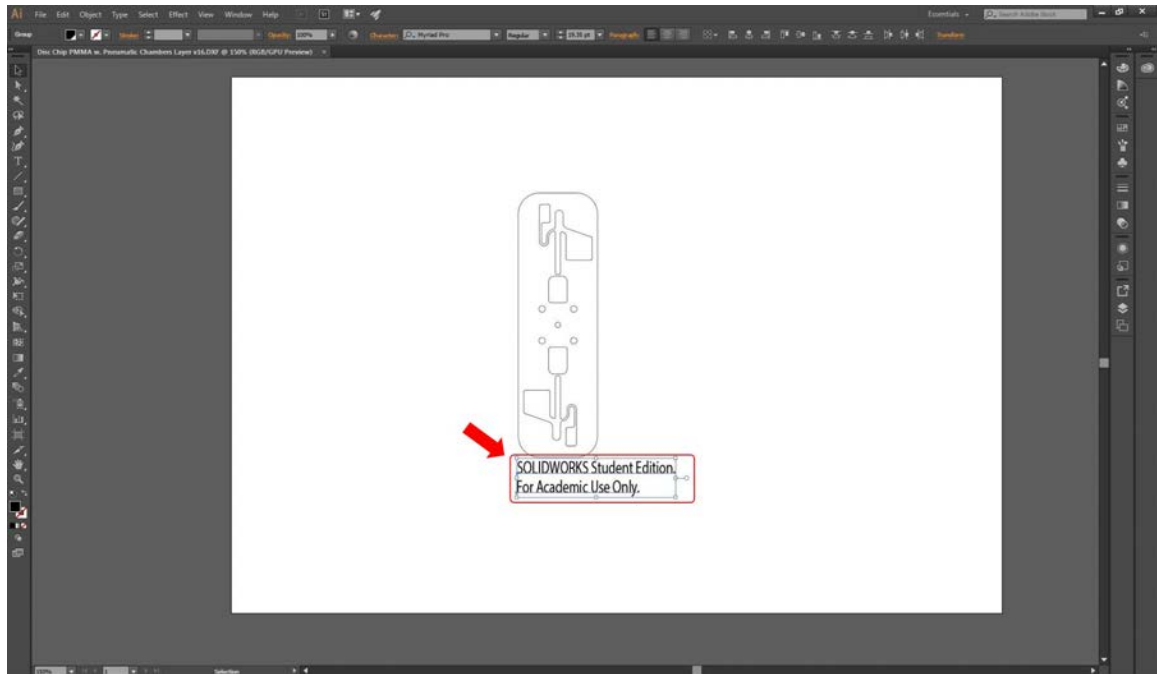


Figure D.12: Step 4: Delete extraneous text.

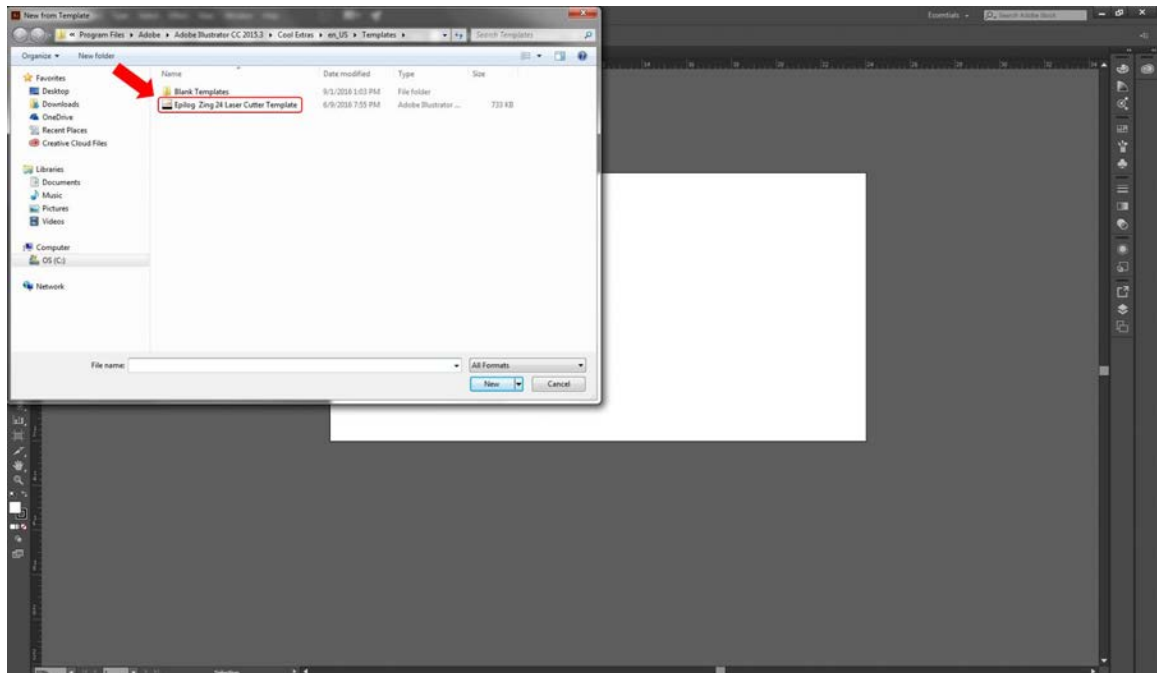


Figure D.13: Step 5: Create a new file using the Epilog Zing Template. The art board size in Illustrator corresponds to the workspace of the laser cutter (i.e., 24 x 12 in.).

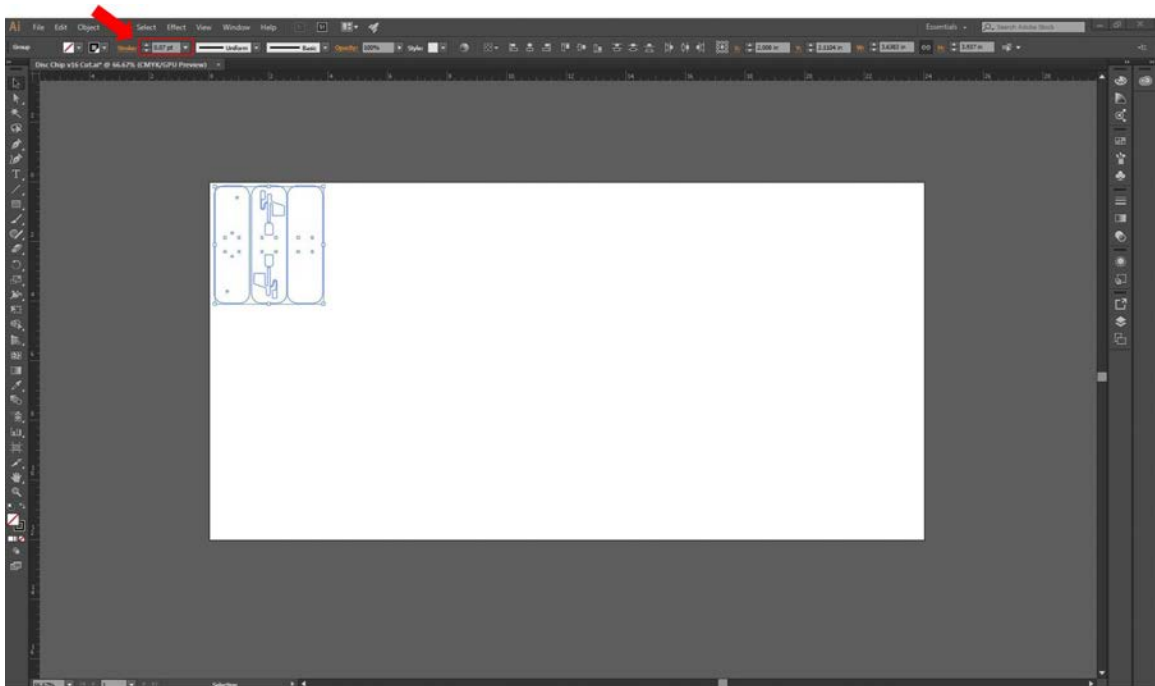


Figure D.14: Step 6: Copy design files into template and change stroke size to 0.07 pt.

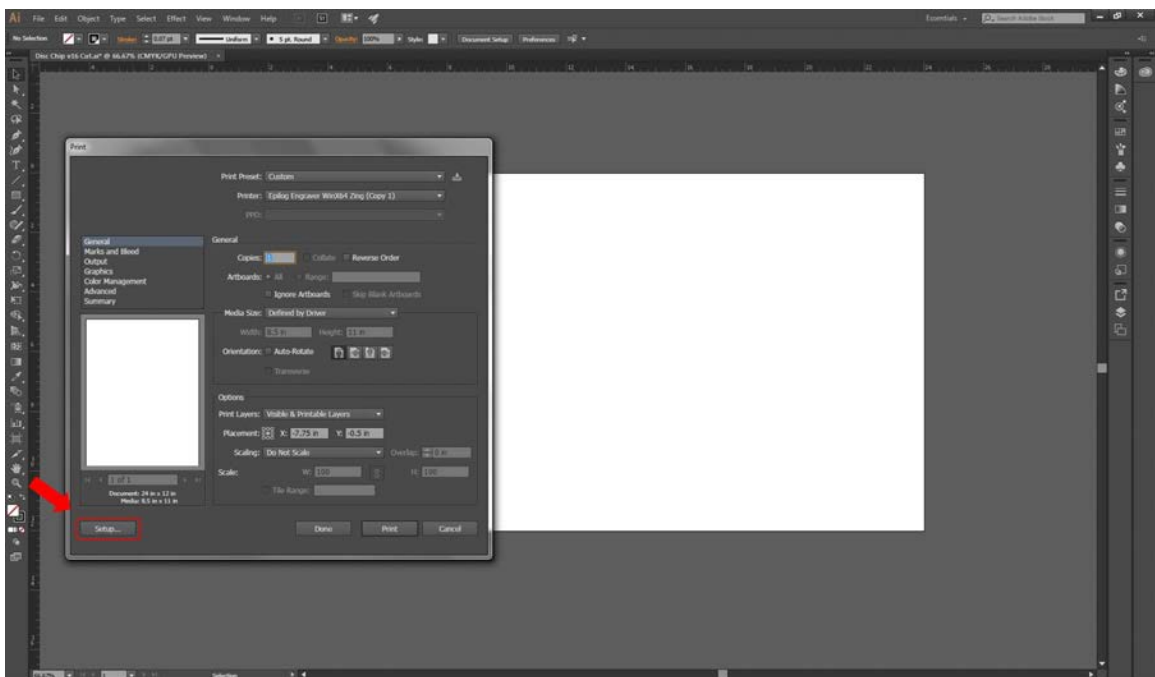


Figure D.15: Step 7: Select File → Print → Setup.

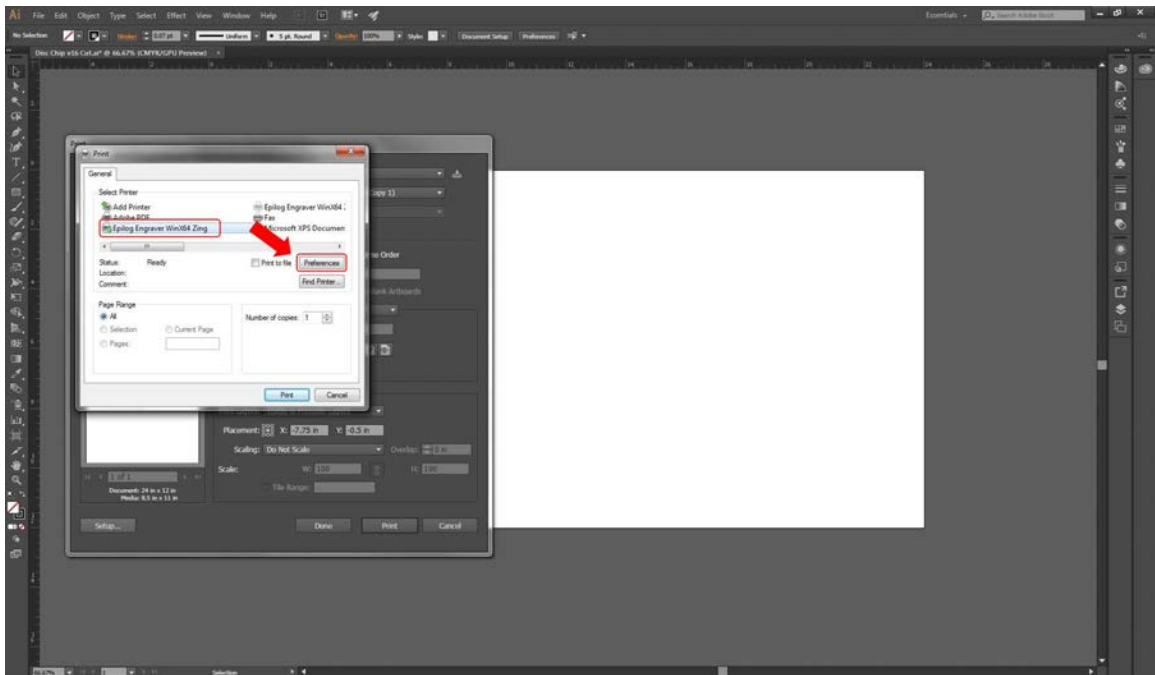


Figure D.16: Step 8: Select the Epilog Engraver under the printer heading.

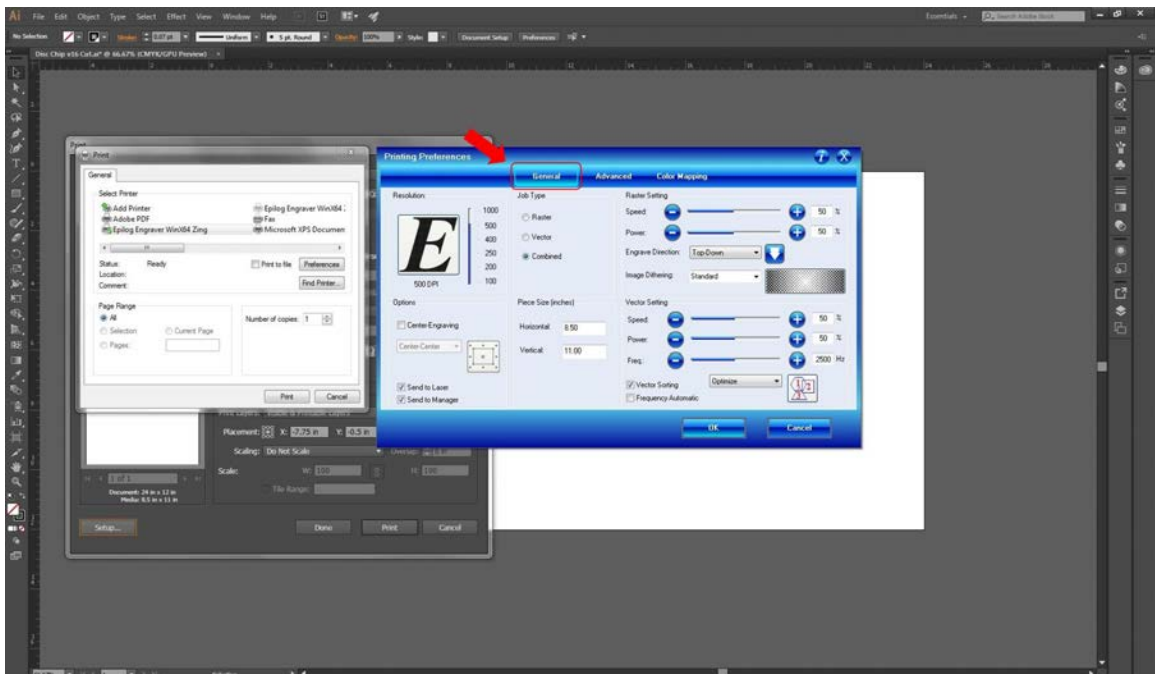


Figure D.17: Step 9: Laser cutter general printer properties.

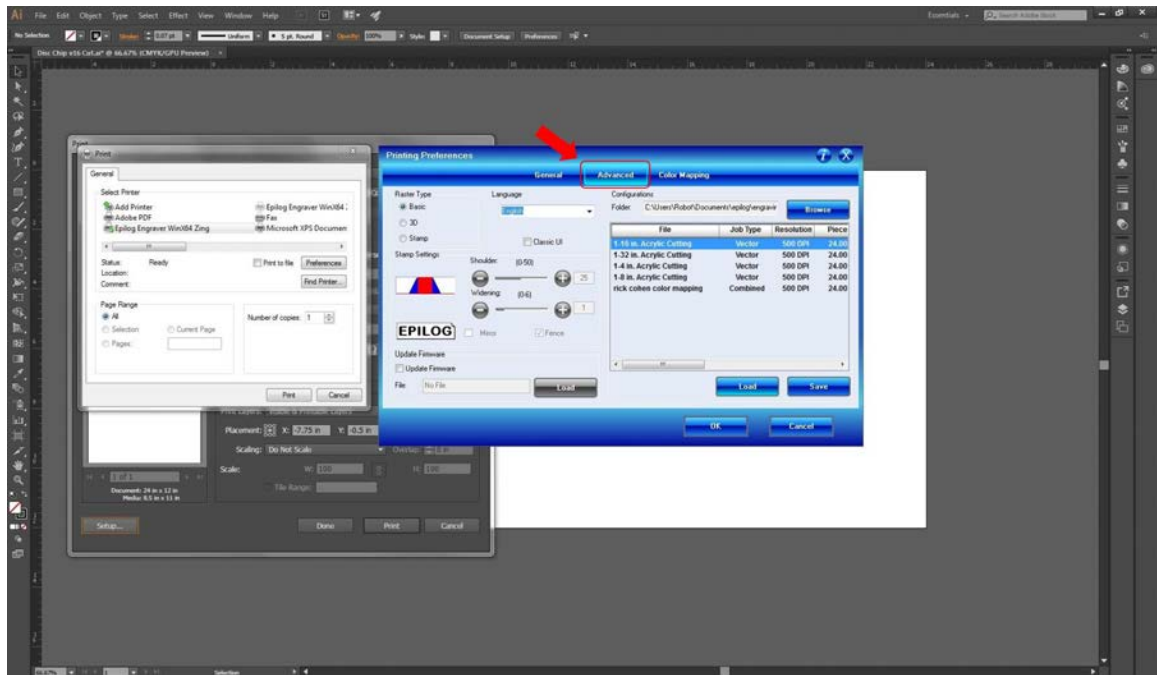


Figure D.18: Step 10: Saved cutting parameters under the Advanced tab.

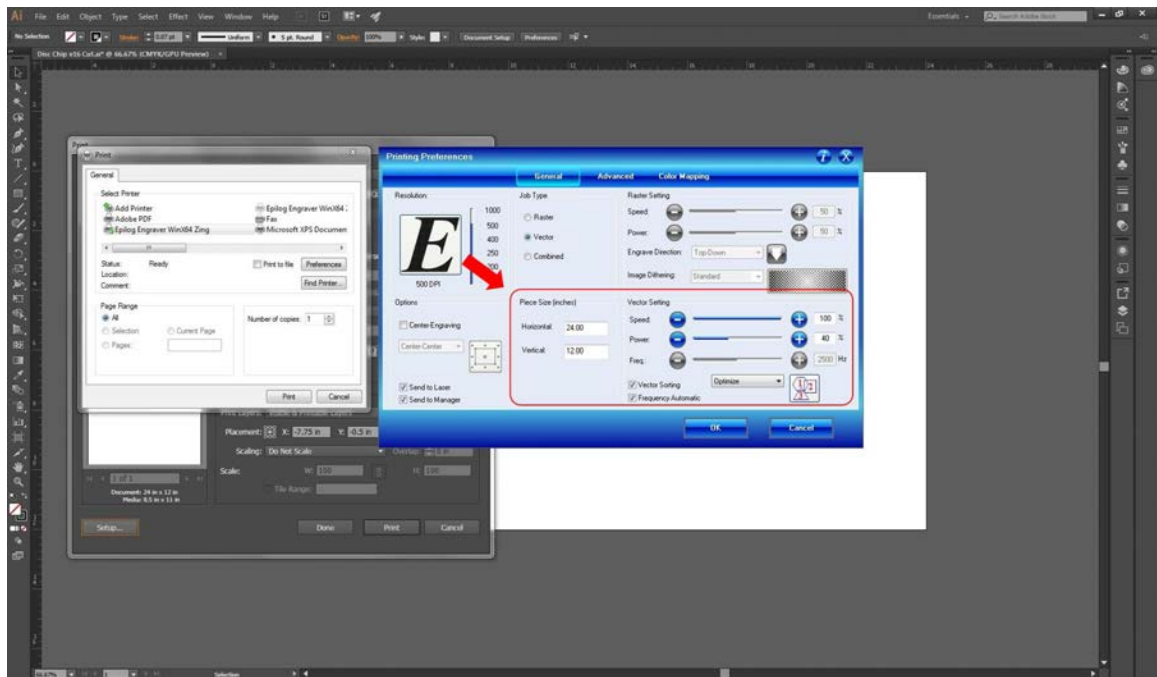


Figure D.19: Step 11: Double check printing preferences under the General tab.

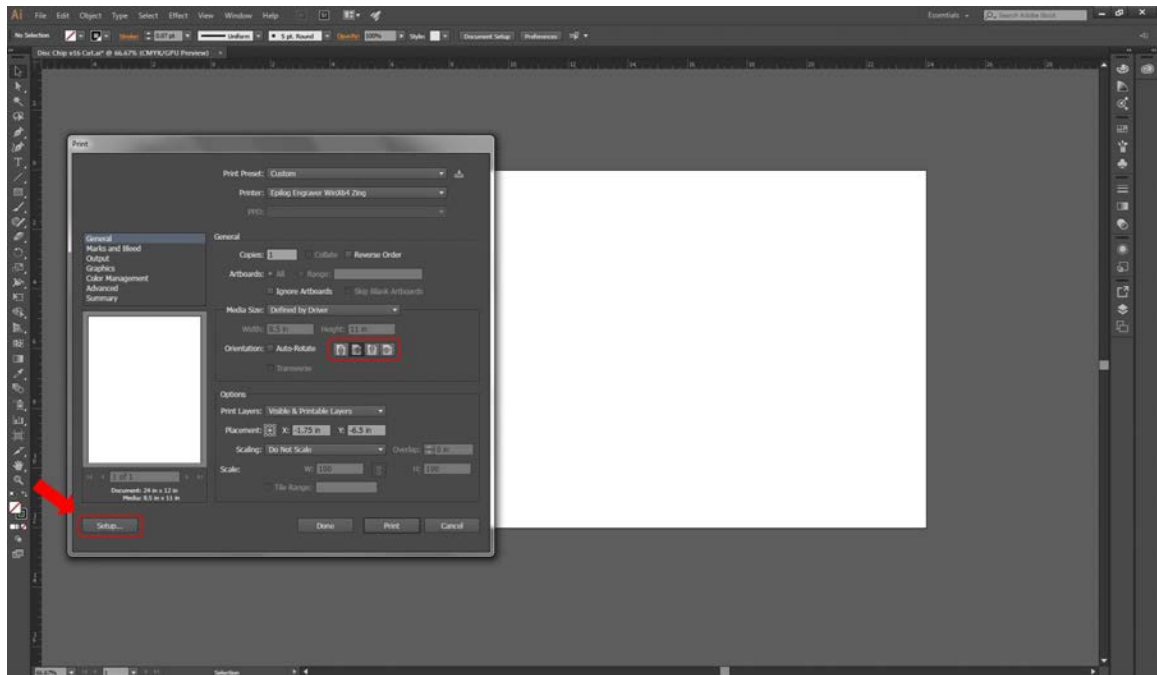


Figure D.20: Step 12: Adjust the document orientation.

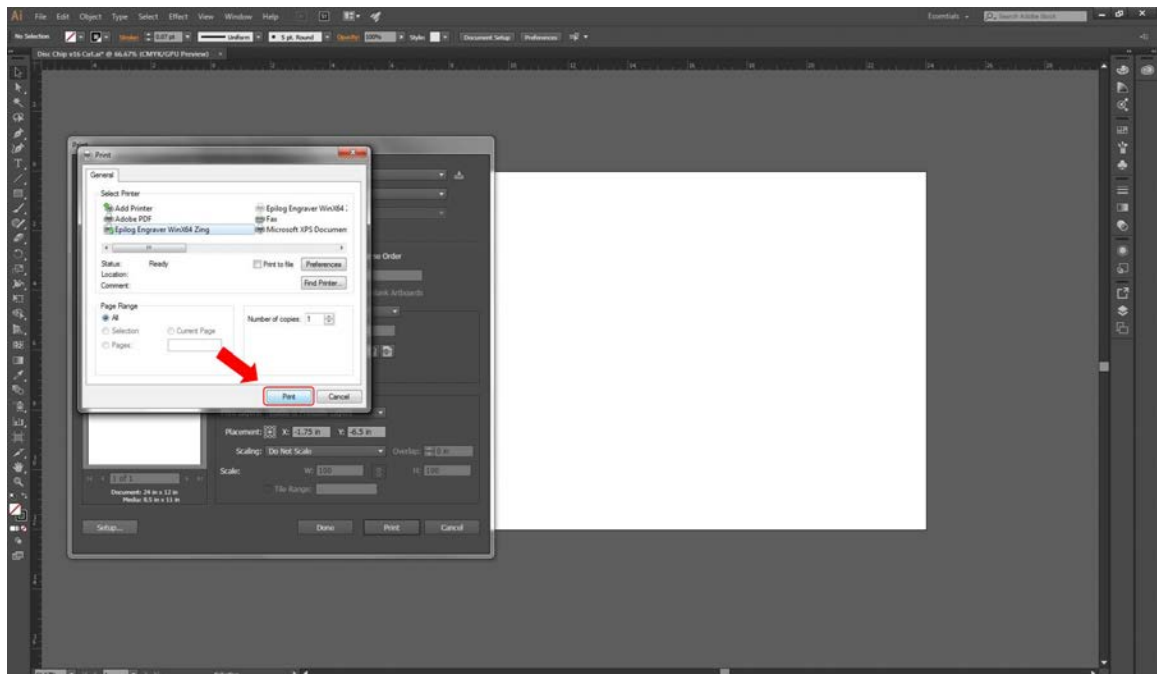


Figure D.21: Step 13: Select print again to adjust the document orientation.

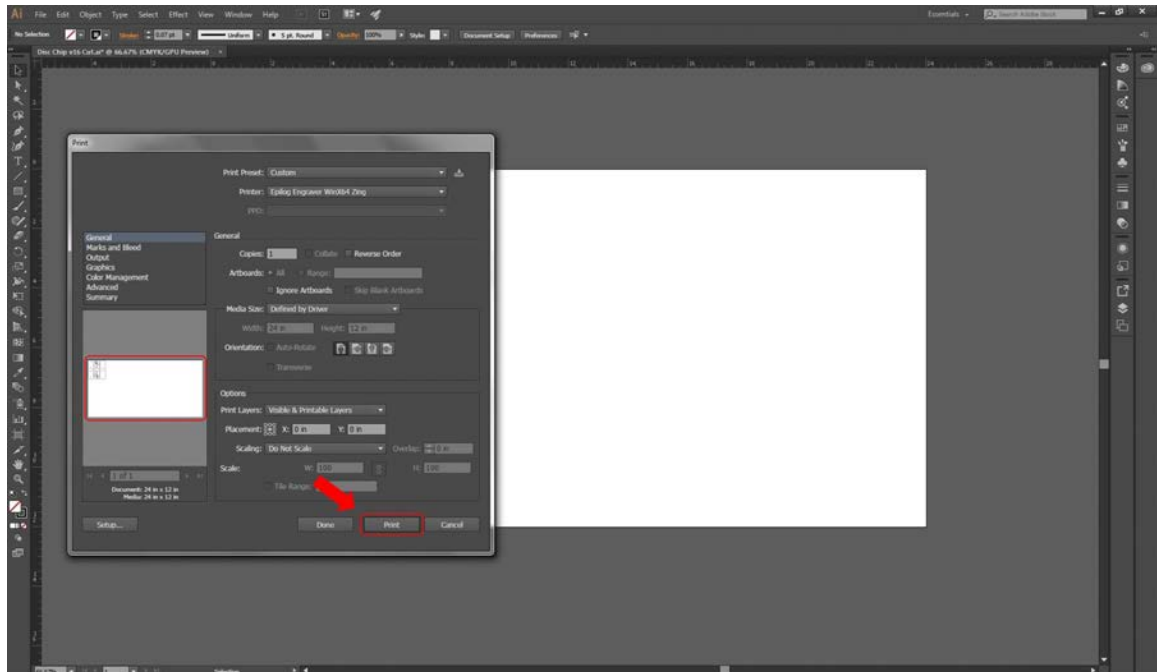


Figure D.22: Step 14: Select print to send the file to the laser cutter.



Figure D.23: Step 15: Press go on the control to panel to run the laser cutter.

D.3 Stika Vinyl Cutter

Contact: Joanne Tiscareno (jtiscareno@rolanddga.com, (800) 542-2307)

To use the vinyl cutter, first, a sheet of material must be prepared for cutting. In the case of shaping PSA for fabricating microfluidic chips, a section of approximately 7 x 10 in can be cut from the stock roll of PSA. Then, the material should be mounted on a piece of 8.5 x 11 in printer paper using scotch tape around the edges of the PSA. Once sealed to the paper, the PSA can then be loaded into the vinyl cutter, as seen in Fig. D.24. Be sure to turn on the cutter by pressing the button on the right-side of the machine (a blue LED on the right confirms that the device is powered).

The vinyl cutter also uses Illustrator to prepare the design file for cutting. Similar to steps 3–4 in Section D.2 (Fig. D.11 and D.12), the .dxf file is imported into Illustrator and the extraneous text is removed. Then, however, any document size can be used.

Once the vector art is imported, the file must be saved as a legacy Illustrator file (i.e., Illustrator 8 or earlier) for use in the vinyl cutter software: *CutStudio* (Fig. D.25). The Illustrator file can be then dragged/imported into the *CutStudio* program. Here, it is important to group sections that were previously dimensioned when designing the parts. In the case of the channel layer design shown in Fig. D.26, each layer is grouped to keep the vector art intact. If this step is skipped, sometimes the geometry can shift when moving around the part in *CutStudio*. Once grouped, the whole design can be moved together.

When aligning the designs in *CutStudio*, the axis in the top left-hand corner indicates the location of the sharp edge in the vinyl cutter—that is, the hardware that performs the cutting. Be sure to align the designs properly in *CutStudio* in relation to how you inserted the material to cut. Also note, the workspace of the vinyl cutter is only 6 in. across. The width of the grid template in *CutStudio* represents this dimension.

After the designs are properly aligned in the software and the material is properly aligned in the hardware, you are ready for cutting! Select *Cutting* on the menu bar (D.27) and watch the vinyl cutter cut away. Unlike the laser cutter, there is no need to monitor the vinyl cutter while it is running, though it is quite enjoyable to watch.



Figure D.24: Loading PSA (backed with a sheet of 8.5 x 11 in. paper) into the vinyl cutter. Blue LED indicates that the machine is powered on.

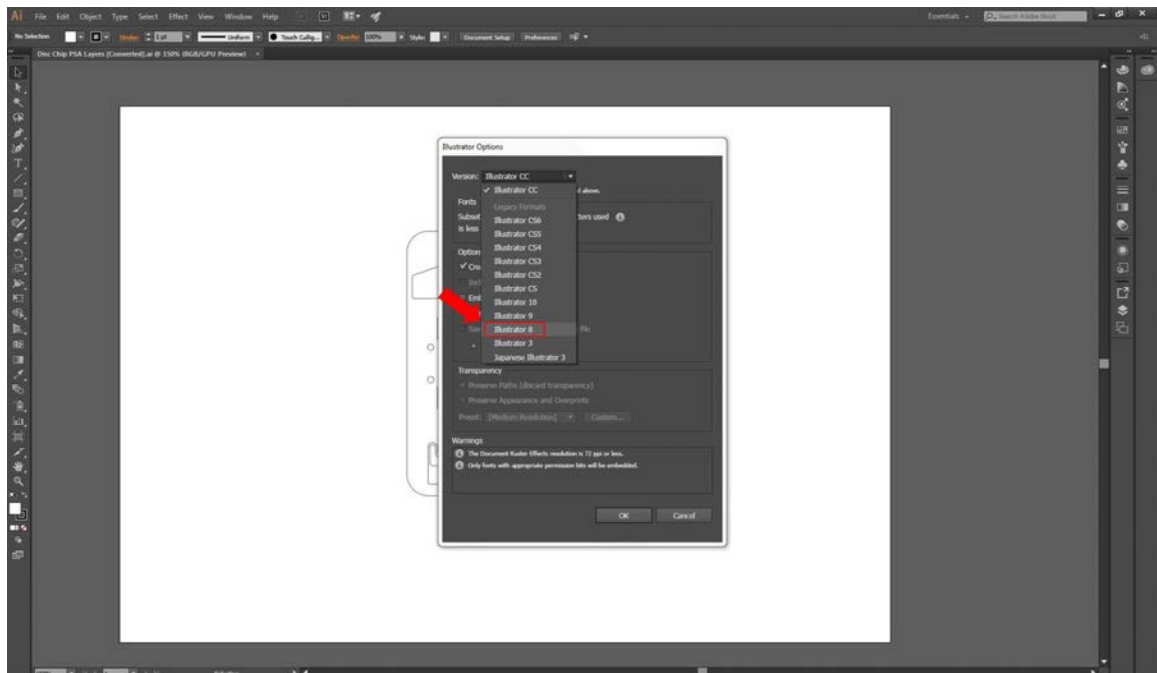


Figure D.25: Step 1: Save design as a legacy Illustrator file.

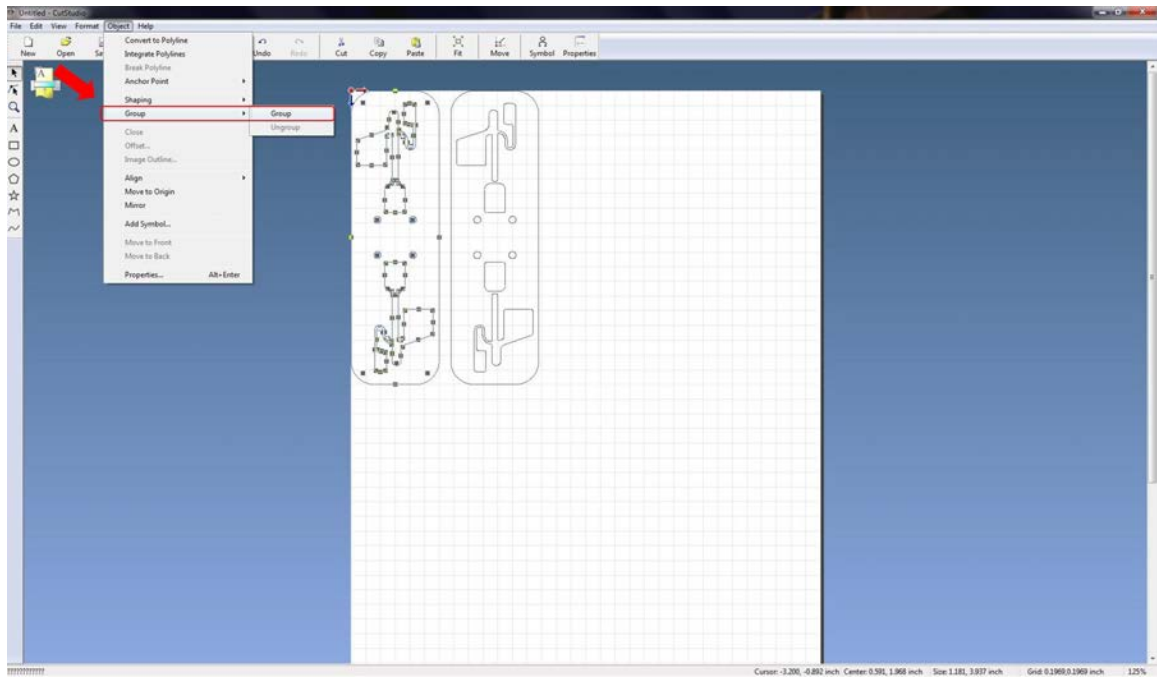


Figure D.26: Step 2: Import Illustrator file into CutStudio and align parts.

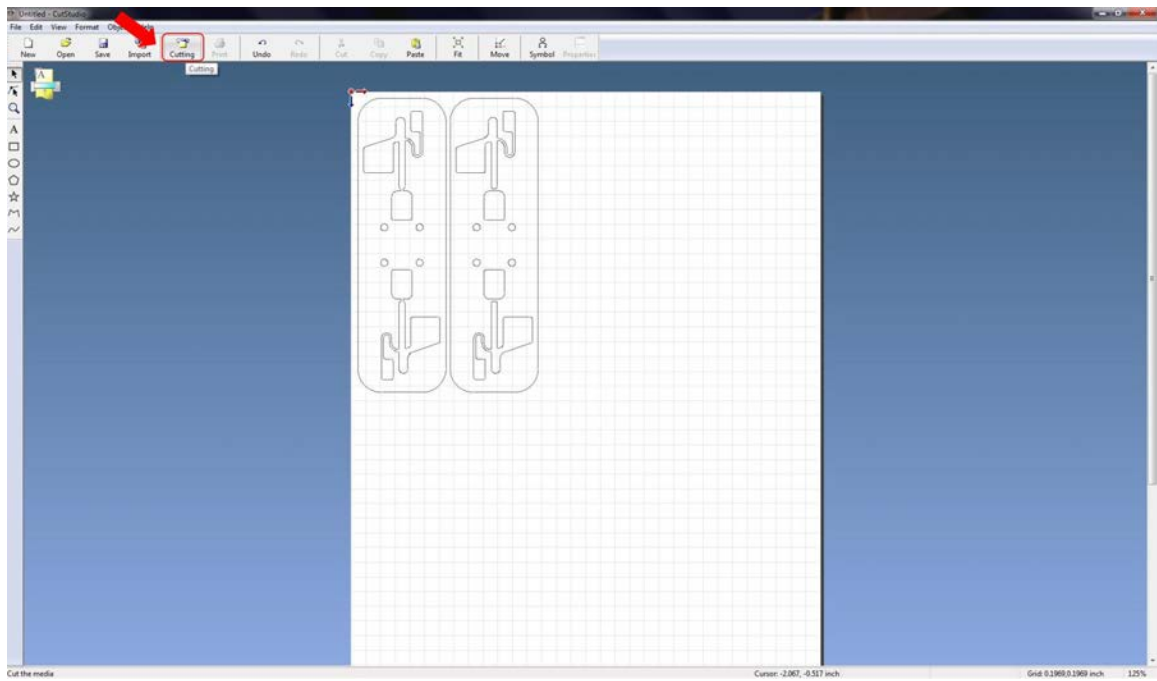


Figure D.27: Step 3: Press cutting to run the vinyl cutter.

References

1. M. L. Balter, A. I. Chen, T. J. Maguire, and M. L. Yarmush, "The System Design and Evaluation of a 7-DOF Image-Guided Venipuncture Robot," *IEEE Trans. Robot.*, vol. 31, no. 4, pp. 1044–1053, 2015.
2. A. I. Chen, M. L. Balter, T. J. Maguire, and M. L. Yarmush, "Real-time Needle Steering in Response to Rolling Vein Deformation by a 9-DOF Image-Guided Venipuncture Robot," in *Proc. 2015 IEEE/RSJ Int. Conf. Intell. Robot. Syst.*, pp. 2633–2638, 2015.
3. M. L. Balter, A. I. Chen, T. J. Maguire, and M. L. Yarmush, "Adaptive Kinematic Control of a Robotic Venipuncture Device Based on Stereo," *IEEE Trans. Ind. Electron.*, vol. 64, no. 2, pp. 1626–1635, 2017.
4. M. L. Balter, A. I. Chen, A. Fromholtz, A. Gorshkov, T. J. Maguire, and M. L. Yarmush, "System Design and Development of a Robotic Device for Automated Venipuncture and Diagnostic Blood Cell Analysis," in *IEEE Int. Conf. Intell. Robot. Syst.*, (Daejeon, Korea), pp. 514–520, 2016.
5. M. L. Balter, A. I. Chen, C. A. Colinco, A. Gorshkov, B. Bixon, V. Martin, F. Alexander, T. J. Maguire, and M. L. Yarmush, "Differential Leukocyte Counting via Fluorescent Detection and Image Processing on a Centrifugal Microfluidic Platform," *Anal. Methods*, vol. 8, no. 47, pp. 8272–8279, 2016.
6. M. L. Balter, A. I. Chen, S. Yedithi, T. J. Maguire, and M. L. Yarmush, "Automated 3D Blood Vessel Localization Combining Near Infrared and Ultrasound Imaging with GPU-enabled Real-time Image Analysis," *Med. Image Anal.*, 2017.
7. M. L. Balter, A. I. Chen, T. J. Maguire, and M. L. Yarmush, "Evaluation of an Automated Blood Draw and Analysis Device: from in vitro Blood Draw to Diagnostic Results," *Technology*, 2017.
8. A. I. Chen, M. L. Balter, and T. J. Maguire, "Developing the World's First Portable Medical Robot for Autonomous Venipuncture," *IEEE Robot. Autom. Mag.*, no. March, pp. 10–11, 2016.
9. A. I. Chen, M. L. Balter, M. I. Chen, D. Gross, S. K. Alam, T. J. Maguire, and M. L. Yarmush, "Multilayered tissue mimicking skin and vessel phantoms with tunable mechanical, optical, and acoustic properties," *Med. Phys.*, vol. 43, no. 6, pp. 3117–3131, 2016.
10. A. I. Chen, M. L. Balter, T. J. Maguire, and M. L. Yarmush, "3D Near Infrared and Ultrasound Imaging of Peripheral Blood Vessels for Real-Time Localization and Needle Guidance," in *Int. Conf. Med. Image Comput. Comput. Interv.*, pp. 388–396, 2016.

11. B. A. Kidd, G. Hoffman, N. Zimmerman, L. Li, J. W. Morgan, P. K. Glowe, G. J. Botwin, S. Parekh, N. Babic, M. W. Doust, G. B. Stock, E. E. Schadt, and J. T. Dudley, "Evaluation of direct-to-consumer low-volume lab tests in healthy adults," *J. Clin. Invest.*, vol. 1, no. 8, pp. 1–11, 2016.
12. T. F. Group, *In vitro diagnostics: United States*, vol. 59. The Freedonia Group, 2011.
13. R. Niska, F. Bhuiya, and J. Xu, "National Hospital Ambulatory Medical Care Survey: 2007 emergency department summary," *Natl. Health Stat. Report.*, pp. 1–31, aug 2010.
14. J. a. Hammerling, "A Review of Medical Errors in Laboratory Diagnostics and Where We Are Today," *Lab. Med.*, vol. 43, no. 2, pp. 41–44, 2012.
15. R. C. Hawkins, "Laboratory turnaround time.," *Clin. Biochem. Rev.*, vol. 28, pp. 179–94, nov 2007.
16. H. P. Pati and G. Singh, "Turnaround Time (TAT): Difference in Concept for Laboratory and Clinician.," *Indian J. Hematol. Blood Transfus.*, vol. 30, pp. 81–84, jun 2012.
17. B. A. Stotler and A. Kratz, "Determination of turnaround time in the clinical laboratory: "accessioning-to-result" time does not always accurately reflect laboratory performance.," *Am. J. Clin. Pathol.*, vol. 138, pp. 724–9, nov 2012.
18. M. Zhi, E. L. Ding, J. Theisen-Toupal, J. Whelan, and R. Arnaout, "The landscape of inappropriate laboratory testing: A 15-year meta-analysis," *PLoS One*, vol. 8, no. 11, pp. 1–8, 2013.
19. G. Lippi, G. C. Guidi, C. Mattiuzzi, and M. Plebani, "Preanalytical variability: The dark side of the moon in laboratory testing," *Clin. Chem. Lab. Med.*, vol. 44, no. 4, pp. 358–365, 2006.
20. P. J. Howanitz, "Errors in laboratory medicine: Practical lessons to improve patient safety," *Arch. Pathol. Lab. Med.*, vol. 129, no. 10, pp. 1252–1261, 2005.
21. L. L. Kuensting, S. DeBoer, R. Holleran, B. L. Shultz, R. a. Steinmann, and J. Venella, "Difficult venous access in children: taking control," *J. Emerg. Nurs.*, vol. 35, pp. 419–424, sep 2009.
22. D. Schwartz and K. Raghunathan, "Difficult venous access.," *Paediatr. Anaesth.*, vol. 19, p. 60, jan 2009.
23. A. M. Frey, "Success rates for peripheral IV insertin in a children's hospital.pdf," *J. Intraven. Nurs.*, vol. 21, no. 3, pp. 160–165, 1998.
24. M. Jalili, K. Shalileh, A. Mojtahed, M. Mojtahed, and M. Moradi-Lakeh, "Identifying causes of laboratory turnaround time delay in the emergency department.," *Arch. Iran. Med.*, vol. 15, pp. 759–63, dec 2012.
25. L. L. Holland, L. L. Smith, and K. E. Blick, "Reduce Emergency Department Patient Length of Stay An 11-Hospital Study," *Clin. Chem.*, pp. 672–674, 2005.

26. V. Prijatelj, A. Vuckovic, and D. Cerne, "The optimization of turnaround time for blood samples in an emergency clinical laboratory," *Stud. Health Technol. Inform.*, vol. 68, pp. 610–3, jan 1999.
27. M. McCann, H. Einarsdottir, J. P. Van Waelegheem, F. Murphy, and J. Sedgewick, "Vascular Access Management 1: An Overview," *J. Ren. Care*, vol. 34, no. 2, pp. 77–84, 2008.
28. H. Ogden-Grable and G. W. Gill, "Phlebotomy Puncture Junctionure: Preventing Phlebotomy Errors–Potential For Harming Your Patients," *Lab. Med.*, vol. 36, pp. 430–433, jul 2005.
29. G. Walsh, "Difficult peripheral venous access: recognizing and managing the patient at risk," *J. Assoc. Vasc. Access*, vol. 13, pp. 198–203, jan 2008.
30. R. A. Lininger, "Pediatric peripheral i.v. insertion success rates," *Pediatr Nurs*, vol. 29, no. 5, pp. 351–354, 2003.
31. D. Rauch, D. Dowd, D. Eldridge, S. Mace, G. Schears, and K. Yen, "Peripheral difficult venous access in children," *Clin Pediatr*, vol. 48, no. 9, pp. 895–901, 2009.
32. J. C. Möller, I. Reiss, and T. Schaible, "Vascular access in neonates and infants—indications, routes, techniques and devices, complications.," *Intensive Care World*, vol. 12, pp. 48–53, jun 1995.
33. J. Campbell, "Intravenous cannulation: potential complications.," *Prof. Nurse*, vol. 12, pp. S10–3, may 1997.
34. M. A. Zaidi, S. A. Beshyah, and R. Griffith, "Needle Stick Injuries - An Overview of the Size of the Problem , Pre-vention & Management," *Ibnosina J. Med. Biomed. Sci.*, vol. 2, no. 2, pp. 53–61, 2010.
35. S. Q. Wilburn and G. Eijkemans, "Preventing needlestick injuries among healthcare workers;," *Int J Occup Env. Heal.*, pp. 451–456, 2003.
36. S. Wicker, J. Jung, R. Allwinn, R. Gottschalk, and H. F. Rabenau, "Prevalence and prevention of needlestick injuries among health care workers in a German university hospital.," *Int. Arch. Occup. Environ. Health*, vol. 81, pp. 347–54, jan 2008.
37. C. Porta, E. Handelman, and P. McGovern, "Needlestick injuries among health care workers. A literature review," *AAOHN J. Off. J. Am. Assoc. Occup. Heal. Nurses*, vol. 47, pp. 237–244, jun 1999.
38. U. B. o. L. Statistics, "31-9097 Phlebotomists," tech. rep., US Bureau of Labor, 2012.
39. Luminetx, "VeinViewer integrated solutions," tech. rep., Luminetx, 2013.
40. J. P. Kline, "Ultrasound guidance in anesthesia.," *AANA J.*, vol. 79, pp. 209–17, jun 2011.
41. T. Maecken and T. Grau, "Ultrasound imaging in vascular access.," *Crit. Care Med.*, vol. 35, pp. S178–85, may 2007.

42. Y. L. Katsogridakis, R. Seshadri, C. Sullivan, and M. L. Waltzman, "Veinlite Transillumination in the Pediatric Emergency Department," *Pediatr. Emerg. Care*, vol. 24, no. 2, pp. 83–88, 2008.
43. C. Yucha and P. Russ, "Detecting IV infiltrations using a venoscope," *J. Intraven. Nurs.*, vol. 20, pp. 50–55, 1997.
44. L. L. Chapman, B. Sullivan, A. L. Pacheco, C. P. Dralean, and B. M. Becker, "Vein-Viewer-assisted Intravenous Catheter Placement in a Pediatric Emergency Department," *Acad. Emerg. Med.*, vol. 18, pp. 966–971, sep 2011.
45. B. L. Hadaway and L. H. Associates, "A new imaging technology to improve peripheral access success," tech. rep., InfraRed Imaging Systems, Inc, 2002.
46. H. A. Hess, "Practice applications of research a biomedical device to improve pediatric vascular access success," *Pediatr Nurs*, vol. 36, no. 5, pp. 259–263, 2010.
47. R. K. Miyake, H. D. Zeman, F. H. Duarte, R. Kikuchi, E. Ramacciotti, G. Lovhoiden, and C. Vrancken, "Vein imaging: a new method of near infrared imaging, where a processed image is projected onto the skin for the enhancement of vein treatment.," *Dermatol. Surg.*, vol. 32, pp. 1031–8, aug 2006.
48. H. D. Zeman, "Prototype vein contrast enhancer," *Opt. Eng.*, vol. 44, p. 086401, aug 2005.
49. V. P. Zharov, S. Ferguson, J. F. Eidt, P. C. Howard, L. M. Fink, and M. Waner, "Infrared imaging of subcutaneous veins.," *Lasers Surg. Med.*, vol. 34, pp. 56–61, jan 2004.
50. V. C. Paquit, K. W. Tobin, J. R. Price, and F. Mèriaudeau, "3D and multispectral imaging for subcutaneous veins detection.," *Opt. Express*, vol. 17, pp. 11360–5, jul 2009.
51. D. Prabhu, K. Mohanavelu, B. S. Sundershesu, and V. C. Padaki, "Vein identification and localization for automated intravenous drug delivery," *ICIP*, pp. 270–281, 2012.
52. A. M. Perry, A. C. Caviness, and D. C. Hsu, "Efficacy of a near-infrared light device in pediatric intravenous cannulation: a randomized controlled trial," *Pediatr Emerg Care*, vol. 27, no. 1, pp. 5–10, 2011.
53. J. Powers and F. Kremkau, "Medical ultrasound systems.," *Interface Focus*, vol. 1, pp. 477–89, aug 2011.
54. W. Richard, D. Zar, and R. Solek, "A low-cost B-mode USB ultrasound probe," *Ultrason. Imaging*, vol. 30, pp. 21–28, 2008.
55. W. Brunette, R. Nathan, W. Gerard, M. a. Hicks, A. Hope, M. Ishimitsu, P. Prasad, R. E. Anderson, G. Borriello, and B. E. Kolko, "Portable antenatal ultrasound platform for village midwives," in *Proc. First ACM Symp. Comput. Dev. - ACM DEV '10*, (New York, New York, USA), ACM Press, 2010.
56. M. I. Fuller, K. Owen, T. N. Blalock, J. a. Hossack, and W. F. Walker, "Real time imaging with the Sonic Window: A pocket-sized, C-scan, medical ultrasound device," *2009 IEEE Int. Ultrason. Symp.*, pp. 196–199, sep 2009.

57. H.-d. Liang, J. A. Noble, and P. N. T. Wells, "Recent advances in biomedical ultrasonic imaging techniques," *Interface Focus*, vol. 1, no. June, pp. 475–476, 2011.
58. W. Fiegler, R. Felix, M. Langer, and E. Schultz, "Fat as a factor affecting resolution in diagnostic ultrasound: possibilities for improving picture quality.," *Eur. J. Radiol.*, vol. 5, pp. 304–9, nov 1985.
59. T. G. Costantino, A. K. Parikh, W. a. Satz, and J. P. Fojtik, "Ultrasonography-guided peripheral intravenous access versus traditional approaches in patients with difficult intravenous access," *Ann. Emerg. Med.*, vol. 46, no. 5, pp. 456–461, 2005.
60. D. Wang, N. Amesur, G. Shukla, A. Bayless, A. Scharl, D. Mockel, C. Banks, B. Mandella, R. Klatzky, and G. Stetten, "Peripherally Inserted Central Catheter Placement with the Sonic Flashlight : Initial Clinical Trial by Nurses," *J Ultrasound Med*, vol. 28, no. 5, pp. 651–656, 2010.
61. B. Ultrasound, "Sonic Window," 2016.
62. Veinlite, "Veinlite," 2016.
63. G. A. Bellotti, R. F. Bedford, and W. P. Arnold, "Fiberoptic Transillumination for Intravenous Cannulation under General Anesthesia," *Anesth. Analg.*, vol. 60, no. 5, pp. 348–351, 1981.
64. F. Wood, V. Luciano, and R. Goldman, "Vein scanner," 2013.
65. E.-M. Strehle, "Making the invisible visible: near-infrared spectroscopy and phlebotomy in children.," *Telemed. J. E. Health.*, vol. 16, pp. 889–93, oct 2010.
66. H. D. Zeman, G. Lovhoiden, and C. Vrancken, "The clinical evaluation of vein contrast enhancement.," *Annu. Int. Conf. IEEE Eng. Med. Biol. Soc.*, vol. 2, pp. 1203–6, jan 2004.
67. S. Juric, V. Flis, M. Debevc, A. Holzinger, and B. Zalik, "Towards a Low-Cost Mobile Subcutaneous Vein Detection Solution Using Near-Infrared Spectroscopy.," *Sci. World J.*, vol. 2014, p. 365902, jan 2014.
68. J. C. de Graaff, N. J. Cuper, R. a. a. Mungra, K. Vlaardingerbroek, S. C. Numan, and C. J. Kalkman, "Near-infrared light to aid peripheral intravenous cannulation in children: a cluster randomised clinical trial of three devices.," *Anaesthesia*, vol. 68, pp. 835–45, aug 2013.
69. D. Waller, P. Mondy, T. Brama, J. Fisher, A. King, K. Malkov, D. Wall-Smith, L. Ryan, and D. O. Irving, "Determining the effect of vein visualization technology on donation success, vasovagal symptoms, anxiety and intention to re-donate in whole blood donors aged 18???30 years: A randomized controlled trial," *Vox Sang.*, vol. 111, no. 2, pp. 135–143, 2016.
70. P. Guillon, M. Makhoulfi, S. Baillie, C. Roucoulet, E. Dolimier, and a. M. Masquelier, "Prospective evaluation of venous access difficulty and a near-infrared vein visualizer at four French haemophilia treatment centres," *Haemophilia*, vol. 21, no. 1, pp. 21–26, 2015.

71. R. N. Kaddoum, D. L. Anghelescu, M. E. Parish, B. B. Wright, L. Trujillo, J. Wu, Y. Wu, and L. L. Burgoyne, "A randomized controlled trial comparing the AccuVein AV300 device to standard insertion technique for intravenous cannulation of anesthetized children," *Paediatr. Anaesth.*, vol. 22, no. 9, pp. 884–889, 2012.
72. O. C. P. Van Der Woude, N. J. Cuper, C. Getrouw, C. J. Kalkman, and J. C. De Graaff, "The effectiveness of a near-infrared vascular imaging device to support intravenous cannulation in children with dark skin color: A cluster randomized clinical trial," *Anesth. Analg.*, vol. 116, no. 6, pp. 1266–1271, 2013.
73. J. W. Steiner, P. Szmuk, A. Farrow-gillespie, R. B. Pop, and D. I. Sessler, "Skilled Nurses are More Successful When Using Standard Techniques than the Vein Viewer for First Attempt of Intravenous Cannulation in Pediatric Patients with Difficult Access," *ASA Chicago*, vol. October, pp. 15–19, 2011.
74. AccuVein, "AV400 Vein Viewing System," 2015.
75. P. J. Stolka, X. L. Wang, G. D. Hager, and E. M. Boctor, "Navigation with local sensors in handheld 3D ultrasound - initial in-vivo experience," in *SPIE Med. Imaging* (J. D'hooge and M. M. Doyley, eds.), vol. 7968, pp. 1–9, mar 2011.
76. P. J. Stolka, P. Foroughi, M. Rendina, and C. R. Weiss, "Needle Guidance Using Handheld Stereo Vision and Projection for Ultrasound-Based Interventions State of the Art," in *MICCAI*, pp. 684–691, 2014.
77. R. A. Beasley, "Medical robots: current systems and research directions," *J. Robot.*, vol. 2012, 2012.
78. K. Cleary, A. Melzer, V. Watson, G. Kronreif, and D. Stoianovici, "Interventional robotic systems: applications and technology state-of-the-art.," *Minim. Invasive Ther. Allied Technol.*, vol. 15, pp. 101–13, jan 2006.
79. D. Kragic, P. Marayong, M. Li, a. M. Okamura, and G. D. Hager, "Human-Machine Collaborative Systems for Microsurgical Applications," *Int. J. Rob. Res.*, vol. 24, pp. 731–741, sep 2005.
80. M. Zoppi, M. A. Khan, F. Schäfer, and R. Molfino, "Toward lean minimally invasive robotic surgery," *Robotica*, vol. 28, p. 185, sep 2009.
81. H.-y. Yu, N. D. Hevelone, S. R. Lipsitz, K. J. Kowalczyk, and J. C. Hu, "Use, costs and comparative effectiveness of robotic assisted, laparoscopic and open urological surgery," *J. Urol.*, vol. 187, pp. 1392–8, apr 2012.
82. K. Cleary, M. Clifford, D. Stoianovici, M. Freedman, S. K. Mun, and V. Watson, "Technology improvements for image-guided and minimally invasive spine procedures.," *IEEE Trans. Inf. Technol. Biomed.*, vol. 6, pp. 249–61, dec 2002.
83. B. D. Stoianovici, "Revolutionizing urologic surgery," *Contemp. Urol.*, no. October, pp. 58–68, 2002.
84. M. W. Gilbertson, S. Member, and B. W. Anthony, "Force and Position Control System for Freehand Ultrasound," *IEEE Trans. Robot.*, vol. 31, no. 4, pp. 835–849, 2015.

85. E. C. Pua, M. P. Fronheiser, J. R. Noble, E. D. Light, P. D. Wolf, D. von Allmen, and S. W. Smith, "3-D ultrasound guidance of surgical robotics: a feasibility study.," *IEEE Trans. Ultrason. Ferroelectr. Freq. Control*, vol. 53, pp. 1999–2008, nov 2006.
86. J. Whitman, M. Fronheiser, N. Ivancevich, and S. Smith, "Autonomous Surgical Robotics Using 3-D Ultrasound Guidance: Feasibility Study," *Ultrason. Imaging*, vol. 29, pp. 213–219, 2007.
87. J. Whitman, M. P. Fronheiser, and S. W. Smith, "3-D ultrasound guidance of surgical robotics using catheter transducers: feasibility study.," *IEEE Trans. Ultrason. Ferroelectr. Freq. Control*, vol. 55, pp. 1143–5, may 2008.
88. A. Vilchis, J. Troccaz, P. Cinquin, K. Masuda, and F. Pellissier, "A New Robot Architecture for Tele-Echography," *IEEE Trans. Robot. Autom.*, vol. 19, no. 5, pp. 922–926, 2003.
89. N. Haouchine, J. Dequidt, I. Peterlik, E. Kerrien, M. O. Berger, and S. Cotin, "Image-guided simulation of heterogeneous tissue deformation for augmented reality during hepatic surgery," in *2013 IEEE Int. Symp. Mix. Augment. Reality, ISMAR*, pp. 199–208, 2013.
90. S. McKinley, A. Garg, S. Sen, R. Kapadia, A. Murali, K. Nichols, S. Lim, S. Patil, P. Abbeel, A. M. Okamura, and K. Goldberg, "A single-use haptic palpation probe for locating subcutaneous blood vessels in robot-assisted minimally invasive surgery," in *IEEE Int. Conf. Autom. Sci. Eng.*, pp. 1151–1158, 2015.
91. N. Navab, M. Fellow, C. Hennesperger, B. Frisch, and B. F??rst, "Personalized, relevance-based Multimodal Robotic Imaging and augmented reality for Computer Assisted Interventions," *Med. Image Anal.*, vol. 33, pp. 64–71, 2016.
92. J. Dumpert, A. C. Lehman, N. A. Wood, D. Oleynikov, and S. M. Farritor, "Semi-autonomous Surgical Tasks Using a Miniature In vivo Surgical Robot," in *Int. Conf. IEEE EMBS*, pp. 266–269, 2009.
93. C. Staub, T. Osa, A. Knoll, and R. Bauernschmitt, "Automation of Tissue Piercing using Circular Needles and Vision Guidance for Computer Aided Laparoscopic Surgery," in *IEEE Int. Conf. Robot. Autom.*, pp. 4585–4590, 2010.
94. A. Shademan, R. S. Decker, J. D. Opfermann, S. Leonard, A. Krieger, and P. C. W. Kim, "Supervised autonomous robotic soft tissue surgery," *Sci. Transl. Med.*, vol. 8, no. 337, pp. 1–8, 2016.
95. Intuitive Surgical, "Webpage on da Vinci robot."
96. G. S. Guthart and J. K. Salisbury, "The Intuitive TM Telesurgery System: Overview and Application," in *Int. Conf. Robot. Autom.*, pp. 618–621, 2000.
97. S. Matich, C. Neupert, A. Kirschniak, H. F. Schlaak, and P. Pott, "3-D force measurement using single axis force sensors in a new single port parallel kinematics surgical manipulator," in *IEEE Int. Conf. Intell. Robot. Syst.*, pp. 3665–3670, 2016.

98. A. W. Mahoney, P. L. Anderson, S. Member, P. J. Swaney, S. Member, F. Maldonado, R. J. Webster, and I. I. I. Senior, "Reconfigurable Parallel Continuum Robots for Incisionless Surgery," in *Int. Conf. Intell. Robot. Syst.*, pp. 4330–4336, 2016.
99. M. Cianchetti, T. Ranzani, G. Gerboni, I. De Falco, C. Laschi, and A. Menciassi, "STIFF-FLOP surgical manipulator: Mechanical design and experimental characterization of the single module," in *IEEE Int. Conf. Intell. Robot. Syst.*, pp. 3576–3581, 2013.
100. Y. Sekiguchi, Y. Kobayashi, Y. Tomono, H. Watanabe, K. Toyoda, K. Konishi, M. Tomikawa, S. Ieiri, K. Tanoue, M. Hashizume, and M. G. Fujie, "Development of Tool Manipulator Driven by Flexible Shaft for Single Port Endoscopic Surgery," in *Int. Conf. Biomed. Robot. Biomechatronics*, pp. 120–125, 2010.
101. M. Piccigallo, U. Scarfogliero, C. Quaglia, G. Petroni, P. Valdastrì, A. Menciassi, and P. Dario, "Design of a novel bimanual robotic system for single-port laparoscopy," *IEEE/ASME Trans. Mechatronics*, vol. 15, no. 6, pp. 871–878, 2010.
102. D. J. Abbott, C. Becke, R. I. Rothstein, and W. J. Peine, "Design of an endoluminal NOTES robotic system," in *IEEE Int. Conf. Intell. Robot. Syst.*, pp. 410–416, 2007.
103. B. Azizi Koutenaei, E. Wilson, R. Monfaredi, C. Peters, G. Kronreif, and K. Cleary, "Robotic natural orifice transluminal endoscopic surgery (R-NOTES): Literature review and prototype system," *Minim. Invasive Ther. Allied Technol.*, vol. 24, no. 1, pp. 18–23, 2015.
104. J. Burgner, D. C. Rucker, H. B. Gilbert, P. J. Swaney, P. T. Russell, K. D. Weaver, and R. J. Webster, "A Telerobotic System for Transnasal Surgery," *IEEE/ASME Trans. Mechatronics*, vol. 19, no. 3, pp. 996–1006, 2014.
105. D. Stoianovici, D. Song, D. Petrisor, D. Ursu, D. Mazilu, M. Muntener, M. Mutener, M. Schar, and A. Patriciu, "'MRI Stealth' robot for prostate interventions," *Minim. Invasive Ther. Allied Technol.*, vol. 16, pp. 241–8, jan 2007.
106. G. Fichtinger, "Research Issues in Robot - Assisted Needle Interventions Systems and Technology," tech. rep., Johns Hopkins University, 2003.
107. A. N. Sridhar, A. Hughes-Hallett, E. K. Mayer, P. J. Pratt, P. J. Edwards, G.-Z. Yang, A. W. Darzi, and J. A. Vale, "Image-guided robotic interventions for prostate cancer," *Nat. Rev. Urol.*, vol. 10, pp. 452–62, aug 2013.
108. G. Brandt, a. Zimolong, L. Carrat, P. Merloz, H. W. Staudte, S. Lavallée, K. Radermacher, and G. Rau, "CRIGOS: a compact robot for image-guided orthopedic surgery," *IEEE Trans. Inf. Technol. Biomed.*, vol. 3, pp. 252–60, dec 1999.
109. M. Shoham, M. Burman, E. Zehavi, L. Joskowicz, S. Member, and E. Batkilin, "Bone-Mounted Miniature Robot for Surgical Procedures : Concept and Clinical Applications," *IEEE Trans. Robot. Autom.*, vol. 19, no. 5, pp. 893–901, 2003.
110. D. Glauser, H. Fankhauser, M. Epitau, J. L. Hefti, and A. Jaccottet, "Neurosurgical robot minerva: first results and current developments," *J. Image Guid. Surg.*, vol. 1, pp. 266–72, jan 1995.

111. P. Eldridge and T. Varma, "Use of the NeuroMate stereotactic robot in a frameless mode for functional neurosurgery," *Int J Med Robot. Comput Assist Surg*, vol. 2, no. March, pp. 107–113, 2006.
112. Q. H. Li, L. Zamorano, A. Pandya, R. Perez, J. Gong, and F. Diaz, "The application accuracy of the NeuroMate robot—A quantitative comparison with frameless and frame-based surgical localization systems.," *Comput. Aided Surg.*, vol. 7, pp. 90–8, jan 2002.
113. R. Shamir, *Miniature robot system for keyhole neurosurgery*. Master of science, The Hewbrew University of Jerusalem, 2005.
114. D. Stoianovici, K. Cleary, a. Patriciu, D. Mazilu, a. Stanimir, N. Craciunoiu, V. Watson, and L. Kavoussi, "Acubot: a robot for radiological interventions," *IEEE Trans. Robot. Autom.*, vol. 19, pp. 927–930, oct 2003.
115. H. Bassan, R. Patel, and M. Moallem, "A Novel Manipulator for Percutaneous Needle Insertion: Design and Experimentation," *IEEE/ASME Trans. Mechatronics*, vol. 14, pp. 746–761, dec 2009.
116. I. Bricault, N. Zemiti, E. Jouniaux, C. Fouard, E. Taillant, F. Dorandeu, and P. Cinquin, "A Light Puncture Robot for CT and MRI Interventions," *IEEE Eng. Med. Biol.*, vol. May/June, pp. 42–50, 2008.
117. D. Stoianovici, L. L. Whitcomb, J. H. Anderson, R. H. T. D, and L. R. Kavoussi, "A modular surgical robotic system for image guided percutaneous procedures," in *Int. Conf. Med. Image Comput. Comput. Interv.*, pp. 404–410, 1998.
118. A. Garg, T. Siau, D. Berenson, A. Cunha, I.-C. Hsu, J. Pouliot, D. Stoianovici, and K. Goldberg, "Initial experiments toward automated robotic implantation of skew-line needle arrangements for HDR brachytherapy," *2012 IEEE Int. Conf. Autom. Sci. Eng.*, pp. 26–33, aug 2012.
119. a. Ayadi, G. Bour, M. Aprahamian, B. Bayle, P. Graebbling, J. Gangloff, L. Soler, J. M. Egly, and J. Marescaux, "Fully automated image-guided needle insertion: application to small animal biopsies.," *Conf. Proc. IEEE Eng. Med. Biol. Soc.*, vol. 2007, pp. 194–7, jan 2007.
120. B. N. Berry-Pusey, Y. C. Chang, S. W. Prince, K. Chu, J. David, R. Taschereau, R. W. Silverman, D. Williams, W. Ladno, D. Stout, T. C. Tsao, and a. Chatziioannou, "A semi-automated vascular access system for preclinical models.," *Phys. Med. Biol.*, vol. 58, pp. 5351–62, aug 2013.
121. A. Mahdi, M. Khoshnam, N. Najmael, and R. V. Patel, "Visual servoing in medical robotics: a survey. Part I: endoscopic and direct vision imaging - techniques and applications," *Int. J. Med. Robot. Comput. Assist. Surg. MRCAS*, vol. 10, pp. 263–274, 2014.
122. A. Mahdi, M. Khoshnam, N. Najmael, and R. V. Patel, "Visual servoing in medical robotics: a survey. Part II: tomographic imaging modalities - techniques and applications," *Int. J. Med. Robot. Comput. Assist. Surg. MRCAS*, vol. 11, pp. 67–79, 2015.
123. P. K. Allen, "Next-Generation Robotic Surgery," tech. rep., Columbia University, 2010.

124. G. P. Moustris, S. C. Hiridis, K. Deliparaschos, and K. Konstantinidis, "Evolution of autonomous and semi-autonomous robotic surgical systems: a review of the literature," *Int. J. Med. Robot. Comput. Assist. Surg.*, vol. 7, no. May, pp. 375–392, 2011.
125. R. Taylor and D. Stoianovici, "Medical robotics in computer-integrated surgery," *IEEE Trans. Robot. Autom.*, vol. 19, pp. 765–781, oct 2003.
126. N. Vitiello, T. Lenzi, S. Member, S. Roccella, S. Marco, M. D. Rossi, E. Cattin, F. Giovacchini, F. Vecchi, and M. C. Carrozza, "NEUROExos : A Powered Elbow Exoskeleton for Physical Rehabilitation," *IEEE Trans. Robot.*, vol. 29, no. 1, pp. 220–235, 2013.
127. Y. Kobayashi, A. Onishi, H. Watanabe, T. Hoshi, K. Kawamura, M. Hashizume, and M. G. Fujie, "Development of an integrated needle insertion system with image guidance and deformation simulation.," *Comput. Med. Imaging Graph.*, vol. 34, pp. 9–18, jan 2010.
128. Y. Kobayashi, R. Hamano, H. Watanabe, T. Koike, J. Hong, K. Toyoda, M. Uemura, S. Ieiri, M. Tomikawa, T. Ohdaira, M. Hashizume, and M. G. Fujie, "Preliminary in vivo evaluation of a needle insertion manipulator for central venous catheterization," *ROBOMECH J.*, vol. 1, p. 18, 2014.
129. H. Tanaka, K. Ohnishi, H. Nishi, T. Kawai, Y. Morikawa, S. Ozawa, and T. Furukawa, "Implementation of Bilateral Control System Based on Acceleration Control Using FPGA for Multi-DOF Haptic Endoscopic Surgery Robot," *Ieee Trans. Ind. Electron.*, vol. 56, no. 3, pp. 618–627, 2009.
130. A. Maghsoudi and M. Jahed, "A comparison between disturbance observer-based and model-based control of needle in percutaneous applications," *IECON 2012 - 38th Annu. Conf. IEEE Ind. Electron. Soc.*, pp. 2104–2108, 2012.
131. A. Asadian, R. V. Patel, and M. R. Kermani, "A distributed model for needle-tissue friction in percutaneous interventions," in *2011 IEEE Int. Conf. Robot. Autom.*, pp. 1896–1901, Ieee, may 2011.
132. R. J. Roesthuis, Y. R. J. V. Veen, A. Jahya, and S. Misra, "Mechanics of Needle-Tissue Interaction," in *IEEE/RSJ Int. Conf. Intell. Robot. Syst.*, pp. 2557–2563, 2011.
133. J. H. Cho, H. I. Son, D. G. Lee, T. Bhattacharjee, and D. Y. Lee, "Gain-scheduling control of teleoperation systems interacting with soft tissues," *IEEE Trans. Ind. Electron.*, vol. 60, no. 3, pp. 946–957, 2013.
134. R. J. Webster III, J. Memisevic, and a. M. Okamura, "Design considerations for needle steering," *Proc. IEEE Int. Conf. Robot. Autom.*, no. April, pp. 3599–3605, 2005.
135. A. Zivanovic and B. Davies, "The development of a haptic robot to take blood samples from the forearm," *MICCAI*, pp. 614–620, 2001.
136. D. Okuno, T. Togawa, K. Tsuchiya, M. Engineering, and T. Med, "Development of an automatic blood sampling system: control of the puncturing needle by measuring forces," *Proc. 20th Annu. Int. Conf. IEEE Eng. Med. Biol. Soc.*, vol. 20, no. 4, pp. 3–4, 1998.

137. A. Zivanovic and B. L. Davies, "A robotic system for blood sampling.," *IEEE Trans. Information Technol. Biomed.*, vol. 4, no. 1, pp. 8–14, 2000.
138. T. De Boer, M. Steinbuch, S. Neerken, and A. Kharin, "Laboratory study on needle-tissue interaction: towards the development of an instrument for automatic venipuncture," *J. Mech. Med. Biol.*, vol. 07, pp. 325–335, sep 2007.
139. R. Brewer, A. Leeper, and J. K. Salisbury, "A friction differential and cable transmission design for a 3-DOF haptic device with spherical kinematics," in *IEEE Int. Conf. Intell. Robot. Syst.*, pp. 2570–2577, 2011.
140. R. D. Brewer, *Improving Peripheral IV Catheterization Through Robotics: From Simple Assistive Devices To a Fully-Autonomous System*. Doctor of philosophy, Stanford University, 2015.
141. P. Carvalho, A. Kesari, S. Weaver, P. Flaherty, and G. Fischer, "Robotic assistive device for phlebotomy," in *Proc. ASME 2015 Int. Des. Eng. Tech. Conf. Comput. Inf. Eng. Conf.*, pp. 1–6, 2015.
142. T. S. Perry, "Profile: Veebot - Drawing blood faster and more safely than a human can," *IEEE Spectr.*, p. 2013, 2013.
143. A. I. Chen, K. Nikitczuk, J. Nikitczuk, T. J. Maguire, and M. L. Yarmush, "Portable Robot for Autonomous Venipuncture Using 3D Near Infrared Image Guidance," *Technology*, vol. 1, no. 1, pp. 72–87, 2013.
144. K. E. Volmar, D. S. Wilkinson, E. a. Wagar, and C. M. Lehman, "Utilization of stat test priority in the clinical laboratory: A college of American Pathologists Q-Probes Study of 52 Institutions," *Arch. Pathol. Lab. Med.*, vol. 137, no. 2, pp. 220–227, 2013.
145. S. Woeste, "Technology to Reduce Specimen Collection Errors," *Lab. Med.*, vol. 35, no. 8, pp. 471–474, 2004.
146. G. J. Kost, MD, PhD, Z. Tang, MD, D. G. Shelby, MT, and R. F. Louie, "Point-of-Care Testing: Millennium Technology for Critical Care," *Lab. Med.*, vol. 31, pp. 402–408, jul 2000.
147. C. D. Chin, V. Linder, and S. K. Sia, "Commercialization of microfluidic point-of-care diagnostic devices.," *Lab Chip*, vol. 12, pp. 2118–34, jun 2012.
148. G. J. Fermann and J. Suyama, "Point of care testing in the emergency department," *J. Emerg. Med.*, vol. 22, pp. 393–404, may 2002.
149. M. J. Galloway, R. S. Woods, S. L. Nicholson, J. J. Foggin, and L. Elliott, "An audit of waiting times in a haematology clinic before and after the introduction of point-of-care testing," *Clin. Lab. Haematol.*, vol. 21, pp. 201–205, 1999.
150. Y.-J. Jung, J. Gonzalez, and A. Godavarty, "Functional near-infrared imaging reconstruction based on spatiotemporal features: venous occlusion studies," *Appl. Opt.*, vol. 54, no. 13, pp. 82–90, 2015.
151. A. J. Singer, J. Ardise, J. Gulla, and J. Cangro, "Point-of-care testing reduces length of stay in emergency department chest pain patients," *Ann. Emerg. Med.*, vol. 45, no. 6, pp. 587–591, 2005.

152. C. L. Martin, "i-STAT - Combining Chemistry and Haematology in PoCT.," *Clin. Biochem. Rev.*, vol. 31, pp. 81–4, aug 2010.
153. L. V. Rao, B. a. Ekberg, D. Connor, F. Jakubiak, G. M. Vallaro, and M. Snyder, "Evaluation of a new point of care automated complete blood count (CBC) analyzer in various clinical settings.," *Clin. Chim. Acta.*, vol. 389, pp. 120–5, mar 2008.
154. a. Osei-Bimpong, C. Jury, R. McLean, and S. M. Lewis, "Point-of-care method for total white cell count: an evaluation of the HemoCue WBC device.," *Int. J. Lab. Hematol.*, vol. 31, pp. 657–64, dec 2009.
155. R. G. Cable, W. R. Steele, R. S. Melmed, B. Johnson, A. E. Mast, P. M. Carey, J. E. Kiss, S. H. Kleinman, and D. J. Wright, "The difference between fingerstick and venous hemoglobin and hematocrit varies by sex and iron stores," *Transfusion*, vol. 52, no. 5, pp. 358–366, 2012.
156. Z. W. Yang, S. H. Yang, L. Chen, J. Qu, J. Zhu, and Z. Tang, "Comparison of blood counts in venous, fingertip and arterial blood and their measurement variation.," *Clin. Lab. Haematol.*, vol. 23, pp. 155–9, jun 2001.
157. D. Loewenstein, C. Stake, and M. Cichon, "Assessment of using fingerstick blood sample with i-STAT point-of-care device for cardiac troponin I assay.," *Am. J. Emerg. Med.*, vol. 31, pp. 1236–9, aug 2013.
158. G. W. Moore, A. Henley, S. S. Cotton, S. Tugnait, and S. Rangarajan, "Clinically significant differences between point-of-care analysers and a standard analyser for monitoring the International Normalized Ratio in oral anticoagulant therapy: a multi-instrument evaluation in a hospital outpatient setting.," *Blood Coagul. Fibrinolysis*, vol. 18, pp. 287–92, apr 2007.
159. L. Neufeld, A. García-Guerra, D. Sánchez-Francia, O. Newton-Sánchez, M. D. Ramírez-Villalobos, and J. Rivera-Dommarco, "Hemoglobin measured by Hemocue and a reference method in venous and capillary blood: a validation study.," *Salud Publica Mex.*, vol. 44, no. 3, pp. 219–27, 2002.
160. M. Siedner, V. Zapitz, M. Ishida, R. De La Roca, and J. D. Klausner, "Performance of Rapid Syphilis Tests in Venous and Fingerstick Whole Blood Specimens," *Sex. Transm. Dis.*, vol. 31, pp. 557–560, sep 2004.
161. S. S. Morris, M. T. Ruel, R. J. Cohen, K. G. Dewey, B. de la Brière, and M. N. Hassan, "Precision, accuracy, and reliability of hemoglobin assessment with use of capillary blood.," *Am. J. Clin. Nutr.*, vol. 69, pp. 1243–8, jun 1999.
162. Masimo, "Total Hemoglobin Measurements : Accuracy of Laboratory Devices and Impact of Physiologic Variation," tech. rep., Masimo, 2003.
163. M. Teli, Y. Ng, and R. Ingram, "Evaluation of the Hemocue portable hemoglobinometer after major joint arthroplasty," *J. Arthroplasty*, vol. 17, pp. 224–226, feb 2002.
164. H. Radtke, G. Polat, U. Kalus, A. Salama, and H. Kiesewetter, "Hemoglobin screening in prospective blood donors: comparison of different blood samples and different quantitative methods.," *Transfus. Apher. Sci.*, vol. 33, pp. 31–5, aug 2005.

165. M. M. Bond and R. R. Richards-Kortum, "Drop-to-drop variation in the cellular components of fingerprick blood: Implications for point-of-care diagnostic development," *Am. J. Clin. Pathol.*, vol. 144, no. 6, pp. 885–894, 2015.
166. M. J. Randels, R. G. Strauss, and T. J. Raife, "Fingerstick blood samples in platelet donor screening: Reliability and impact on predict yield programs," *J. Clin. Apher.*, vol. 12, no. 3, pp. 105–109, 1997.
167. M. J. Kampelmacher, R. G. Van Kesteren, and E. K. a. Winckers, "Instrumental variability of respiratory blood gases among different blood gas analysers in different laboratories," *Eur. Respir. J.*, vol. 10, no. 6, pp. 1341–1344, 1997.
168. P. Greenland, N. L. Bowley, B. Meiklejohn, K. L. Doane, and C. E. Sparks, "Blood cholesterol concentration: Fingerstick plasma vs venous serum sampling," *Clin. Chem.*, vol. 36, no. 4, pp. 628–630, 1990.
169. M. Vann, "8 tips to reduce finger prick pain,," 2013.
170. A. B. Storrow and W. B. Gibler, "The role of cardiac markers in the emergency department," *Clin. Chim. Acta.*, vol. 284, pp. 187–196, 1999.
171. K. J. Boudonck, D. J. Rose, E. D. Karoly, D. P. Lee, K. A. Lawton, and P. J. Lapinskas, "Metabolomics for early detection of drug-induced kidney injury: review of the current status,," *Bioanalysis*, vol. 1, pp. 1645–63, dec 2009.
172. W. Shoemaker, C. Wo, S. Yu, F. Farjam, and D. Thangathurai, "Invasive and noninvasive haemodynamic monitoring of acutely ill sepsis and septic shock patients in the emergency department.pdf," *Eur. J. Emerg. Med.*, vol. 7, pp. 169–175, 2000.
173. B. J. Bain, "Diagnosis from the blood smear,," *N. Engl. J. Med.*, vol. 353, pp. 498–507, aug 2005.
174. D. J. Karras and D. L. Kane, "Serum markers in the emergency department diagnosis of acute myocardial infarction," *Emerg Med Clin North Am*, vol. 19, no. 2, pp. 321–327, 2001.
175. C. C. Young, "Evolution of Blood Chemistry Analyzers Based on Ion Selective Electrodes," *J. Chem. Educ.*, vol. 74, p. 177, feb 1997.
176. E. Lee-Lewandrowski, K. Gregory, and K. Lewandrowski, "Point of care testing in a large urban academic medical center: Evolving test menu and clinical applications," *Clin. Chim. Acta*, vol. 411, no. 21-22, pp. 1799–1805, 2010.
177. M. M. M. D. Johnson and K. B. M. D. Lewandrowski, "Analysis of Emergency Department Test Ordering Patterns in an Urban Academic Medical Center: Can the Point-of-Care Option in a Satellite Laboratory Provide Sufficient Menu to Permit Full Service Testing," *Point Care J. Near-Patient Test. Technol.*, vol. 6, no. 2, pp. 134–138, 2007.
178. B. Seamonds, "Medical, economic, and regulatory factors affecting point-of-care testing. A report of the conference on factors affecting point-of-care testing, Philadelphia, PA 6-7 May 1994.,," *Clin. Chim. Acta.*, vol. 249, pp. 1–19, may 1996.

179. G. Lippi, G. L. Salvagno, G. Brocco, and G. C. Guidi, "Preanalytical variability in laboratory testing: Influence of the blood drawing technique," *Clin. Chem. Lab. Med.*, vol. 43, no. 3, pp. 319–325, 2005.
180. G. Lippi, G. L. Salvagno, M. Montagnana, M. Franchini, and G. C. Guidi, "Phlebotomy issues and quality improvement in results of laboratory testing," *Clin. Lab.*, vol. 52, no. 5-6, pp. 217–230, 2006.
181. T. van Oordt, Y. Barb, J. Smetana, R. Zengerle, and F. von Stetten, "Miniature stick-packaging—an industrial technology for pre-storage and release of reagents in lab-on-a-chip systems.," *Lab Chip*, vol. 13, no. 15, pp. 2888–92, 2013.
182. M. Amasia and M. Madou, "Large-volume centrifugal microfluidic device for blood plasma separation.," *Bioanalysis*, vol. 2, no. 10, pp. 1701–1710, 2010.
183. R. Burger, N. Reis, J. G. da Fonseca, and J. Ducrée, "Plasma extraction by centrifugo-pneumatically induced gating of flow," *J. Micromechanics Microengineering*, vol. 23, no. 3, p. 035035, 2013.
184. N. Godino, R. Gorkin, A. V. Linares, R. Burger, and J. Ducrée, "Comprehensive integration of homogeneous bioassays via centrifugo-pneumatic cascading.," *Lab Chip*, vol. 13, no. 4, pp. 685–94, 2013.
185. F. Schwemmer, S. Zehnle, D. Mark, F. von Stetten, R. Zengerle, and N. Paust, "A microfluidic timer for timed valving and pumping in centrifugal microfluidics.," *Lab Chip*, vol. 15, no. 6, pp. 1545–53, 2015.
186. J. Steigert, T. Brenner, M. Grumann, L. Riegger, S. Lutz, R. Zengerle, and J. Ducrée, "Integrated siphon-based metering and sedimentation of whole blood on a hydrophilic lab-on-a-disk," *Biomed. Microdevices*, vol. 9, no. 5, pp. 675–679, 2007.
187. J. M. Chen, P. C. Huang, and M. G. Lin, "Analysis and experiment of capillary valves for microfluidics on a rotating disk," *Microfluid. Nanofluidics*, vol. 4, no. 5, pp. 427–437, 2008.
188. S. Haeberle, T. Brenner, H. P. Schlosser, R. Zengerle, and J. Ducrée, "Centrifugal micromixer," *Chem. Eng. Technol.*, vol. 28, no. 5, pp. 613–616, 2005.
189. R. Burger, L. Amato, and A. Boisen, "Detection Methods for Centrifugal Microfluidic Platforms," *Biosens. Bioelectron.*, vol. 76, pp. 1–14, 2015.
190. J. Ducrée, S. Haeberle, S. Lutz, S. Pausch, F. V. Stetten, and R. Zengerle, "The centrifugal microfluidic Bio-Disk platform," *J. Micromechanics Microengineering*, vol. 17, no. 7, pp. S103–S115, 2007.
191. R. Gorkin, J. Park, J. Siegrist, M. Amasia, B. S. Lee, J.-M. Park, J. Kim, H. Kim, M. Madou, and Y.-K. Cho, "Centrifugal microfluidics for biomedical applications.," *Lab Chip*, vol. 10, pp. 1758–73, jul 2010.
192. M. Madou, J. Zoval, G. Jia, H. Kido, J. Kim, and N. Kim, "Lab on a Cd," *Annu. Rev. Biomed. Eng.*, vol. 8, no. 1, pp. 601–628, 2006.

193. O. Strohmeier, M. Keller, F. Schwemmer, S. Zehnle, D. Mark, F. von Stetten, R. Zengerle, and N. Paust, "Centrifugal microfluidic platforms: advanced unit operations and applications.," *Chem. Soc. Rev.*, vol. 44, pp. 6187–6229, 2015.
194. J. Steigert, M. Grumann, T. Brenner, L. Riegger, J. Harter, R. Zengerle, and J. Ducrée, "Fully integrated whole blood testing by real-time absorption measurement on a centrifugal platform.," *Lab Chip*, vol. 6, no. 8, pp. 1040–4, 2006.
195. C. E. Nwankire, M. Czugala, R. Burger, K. J. Fraser, T. M. Connell, T. Glennon, B. E. Onwuliri, I. E. Nduaguibe, D. Diamond, and J. Ducrée, "A portable centrifugal analyser for liver function screening," *Biosens. Bioelectron.*, vol. 56, pp. 352–358, 2014.
196. B. S. Lee, J.-N. Lee, J.-M. Park, J.-G. Lee, S. Kim, Y.-K. Cho, and C. Ko, "A fully automated immunoassay from whole blood on a disc.," *Lab Chip*, vol. 9, no. 11, pp. 1548–1555, 2009.
197. J. Park, V. Sunkara, T. H. Kim, H. Hwang, and Y. K. Cho, "Lab-on-a-disc for fully integrated multiplex immunoassays," *Anal. Chem.*, vol. 84, no. 5, pp. 2133–2140, 2012.
198. F. Stumpf, F. Schwemmer, T. Hutzenlaub, D. Baumann, O. Strohmeier, G. Dingemans, G. Simons, C. Sager, L. Plobner, F. von Stetten, R. Zengerle, and D. Mark, "LabDisk with complete reagent prestorage for sample-to-answer nucleic acid based detection of respiratory pathogens verified with influenza A H3N2 virus," *Lab Chip*, vol. 16, pp. 199–207, 2016.
199. a. Kloke, a. R. Fiebach, S. Zhang, L. Drechsel, S. Niekrawietz, M. M. Hoehl, R. Kneusel, K. Panthel, J. Steigert, F. von Stetten, R. Zengerle, and N. Paust, "The LabTube - a novel microfluidic platform for assay automation in laboratory centrifuges.," *Lab Chip*, vol. 14, no. 9, pp. 1527–37, 2014.
200. M. Glynn, C. Nwankire, K. Lemass, D. Kinahan, and J. Ducrée, "Cluster size distribution of cancer cells in blood using stopped-flow centrifugation along scale-matched gaps of a radially inclined rail," *Microsystems Nanoeng.*, vol. 1, no. February, p. 15018, 2015.
201. M. Glynn, D. Kirby, D. Chung, D. J. Kinahan, G. Kijanka, and J. Ducrée, "Centrifugo-Magnetophoretic Purification of CD4+ Cells from Whole Blood Toward Future HIV/AIDS Point-of-Care Applications.," *J. Lab. Autom.*, vol. 19, no. 3, pp. 285–296, 2013.
202. Abaxis, "Piccolo Xpress," 2015.
203. Samsung, "LabGEO IB10," 2016.
204. C. van Berkel, J. D. Gwyer, S. Deane, N. G. Green, N. Green, J. Holloway, V. Hollis, and H. Morgan, "Integrated systems for rapid point of care (PoC) blood cell analysis.," *Lab Chip*, vol. 11, pp. 1249–55, apr 2011.
205. B. Bain, *Blood Cells: A Practical Guide*. Australia: Blackwell Publishing Asia Pty Ltd, 4th ed., 2006.

206. H. Shiono and Y. Ito, "Novel method for continuous cell separation by density gradient centrifugation: evaluation of a miniature separation column.," *Prep. Biochem. Biotechnol.*, vol. 33, no. 2, pp. 87–100, 2003.
207. U. Y. Schaff, A. M. Tentori, and G. J. Sommer, "Differential White Cell Count by Centrifugal Microfluidics," *14th Int. Conf. Miniaturized Syst. Chem. Life Sci.*, no. October, pp. 103–105, 2010.
208. D. J. Kinahan, S. M. Kearney, N. A. Kilcawley, P. L. Early, M. T. Glynn, and J. Ducrée, "Density-Gradient Mediated Band Extraction of Leukocytes from Whole Blood Using Centrifugo-Pneumatic Siphon Valving on Centrifugal Microfluidic Discs," *PLoS One*, vol. 11, no. 5, p. e0155545, 2016.
209. H. Russcher, N. V. Deursen, T. Ermens, and R. D. Jonge, "Evaluation of the HemoCue WBC DIFF system for point-of-care counting of total and differential white cells in pediatric samples," *Ned Tijdschr Klin Chem Labgeneesk*, vol. 38, no. 3, pp. 140–141, 2013.
210. HemoCue, "HemoCue WBC system user manual," tech. rep., HemoCue, 2010.
211. B. R. A. Levine, "Dry hematology: its development, function, and role in point of care testing," *Clin. Issues*, no. February, pp. 14–17, 2013.
212. O. Erhabor, G. Richardson, I. Mohammed, C. Thorton, J. Bark, M. Hurst, D. Hamer, and P. Kinsella, "Evaluation of the QBC Star centrifugal three-part differential haematology system," *Br. J. Biomed. Sci.*, vol. 70, no. 2, pp. 67–74, 2013.
213. L. J. Kricka, T. G. Polsky, J. Y. Park, and P. Fortina, "The future of laboratory medicine - a 2014 perspective.," *Clin. Chim. Acta.*, vol. 438, pp. 284–303, 2015.
214. D. Gurevitch, "Economic justification of laboratory automation," *J. Assoc. Lab. Autom.*, vol. 9, no. 1, pp. 33–43, 2004.
215. S. E. F. Melanson, N. I. Lindeman, and P. Jarolim, "Selecting automation for the clinical chemistry laboratory.," *Arch. Pathol. Lab. Med.*, vol. 131, no. 7, pp. 1063–1069, 2007.
216. C. D. Hawker, "Laboratory Automation: Total and Subtotal," *Clin. Lab. Med.*, vol. 27, no. 4, pp. 749–770, 2007.
217. L. L. Holland, L. L. Smith, and K. E. Blick, "Total laboratory automation can help eliminate the laboratory as a factor in emergency department length of stay," *Am. J. Clin. Pathol.*, vol. 125, no. 5, pp. 765–770, 2006.
218. a. Osei-Bimpong, R. McLean, E. Bhonda, and S. M. Lewis, "The use of the white cell count and haemoglobin in combination as an effective screen to predict the normality of the full blood count.," *Int. J. Lab. Hematol.*, vol. 34, pp. 91–7, feb 2012.
219. A. I. Chen, M. L. Balter, T. J. Maguire, and M. L. Yarmush, "Performance of an Automated, Image-guided Vessel Cannulation Robot on Multilayered Tissue Phantoms in Comparison to Manual Cannula Insertion," *IEEE Trans Med Imaging*, 2017.

220. A. I. Chen, M. L. Balter, T. J. Maguire, and M. L. Yarmush, "Automated Lateral Tail Vein Cannulation in Rodents Using an Image-guided, Robotic Vessel Cannulation Device," *Phys. Med. Biol.*, 2017.
221. a. N. Bashkatov, E. a. Genina, V. I. Kochubey, and V. V. Tuchin, "Optical properties of human skin, subcutaneous and mucous tissues in the wavelength range from 400 to 2000nm," *J. Phys. D. Appl. Phys.*, vol. 38, pp. 2543–2555, aug 2005.
222. J. Bouguet, "Camera Calibration Toolbox for Matlab," 2015.
223. J. Heikkila, "Using Circular Control Points," *IEEE Trans. Pattern Anal. Mach. Intell.*, vol. 22, no. 10, pp. 1066–1077, 2000.
224. A. Berkhoff, H. Huisman, J. Thijssen, E. Jacobs, and R. Homan, "Fast scan conversion algorithms for displaying ultrasound sector images," *Ultrason. Imaging*, vol. 16, pp. 97–108, 1994.
225. A. Lasso, T. Heffter, A. Rankin, C. Pinter, T. Ungi, and G. Fichtinger, "PLUS: open-source toolkit for ultrasound-guided intervention systems.," *IEEE Trans. Biomed. Eng.*, vol. 61, pp. 1–11, may 2014.
226. A. F. Frangi, W. J. Niessen, K. L. Vincken, and M. A. Viergever, "Multiscale vessel enhancement filtering," in *Med. Image Comput. Comput. Interv.*, pp. 130–137, Springer, 1998.
227. R. Adams and L. Bischof, "Seeded Region Growing," *IEEE Trans. Pattern Anal. Mach. Intell.*, vol. 16, no. 6, pp. 641–647, 1994.
228. B. Hannaford, J. Rosen, D. W. Friedman, H. King, P. Roan, L. Cheng, D. Glozman, J. Ma, S. N. Kosari, and L. White, "Raven-II: an open platform for surgical robotics research.," *IEEE Trans. Biomed. Eng.*, vol. 60, pp. 954–9, apr 2013.
229. J. McGuinn and S. Editor, "These Bots are Cutting Edge," *Power Transm. Eng.*, no. October, pp. 32–36, 2008.
230. T. Liu, *Design and Prototyping of a Three Degrees of Freedom Robotic Wrist Mechanism for a Robotic Surgery System*. PhD thesis, Case Western Reserve University, 2011.
231. Maxon, "Maxon Precision Motors."
232. R. S. H. J Denavit, "A kinematic notation for lower-pair mechanisms based on matrices," *ASME J. Appl. Mech.*, vol. 22, pp. 215 – 221, 1955.
233. J. J. Craig, *Introduction to robotics : mechanics and control*. Upper Saddle River, N.J.: Pearson/Prentice Hall, 3rd ed., 2005.
234. Mojo, "Stratasys Mojo 3D Printer."
235. B. M. Wilamowski, *Power electronics and motor drives*. CRC Press, 2011.
236. J. J. Craig and P. P. Hall, *Introduction to Robotics*. Upper Saddle River, N.J.: Pearson/Prentice Hall, third ed., 1989.

237. D. G. Lowe, "Distinctive Image Features from Scale-Invariant Keypoints," *Int. J. Comput. Vis.*, vol. 60, no. 2, pp. 91–110, 2004.
238. B. K. Horn and B. G. Schunck, "Determining optical flow," *Artif. Intell.*, vol. 17, pp. 185–203, aug 1981.
239. M. Mahvash and P. E. Dupont, "Mechanics of dynamic needle insertion into a biological material," *IEEE Trans. Biomed. Eng.*, vol. 57, no. 4, pp. 934–943, 2010.
240. N. Garcia-Aracil, C. Perez-Vidal, J. M. Sabater, R. Morales, and F. J. Badesa, "Robust and cooperative image-based visual servoing system using a redundant architecture," *Sensors*, vol. 11, no. 12, pp. 11885–11900, 2011.
241. S. Hutchinson, G. D. Hager, and P. Corke, "A tutorial on visual servo control," *IEEE Trans. Robot. Autom.*, vol. 12, no. 5, pp. 651–670, 1996.
242. Y. Kang, C. Roh, S.-B. Suh, and B. Song, "A Lidar-Based Decision-Making Method for Road Boundary Detection Using Multiple Kalman Filters," *IEEE Trans. Ind. Electron.*, vol. 59, no. 11, pp. 4360–4368, 2012.
243. S. J. Julier and J. K. Uhlmann, "A new extension of the Kalman filter to nonlinear systems," in *Int Symp AerospaceDefense Sens. Simul Control.*, vol. 3, pp. 182–193, 1997.
244. A. Yilmaz, O. Javed, and M. Shah, "Object Tracking: A Survey," *ACM Comput. Surv.*, vol. 38, pp. 1–45, dec 2006.
245. A. M. Okamura, C. Simone, and M. D. O’Leary, "Force modeling for needle insertion into soft tissue," *IEEE Trans. Biomed. Eng.*, vol. 51, no. 10, pp. 1707–1716, 2004.
246. F. M. Hendriks, D. Brokken, C. W. J. Oomens, D. L. Bader, and F. P. T. Baaijens, "The relative contributions of different skin layers to the mechanical behavior of human skin in vivo using suction experiments," *Med. Eng. Phys.*, vol. 28, no. 3, pp. 259–266, 2006.
247. G. Konig, T. N. McAllister, N. Dusserre, S. A. Garrido, C. Iyican, A. Marini, A. Fiorillo, H. Avila, W. Wystrychowski, K. Zagalski, M. Maruszewski, A. L. Jones, L. Cierpka, L. M. de la Fuente, and N. L’Heureux, "Mechanical properties of completely autologous human tissue engineered blood vessels compared to human saphenous vein and mammary artery," *Biomaterials*, vol. 30, no. 8, pp. 1542–1550, 2009.
248. Y. Kobayashi, R. Hamano, H. Watanabe, J. Hong, K. Toyoda, M. Hashizume, and M. G. Fujie, "Use of puncture force measurement to investigate the conditions of blood vessel needle insertion," *Med. Eng. Phys.*, vol. 35, no. 5, pp. 684–689, 2013.
249. J. Smisek, M. Jancosek, and T. Pajdla, "3D with Kinect," in *Proc. IEEE Int. Conf. Comput. Vis.*, pp. 1154–1160, 2011.
250. C. Nadeau and A. Krupa, "Intensity-based direct visual servoing of an ultrasound probe," in *Proc. - IEEE Int. Conf. Robot. Autom.*, pp. 5677–5682, 2011.
251. K. Ferrara and G. DeAngelis, "Color flow mapping," *Ultrasound Med. Biol.*, vol. 23, pp. 321–345, jan 1997.

252. A. Pozniak and A. Zagzebski, "Spectral Doppler and Color," *RadioGraphics*, vol. 12, pp. 35–44, 1992.
253. D. J. Rubens, S. Bhatt, S. Nedelka, and J. Cullinan, "Doppler artifacts and pitfalls.," *Radiol. Clin. North Am.*, vol. 44, pp. 805–35, nov 2006.
254. Y. Wang, B. A. Bower, J. A. Izatt, O. Tan, and D. Huang, "Retinal blood flow measurement by circumpapillary Fourier domain Doppler optical coherence tomography," *J. Biomed. Opt.*, vol. 13, no. 6, p. 064003, 2008.
255. B. S. Ramamurthy and G. E. Trahey, "Potential and limitations of angle-independent flow detection algorithms using radio-frequency and detected echo signals.," *Ultrason. Imaging*, vol. 13, pp. 252–68, jul 1991.
256. W. Qiu, H. Zhou, M. Ding, and S. Zhang, "New real time needle segmentation technique using grayscale Hough transformation," in *Int. Symp. Multispectral Image Process. Pattern Recognit.* (J. Liu, K. Doi, P. S. P. Wang, and Q. Li, eds.), vol. 6789, pp. 67890Q–67890Q–8, International Society for Optics and Photonics, dec 2007.
257. J. Shi and C. Tomasi, "Good Features to Track," *IEEE*, pp. 593–600, 1994.
258. S. Y. Chen, "Kalman filter for robot vision: a survey," *Ind. Electron. IEEE Trans.*, vol. 59, no. 11, pp. 4409–4420, 2012.
259. M. Kaya and O. Bebek, "Needle Localization Using Gabor Filtering in 2D Ultrasound Images," in *Proc. IEEE Conf. Robot. Autom.*, pp. 4881–4886, 2014.
260. J. Matas, C. Galambos, and J. Kittler, "Robust Detection of Lines Using the Progressive Probabilistic Hough Transform," *Comput. Vis. Image Underst.*, vol. 78, pp. 119–137, apr 2000.
261. T. J. Persoon, S. Zaleski, and J. Frerichs, "Improving Preanalytic Processes Using the Principles of Lean Production (Toyota Production System)," *Am. J. Clin. Pathol.*, vol. 125, pp. 16–25, jan 2006.
262. G. Lippi and M. Plebani, "Laboratory medicine does matter in science (and medicine) ... yet many seem to ignore it," *Clin Chem Lab Med*, vol. 53, no. 11, pp. 9–10, 2015.
263. B. J. McKenna, "The Pathology and Laboratory Medicine Workforce Shortage: an Impending Perfect Storm," tech. rep., University of Michigan, 2012.
264. Labcorp, "LabCorp Hematology Automation Project," tech. rep., LabCorp, 2011.
265. M. Lyon and A. Lyon, "Evolutionary Economics of point-of-care testing," *Point Care J. Near-Patient Test. Technol.*, vol. 14, no. 4, pp. 108–109, 2015.
266. B. A. Ekberg, U. D. Larsen, and N. Fogh-andersen, "A Real Point-of-Care System for Complete Blood Counting," *Point Care*, vol. 4, no. 1, pp. 64–65, 2005.
267. D. Heikali and D. Di Carlo, "A Niche for Microfluidics in Portable Hematology Analyzers," *J. Assoc. Lab. Autom.*, vol. 15, pp. 319–328, aug 2010.
268. V. Bush and R. Cohen, "The Evolution of Evacuated Blood Collection Tubes," *Lab. Med.*, vol. 34, no. 4, pp. 304–310, 2003.

269. J. Antony and M. Kaye, "Methodology for Taguchi Design of experiments for continuous quality improvement," *Qual. World*, pp. 98–102, 1995.
270. M. Pierce, D. Yu, and R. Richards-Kortum, "High-resolution fiber-optic microendoscopy for in situ cellular imaging.," *J. Vis. Exp.*, pp. 8–11, jan 2011.
271. M. C. Pierce, S. E. Weigum, J. M. Jaslove, R. Richards-Kortum, and T. S. Tkaczyk, "Optical systems for point-of-care diagnostic instrumentation: analysis of imaging performance and cost.," *Ann. Biomed. Eng.*, vol. 42, pp. 231–40, jan 2014.
272. D. Y. Stevens, C. R. Petri, J. L. Osborn, P. Spicar-Mihalic, K. G. McKenzie, and P. Yager, "Enabling a microfluidic immunoassay for the developing world by integration of on-card dry reagent storage.," *Lab Chip*, vol. 8, pp. 2038–45, dec 2008.
273. P. Bhaskaram, N. Balakrishna, K. V. Radhakrishna, and K. Krishnaswamy, "Validation of hemoglobin estimation using Hemocue.," *Indian J. Pediatr.*, vol. 70, pp. 25–8, jan 2003.
274. W. Shi, L. Guo, H. Kasdan, and Y.-C. Tai, "Four-part leukocyte differential count based on sheathless microflow cytometer and fluorescent dye assay.," *Lab Chip*, vol. 13, pp. 1257–65, apr 2013.
275. W. Shi, H. L. Kasdan, A. Fridge, and Y.-c. Tai, "Four-part differential leukocyte count using microflow cytometer," in *IEEE 23rd Int. Conf. Micro Electro Mech. Syst.*, pp. 1019–1022, 2010.
276. N. Tatsumi and R. V. Pierre, "Automated Image Processing - Past, present, and future of blood cell morphology identification," *Interpret. Peripher. Blood Film*, vol. 22, no. 1, pp. 299–315, 2002.
277. J. Canny, "A Computational Approach to Edge Detection," *IEEE Trans. Pattern Anal. Mach. Intell.*, vol. PAMI-8, pp. 679–698, nov 1986.
278. B. Kumar, D. Joseph, and T. Sreenivas, "Teager energy based blood cell segmentation," *2002 14th Int. Conf. Digit. Signal Process. Proceedings. DSP 2002 (Cat. No.02TH8628)*, vol. 2, no. 3, pp. 619–622, 2002.
279. N. I. Nativ, A. I. Chen, G. Yarmush, S. D. Henry, J. H. Lefkowitz, K. M. Klein, T. J. Maguire, R. Schloss, J. V. Guarrera, F. Berthiaume, and M. L. Yarmush, "Automated image analysis method for detecting and quantifying macrovesicular steatosis in hematoxylin and eosin-stained histology images of human livers.," *Liver Transpl.*, vol. 20, pp. 228–36, feb 2014.
280. S. Eom, S. Kim, V. Shin, and B. Ahn, "Leukocyte Segmentation in Blood Smear Images Using Region-Based Active Contours," *ACIVS*, pp. 867–876, 2006.
281. G. Ongun, U. Hahci, K. Leblebicioglu, V. Atalay, S. Beksac, and M. Beksac, "Automated contour detection in blood cell images by an efficient snake algorithm," *Non-linear Anal.*, vol. 47, pp. 5839–5847, 2001.
282. I. Cseke, "A fast segmentation scheme for white blood cell images," *Proceedings., 11th IAPR Int. Conf. Pattern Recognition. Vol. IV. Conf. D Archit. Vis. Pattern Recognition.*, pp. 530–533, 1992.

283. L. Yang, P. Meer, S. Member, and D. J. Foran, "Unsupervised Segmentation Based on Robust Estimation and Color Active Contour Models," *IEEE Trans. Inf. Technol. Biomed.*, vol. 9, no. 3, pp. 475–486, 2005.
284. S. Nikhil, "Chronic Myeloid Neoplasms - Chronic myelogenous leukemia (CML)," 2011.
285. N. Ramesh, B. Dangott, M. E. Salama, and T. Tasdizen, "Isolation and two-step classification of normal white blood cells in peripheral blood smears," *J. Pathol. Inform.*, vol. 3, p. 13, jan 2012.
286. D. Huh, W. Gu, Y. Kamotani, J. B. Grotberg, and S. Takayama, "Microfluidics for flow cytometric analysis of cells and particles," *Physiol. Meas.*, vol. 26, pp. R73–98, jun 2005.
287. V. a. Kovalev, A. Y. Grigoriev, H.-S. Ahn, and N. K. Myshkin, "Segmentation technique of complex image scene for an automatic blood cell counting system," *Med. Imaging*, vol. 2710, pp. 805–810, apr 1996.
288. S. Lindberg, "A Novel Technology for 5-Part Differentiation of Leukocytes Point-of-Care," in *AACC CPOCT 24th Int. Symp.*, 2012.
289. C. E. Rippmann, P. C. Nett, D. Popovic, B. Seifert, T. Pasch, and D. R. Spahn, "Hemocue, an accurate bedside method of hemoglobin measurement?," *J. Clin. Monit.*, vol. 13, pp. 373–7, nov 1997.
290. K. Gregory, "HemoCue Hb201 Hemoglobin procedure," tech. rep., POCT Program Massachusetts General Hospital - Pathology Service, 2008.
291. T. Srivastava, H. Negandhi, S. B. Neogi, J. Sharma, and R. Saxena, "Methods for Hemoglobin Estimation: A Review of What Works ," *J. Hematol. Transfus.*, vol. 2, no. 3, pp. 2005–2006, 2014.
292. N. Otsu, "A Threshold Selection Method from Gray-Level Histograms," *IEEE Trans Syst. man, Cybern.*, vol. 20, no. 1, pp. 62–66, 1979.
293. S. Janhanmehr, K. Hyde, C. Geary, K. Cinkotai, and J. Maciver, "Simple technique for fluorescence staining of blood cells with acridine orange," *Tech. Methods*, pp. 926–929, 1987.
294. G. McLachlan and D. Peel, "Mixtures of factor analyzers," *Finite Mix. Model.*, pp. 238–256, 2000.
295. D. J. Guckenberger, T. de Groot, A. M.-D. Wan, D. Beebe, and E. Young, "Micromilling: A method for ultra-rapid prototyping of plastic microfluidic devices," *Lab Chip*, vol. 15, no. 11, pp. 2364–2378, 2015.
296. T. van Oordt, Y. Barb, J. Smetana, R. Zengerle, and F. von Stetten, "Miniature stick-packaging—an industrial technology for pre-storage and release of reagents in lab-on-a-chip systems," in *15th Int. Conf. Miniaturized Syst. Chem. Life Sci. Oct. 2-6, 2011, Seattle, Washington, USA*, vol. 13, pp. 2888–2892, 2011.
297. I. Michael, T.-H. Kim, V. Sunkara, and Y.-K. Cho, "Challenges and Opportunities of Centrifugal Microfluidics for Extreme Point-of-Care Testing," *Micromachines*, vol. 7, no. 2, p. 32, 2016.

298. J.-M. Park, Y.-K. Cho, B.-S. Lee, J.-G. Lee, and C. Ko, "Multifunctional microvalves control by optical illumination on nanoheaters and its application in centrifugal microfluidic devices.," *Lab Chip*, vol. 7, no. 5, pp. 557–564, 2007.
299. J. Siegrist, R. Gorkin, M. Bastien, G. Stewart, R. Peytavi, H. Kido, M. Bergeron, and M. Madou, "Validation of a centrifugal microfluidic sample lysis and homogenization platform for nucleic acid extraction with clinical samples," *Lab Chip*, vol. 10, no. 3, pp. 363–371, 2010.
300. S. Zehnle, M. Rombach, R. Zengerle, and N. Paust, "Microfluidic Centrifugo-Pneumatic Siphon Enables Fast Blood Plasma Extraction with High Yield and Purity," in *16th Int. Conf. Miniaturized Syst. Chem. Life Sci.*, pp. 869–871, 2012.
301. A. K. Au, H. Lai, B. R. Utela, and A. Folch, "Microvalves and micropumps for BioMEMS," *Micromachines*, vol. 2, pp. 179–220, 2011.
302. K. W. Oh and C. H. Ahn, "A review of microvalves," *J. Micromechanics Microengineering*, vol. 16, no. 5, pp. R13–R39, 2006.
303. S. E. Hulme, S. S. Shevkoplyas, and G. M. Whitesides, "Incorporation of prefabricated screw, pneumatic, and solenoid valves into microfluidic devices.," *Lab Chip*, vol. 9, no. 1, pp. 79–86, 2009.
304. X. Liu and S. Li, "An electromagnetic microvalve for pneumatic control of microfluidic systems.," *J. Lab. Autom.*, vol. 19, no. 5, pp. 444–53, 2014.
305. H. Cho, H. Y. Kim, J. Y. Kang, and T. S. Kim, "How the capillary burst microvalve works," *J. Colloid Interface Sci.*, vol. 306, no. 2, pp. 379–385, 2007.
306. K. Aran, A. Fok, L. a. Sasso, N. Kamdar, Y. Guan, Q. Sun, A. Ündar, and J. D. Zahn, "Microfiltration platform for continuous blood plasma protein extraction from whole blood during cardiac surgery.," *Lab Chip*, vol. 11, pp. 2858–68, sep 2011.
307. T. a. Crowley and V. Pizziconi, "Isolation of plasma from whole blood using planar microfilters for lab-on-a-chip applications.," *Lab Chip*, vol. 5, pp. 922–9, sep 2005.
308. A. J. Mach and D. di Carlo, "Continuous scalable blood filtration device using inertial microfluidics," *Biotechnol. Bioeng.*, vol. 107, no. 2, pp. 302–311, 2010.
309. D. Di Carlo, D. Irimia, R. G. Tompkins, and M. Toner, "Continuous inertial focusing, ordering, and separation of particles in microchannels.," *Proc. Natl. Acad. Sci. U. S. A.*, vol. 104, no. 48, pp. 18892–18897, 2007.
310. S. Yang, A. UNdar, and J. D. Zahn, "Blood Plasma Separation in Microfluidic Channels Using Flow Rate Control," *ASAIO J.*, vol. 51, pp. 585–590, sep 2005.
311. S. Yang, A. Undar, and J. D. Zahn, "A microfluidic device for continuous, real time blood plasma separation.," *Lab Chip*, vol. 6, pp. 871–80, jul 2006.
312. D. J. Laser and J. G. Santiago, "A review of micropumps," *J. Micromechanics Microengineering*, vol. 14, no. 6, pp. R35–R64, 2004.

313. A. Kazarine and E. D. Salin, "Volumetric measurements by image segmentation on centrifugal microfluidic platforms in motion.," *Lab Chip*, vol. 14, no. 18, pp. 3572–81, 2014.
314. D. C. Duffy, J. C. McDonald, O. J. Schueller, and G. M. Whitesides, "Rapid Prototyping of Microfluidic Systems in Poly(dimethylsiloxane).," *Anal. Chem.*, vol. 70, pp. 4974–84, dec 1998.
315. Y. Xia and G. M. Whitesides, "Soft lithography," *Annu. Rev. Mater. Sci.*, vol. 28, no. 12, pp. 153–184, 1998.
316. Contributor, "How Will Medtronic's Success in the Surgical Robot Market be Determined?," *Forbes*, 2016.
317. H. Mayer, F. Gomez, D. Wierstra, I. Nagy, A. Knoll, and J. J. Schmidhuber, "A System for Robotic Heart Surgery that Learns to Tie Knots Using Recurrent Neural Networks," in *Int. Conf. Intell. Robot. Syst.*, pp. 1521–1537, 2006.
318. A. Murali, S. Sen, B. Kehoe, A. Garg, S. Mcfarland, S. Patil, W. D. Boyd, S. Lim, P. Abbeel, and K. Goldberg, "Learning by Observation for Surgical Subtasks : Multilateral Cutting of 3D Viscoelastic and 2D Orthotropic Tissue Phantoms," in *IEEE Int. Conf. Robot. Autom.*, 2015.
319. L. Zappella, B. Béjar, G. Hager, and R. Vidal, "Surgical gesture classification from video and kinematic data," *Med. Image Anal.*, vol. 17, no. 7, pp. 732–745, 2013.
320. T. Osa, C. Staub, and A. Knoll, "Framework of automatic robot surgery system using Visual servoing," in *Intell. Robot. Syst. (IROS), 2010 IEEE/RSJ Int. Conf.*, pp. 1837–1842, 2010.
321. J. Van Den Berg, S. Miller, D. Duckworth, H. Hu, A. Wan, X. Y. Fu, K. Goldberg, and P. Abbeel, "Superhuman performance of surgical tasks by robots using iterative learning from human-guided demonstrations," in *Proc. - IEEE Int. Conf. Robot. Autom.*, pp. 2074–2081, 2010.
322. Y. LeCun, Y. Bengio, G. Hinton, L. Y., B. Y., and H. G., "Deep learning," *Nature*, vol. 521, no. 7553, pp. 436–444, 2015.
323. E. Holmes, "Theranos Science & Technology: The Miniaturization of Laboratory Testing," in *68th AACC Annu. Sci. Meet. Clin. Lab Expo*, 2016.
324. E. P. Diamandis and M. Plebani, "Theranos phenomenon Part 5: Theranos' presentation at the American Association for Clinical Chemistry Annual Conference 2016," *Clin. Chem. Lab. Med.*, vol. 54, no. 10, pp. 313–314, 2016.
325. M. Plebani, "Evaluating and using innovative technologies: A lesson from Theranos?," *Clin. Chem. Lab. Med.*, vol. 53, no. 7, pp. 961–962, 2015.
326. E. P. Diamandis, "Theranos phenomenon: Promises and fallacies," *Clin. Chem. Lab. Med.*, vol. 53, no. 7, pp. 989–993, 2015.
327. M. Li and E. P. Diamandis, "Theranos phenomenon - Part 2," *Clin. Chem. Lab. Med.*, vol. 53, no. 12, pp. 1911–1912, 2015.

328. M. Li and E. P. Diamandis, "Theranos promises a new era of preventive health care - but where's the physician?," *Clin. Biochem.*, vol. 48, no. 16-17, p. 1027, 2015.
329. M. Li and E. P. Diamandis, "Theranos phenomenon - Part 3," *Clin. Chem. Lab. Med.*, vol. 54, no. 5, pp. e145–e146, 2016.
330. J. Carreyrou, "A prized startup's struggles - silicon valley lab theranos is valued at \$9 billion but isn't using its technology for all the tests it offers," 2015.
331. J. Carreyrou, "Hot startup dials back lab tests at FDA's behest," 2015.
332. J. Carreyrou, "Theranos remains in a pause period," 2015.
333. E. P. Diamandis, "Theranos phenomenon part 4: Theranos at an International Conference," *Clin. Chem. Lab. Med.*, vol. 54, no. 8, pp. 243–244, 2016.
334. L. Grossman, "The Fall of Theranos and the Future of Science In Silicon Valley," *Time Mag.*, pp. 25–26, 2016.
335. D. Kirby, M. Glynn, G. Kijanka, and J. Ducrée, "Rapid and cost-efficient enumeration of rare cancer cells from whole blood by low-loss centrifugo-magnetophoretic purification under stopped-flow conditions," *Cytom. Part A*, vol. 87, no. 1, pp. 74–80, 2015.
336. M. G. Lee, J. H. Shin, S. Choi, and J. K. Park, "Enhanced blood plasma separation by modulation of inertial lift force," *Sensors Actuators, B Chem.*, vol. 190, pp. 311–317, 2014.
337. C. E. Nwankire, M. Glynn, D. Kirby, D. Kernan, I. Maguire, and J. Ducrée, "Size- and deformability-based particle sorting by strategic design of obstacle arrays in continuous centrifugal sedimentation mode," in *Solid-State Sensors, Actuators and Microsystems*, pp. 1854–1856, 2015.
338. M. Glynn, D. Kirby, R. Burger, and J. Ducrée, "Integration of Centrifugo-Magnetophoresis and Bright-Field Based T-Cell Enumeration for HIV Diagnostics in Resource-Poor Settings," in *17th Int. Conf. Miniaturized Syst. Chem. Life Sci.*, pp. 964–966, 2013.
339. R. Burger, D. Kirby, M. Glynn, C. Nwankire, G. Kijanka, R. Gorkin, and J. Ducree, "Centrifugal microfluidics for cell analysis," *Curr. Opin. Chem. Biol.*, vol. 16, pp. 409 – 414, 2012.